UNIVERSITY OF LIVERPOOL

The Energy-absorbing Characteristics of Novel Tube-reinforced Sandwich Structures

Thesis submitted in accordance with the requirements of the
University of Liverpool for the degree of
Doctor of Philosophy

by
Alia Ruzanna Aziz
June 2015

LIST OF PUBLICATIONS

JOURNALS:

- R.A. Alia, W.J. Cantwell, G.S. Langdon, S.C.K. Yuen and G.N. Nurick, The energy-absorbing characteristics of composite tube-reinforced foam structures, Composites Part B: Engineering, 61, 2014, pp127–135.
- R.A. Alia, Z.W. Guan, N. Jones and W.J. Cantwell, The energy-absorption characteristics of metal tube-reinforced polymer foams, Journal of Sandwich Structures and Materials, 17, 2015, pp74-94.
- R.A. Alia, Z.W. Guan, R. Umer, and W.J. Cantwell, The energy-absorbing properties of internally reinforced composite-metal cylinders with various diameter-to-thickness ratios, Journal of Reinforced Plastics and Composites, 34, 2015, pp731-741.
- R.A. Alia, Z.W. Guan, W.J. Cantwell and A.K. Haldar, A numerical study of the energy-absorption characteristics of metal tube reinforced polymer foams, Accepted for publication, Journal of Sandwich Structures and Materials, 2015.

CONFERENCE PROCEEDINGS:

- R.A. Alia, W.J. Cantwell and Z.W. Guan, The energy-absorbing behaviour of polymer foams reinforced with composite tubes, In: Presented at the ECCM16 Conference, Seville, 2014.
- A.K. Haldar, W.J. Cantwell, Z.W. Guan and R.A. Alia, The compressive characteristics of novel contour core, In: Presented at the ECCM16 Conference, Seville, 2014.

- W.J. Cantwell, R.A. Alia, Z.W. Guan, R. Umer and S. Balawi, The energy-absorbing characteristics of tube-reinforced foam structures. In: Presented at the 4th International Conference on Impact Loading of Lightweight Structures, Cape Town, 2014.
- R.A. Alia, Z.W. Guan, W.J. Cantwell and A.K. Haldar, Modelling of energy-absorbing behaviour of metallic tubes reinforced polymer foams, In: Presented at the ICCM2014 Conference, Fitzwilliam College, University of Cambridge, 2014.
- A.K. Haldar, W.J. Cantwell, Z.W. Guan and R.A. Alia, Mechanical characterization of CFRP contour core panels. In: Presented at the ICCM2014 Conference, Fitzwilliam College, University of Cambridge, 2014.
- R.A. Alia, Novel lightweight structures for blast protection, In: Presented at the UAE GSRC 2015, Abu Dhabi, 2015.
- R.A. Alia, Z.W. Guan, W.J. Cantwell and T. Boonkong, Modelling the macro-mechanical axial progressive damage of carbon/glass epoxy circular tubes, In: Presented at the 13th U.S. National Congress for Computational Mechanics USNCCM13, San Diego, 2015.
- T. Boonkong, Z.W. Guan, W.J. Cantwell and R.A. Alia, The mechanical behaviour of new hybrid sandwich structures based on corrugated-core and fibre metal laminates under low velocity impact loading, In: Presented at the 13th U.S. National Congress for Computational Mechanics USNCCM13, San Diego, 2015.

ACKNOWLEDGEMENTS

Firstly, I should like to express my deep and sincere gratitude to my supervisors, Professor W.J. Cantwell and Dr. Z.W. Guan for their supervision, inspiration and invaluable support throughout the research period. Also, they have been actively interested in my work and have always been available to advise me and provide assistance in numerous ways. I am also grateful for the scholarship, financial support and encouragement from the Universiti Kuala Lumpur (UniKL) and the Government of Malaysia. My sincere gratitude to the technical staff of the School of Engineering at the University of Liverpool, Mr. Stephen Pennington and Mr. Dave Atkinson for all of their help and support as well as my colleagues in the Structural Materials and Mechanics Research Group, including Dr. Mohd Zaki Hassan, Dr. Siti Hajar, Dr. Mohd Ruzaimi, Dr. Mohd Zuhri, Mr. Boonkong, Mr. Haldar, Mr. Jamil, Mr. Kanna, Mr. Nassier and Mr. Azimin. My appreciation is also due to all of the staffs and my friends at the university with whom I have been associating directly or indirectly during my stay in Liverpool.

I should also like to heartily thank my family, especially my mother and father, for all of the support, love, patience and encouragement that they have given me over the years. I am delighted to thank my sister Ayuni Athirah Smith and her husband Lewis Cyril Smith for their love and encouragement throughout my stay in Liverpool. Special thanks to my friends, Dr. Juriah Kamaludeen (Veterinary Parasitology, University of Liverpool) and Dr. Mazlinda Ibrahim (Mathematics, University of Liverpool), for their prayers, thoughts and motivation. I wish to thank my lovely husband, Mohd Naim Mohd Shabri, for his love, support, understanding and patience throughout the ups and downs in finishing this study.

ABSTRACT

This thesis presents the findings of a research study investigating the energy-absorbing characteristics of the foam sandwich cores reinforced with aluminium, steel and carbon fibre-reinforced polymer (CFRP) cylindrical tubes under quasi-static and dynamic loading conditions. Initial testing focused on establishing the influence of the length and inner diameter to thickness ratio (D/t) of the tubes on their specific energy absorption (SEA) characteristics. Following this, individual aluminium, steel and CFRP tubes were embedded in a range of foams with varying densities and the SEA was determined. The effect of increasing the number of tubes on the energy-absorbing response was also studied. In addition, preliminary blast tests were conducted on a limited number of sandwich panels. It has been shown that the stiffness of the foam does not significantly enhance the energy-absorbing behaviour of the metal tubes, suggesting that the density of the foam should be as low as possible, whilst maintaining the structural integrity of the part. Tests on the CFRP tube-reinforced foams have shown that the tubes absorb greater levels of energy with increasing foam density, due to increased levels of fragmentation. Values of SEA as high as 86 kJ/kg can be achieved using a low density foam in conjunction with dense packing of tubes. The SEA values of these structures compare very favourably with data from tests on a wide range of honeycombs, foams and foldcore structures. The crushing responses of the structures were predicted using the finite element method Abaqus and the predictions of the load–displacement responses and the associated failure modes are compared to experimental results. It is proposed that these models can be used for further parametric studies to assist in designing and optimising the structural behaviour of tube-reinforced sandwich structures.

CONTENTS

LIST OF FIGURES

LIST OF TABLES

CHAPTER 1

INTRODUCTION

This chapter contains a brief introduction to the research project and an overview of composite materials along with their applications. The rationale behind the need for an efficient and lightweight energy-absorbing structure will be presented. Additionally, the motivation, objectives of the research and significance of the study are discussed. The chapter closes with an overview of the thesis.

1.1 Overview

In recent years, there has been a growing interest in the research of sandwich structures, particularly in enhancing the energy-absorbing ability of lightweight structures. This is related to the increasing demand for developing better performing transportation systems that are more fuel efficient, without compromising passenger safety. This work presents contributions towards the development of lightweight tube-reinforced foam structures. Tube-reinforced foam is a material system whereby a metal or composite tube is inserted into a foam panel with a view to enhancing the energy absorption capabilities of the structure. The process of discovering tube-reinforced foam structures was achieved through extensive experimental testing and knowledge gathered from previous investigations. This study assesses the specific energy absorption (SEA) and the corresponding failure modes by executing a range of tests based on several parameters.

1.2 Light-weighting Technologies and Demands

These days, the need to travel has greatly increased the number of vehicles on the road. This increase is evident in virtually every transportation sector and consequently, accidents have become one of the major causes of death worldwide resulting in great economic loss to society. Typically, crash events involving a motor vehicle lead to a range of human injuries of varying severity. According to the annual road fatalities report by the UK Department of Transport [1], car occupants are at the greatest risk of road death compared to other road users, as shown in Figure 1.1. The majority of fatalities result from frontal impact car accidents followed by side impacts in second place.

In 2013, it was reported that 1,713 people in Great Britain were killed in road traffic accidents. Although road deaths have fallen every year since 2004 (with the exception of 2.8% increase in 2011), there is still a need to lower overall fatal accident rates [1]. Thus, improving vehicle safety is a key strategy used to overcome this significant problem. The main challenge is to employ materials and designs with the primary focus of dissipating high levels of crash energy in a controlled manner.

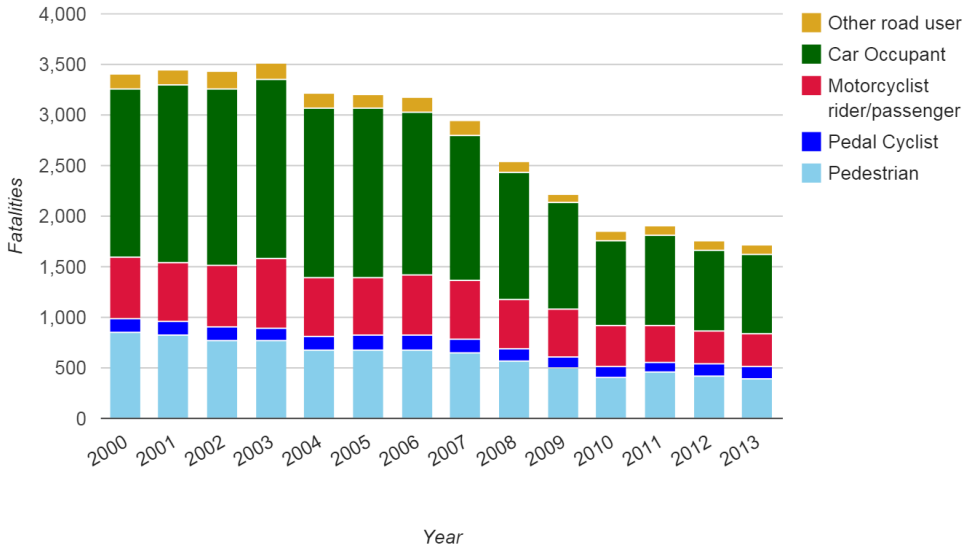

Figure 1.1 Number of fatalities resulting from road accidents in Great Britain [1].

Typically, metals are used in the passenger vehicles to deform in a progressive folding manner through a series of crumple zones designed to form upon impact, as shown in Figure 1.2. The outer parts of the vehicle absorb most of the energy which results in the deformation of the cabin area being limited. Here, the energy from the crash is transferred into the vehicle, rather than being transmitted to the occupants. This process of deformation in the vehicle will indirectly slow down the accident, thus lowering the impact experienced by the occupants.

As there are trends toward the use of composite materials in vehicle construction, manufacturers have to ensure that composite structures are capable of absorbing impact during an accident. In contrast to the folding deformation of metals, compression of most composites results in brittle failure [2]. Hamouda et al. [3] concluded that composite tubes are capable of absorbing more energy, since the specific energy was found to be about four times greater than metals. Composite materials absorb large amounts of energy by progressive crushing, which involves extensive localised microfracture and deformation in a crush zone which propagates through the structure.

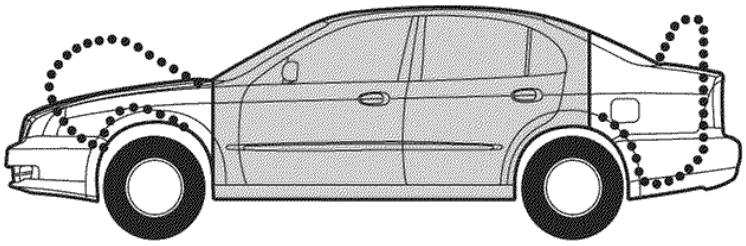

Figure 1.2 Deformation in the frontal and rear of a vehicle [4].

Performance and economy are the main concerns of manufacturers in designing a vehicle. A dramatic rise in fuel price in the UK of more than 70% from the year 2000 to 2011 has encouraged manufacturers to build highly efficient vehicles [5]. Figure 1.3 shows the trend in the average petrol and diesel prices in the UK from the year of 2000 to 2011. In addition, global energy consumption and greenhouse gas emissions have been impacted significantly by the transport sector. Based on the International Energy Agency (IEA), approximately 26% of the global energy production was consumed by the transport sector in 2001. Furthermore, the transport sector also consumed nearly 58% of the global oil production. One way to reduce energy consumption and the CO_2 emissions caused by the transport sector is through

reduction in the weight of vehicle [6]. Composite materials are very attractive, as they offer great potential for weight saving, while improving the performance of a structure. Weight saving in vehicles is crucial, as it helps to reduce fuel consumption, which reflects in the overall long-term cost. In the aircraft industry, composite materials have been rapidly replacing conventional metallic materials, even though they are more costly. Carbon composites, used as a replacement of metals for the aircraft floor have contributed to a 20% weight reduction, which is significant in the aircraft industry [7].

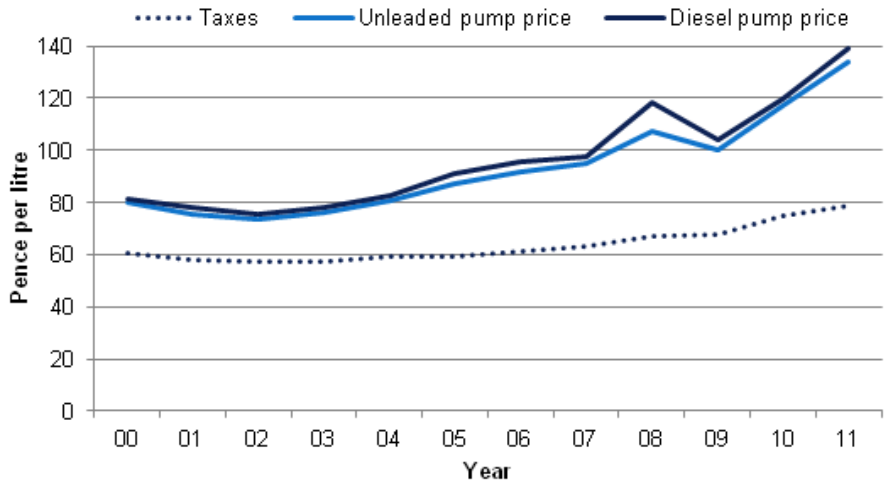

Figure 1.3 Fuel price in UK (average petrol/diesel), 2000-2011 [5].

1.3 Composite Materials

Composite materials are widely known for having the property of a high-strength to weight ratio compared to other conventional materials. The relative ease of combination of strong fibres surrounded by a weaker matrix material serves specific purposes and exhibits desirable properties. Their unique properties and adaptability to different conditions offer the possibility of new solutions to challenging engineering problems.

Apart from easy availability of raw materials, the flexibility in design and processing make composite materials the desirable choice for various applications. In general, the principal fibre materials are glass, carbon, aramid or Kevlar, boron and silicon [7]. Figure 1.4 shows the principle composition of composite materials. Depending on its application, the fibres are selected and the matrix holds them aligned in the important stressed directions, enabling the composite to withstand compression, flexural and shear forces as well as tensile loads.

Research and development are extensively being carried out to improve the efficiency, cost and reliability of composite materials, as they possess superior specific energy absorption properties and have been widely used for many purposes. Applications in various market sectors include aircraft, marine, automotive, construction and sports equipment as well as other markets [2], [8]. Advances in the production of high quality composite materials have resulted in better mechanical properties, durability and damage tolerance performance.

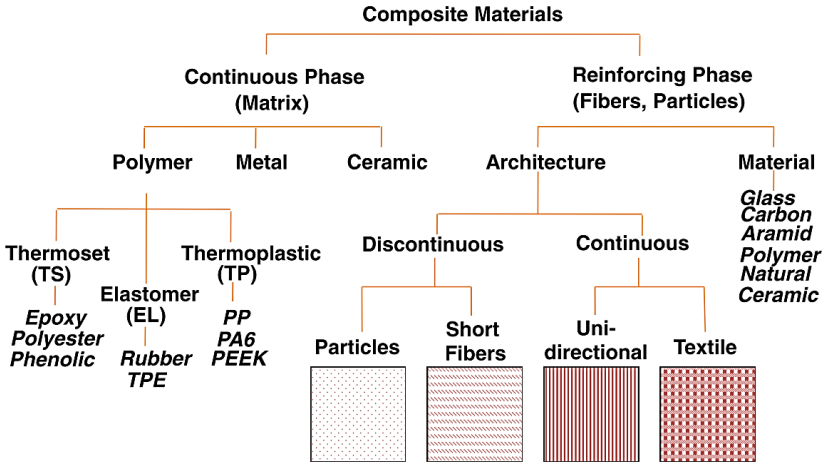

Figure 1.4 Principle composition of composite materials [9].

Components of a composite structure can be described as follows:

(a) **Fibre reinforcements** - Fibre reinforcements have high-stiffness and low-density. Their main function is to carry loads along their longitudinal directions. Carbon and glass are used extensively in polymer composites.

(b) **Matrix** - The functions of the matrix are to transfer stresses between the fibre reinforcements and to protect the fibres from any mechanical or environmental damage. The popular resin matrices are epoxy, polyester, polyurethane, and vinyl ester.

(c) **Cores** - The core material is generally a low-strength material with a high thickness. Commonly used core materials are polymer foams, woods and honeycombs. The core is bonded to the top and bottom skins to construct a sandwich structure.

(d) **Laminates** - Laminates are composite materials that are stacked in different layers/ plies of fabric reinforcement material to give them the specific character of a composite to perform a specific function. Composite fabric configurations are continuous fibre, plain woven or twill woven.

1.4 Application of Composite Materials

Composite materials are well known and have been around for over 50 years, with dramatic growth in the composites market observed in sectors such as aircraft, automotive, marine, wind energy and construction. The percentage of application in various industries is shown in Figure 1.5. Manufacturers in many industries are becoming increasingly interested in composite materials, as they are useful in all areas from simple to complex applications.

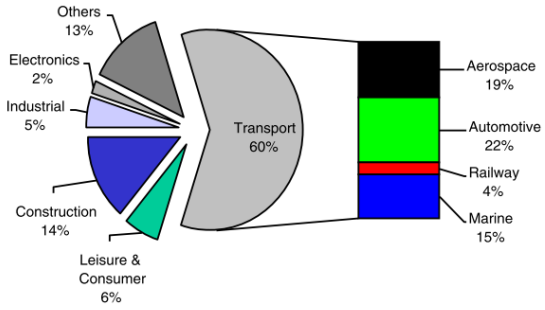

Figure 1.5 Application of composite materials in various industries [9].

A wide range of components in both military and civilian aircraft are made of composite materials, due mainly to their high-strength, high-stiffness and low-density characteristics. In addition, more modern aircraft are built using these lightweight materials since they offer greater flexibility as the materials can be tailored according to design requirements. The material can be designed to have a favourable coefficient of thermal expansion, to achieve a very high degree of dimensional stability, in order to withstand severe environmental conditions [10].

Commonly, the fibres used for composite materials are carbon, aramid and glass which are embedded in an epoxy resin with a high curing temperature of about 180°C. Carbon fibre reinforced polymer is used for elevated temperature applications. Over the years, composite materials have become one of the standard

materials in aircraft applications for the fuselage, engine, wings, tails, fairings, landing gear doors, floor panels, fan ducts and so on. For example, the latest Boeing 787, which is 20% more fuel efficient than similarly-sized aircraft, uses 50% of composite materials in its construction, for improved performance and reduced direct operating costs [11].

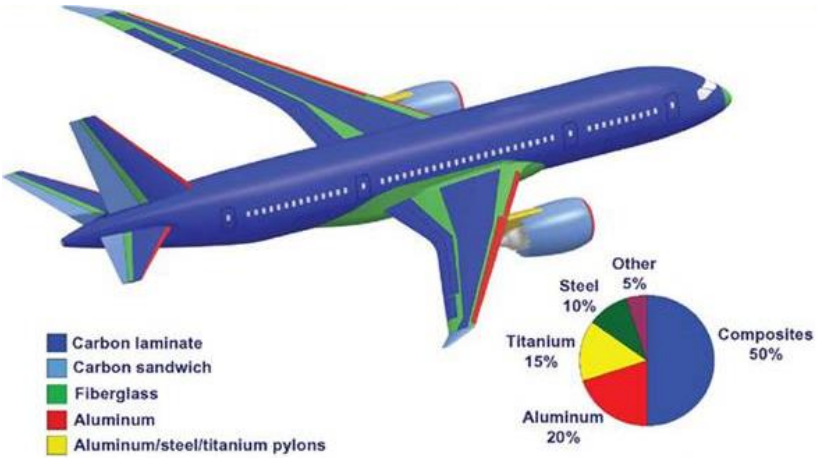

Figure 1.6 Materials distribution for the Boeing 787 [11].

Previously, the benefits of the low-weight and high-strength of advanced composites were not of great interest to general automotive applications, due to the high raw material costs when compared to existing materials. However, recent pressure for the production of fuel efficient vehicles, with lower emissions levels, means that composite materials have become the favourable option for the automotive industry.

Automotive manufacturers are continuously developing composite automotive structures for hood covers, bumpers, driveshafts, suspension arms, filament wound fuel tanks and so on. The majority of automotive applications involve glass reinforced polymers, as they are promising materials for weight reduction, given the relatively low-cost of the fibre, as well as the fast cycle time and ability to facilitate parts integration. Carbon fibre-reinforced composites are another option but they are

rarely considered to be acceptable in the automotive market, due to the extra cost in materials and in the manufacturing techniques. In the automotive sports industry, composite materials have been widely used in Formula 1 (F1) cars, where the resulting improvements to performance and safety issues are significant. Often in F1 accidents, the lives of drivers have been saved due to the enormous amount of impact energy the composite body can absorb [10].

The last decade has seen an increased use of composites in applications outside of the aircraft industry. The advanced development of composite materials can be seen in the marine industry, high-speed trains, underground trains, buildings and biomaterial in medical sectors. Sporting goods, such as bicycles, tennis and squash rackets as well as golf shafts are some of the major applications for composite materials. Interestingly, musical instruments such as guitars and violins are also made using composite materials, due to their superior quality and strength when compared to traditional wood and their very attractive lacquer finish. Other benefits associated with composites include their ability to cope with extreme environments, their reliability, maintainability, life cycle costs and service life extension [12].

(a) (b)

Figure 1.7 Composite applications in (a) bicycles and (b) musical instruments [12].

1.5 Motivation of the Research Work

With the increasing drive to develop high-speed and energy-efficient transport systems, there is an ever-growing need to protect occupants against extreme loading conditions, such as those associated with sudden deceleration or external impact. There have been many attempts to develop crashworthy structures, which are usually based on the introduction of either metallic or composite tubular structures at strategic locations within the design. The majority of studies published to date have focused primarily on metal or composite tubes and the use of foam as a filler in tubular energy-absorbing structures. Therefore, the aim of this research is to undertake an experimental and finite element investigation into the response of tube-reinforced foam structures subjected to axial compression loading.

1.6 Research Objectives

The primary objective of this research is to study the energy-absorbing characteristics of novel tube-reinforced sandwich structures. This research considers the influence of several parameters and concerns the failure behaviour of tube-reinforced foam structures.

Details of the objectives of this study can be summarised as follows:

i. To design and manufacture tube-reinforced foam structures.
ii. To investigate the mechanical performance of tube-reinforced foam structures subjected to quasi-static, dynamic and blast loading.
iii. To gain an in-depth understanding of the crushing response by examining the failure mechanisms in each structure.

iv. To compare the energy absorption capability of tube-reinforced foam structures with the current widely used sandwich structures.

v. To develop finite element models of tube-reinforced sandwich structures by proposing suitable constitutive models.

vi. To validate these finite element models using experimental results.

1.7 Significance of the Study

The outcomes of this research have wider significance and implications:

i. The use of tube-reinforced foam structures as energy-absorbers is innovative and this thesis contributes new knowledge for their design and use in sandwich applications.

ii. This study will be highly beneficial to applications in various engineering fields, particularly those that are related to energy-absorbing structures where safety and enhanced levels of protection are among the main interests.

iii. Deeper understanding of the relative effects of geometry, material and loading parameters on the tube-reinforced foam response make it possible to build lightweight energy-absorbing structures.

iv. The comprehensive resulting data generated from this research can be adopted for developing design guidelines for the use of tube-reinforced foam structures as efficient energy-absorber devices.

1.8 Thesis Outline

At the beginning of each chapter, an overview of the topic will be given. A summary, if relevant, will be presented at the end of each chapter to highlight the main findings. This thesis consists of six chapters as follows:

Chapter 1: Introduction; this chapter presents the significance of the research, as well as underlining its main objectives for accomplishing the benefits of this study.

Chapter 2: Literature Review; this chapter gives an overview of the experimental work, theoretical analysis and numerical modelling relevant to the topic. Attention is focused on material response under quasi-static and dynamic loading.

Chapter 3: Experimental Procedure; this chapter describes the specimen preparation and experimental testing (tensile test, burn-off test, quasi-static test, low-velocity impact test and blast test) conducted in this research.

Chapter 4: Results and Discussion of the Experimental Work; this chapter presents and discusses the results obtained following tests on energy-absorbing structures.

Chapter 5: Finite Element Modelling; this chapter presents the construction and constitutive models for the energy-absorbing structures. Numerical prediction values are validated and compared with experimental results.

Chapter 6: Conclusions and Recommendations; this chapter summarises the overall findings and observations based on the research performed. In closing, recommendations of possible future work will also be given.

CHAPTER 2

LITERATURE REVIEW

This chapter presents an overview of past and recent publications on the research and development of the subject area related to this thesis. First, the crashworthiness and energy absorption concept will be introduced. The second part reviews energy-absorbing structures with a special emphasis on experimental and numerical crushing responses and the associated techniques. This is followed by a discussion of the crushing characteristics of composite materials, triggering effects and the failure modes involved. The chapter closes with concluding comments on the main findings of these studies and their link to the subject matter of this thesis.

2.1 Crashworthiness

The transportation industry is clearly enormous encompassing the automotive, aircraft, train and ship industries. However, with the development of these industries, traffic accidents today are among the leading causes of death, particularly in highly industrialised countries. A car accident is a road traffic incident which usually involves at least one road vehicle being in a collision, which may result in property damage, injury and even death in serious situations. The Transportation Research Initiative at the University of Michigan [13] 2014 reported that the estimated world average is 18 fatalities from a vehicle accident per 100,000 individuals. The country with the highest rate reported was Namibia (45 fatalities per 100,000).

This has increased the need to research and develop energy-absorbing structures with the objective of minimising injury. In recent years, there has been an increased drive to develop high speed, energy-efficient transport systems. One of the most important aspects to be improved in crashworthiness is the ability to absorb the impact energy during a crash. Future structures must be designed to ensure light weight, high stiffness and strength without disregard for an impact damage tolerance and crashworthiness design for safety [14].

Many safety features have been developed, including front and side airbags, seat belts and anti-lock braking systems (ABS) to minimise injuries to the occupant from a collision. In addition, journal publications and international conferences on crashworthiness such as the International Journal of Impact Engineering, Thin-Walled Structures and Journal of Sandwich Structures were formed to provide scientists and engineers with a platform to explore, discuss and present their research in the field of structural crashworthiness [15].

In a crash analysis, the basic concepts of structural crashworthiness and impact mechanics need to be fully understood and extensively explored prior to developing efficient energy-absorbing systems. In theory, crashworthiness is a measure of the ability of a structure to absorb impact energy in a controlled manner. Thereby, it ensures that vehicle can absorb the majority of the crash energy and minimises the impact experienced by occupants, thus ensuring survival of the occupants [14].

The assessment of crashworthiness is determined by conducting a series of tests and numerical methods [15]. As an example in Figure 2.1, the crashworthiness of an aircraft fuselage structure is assessed by a vertical drop test on to solid ground. The lower part of the fuselage should absorb energy by sustaining the crush force and bringing the passenger compartment to rest with a minimum change in deceleration [16]. Commonly, severe head injuries have been the main cause of death in accidents [17]. Rapid changes in deceleration that could cause brain injuries should be avoided. The structure that lessens the effect of the impact is known as the energy-absorbing structure [15].

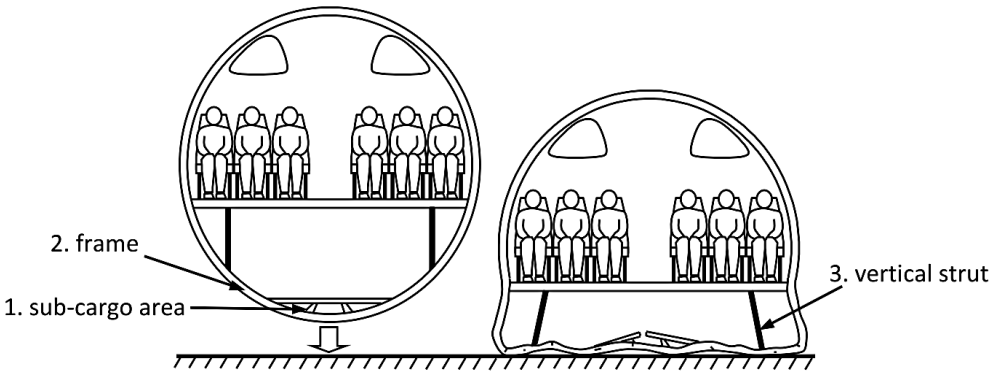

Figure 2.1 Crashworthiness of an aircraft fuselage structure is assessed by a vertical drop test on to solid ground [16].

2.2 Concept of Energy Absorption

2.2.1 Energy and Work

The energy of a body or a system refers to its capacity to do work and overcome resistance. In the context of crashworthiness, a structure with high energy will be able to deform extensively in order to dissipate the force. The kinetic energy or crush energy, E_{crush}, which is the energy of the motion of a body, is expressed by the following relationship [18]:

$$E_{crush} = \frac{1}{2}mv^2 \tag{2.1}$$

where m and v are the mass and velocity of the body respectively. The Law of Conservation of Energy states that the energy within a body or a system cannot be created or destroyed, and it may be transferred from one form to another, but the total amount of energy never changes. Hence, the transfer of energy from one body to the other is termed as work. In a collision, a force does work, W_{crush}, on a body, where a component of the body will be displaced in the direction of force. As illustrated in Figure 2.2, the product of the force, F_{crush}, exerted and the distance travelled, L_{crush}, is equal to the energy transmitted to a system and can be expressed by:

$$W_{crush} = F_{crush}.L_{crush} \tag{2.2}$$

where, from Newton's Second Law of motion, the acceleration, a is related to the mass, m, and the crush force, F_{crush} which is given by:

$$F_{crush} = m.a \tag{2.3}$$

The ideal energy absorber is defined as:

$$E_{crush} = W_{crush} = m.a.L_{crush} \tag{2.4}$$

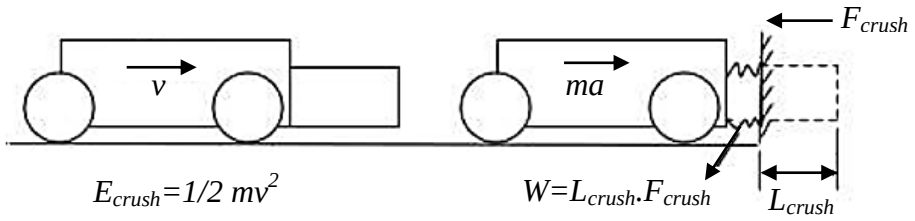

Figure 2.2 Energy and work of the crushing force [19].

An ideal energy-absorbing structure transforms all of the work input to work output. As the safety of occupants is the primary concern in crashworthiness, it is desirable to maximise the efficiency in the designing of energy-absorbing structures [20]. Efficiency is defined as the ratio of the work input into a system to the useful work output [19]:

$$Efficiency = \frac{Work\ done}{Energy\ used} \tag{2.5}$$

2.2.2 Load-displacement Curves

The energy absorption capability of a component can be analysed by conducting a compression test [21]. Quasi-static load-displacement curves are commonly studied to characterise the performance of a particular energy-absorbing structure. This test provides an indication of an actual response during the course of the crushing process. The crushing load and the estimation of the energy-absorbing capacity can be deduced from the load-displacement curves [22].

The experimental set-up for conducting quasi-static tests is usually simpler and easier to control than that for dynamic testing and enables clearer information about the failure mechanism. For that reason, the majority of previous studies aimed at understanding energy absorption capability start with a quasi-static test. The experimental arrangements of quasi-static and dynamic testing are presented in detail in Chapter 3.

Data obtained from the axial crushing of a structure is used to plot load-displacement curves, as shown in Figure 2.3. The first phase of a typical load-displacement curve starts with a rapid increase in load until it reaches a peak load. A slight drop in load will occur, this is followed by a sustained crushing zone. A sustained crush load will be observed as the material is continuously compressed until it reaches a point where the curve begins to rise up. This point is identified as the compaction or densification point, when sustained crushing is completed [23], [24].

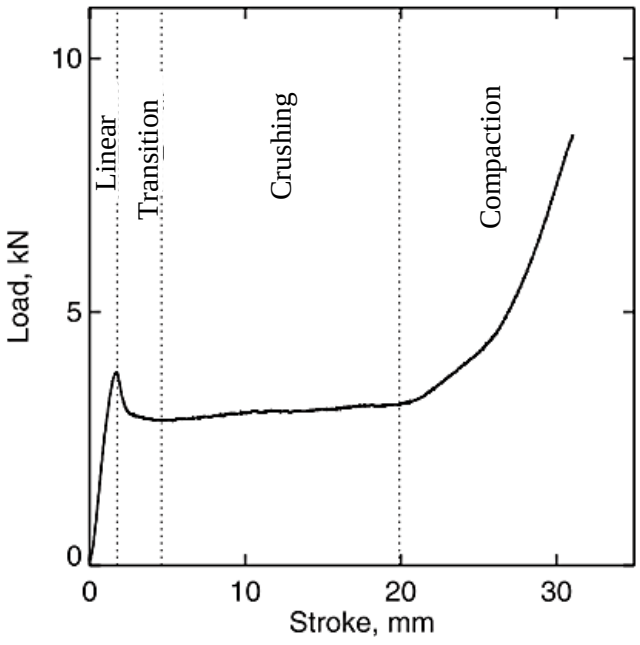

Figure 2.3 Typical load-displacement regions of a specimen tested under quasi-static compression [25].

The curve consists of a linear, a transition, a crushing and a compaction region, as shown in Figure 2.3. Laurin [25] in his study of energy absorption in sandwich panels with a composite-reinforced foam core, indicated the key points on graphs to show the point of initial damage, the maximum stress and the point of compaction. Commonly, specimens are compressed to about 80% of their original thickness [25].

2.2.3 Total Energy Absorbed

The area under the load-displacement curve following a compression test on a structure represents the total energy absorbed, E_A during progressive crushing is calculated up to the point before compaction occurs. The area under the load-displacement curve as shown in Figure 2.4 is given by [26]:

$$Total\ energy\ absorbed, E_A = \int_0^{S_b} P\ dS \tag{2.6}$$

where P is the applied load and dS is the incremental displacement during the crushing process. This calculation includes the energy at the initial stage of the crushing process. It is possible to obtain a more characteristic property of progressive crushing by considering the calculation to start at the point S_i. The equation can be expressed as:

$$E_A = \int_{S_i}^{S_b} P\ dS\ = \bar{P}(S_b - S_i) \tag{2.7}$$

where $\bar{P}$ is the mean crush load, while S_b and S_i are the crush displacement as indicated in Figure 2.4.

2.2.4 Specific Energy Absorption

The specific energy absorption parameter in kJ/kg unit is generally used to compare the results between different studies when lightweight design is the priority [16]. Higher SEA value indicates better efficiency in absorbing energy relative to weight. However, it is important that weight-saving does not comprise safety or structural performance. The specific energy absorption (SEA) of a structure is determined from the energy under the load-displacement curve (Figure 2.4) up to the densification point and the initial mass of the specimen, which is given by [26]:

$$SEA = \frac{Total\ energy\ absorbed, E_A}{Mass, m} = \frac{\int P\ dS}{m} \tag{2.8}$$

where P is the applied load, dS is the incremental displacement during the crushing process and m is the mass of the material.

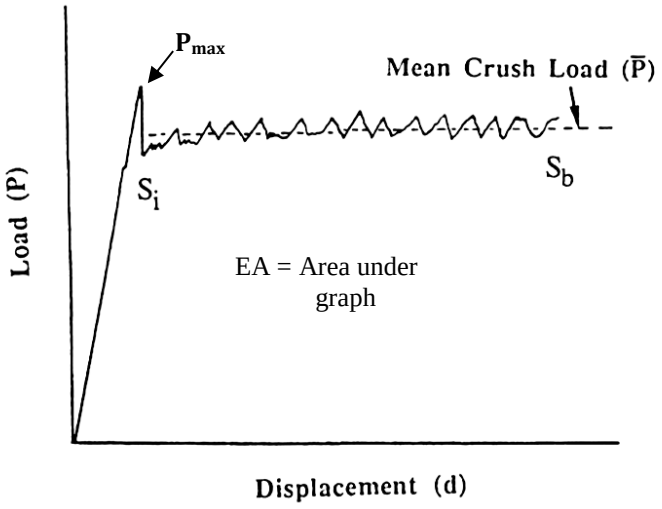

Figure 2.4 A load-displacement graph indicating the mean crush load and the energy absorption [26].

2.2.5 Ideal Energy Absorber and Efficiency

An ideal energy-absorbing structure collapses plastically over a long and flat plateau force, F_{pl}, producing the maximum area under the curve that is close to an ideal square wave [27], as shown in Figure 2.5. In designing an energy-absorbing structure, the plateau force level is purposely chosen to be lower than the force that can cause injury to the occupants.

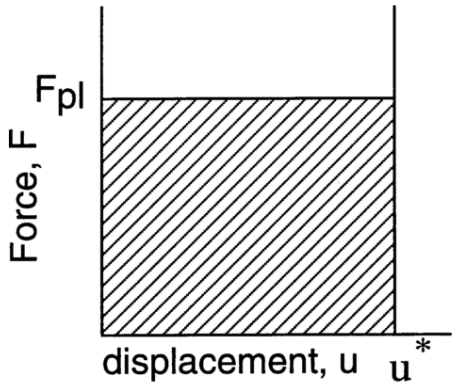

Figure 2.5 An ideal square wave load-displacement characteristic for an energy absorber structure [28].

Typically, energy absorbers have a characteristic maximum initial peak force value, P_{max}, that drops abruptly to the mean crush force value, $\bar{P}$, as shown in Figure 2.4. The larger the difference between P_{max} and $\bar{P}$, the greater the sudden increase in acceleration. This can potentially cause severe impact injuries to the occupants. The crush force efficiency, η, is defined as the mean crush force, $\bar{P}$, divided by the initial peak force, P_{max}, and is given by:

$$\eta = \frac{\bar{P}}{P_{max}} \tag{2.9}$$

where, for an ideal energy-absorbing structure, the crush force efficiency is $\eta = 1$. Another parameter that determines whether a structure is an ideal energy absorber is the ability of the structure to deform as compactly as possible following compression. The larger value of displacement, u^*, is desired to maximise the area under the graph. The stroke efficiency, S_E, is a measure of the total crush length relative to the original length, L, and is given as [29]:

$$S_E = \frac{u^*}{L} \tag{2.10}$$

In the case where the space available is limited for energy to be absorbed, the stroke efficiency is a useful measure. Clearly, crashworthiness of an energy absorber is maximised by ensuring that the difference between the peak force and the plateau force is at a minimum, allowing the structure to deform over as much of its length as possible. The aim of engineers is to produce an energy-absorbing structure that is close to an ideal square wave form [30], [31].

2.3 Energy-absorbing Structures

An energy absorber is a structure which transfers part or all of the kinetic energy into another form of energy. The energy converted can either be reversible, such as in the case of compressible fluids, or it can be irreversible, such as plastic dissipation of energy related to permanent deformation of the solid structure [32]. In this thesis, the main focus of the research is on the irreversible energy absorber associated with a collapsible system. Various types of irreversible energy-absorbing structures are used in engineering applications. The structures are made mostly from metal materials, nevertheless recent energy-absorbing structures are made of composite materials,

plastic, wood, natural fibres and many more potential materials that are still under development. Generally, those collapsible energy absorber structures in evidence in the literature are associated with one of the following categories [21], [33]:

a) cellular solids (polymeric foams, metallic foams, honeycombs)
b) thin-walled tubes (metals, composites)

Figure 2.6 shows the typical energy-absorbing structures in each category. Solid structures do not perform well in absorbing energy, due to their inefficient deformation manner and their weight. Hence, cellular solids and thin-walled tubes structures are commonly used, as these structures exhibit good energy-absorption characteristics [33]. Gibson and Ashby [21] defined cellular solids as a structure constructed as an interconnected network of solid struts or plates which form the edges and faces of cells. One of the distinct features of cellular solids is the outstanding strength and stiffness to weight ratio.

Thin-walled tubes subjected to axial crushing have been extensively employed as vehicle structural parts. They are specially designed to undergo controlled plastic deformation in the event of an accident. This is to prevent the passenger area from being deformed, therefore protecting the passengers. Thin-walled tubes are considered to be one of the most efficient energy absorbers as these tubes are lightweight, easy to fabricate, low cost and stable during crushing [34]. Typically, metal thin-walled tubes, such as aluminium, titanium and steel deform by extensive progressive folding [29], [35]–[37]. Whereas, fibre-reinforced composite tubes absorb energy by brittle fracture, fragmentation and lamina bending [33]. This section presents a comprehensive review of energy-absorbing structures found in the literature that are pertinent to this research.

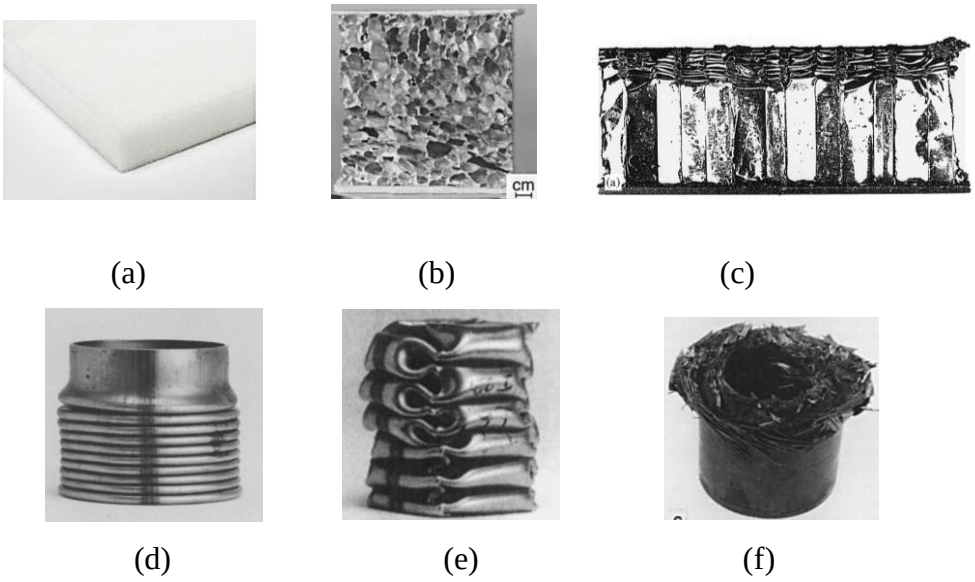

Figure 2.6 Typical energy-absorbing structures (a) polymeric foam [16], (b) metallic foam [38], (c) aluminium honeycomb [39], (d) circular aluminium tube [40], (e) square steel tube [34] and (f) carbon fibre/epoxy circular tube [41].

2.3.1 Sandwich Structures

Often, when bending stresses and super light-weight construction are the major concern in design, thin laminates are combined with a light weight core [42]. This is known as a sandwich structure, as shown in Figure 2.7. There are two basic principles in the construction of a sandwich structure. The first component consists of a thick core that is made of a light weight material or a structure with good properties under compression. The core can be in the form of a foam, a honeycomb, a functional core, wood or various types of lattice [9].

The second component is the stiff and strong skin on both sides, which protect the core. The core is bonded together with both of the skins using an adhesive. Sandwich panels imitate a solid I-beam structure, but at only a small fraction of the weight. It is

generally associated with low-weight and is a highly efficient structure for resisting bending and buckling. This has resulted in the growing popularity of sandwich panels, since they reduce weight and save fuel [32].

Sandwich panels are more efficient in absorbing energy compared to composite laminates [43]. The impact resistance of sandwich panels increases as the core thickness is increased [43]. Numerous energy-absorbing cellular core structures are used, either on their own or in a sandwich structure with face sheets for crash or blast loading conditions [16]. Gibson and Ashby [21] stated that foam materials have a unique characteristic, whereby they can deform extensively while sustaining low levels of stress before reaching the densification region.

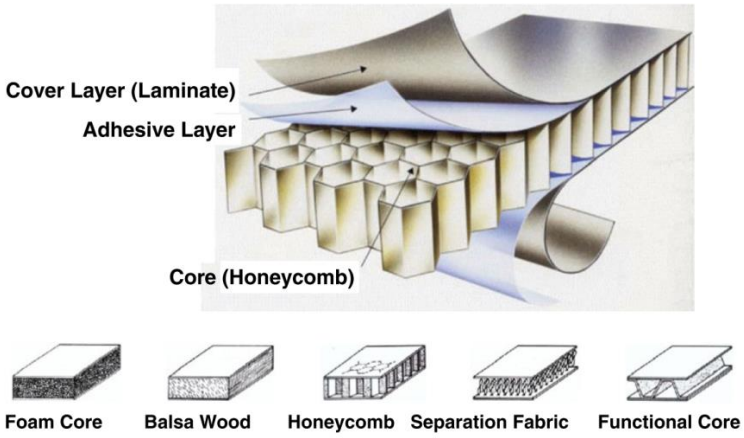

Figure 2.7 Construction of a sandwich structure [9].

Foam materials can be divided into two groups namely opened-cell and closed-cell, as shown in Figure 2.8. The construction of opened-cell foams consists of a single cell which is connected by beam-type edges such that only fluid can flow through the cells. Whereas, the cell walls of closed-cell foams are fully bounded, which obstructs fluid from flowing between the cells [21]. Both morphologies require space in the

cells to allow the foam to be compressible. The trapped air inside of the closed-cell foam causes bending, buckling and stretching of the cell walls, in order to absorb the impact energy. Closed-cell polymer foams are particularly useful in buoyancy applications due to their low density [21]. For opened-cell foams, the energy absorbed is dependent entirely on the mechanical properties of the foam [44].

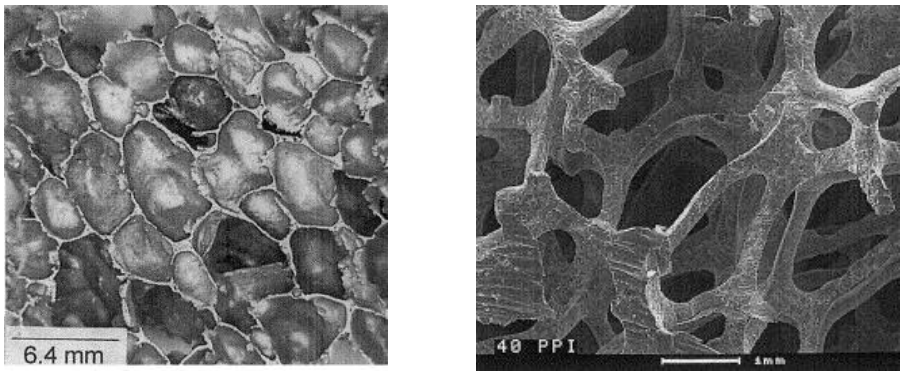

(a) (b)

Figure 2.8 The microstructures of (a) closed-cell and (b) opened-cell foams [45].

Polymeric foam is considered as an ideal energy absorber in a wide range of engineering applications where high energy absorption coupled with the low-weight characteristic is desired [14]. In addition, polymeric foams offer design flexibility as they can be easily shaped into a complex geometric, are capable of absorbing energy in any loading direction and are relatively cheap [21].

The most common polymers used for closed-cell foams are polystyrene (PS), polyvinylchloride (PVC), polyurethanes (PU) and polypropylene (PP). The opened-cell foams, which are generally soft and lightweight, are usually made of polyurethanes (PU) [46], [47]. Generally, closed-cell PVC foams are used as core materials for the manufacture of high-performance sandwich structures [48]. Lim et al. [47] studied the compressive behaviour of linear and crosslinked PVC foams.

They observed that linear foams have a similar cell size, but thicker cell walls as the density increases. In contrast, the denser crosslinked foams have a finer cell size distribution. Lim and his co-workers reported that the compressive properties of crosslinked foams are generally superior to their linear counterparts. The energy absorption of linear and crosslinked PVC foams increases with increasing foam density and is proportional to strain-rate [47]–[49].

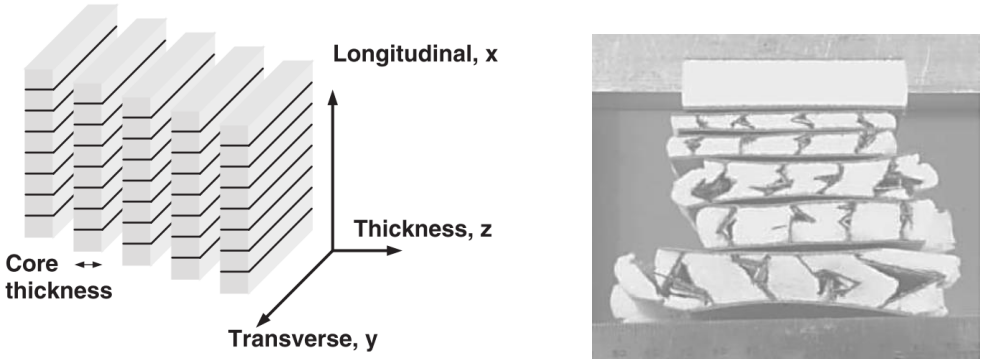

(a) (b)

Figure 2.9 Composite strip reinforced foam core (a) fabrication of core pieces from reinforced foam brick and (b) crushed specimens [25].

There have been several attempts [25], [50], [51] focused on the use of strips and pins in core materials with the aim of improving energy absorption. Laurin and Vizzini [25] added carbon/epoxy strips as reinforcements in a foam core. The cores were alternated with pre-preg layers, vacuum bagged and machined into individual panels, as shown in Figure 2.9(a). Despite the fact that they observed an increase in the sustained load, energy absorption was not maximised since the failure mode of the reinforcing strips did not occur in a controlled manner, due to buckling.

Many of the previous efforts [52]–[54] involving incorporation of reinforcements into sandwich cores have concentrated on edgewise compressive loading. This is

particularly for the impact resistance of sandwich panels to prevent the occurrence of buckling and skin debonding. Vaidya et al. [52] embedded titanium, pultruded glass/epoxy rods and steel Z-pins to reinforce foam cores. The rods penetrated into skins during curing process. It was found that the transverse stiffness was increased compared to unreinforced foam, due to the buckling of the pins.

Raju and Tomblin [53] investigated the energy absorption characteristics of stitched sandwich panels focusing on edgewise loading. The incorporation of stitches in the sandwich panels increased the energy absorption capability of the structure in the through-the-thickness direction. Since the energy absorption improved only slightly, it is not feasible for commercial use due to the impractical manufacturing techniques associated with incorporating the reinforcement to the core.

Found et al. [55] performed quasi-static compression tests to investigate the energy absorption properties of a polyurethane foam sandwich panel with four fibre-reinforced plastic tubular inserts incorporated within the core by resin transfer moulding technique. They reported that by ensuring progressive brittle failure of the structure, higher specific energy absorption values were obtained. As a result of variations in the fibre distribution within the inserts, the sandwich tended to collapse in a catastrophic failure mode, leading to lower SEA values. Found and his coworkers also noted that a less labour intensive design of the structure would be preferable, given the fabrication process was rather difficult.

2.3.2 Metal Tubes

There have been many attempts to develop crashworthy structures, most of which are usually based on the introduction of metallic tubular structures at strategic locations within the design. It is now well established that, if designed and used correctly, tube-like structures are capable of absorbing significant energy when loaded in an axial direction [34].

Research has shown that parameters, such as material properties, the geometry of the cross-section of tube, the diameter to thickness ratio and the loading conditions can affect the energy-absorbing capability of a metallic tube [56], [57]. It has been shown that thin-walled circular tubes frequently collapse in an axisymmetric mode (also known as a concertina mode) and non-axisymmetric modes (known as a mixed or a diamond mode) [40], [56]. Alexander [56] pioneered the development of theoretical methods to predict the mean collapse load for circular tubes failing in a concertina collapse mode. The expression for the mean crush load, P_{av}, is given as [56]:

$$P_{av} = 6Yt(Dt)^{1/2} \tag{2.11}$$

where t is the tube thickness, D represents the mean tube diameter and Y is the yield strength of the material. This equation can be used to predict the mean crushing load for materials with values of D/t below thirty [32]. During crushing of a metallic tube, energy is primarily absorbed through irreversible plastic deformation mechanisms that dominate the progressive buckling process [58].

Abramowicz and Jones [40] conducted a series of crushing tests on steel circular cylindrical shells loaded either statically or dynamically. They investigated [37] the transition of the axially crushed tubes from the Euler (global) bending mode to the progressive buckling mode. It was found that the transition point depends on tube

length, cross-section, material type, strain-hardening, strain-rate and end conditions. Abramowicz and Jones [40] improved the above expression and described the average crushing load of concertina deformation mode, P_{av}, by:

$$P_{av} = Yt(6Dt)^{1/2} + 3.44t \tag{2.12}$$

Reid [58] studied the plastic deformation mechanisms in axially-compressed metal tubes used as impact energy absorbers. He showed that a fundamental parameter is the ductility of the material, which permits large plastic strains to be generated and large geometry changes to be achieved without global failure. The experimental works by Reid were found to be in a good agreement with the predictions using Equation (2.12).

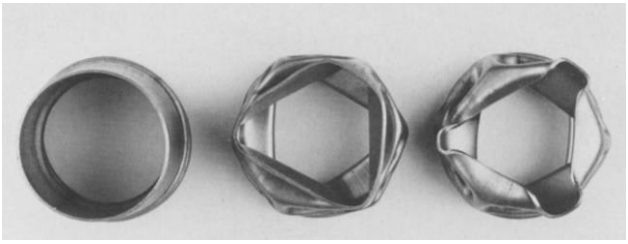

Figure 2.10 Crushed tube specimens exhibiting concertina (left) and diamond (centre and right) deformation modes [40].

Andrew et al. [59] categorised the axial crushing of circular tubes under quasi-static loading into seven different groups, i. euler bending, ii. simultaneous axisymmetric concertina, iii. concertina starting from one end of the tube, iv. non-axisymmetric diamond, v. simultaneous 2-lobe diamond, vi. concertina and 2-lobe; concertina followed by diamond and vii. tilting of tube axis. The concertina and diamond deformation modes are shown in Figure 2.10.

Andrew et al. [59] showed that thick circular tubes with a small D/t buckle in the axisymmetric concertina mode whereas thin circular tubes, with a high value of D/t, buckles in the non-axisymmetric diamond mode of deformation. As for tubes that tend to undergo this diamond fold mode of deformation, increasing the D/t ratio will result in an increase in the number of lobes. It was also found that the concertina mode shows a higher specific energy absorption than the diamond failure mode due to the greater degree of plastic deformation [59]. In contrast, Euler buckling, frequently associated with catastrophic failure, is the least efficient in absorbing energy [34], [37].

Jones [57] developed an energy-absorbing effectiveness factor, which was used to study the behaviour of thin-walled structural sections with different shapes, made from various ductile materials and subjected to static and dynamic axial loading. It was observed that a circular shape is the most efficient geometry, findings that agree with those of other researchers [60]–[63].

Hsu and Jones [35] conducted quasi-static and dynamic axial crushing tests on circular thin-walled sections based on a 304 stainless steel, a 6063-T6 aluminium alloy, and mild steel. It was found that although the stainless steel tubes absorbed the greatest level of energy, they are the least efficient in terms of the energy absorption effectiveness factor. Their results showed that aluminium tubes are the most efficient of the three materials in terms of the energy absorption effectiveness factor.

Guillow et al. [64] conducted quasi-static axial compressive tests on thin-walled circular aluminium (6060-T5) tubes, with a range of diameter to thickness, D/t ratios. The average crush force was non-dimensionalised and was plotted against the logarithm of D/t. It was found that test results for axisymmetric, non-symmetric and

mixed failure modes all lay on a single curve, yielding a simple empirical relationship based on the tube geometry. Similarly, Gupta and Venkatesh [65] investigated the influence of D/t ratio (mean diameter to thickness) on the energy absorbing characteristics of circular aluminium tubes at both quasi-static and dynamic impact rates of loading. Their results showed that the mean collapse load and initial peak load increased with decreasing values of D/t.

Davies and Magee [66] studied strain-rate effects in a 6061-T6 aluminium and concluded that the aluminium alloy exhibited a minimal strain-rate sensitivity in the range between $1.6x10^{-4}$ and 833 s^{-1}. Hsu and Jones [67] also showed that the yield stress and the ultimate tensile strength of aluminium 6063-T6 are rate-insensitive in the range of $5\times10^{-4}s^{-1}$ to $118s^{-1}$, this being consistent with the findings of Davies and Magee. The dynamic low velocity impact response is classified for speeds of those up to 10 m/s [68].

Langseth and Hooperstad [69] studied the static and dynamic performance of square thin-walled aluminium extrusions. Their results showed that the mean load under dynamic loading was higher than static loading, due to vibrations of impact rig structure, as the aluminium alloy was recognised as strain-rate insensitive in the range of strain-rate tested. Langseth and Hooperstad [69] stated that inertial effects are caused by vibrations of impactor during the folding process and also due to vibrations of platen fixed to the load cell. Increasing the mass of impactor will only increase the axial deformation without causing any significant changes in the force-displacement curve [36]. A cut-off frequency of 2.5 kHz was used to normalise the inertial effect in the dynamic test results [36]. As inertial effects within the device are relatively unimportant and the material is rate-insensitive, the dynamic kinetic energy is considered to be converted in a quasi-static deformation mode [69], [70].

Many researchers [58], [71]–[75] investigated foam–filled tube structures under axial crushing. Seitzberger et al. [74] studied the crushing characteristics of axially compressed steel tubes filled with aluminium foam. Their results showed that filling square tubes in this way improved their energy absorption efficiency. Aluminium foam was found to be enhancing thin-walled steel tube as the interaction between tube and aluminium foam changes the deformation mode of the steel tube [74]. Extensive experimental work [72], [76] was also undertaken to study the axial deformation behaviour of triggered, circular AA6060 aluminium extrusions filled with aluminium foam under both quasi-static and dynamic loading conditions. The crushing force increases as a result of the direct compressive strength of foam and interaction between the foam and tube wall. Design formulae for the prediction of the average force, the maximum force and the effective crushing distance were proposed.

Contradictory remarks have been made on the weight saving effectiveness of the foam filling technique. Kavi et al. [75] studied the energy absorption behaviour of a foam-filled thin-walled circular aluminium tube. It was shown that although foam filling resulted in a higher level of energy absorption than the sum of the energy absorptions of the tube alone and foam alone, it is less effective in increasing the specific energy absorption than simply increasing the thickness of the tube walls. Lampinen and Jeryan [73] investigated the effectiveness of polyurethane foam in energy-absorbing structures. They identified that below a certain tube wall thickness, inserting foam into a tube tends to increase the weight well above that of the original structure, therefore increasing the thickness of the tube is more effective [58], [73]. Foam filling is principally of benefit in tube sections made from high density, low strength materials such as mild steel [77].

Recent studies have investigated thin-walled tubes containing various metal cellular structures [78]. These studies explored the behaviour of both square [79] and circular [80] aluminium cross-sections. The work has shown that cellular structures can be more effective than filling the same tubes with aluminium foam, due to the difference in the collapse modes [79]. However, some researchers [81] have observed the contradicting behaviour for square tubes, which is likely to be due to the plethora of variables in these problems.

A number of researchers [36], [74], [82], [81] have investigated the axial crushing behaviour of metal tubes using numerical techniques and reported that the boundary conditions in numerical modelling influence the resulting crushing response. It is sufficient to construct only one quarter of the tube with symmetrical boundary conditions is applied to the model [74]. Galib and Limam [36] conducted both experimental and numerical studies on the crush behaviour of circular aluminium tubes subjected to axial compressive loading. They used a self-contact interface to prevent inter-penetration between adjacent folds of the tube surfaces in their models. They included initial imperfections to model the buckling deformation characteristics during the axisymmetric mode of deformation.

Further, Yan et. al [82] stated that the effect of varying the friction coefficient is insignificant, since energy absorption due to friction is a small part of the total energy. They calibrated the hardening data using uniaxial compressive test curves to model the isotropic elastic-plastic behaviour of the tube [81], [82]. The mesh convergence test is important in performing a finite element analysis of thin-walled tube, since various parameters, such as mesh size, element formulation and the number of elements through thickness, can affect the output [83].

Chen and Wierzbicki [81] investigated the axial crushing behaviour of single-cell, multi-cell and foam-filled thin-walled columns both analytically and numerically. They indicated that the SEA can be optimised by varying parameters, such as the sectional width, wall thickness and foam density. A theoretical solution for the mean crushing force of multi-cell sections was shown to be in good agreement with the numerical predictions.

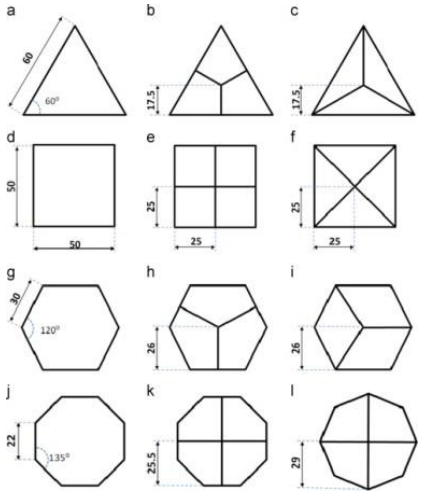

Figure 2.11 Geometry and dimensions of multi-cell thin-walled tubes with triangular, square, hexagonal and octagonal sections [78].

2.3.3 Composite Tubes

The superior energy-absorption and crashworthiness properties of composite materials has, in recent years, attracted the attention of a range of sectors, including those associated with the automotive and aerospace industries. In 2011, Lamborghini Aventador LP700-4 was the first production car to implement a fully carbon fibre monocoque design to absorb the crash energy [84]. Extensive testing on various types of tubular structure have shown that composite materials can offer extremely higher values of specific energy absorption (SEA) than metallic structures [2], [20], [22], [29], [31], [41], [85]–[90].

In a detailed review of energy-absorption in composite structures, Jacob et al. [2] determined that only 0.66 kg of a high-performance thermoplastic matrix composite is required to absorb the energy of a 1000 kg car travelling at 15.5 m/s (35 mph). Published values for the SEA of widely-used composites, such as carbon fibre reinforced epoxy, generally fall in the range 50 to 80 kJ/kg [22], [31],but can be as high as 110 kJ/kg [41].

A number of workers have investigated the influence of tube geometry on energy absorption [29], [88], [89]. Thornton and Edwards concluded that for a given fibre stacking sequence, glass, carbon and Kevlar fibre reinforced circular tubes out-perform their square and rectangular counterparts [88]. The corner sections contributed to higher crush load per unit mass compared to flat section in an approximately 3:1 ratio. The specific energy absorption was found to increase as rectangular < square < round [20], [91], [92].

Mamalis et al. [89] studied the crushing characteristics of a range of glass fibre reinforced composite structures with circular, square and conical cross-sections. They found that circular tubes offered the highest values of energy-absorption, with the crashworthiness of conical structures decreasing with increasing cone angle. It is now well documented that, when loaded in compression, composite cylinders fail in a splaying mode involving a multiplicity of failure modes such as delamination, fibre fracture, matrix cracking and fibre buckling [2], [22], [86], [90].

Farley [90] investigated the influence of specimen size on the energy-absorbing capability of carbon and Kevlar reinforced epoxy cylindrical tubes and observed that the ratio of the inner diameter of the tube to that of its thickness, (D/t), greatly influences the specific crushing stress (SCS) of the tube. An interesting result as shown in Figure 2.12 indicates that the value of SCS for carbon epoxy increased by approximately 180% as the value of D/t decreased from 120 to 3.8. This increase in crushing response at lower values of D/t was attributed to a reduction in interlaminar cracking. Here, it was argued that the buckling load of the fibre bundles increases with a reduction in the number and length of these interlaminar cracks [90]. The standard deviation, s_d, which quantifies the amount of variation of a set of data from the mean value as shown in Figure 2.12 is given [93]:

$$s_d = \sqrt{\frac{\sum(x - \bar{x})^2}{n - 1}} \tag{2.13}$$

where x is each value in the data set, $\bar{x}$ represents the sample mean and n is the number of values in the data set.

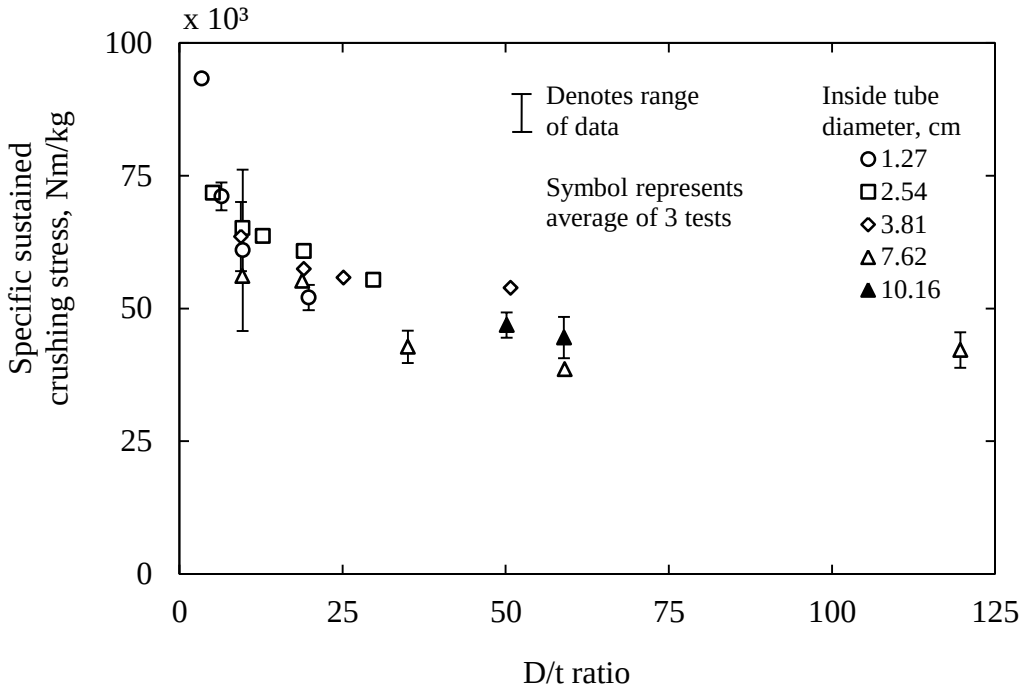

Figure 2.12 The effects of the D/t ratio on the energy absorption of carbon epoxy tubes [90].

Fairfull [94] investigated the effects of tube dimensions with diameter ranging from 16 to 50 mm on the specific energy of glass cloth epoxy tubes. It was also found that the values of specific energy absorption were influenced by the tube wall thickness and diameter, where the specific energy absorption increased with decreasing tube diameter. The mean load and SEA were found to be independent of the tube length.

Several studies have focused on the influence of strain-rate on the energy-absorbing capacity of composite tubes, with the results of these studies being somewhat contradictory [31], [95], [96]. For example, Schmueser and Wickliffe [95] reported reductions in energy absorption of up to 30% following impact tests on carbon, glass and Kevlar fibre tubes based on a [0^o, +/-45^o] configuration. In contrast, Thornton [31] observed very little change in the SEA of such tubes over a wide range of loading rates. Fibre reinforced polymer tube structures are capable of absorbing

significant energy under dynamic loading conditions, given that the tube is triggered to facilitate progressive crushing process by ensuring global failure modes do not occur [20]. Mamalis and his co-workers [97] concluded that dynamic crushing of circular fibreglass tubes dissipated less energy than quasi-static crushing.

The specific energy absorption of composite tubes is related to the fibre and resin type. Thornton et al. [20] found that carbon is better than glass fibre in absorbing energy, since the decrease in density of the fibre leads to higher specific energy absorption capability [14]. The fibre form such as, unidirectional continuous fibre and chopped random fibre, also has an influence on the specific energy absorption [20]. A number of investigators [22], [29], [88], [90], [95] have observed that carbon and glass fibre reinforced thermoset tubes undergo progressive crushing in splaying and fragmentation modes. Whereas, Kevlar fibre reinforced thermoset tubes which are more ductile, deform by progressive folding mode [20], [27], [98].

Hamada et al. [41] conducted axial compressive tests to investigate the energy absorption performance of carbon/epoxy and carbon/PEEK composite tubes made from unidirectional pre-preg materials. They found that due to the higher interlaminar fracture toughness of the thermoplastic PEEK, the energy absorption of carbon/PEEK (180 kJ/kg) was approximately three times more than a carbon/epoxy tube (53 kJ/kg). Additionally, the fibre orientation was found to represent an important parameter in Mode I interlaminar fracture testing [99], [100]. Mahdi and his co-workers [100] investigated different fibre orientations (0^o, 15^o, 30^o, 45^o, 60^o and 75^o) for E-glass woven fabric and epoxy resin produced using a wrapping process. They observed that tubes with fibre orientations of $15^o/75^o$ and $75^o/15^o$ are the most efficient in absorbing energy.

The fabrication of composites using a wrapping method produces high specific energy absorption characteristics compared to those produced using the wet layup process [14]. As for the type of resin for the glass fibre systems, the specific energy absorption tends to increase in the order of phenolic < polyester < epoxy resin [20]. Farley and Jones [101] concluded that in terms of energy absorption, the effect of matrix stiffness is insignificant for materials that crush in a brittle mode or by transverse shearing. Conversely, the matrix stiffness can significantly affect materials that collapse by lamina bending.

A number of researchers [20], [28], [77], [102] have investigated the effect of foam-filled fibre reinforced polymer tubes on the energy absorption. As the crushing mode of low-density with high-strength FRP composite tubes are generally stable, the presence of foam was found to be not weight effective [20]. Palanivelu et. al [102] identified the effect of polyurethane foam–filled glass/polyester tubes based on nine different shapes with 1 and 2 mm wall thicknesses. They found that the foam provided additional wall support and allowing the tubes to crush progressively, as the tubes would fail catastrophically without foam filling. This was beneficial most notably for square and hexagonal shapes with a 1 mm wall thickness. However, in the case of composite tubes which crush progressively without foam filling, a reduction in the specific energy absorption was observed. This is related to suppression of circumferential delamination failure and subsequent fibre fracturing. Consequently, the foam caused a higher peak force for each composite tube [102].

There is a need for reliable finite element models of composite materials in crashworthiness design, given that experimental testing is time-consuming and rather costly. Current numerical codes for metallic materials are well understood and capable of predicting the large plastic deformations and the crushing responses by

applying elastic-plastic material models [81], [82]. However, difficulty of reproducing complex composite failure mechanisms causes the computational models of composites are much more challenging than simulating conventional metallic materials [98], [103]–[105].

Generally, finite element models for crushing of composite materials can be classified into two main groups [106], these being micro-mechanical and macro-mechanical, as shown in Figure 2.13. The micro-mechanical [107], [108] finite element models focus on a very detailed crushing process by adapting an excessively fine solid 3-D mesh to accurately reproduce the matrix crack propagation phenomenon [106]. As the default Abaqus interface is limited, the material model needs to be defined using VUMAT (a routine that describes a custom material model in Abaqus/Explicit) to compute damage independently for the fibres and matrix [108], [109]. Due to the complexity of the model, this analysis involves a very high number of elements, hence longer model run-times and larger disk space requirements. It is recognised that the computational effort is very high for the construction of composite laminates using solid elements for each ply and is not a viable option for engineering crash analysis. The micro-mechanical approach is usually used in the case where the study of a single crack growth is the main attention [106].

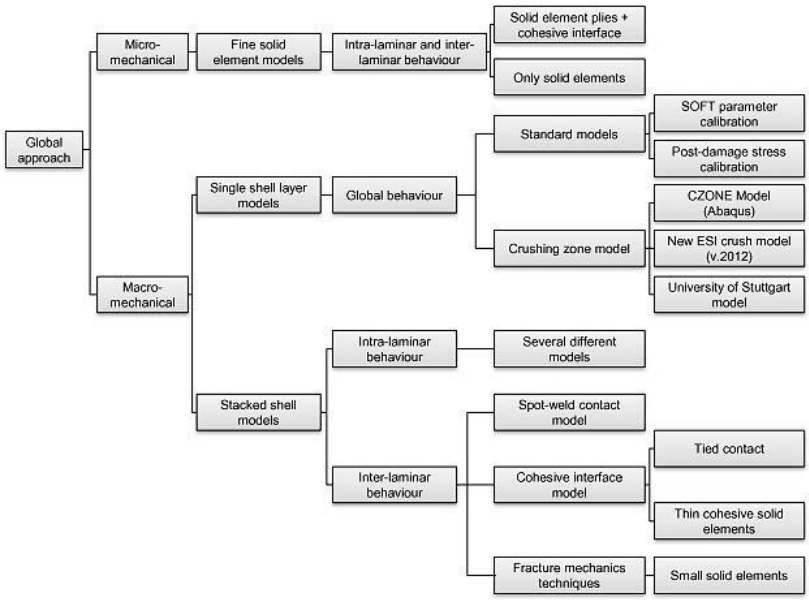

Figure 2.13 Classification of composite crushing numerical models [106].

The second category, the macro-mechanical technique involves a simpler approach, consisting of single or stacked shell elements. The single shell layer is useful in the case where only load and energy prediction are required, since this approach is incapable of modelling the interlaminar collapse mode. The Hashin failure criteria can be employed in this modelling technique. However as it is limited to plane-stress formulae, the Hashin failure criteria is not available for 3D solid elements [110], [111]. The single shell layer model combined with a soft parameter calibration is an attractive modelling method due to its simplicity and computational effectiveness.

Alternatively, add-on application to the commercially available software, such as CZONE Model in Abaqus, allows modelling of the crushing zone. Nevertheless, CZONE is only applicable for materials that crush and continuously sustain a resistive force in the crush region. For that reason, only limited materials can be modelled accurately using the CZONE add-on [111], [112].

Stacked shell models consist of distinct layers of shell elements attached together using cohesive elements between the layers to represent the matrix phase properties. The stacked shell model offers a better physical representation, however, the computational time increases as the number of shell layers stacked together is increased. At present, a limited number [106], [113]–[115] of finite element studies using the Abaqus code are available in the literature, on the subject of the progressive crushing of composite tubes. Bussadori et al. [106] presents FE models using stacked shell and crushing zone techniques in order to simulate the crushing of CFRP tubes. The first approach had significantly underestimated the results, which is due to the inability of the model to reproduce the collapse mechanisms. The crushing zone technique does not attempt to replicate the complex crushing phenomena as the element is eroded from the model when it reaches the maximum allowed value. This technique was able to produce the desired results and the computational time was found to be at least three times better than the stacked shell model.

Palanivelu et al. [113] attempts to simulate circular and square pultruded glass/polyester tubes subjected to axial crushing. It was found that the FE models were not able to predict the axial cracking throughout the crushing process. A further investigation [114] conducted emphasises on the importance of considering the pre-defined seam elements to achieve appropriate deformation patterns. Among other findings, Palanivelu et al. remarks that it is very important to fully understand the failure patterns before implementing the design architecture of an energy-absorbing structure in the FE models. The general conclusion of these studies is that the predictive model is reasonably successful, although an accurate numerical prediction remains challenging. Therefore, numerical studies help to gain an insight into the overall response but experimental testing is still required.

2.4 Failure Mechanisms of Composite Tubes

Numerous parameters including the initial peak load, the sustain crushing load and the stroke displacement are considered in typical crashworthiness designs [25]. The energy absorption capability of a structure is characterised by the area under load-displacement curve, which is heavily dependent on the failure mechanisms. The modes of failure which can be divided into catastrophic failure and progressive failure, are described in detail here. This section will be followed by an explanation of the trigger mechanisms and characteristic types of progressive crushing mode in composite tubes.

2.4.1 Catastrophic and Progressive Failure

An efficient design for an energy-absorbing structure needs to avoid any catastrophic failure modes [104]. This is due to the fact that during catastrophic failure, a sudden increase in load occurs in a short period of time, this is then followed by a rapid drop to a low-post failure load. Hence, in a vehicle crash event, catastrophic failure will cause greater impact to passengers as the structure will absorb much less energy.

Figure 2.14 shows a comparison between typical load-displacement curves for catastrophic and progressive crushing of a composite profile. Catastrophic failure is characterised by mid-plane fracture [116] or longitudinal cracking [102]. Even though the structure can be designed to take the load associated with catastrophic failure, it is likely to be much heavier than a structure designed to react to load associated with a progressive crushing. Given that the area under the load-displacement curve represents the absorbed energy, it is desirable to design a structure that will collapse progressively [104].

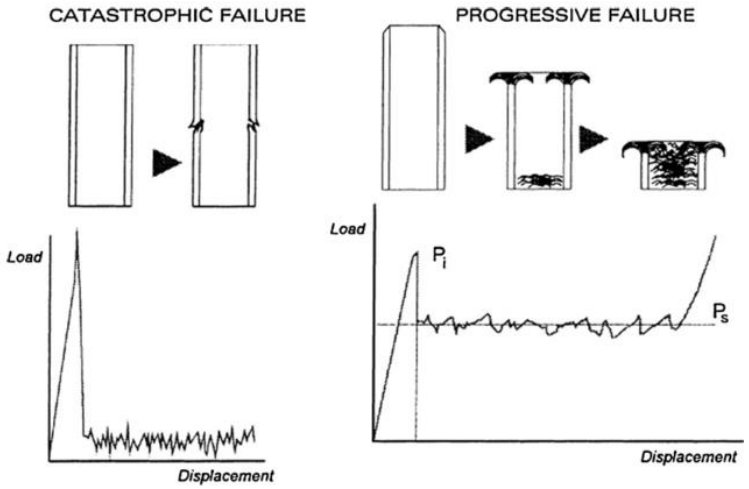

Figure 2.14 Comparison between catastrophic and progressive failure [117].

Many researchers [2], [20], [22], [31], [88], [90], [101] have studied the energy absorption capability of composite materials. The general conclusion of these investigations is that composite materials can be efficient energy-absorbing materials, even though they exhibit very different crushing modes to those of metallic materials. Figure 2.15 shows typical load–displacement curves obtained from crushing of composite and aluminium circular tubes. Previous experimental tests have shown that metallic materials progressively absorb impact energy by forming folds, whereas composites absorb energy by undergoing fracture and delamination [22].

However, Farley [90] and Beardmore [27] reported that ductile composite tubes such as those based on Kevlar will crush in a similar mode to metallic tubes. They observed that when a tube fails by progressive crushing, it exhibits a larger area under the load-displacement curve, thus giving a higher level of energy absorption. Progressive crushing will also yield lower values of the ratio of peak load to mean crush load, compared to structures that fail catastrophically.

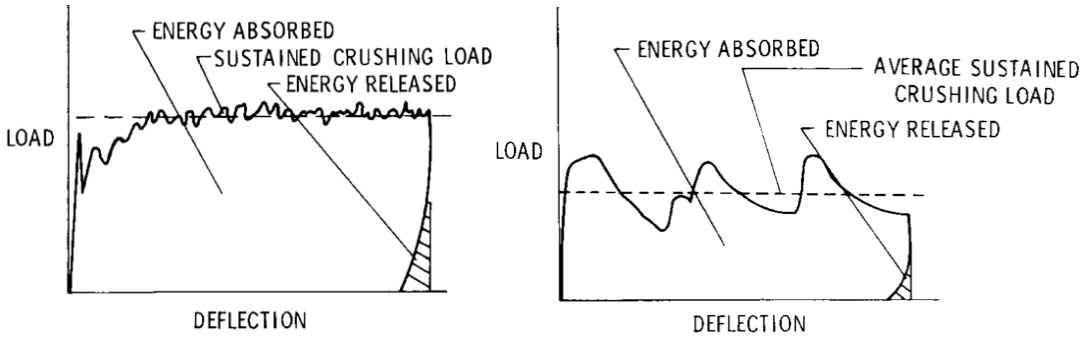

(a) (b)

Figure 2.15 Typical load–displacement curves obtained from crushing of (a) a composite and (b) aluminium circular tubes [22].

2.4.2 Trigger Mechanism in Composite Tubes

Progressive crushing in composite tubes can be achieved using a proper trigger mechanism. No chamfering will be needed on metallic tubes because the tubes will not fail catastrophically as observed with composite tubes [101]. The function of the trigger is to act as a stress concentrator to initiate failure of the structure. The most widely used method for triggering is chamfering one end of the composite tube [2], [22], [31], [88], [104], [118]. Chamfer angles between 30^o to 45^o are recommended to initiate stable crushing [119].

In a study on the effects of chamfer angle on energy absorption, a smaller drop after peak load and insignificant increase in specific energy absorption were observed in tubes with a 35^o chamfer compared to those with a 45^o chamfer [120]. Palanivelu et al. [118] tested composite tube with a chamfer of 45^o and a tulip pattern with an included angle of 60^o between the edges, as shown in Figure 2.16. They reported that the tulip pattern absorbed less energy compared to the 45^o chamfer around the edge of the circular tube as the 45^o chamfer triggers a uniform circumferential delamination and continuous axial cracks within the tubes. In both cases, crushing

could be initiated without causing catastrophic failure. Local failure will occur in composite tubes where small interlaminar and intralaminar cracks are formed, since load is applied to the edge of the crushing initiator. The length of cracks produced will determine the resulting crushing mode of the material.

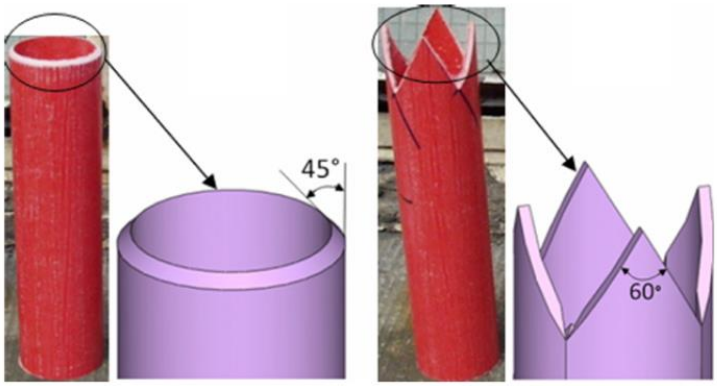

(a) (b)

Figure 2.16 Composite tube specimen triggering method (a) a 45^{o} chamfer (b) a tulip pattern with an included angle of 60^{o} between the edges [118].

In some cases, such as for ductile and certain brittle fibre reinforced composite materials, the load applied to the crushing initiator will cause the material to deform plastically and fail in a local buckling mode. Progressive crushing of a tube is dependent on the fibre and matrix properties and the geometrical structure of the tube [20]. For thin-walled tubes, a lower load is required to cause the wall to buckle, thus the tube will start to buckle before the onset of progressive crushing. While in thick-walled tubes with diameter to wall thickness ratios of the order of unity, the interlaminar cracks do not spread across the crushing initiator. As a result, the stress concentration in circumferential direction increases, reaching the material strength, thereby causing those tubes to fail. Hence, it is quite challenging to initiate progressive crushing for very thin or thick-walled tubes [104].

2.4.3 Characteristics Types of Progressive Crushing Modes

Four kinds of progressive crushing were reported by Farley and Jones [101], these being a transverse shearing or fragmentation mode, a lamina bending or splaying mode, a brittle fracturing and local buckling also known as progressive folding. These crushing modes are very useful in designing a structure to decelerate an object, particularly during an impact event or a crash. Both ductile and brittle fibre reinforced composites exhibited the local buckling modes, however, only brittle fibre reinforced composites can crush in transverse shearing and lamina bending modes. Generally, the combination of shearing and lamina bending crushing modes will result in brittle fracturing. In this section, each mode will be described and further discussed.

2.4.3.1 Transverse Shearing or Fragmentation Mode

The transverse shearing or fragmentation mode can be identified by a wedge-shaped laminate cross-section. When a composite tube is crushed, it produces one or multiple short interlaminar and longitudinal cracks that form partial lamina bundles. Farley and Jones [101] stated that tubes that crush in a transverse shearing mode have a high stiffness and a low failure strain. This failure mode is only exhibited by tubes that are fabricated using brittle fibres. The compression loads results in an uneven load transfer to the composite tube, which form scalloped surface as the tube is crushed, as shown in Figure 2.17. In a composite tube, the number, location and length of the cracks are dependent on the tube geometry and material properties. The process of fragmentation exhibits longitudinal and interlaminar cracks lengths, which are less than the thickness of the laminate [104].

The lamina bundles behave as columns in resisting the load applied. As the crushing load is applied to a tube surface, the interlaminar cracks propagate until wedge-shaped cross section is formed, as shown in Figure 2.17. The main contributors to the energy absorption mechanism in this failure mode are the interlaminar crack growth and fracture of lamina bundles. Interlaminar crack growth is determined by the mechanical properties of the matrix, fibre orientation of the laminate and the failure strain of fibres oriented in the circumferential direction [103].

2.4.3.2 Lamina Bending or Splaying Mode

The lamina bending or splaying mode is characterised by very long interlaminar and intralaminar cracks. The lamina bundles will not fracture as it undergoes bending deformation. During this failure mode, the structure absorbs energy mainly as the growth of matrix cracks. In addition, the crushing of composite tube also creates friction as the lamina bundles bend. The bending of lamina generates friction between adjacent lamina bundles and as it slides along the face of the loading surface [103].

In the lamina bending mode, mechanisms that determine the crushing processes in a structure are interlaminar, intralaminar and frictional effects. Crack growth is similar to the transverse shearing mode but the length of the crack is greater in the lamina bending mode, as shown in Figure 2.17. The level of friction between the composite surface and the loading surface, and among the adjacent lamina, can be a function of crushing speed. Thus, energy absorption will also be influenced by the variations in the crushing speed [121].

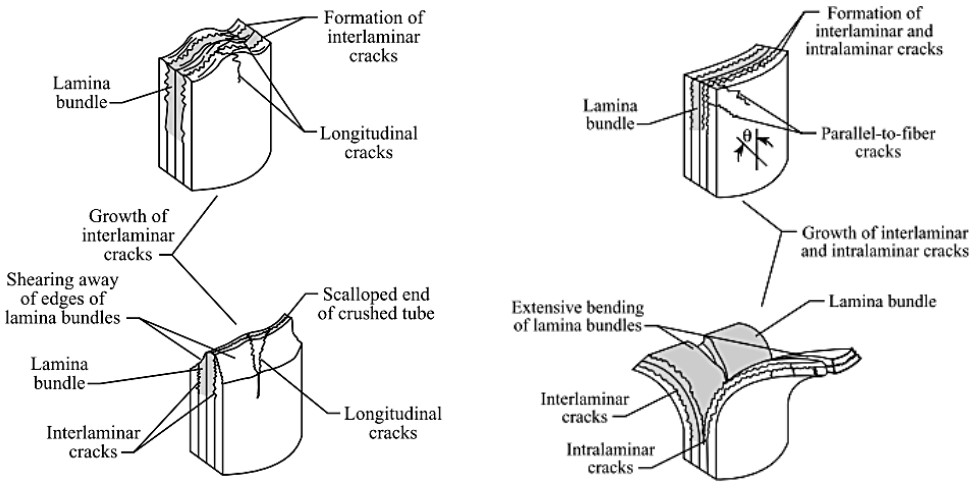

(a) (b)

Figure 2.17 (a) Fragmentation and (b) splaying crushing modes [104].

2.4.3.3 Brittle Fracturing Mode

The brittle fracturing crushing mode occurs from the combination of the transverse shearing mode and lamina bending mode. Previous researchers [8], [30], [92], [102], [103] have noted that this crushing mode is observed mainly in brittle fibre tubes. Formation of interlaminar, longitudinal cracks and scalloped crushing surface in brittle fracturing mode are shown in Figure 2.18. The main energy absorption mechanism is by fracturing of lamina bundles. The crushing efficiency is greatly influenced by the length of fractured lamina bundles, where shorter fractured lamina will result in higher efficiency of energy absorption [2].

Lamina bundles in brittle fracturing mode experience some bending, where the lamina bundles usually fracture at the end of the tube. The fracture results in the load to redistribute within the specimen. Again, the crack growth and lamina bundles fracture will be repeated until the end of crushing process. The brittle mode of fracture is controlled by two mechanisms, these being the strength of the matrix

material and the tensile strength of the lamina bundles. The interlaminar and intralaminar growths are functions of matrix material strength while fracture of the lamina bundles is controlled by the tensile strength of the lamina bundles [103].

2.4.3.4 Local Buckling

Local buckling or progressive folding mode is characterised by the formation of local buckles, as shown in Figure 2.18. This mode which is similar to the deformation of ductile metals, can be exhibited by both brittle and ductile fibre reinforced composite tubes. The plastic deformation mechanism within the fibre and matrix control the crushing process for local buckling mode [2].

Ductile fibre reinforced composite materials such as Kevlar, respond to crushing by deforming plastically. Fibres splitting can also occur along the tension side of the buckled fibres and local delamination among plies can take place. Ductile fibre reinforced composites remain in one piece following the crushing process and thereby exhibit post-crushing integrity. This is the result of the deformation of fibre and matrix plastically without fracturing and fibre splitting [103].

There are several conditions in order for brittle fibre reinforced composite tubes to exhibit the local buckling crushing mode [101]:

i. The interlaminar stresses are below the strength of the matrix material.
ii. The matrix has a higher failure strain than the reinforcing fibre.
iii. The matrix demonstrates plastic deformation when subjected to high stress.

Brittle fibres do not exhibit a plastic strain response. However if the matrix material has a higher failure strain, it will reduces or avoids the interlaminar cracks from forming during the crushing process. As a result, the composite tube may fail in a catastrophic mode or crushing in a local buckling mode as interlaminar cracks are eliminated. Usually, the local interlaminar cracks do not spread to the neighbouring buckles [103].

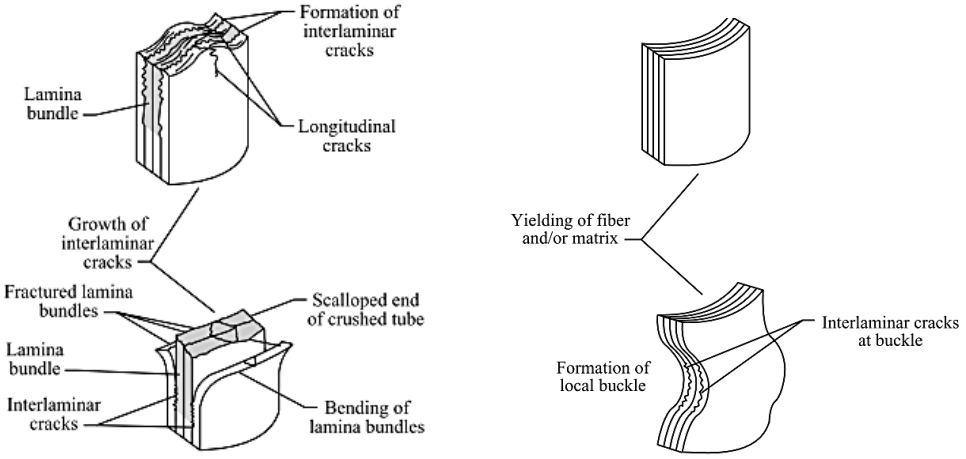

(a) (b)

Figure 2.18 (a) Brittle fracturing and (b) buckling failure modes [104].

2.5 Summary

This chapter has presented a review of past and current research work relevant to this thesis. The first part discussed crashworthiness and energy absorption concepts. This was followed by an overview of energy-absorbing structures, such as sandwich panels, metal tubes and composite tubes. The responses of these structures under compression and the development of numerical modelling techniques have been reviewed. This research proposes two energy-absorbing structures for use in sandwich construction, which are based on metallic and composite tube-reinforced polymer foams.

The majority of studies published up to date have focused primarily on "thin-walled" metal tubes and the use of foam as a filler in tubular energy-absorbing structures which are of particular interest for the protection of motor vehicles. However, the specific energy absorption (SEA) of circular metal tubes reveals that the SEA increases as the diameter to thickness (D/t) ratio decreases. Thus, "thick-walled" metal tubes are more efficient than "thin-walled" ones; though at the expense of higher mean crushing loads, unless the tube diameter is decreased.

This observation leads to the suggestion that small diameter "thick-walled" metal tubes would be an ideal component to improve the response of an energy-absorbing reinforced foam system. Foam has been selected as the substrate (rather than honeycombs), since it is very easy to introduce circular holes into a foam and a foam substrate fully surrounds and supports the tube, which is not the case for a honeycomb-type structure.

Given that the SEA of a composite tube increases significantly with reducing D/t ratio, it is likely that structures based on an array of small composite tubes in a low

density foam could represent an attractive option in the search for new, lightweight energy-absorbing structures. Since they are based on simple cylindrical composite tubes that are widely available in the market place, tube-reinforced sandwich structures should offer a number of potential benefits, including a relative ease of fabrication of complex and curved structures, superior energy-absorbing characteristics and a relatively low cost. Such structures could also offer other attractive characteristics, such as an ability to control the crushing load during compression, e.g. through the use of embedded tubes of different length, as well as the possibility to produce curved core geometries for more complex structures.

The first part of the experimental investigation is focused on the potential offered by lightweight foam panels reinforced with aluminium and steel cylinders. This is followed by an investigation of composite tube-reinforced foams. Initial attention focuses on establishing the influence of the length as well as the diameter to thickness ratio of the tubes on their specific energy absorption characteristics. The tubes were then embedded in a range of polymer foams to investigate the influence of foam stiffness on the SEA of the tubes and the resulting failure modes. It is the purpose of this study to obtain information for the design of energy-absorbing systems which are constructed with multiple tubes embedded in a foam panel.

Following an initial study to characterise the quasi-static and dynamic behaviour of the individual tubes and simple tube/foam configurations, a limited number of blast tests are conducted on tube-reinforced foams. An experimental investigation and finite element models analysis are carried out to understand the response of the structures under compression loading. Finally, the properties of these energy absorbers structures are compared with those offered by other types of core material.

CHAPTER 3

EXPERIMENTAL PROCEDURE

In this chapter, details of the experiments conducted during the course of this research programme will be presented. A variety of mechanical testing and experimental techniques are used to investigate the energy-absorbing characteristics of tube-reinforced foam structures. The first part of this chapter describes the materials used. It is then followed by the specimen preparation process for the various parameters investigated. The experimental arrangement adopted, including quasi-static tensile tests, burn-off tests, quasi-static compression tests, dynamic crush tests and blast tests will be outlined.

3.1 Materials Investigated

In this section, the core materials and the reinforcing tube materials are initially described. The core materials considered in this research programme are PVC and polystyrene foam. As for the benchmark materials, aluminium honeycomb, aluminium foam and polypropylene honeycomb have been selected. The type of tubes examined were extruded aluminium, cold-finished seamless mild steel and carbon fibre reinforced polymer (CFRP).

3.1.1 The Core Materials

Five types of crosslinked PVC foams of various densities were used during the course of the research. The foams were manufactured and supplied in the form of flat panels by Alcan Airex AG where foam densities were differentiated by its colour. Table 3.1 gives a summary of the mechanical properties for density of the foams with densities from 40 to 250 kg/m^3 investigated in this study.

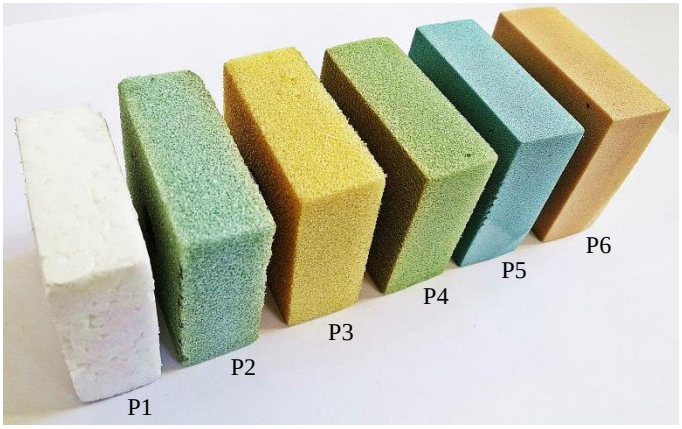

Figure 3.1 The polystyrene and crosslinked PVC (C70) foams.

It is very useful in lightweight applications due to the high stiffness and strength to weight ratios. The fine surface of the foam enables an excellent bond between the skin and core in forming a sandwich structure. In terms of applications for thermal insulation, closed-cell foams have the lowest values of thermal conductivity of any conventional non-vacuum insulation [21].

Expanded polystyrene was selected as a lower density core material in this study. Polystyrene is a versatile material which provides a unique combination of mechanical properties, light weight, excellent insulation and is also cost effective. Table 3.2 lists the relevant material properties from the manufacturer's data sheet. The white polystyrene foams were supplied in the form of rectangular flat panels with dimensions of 400 x 530 x 20 mm and a density of 15 kg/m^3.

Properties	C70.40 (P2)	C70.55 (P3)	C70.75 (P4)	C70.130 (P5)	C70.200 (P6)
Density [kg/m^3]	40	60	80	130	200
Thickness [mm]	20	20	20	20	20
Compressive strength [MPa]	0.45	0.90	1.45	3.0	5.2
Compressive modulus [MPa]	41	69	104	170	280
Shear strength [MPa]	0.45	0.85	1.2	2.4	3.5
Shear modulus [MPa]	13	22	30	54	75
Thermal conductivity [W/mK]	0.031	0.031	0.033	0.039	0.048
Colour	Light green	Yellow	Green	Blue	Brown

Table 3.1 Material properties of the PVC foams [122].

Properties	EPS70 (P1)
Density [kg/m^3]	15
Thickness [mm]	20
Compressive strength [MPa]	0.08
Bending strength [MPa]	0.12
Thermal conductivity [W/mK]	0.038
Colour	White

Table 3.2 Material properties for the polystyrene foam [123].

The performance of the proposed novel structures was evaluated by comparing them to some of the cores which are used in a wide variety of applications. For this purpose, aluminium honeycomb, aluminium foam and polypropylene honeycomb have been selected as benchmark materials. The aluminium honeycomb panels investigated in this study were supplied ready-made in sheet form with a thickness of 20 mm by Hexcel Composites. The relative density of the honeycomb used is 40 kg/m^3 and the thickness of the aluminium foils is 0.064 mm. These hexagonal cell configuration honeycombs consist of a cell size of 7 mm. The panels were produced by expanding stacks of aluminium foils which were bonded by lines of adhesive printed on the surface at regular intervals [21]. A honeycomb structure offers a material with minimal density due to the hollow cells and relative high stiffness to weight ratio [124].

The second benchmark material examined here was based on aluminium foams supplied by the Shinko Wire Company. These commercially-available aluminium porous foams sold under the trade name of Alporas, have a nominal density of 313

kg/m^3 and an average cell size of approximately 4 mm. A process called batch casting was used to prepare the aluminium foams. This was done by adding calcium (Ca) to the molten aluminium, to act as a thickening agent and titanium hydride (TiH_2) was used as a blowing agent [125].

Two densities (40 kg/m^3 and 80 kg/m^3) of polypropylene honeycomb were used to benchmark the novel core structures. The polypropylene (PP) honeycomb structures were supplied by EconCore N.V. in form of panels of 15 mm thickness. The compression strength and modulus for the density of 80 kg/m^3 are 1.2 MPa and 40 MPa respectively [126]. Both densities of the lightweight honeycomb have a cell size of 9.6 mm.

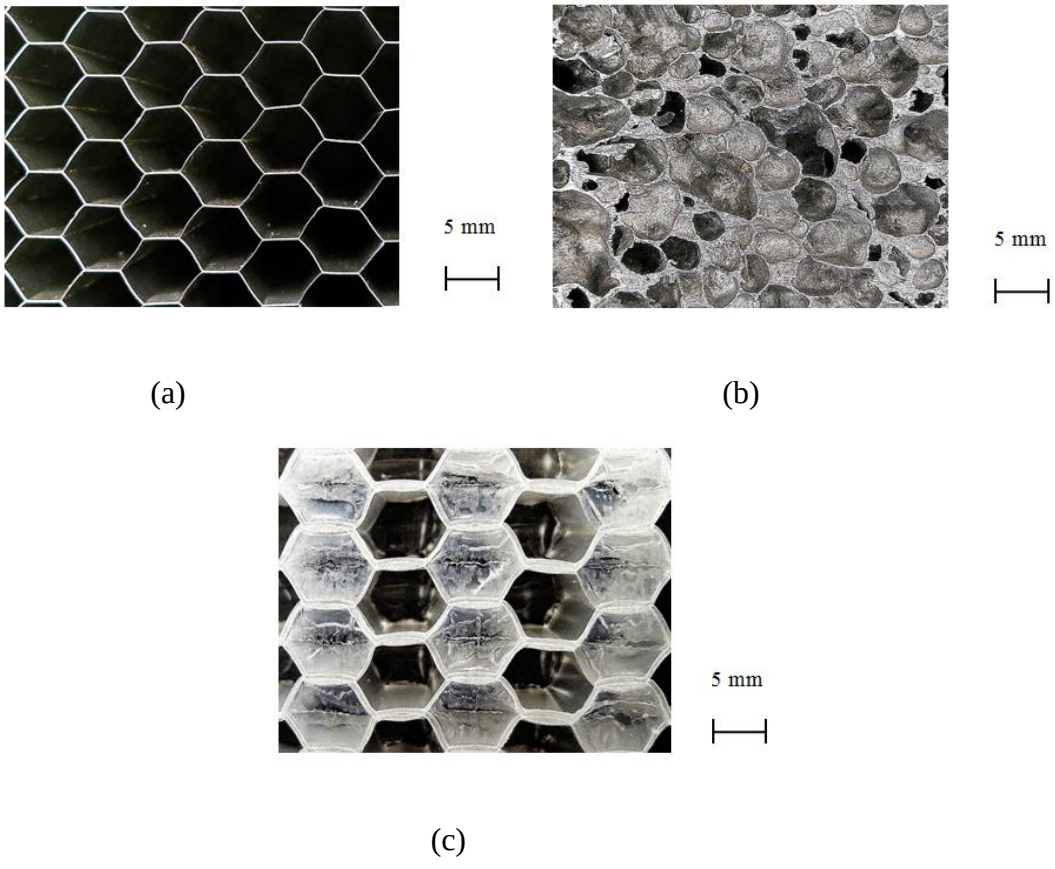

Figure 3.2 The benchmark materials (a) aluminium honeycomb, (b) aluminium foam and (c) polypropylene honeycomb.

3.1.2 Metal Tubes

3.1.2.1 Aluminium Tubes

The initial stage of this study focused on evaluating the energy absorption capabilities of circular aluminium tubes. The aluminium tubes used were based on an aluminium alloy 6063-T6 and were supplied by Aluminium Warehouse Ltd. The extruded aluminium alloy (6063 grade) tubes are commonly referred to as an architectural alloy are mostly used for architecture structures and constructions, such as piping system, window frames and signage frames. The notation T6 indicates the temper or heat treatment of the alloy, which defines the subsequent mechanical properties.

The aluminium tubes were firstly extruded and the profiles were then air or water-cooled. As the temper T6 was applied, the tubes were aged for 8 hours at a temperature of 177^{o}C before being cut into certain length [36]. The alloy composition and mechanical properties of this material are represented in Tables 3.3 and 3.4 respectively. Five different sizes of tubing, with outer diameters ranging from 12.62 mm to 25.40 mm, were investigated. The thickness of the extruded aluminium tubes provided was varied between 1.68 mm and 1.82 mm. The aluminium tubes specimens were supplied in lengths of 1 metre and were cut to the desired length using diamond grit band saw blade.

Component	Weight [%]
Al	Max 97.5
Cr	Max 0.1
Cu	Max 0.1
Fe	Max 0.35
Mg	0.45 – 0.9
Mn	Max 0.1
Si	0.2 – 0.6
Ti	Max 0.1
Zn	Max 0.1

Table 3.3 Typical chemical composition for aluminium alloy 6063-T6 [127].

Properties	Aluminium Tube
Density [kg/m^3]	2700
Modulus of elasticity [GPa]	68.9
Tensile yield strength [MPa]	214
Ultimate tensile strength [MPa]	241
Elongation at break [%]	12
Shear modulus [GPa]	25.8
Shear strength [MPa]	152
Melting point [^{o}C]	616 – 654
Thermal conductivity [W/mK]	200

Table 3.4 Typical mechanical properties for aluminium alloy 6063-T6 [127].

3.1.2.2 Steel Tubes

The cold-finished seamless steel tubes used in the experimental testing program were manufactured by Benteler Group. Seamless tubes were chosen for its equal load-bearing capability in the compressive stress direction compared to welded tubes. The alloy composition and some important mechanical properties of the material, as provided by supplier, are shown in Tables 3.5 and 3.6 respectively.

The primary process, known as cold pilgering, involved reducing the size a number of times until the profile gradually reaches the exact specifications. The first reduction will typically elongate the tube by factors of greater than eight. Following this procedure, the tube (with compliance to EN 10305-4 with a grade E235) was then drawn through a die, which is smaller than the diameter of the tube. In order to fit the draw bench die, the end of each tube was machined. This process gives the tube a more uniform diameter with a tolerance of ±0.08 mm [128].

Here, five different sizes of tubing were considered, with outer diameters ranging from approximately 12.62 mm to 25.60 mm. The tubes were supplied in one batch consisting of 3 metre long sections for each diameter. The steel tube thickness was 16 SWG, where the same thickness of 1.68 mm was obtained by measuring the tube wall of all five tubes. Test specimens were cut to the required length depending on the experimental need, using diamond grit band saw blade.

Component	Weight [%]
C	Max 0.17
Si	Max 0.35
Mn	Max 1.20
P	Max 0.025
S	Max 0.015

Table 3.5 The chemical composition for cold-finished seamless steel tubes [128].

Properties	Steel Tube
Density [kg/m^3]	7900
Modulus of elasticity [GPa]	200
Tensile yield strength [MPa]	Min 235
Ultimate tensile strength [MPa]	340 – 480
Elongation at break [%]	25

Table 3.6 The mechanical properties for cold-finished seamless steel tubes [128].

3.1.3 Carbon Fibre Reinforced Polymer Composite Tubes

The commercially-available composite tubes used in this investigation were supplied by Easy Composites Ltd. The tubes, with a fibre weight fraction of approximately 60%, were produced using a roll-wrapping procedure. This was done by firstly placing a layer of carbon pre-preg layer around a mandrel in order to form the inside diameter of the tubing. The mandrel was covered by a spray-on chemical release agent as this leaves a clean finish on the inside of the tube, making it easier to release the tube after curing [129].

The first carbon pre-preg layer was cut to the correct width to wrap the mandrel and the following layers were measured and cut equal to the circumference of the previous layer. They were based on five plies, consisting of three layers of T700 unidirectional pre-preg carbon fibre reinforced epoxy oriented at 0^o and two layers of unidirectional E-Glass oriented at 90^o, as shown in Figure 3.3(b).

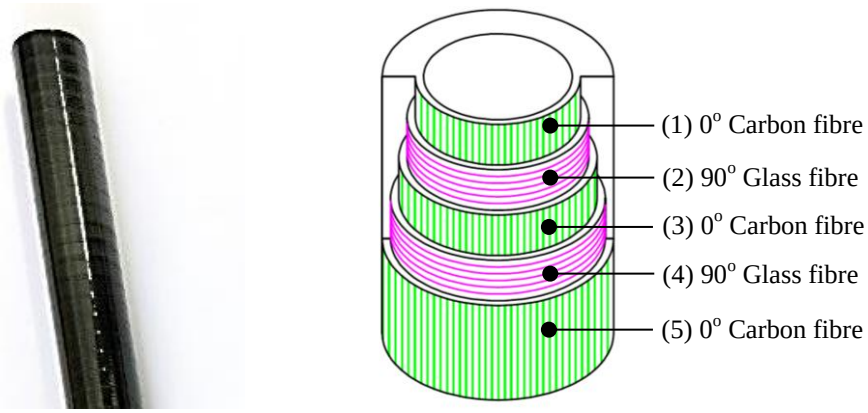

(a) (b)

Figure 3.3 The carbon fibre reinforced polymer (a) ribbed appearance tube finish as a result of using the heat shrinkable tape and (b) the pre-preg layers.

After the five layers of pre-preg were placed on the mandrel, the composite materials were then wrapped using a heat-shrinkable tape. The mandrel was rotated to and the tape was spiral wrapped around the composites starting from one end to the other by overlapping 50% of the tape as it was progressed along the tube. The heat-shrinkable tape provided pressure on the outer surface of the tube which maintained the consistency and quality throughout the tube. Next, the whole assembly was oven-cured as per the manufacturer's recommendations. The heat-shrinkable tape was then removed and the tube was slid from the mandrel [129]. The ribbed appearance of the resulting tube was due to the tape, Figure 3.3(a).

The glass fibre layer was combined with carbon fibre ply to provide a high performance material at a lower cost. The fibres were embedded in an epoxy resin suited for use at temperatures up to 180^{o}C. The multi-axial orientation resulted in excellent properties in both bending and compression crushing, making it suitable for typical heavy duty applications.

Properties	CFRP Tube
Density [kg/m^{3}]	1600
Modulus of elasticity 0^{o} [GPa]	90
Modulus of elasticity 90^{o} [GPa]	19
In-plane Shear Modulus [GPa]	4.6
Major Poisson's Ratio	0.14
Ultimate tensile strength 0^{o} [MPa]	750
Ultimate compressive strength 0^{o} [MPa]	600
Ultimate tensile strength 90^{o} [MPa]	400
Ultimate compressive strength 90^{o} [MPa]	350

Table 3.7 The mechanical properties of the carbon reinforced polymer tubes [129].

When the tube is compressed, the load is predominantly carried by the unidirectional carbon fibres. Six different sizes of tubing were considered, with outer diameters ranging from approximately 10.2 mm to 63.60 mm. The tolerances of the inner and outer diameters were ±0.2 mm and ±0.3 mm respectively. The tubes were supplied in one metre lengths for each diameter and were cut as per the experimental requirements using a wet diamond grit band saw blade.

3.2 Test Specimens and Configurations

The preceding literature review has highlighted the fact that most of the previous studies have focused on the energy absorption behaviour of tube as an individual component. In order to study the capabilities of tube-reinforced foams for use in sandwich structures, a number of design parameters have been used to explore the effect on the crashworthiness characteristics.

In the initial part of this section, the test specimens and configurations for determining the mechanical properties of the core materials and tubes are described. The next part describes the experimental arrangements of tubes with different lengths and diameters. Following this, small diameter tubes were embedded in a range of foam densities. The configuration for multi-tube embedded in foams is explained in detail. Finally, a limited number of blast tests are conducted on the tube-reinforced foam structures.

The basic procedures employed in obtaining consistent and reliable results for this research are as follows:

i. Prior to testing, the weight and dimensions of specimens were measured.
ii. All of the metal tubes were cut to a desired length and ground at both ends using a lathe to ensure that they were parallel.
iii. All of the CFRP tubes were cut to the desired length and ground at one end in order to introduce a forty-five degree chamfer for triggering the crushing process, as shown in Figure 3.4.
iv. In all cases, an interference fit of not more than 0.2 mm was ensured between the tubes and foams.

v. Three identical samples were tested for each case, and the average values were used for data analysis.

vi. The crushing force versus crushing displacement response was recorded for each sample.

vii. All of the tests were carried out under standard laboratory conditions of 23 ± 2^{o}C and 50% ± for relative humidity.

viii. During the crushing process, the mode of failure in each tube was investigated and the images of the axial quasi-static crushing process were captured. The photographs of the final crushed samples were also taken for comparison.

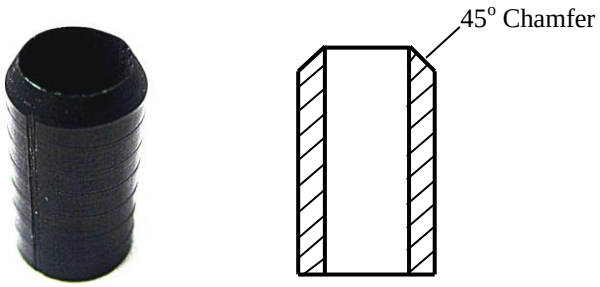

Figure 3.4 Photograph of a chamfered tube and a cross-section showing the chamfer angle of 45^{o} at one end of the tube.

3.2.1 Mechanical Properties

The mechanical properties of the core materials, metals and composite tubes were obtained before conducting further investigation. These material properties are essential in order to predict the behaviour of the structures under axial loading via finite element computational models. The first part of this section examines the compressive properties of the foam core materials by conducting quasi-static compression tests. Here, five different densities of foam, ranging from 15.6 to 224 kg/m^3, aluminium honeycomb, aluminium foam and polypropylene honeycomb, were prepared and cut to blocks with dimensions of 50 mm square. Following this, the samples were tested at quasi-static rates according to the procedure outlined in Section 3.3.3. The energy absorbed by each of the core materials was determined by calculating the area under load-displacement curve.

The properties of the metal and CFRP tubes, having diameters of approximately 12 mm, were investigated by conducting standard tensile tests. Details of the tensile testing procedure are given in Section 3.3.1. The load-displacement output from these tests were analysed and converted to product engineering stress-strain curves. From these curves, the compressive or tensile Young's modulus, yield stress and ultimate stress were determined. Burn-off tests were carried out for all composite tubes to obtain the weight fraction of reinforcement and matrix for each diameter. Samples having a length of 20 mm were cut from composite tubes with diameters of 10.16, 12.70, 29.40, 40.90, 50.42 and 63.60 mm. Section 3.3.2. outlines the procedures used for the burn-off tests and the calculation of the weight fractions of the composite tubes.

3.2.2 The Effect of the Tube Length on SEA

Attention initially focused on establishing the influence of the geometry of the individual metal and composite tubes on their resulting energy-absorbing characteristics. The influence of the tube length was investigated through a series of compression tests on aluminium, steel and composite tubes with diameters of approximately 12 mm and lengths of 15, 20, 25, 30 and 40 mm. In order to maintain a nominal constant strain-rate, the crosshead displacement rate was scaled according to the length of the tube. The relationship is given by,

$$\dot{\varepsilon} = \mathrm{V}/\mathrm{L} \tag{3.1}$$

where $\dot{\varepsilon}$ is the nominal constant strain-rate, V is the crosshead displacement rate and L represents the axial length of the tube. For example, tests on the 15 mm long tubes were conducted at a crosshead displacement rate of 0.75 mm/minute, whereas the 40 mm long tubes were tested at 2 mm/minute.

3.2.3 The Effect of the Tube Diameter on SEA

The effect of varying the ratio of the inner diameter of the tube to its thickness, D/t, on energy absorption was then investigated by conducting compression tests on a range of individual metal and composite tubes. Prior to testing, each of the tubes was cut to a length of 20 mm and measurements of the outer diameter, mean inner diameter, thickness, D/t values and mass were taken. The outer diameters and thicknesses of tubes considered in this study are summarised in Table 3.8.

Aluminium tubes		Steel tubes		Composite tubes	
Outer diameter, D_o [mm]	Thickness, t [mm]	Outer diameter, D_o [mm]	Thickness, t [mm]	Outer diameter, D_o (mm)	Thickness, t (mm)
12.62	1.75	12.62	1.68	10.20	1.23
16.00	1.82	15.78	1.68	12.70	1.35
19.10	1.75	19.05	1.68	29.40	1.56
22.40	1.70	22.22	1.68	40.90	1.68
25.40	1.68	25.40	1.68	50.40	1.68
-	-	-	-	63.60	1.84

Table 3.8 Summary of the dimensions of the 20 mm long aluminium, steel and composite tubes.

Five different sizes of tubing were investigated for the aluminium and steel tubes, with outer diameters ranging from approximately 12.62 to 25.40 mm. The values of D/t for the aluminium tubes ranged from 5.2 to 13.1, while the D/t values for steel tubes ranged from 5.5 to 13.1. For the composite tubes, six sizes of CFRP cylinder were investigated, the outer diameters of which varied from approximately 10.2 mm to 63.6 mm. The corresponding values of the ratio of D/t ranged from approximately 6.3 to 32.6. As mentioned in Section 3.2, a 45^o chamfer was introduced at one end of each of the composite tubes. Here, the chamfered end was placed on the platen facing upwards, forcing failure to start from the top. Following the quasi-static crushing process, these tests were then repeated at dynamic rates of loading using a drop-weight impact tower.

3.2.4 The Effect of the Foam Density on SEA for Systems with Embedded Tubes

Individual tubes based on the smallest diameter of the aluminium, steel and composite cylinders were embedded into polymer foams with densities ranging from 15.6 to 224 kg/m^3. Details of the basic mechanical properties of the six foams are given in Tables 3.1 and 3.2. In preparation for these tests, a hole with the same diameter as the tube was drilled into a 50 mm square block of thickness 20 mm and either a steel, aluminium or composite tube with a length of 20 mm, was inserted into the hole, as shown in Figure 3.5. The dimensions of the structure are presented in Figure 3.6. The tube/foam combinations were subsequently loaded in compression at a crosshead displacement rate of 1 mm/minute.

(a) (b)

Figure 3.5 Tube partially inserted into a 50 x 50 mm P2 foam block. For clarity, the tube has not been fully inserted for (a) aluminium and (b) composite tube.

The tests on the reinforced foam blocks were repeated at dynamic rates of loading using the drop-weight impact tower as indicated in Section 3.3.4. In this case, a 60 mm square steel plate was fixed to the instrumented carriage to load the 50 mm square samples. During the impact test, the force was again measured using the piezoelectric load-cell. The displacement data were recorded using the high speed video camera.

3.2.5 Test on Multi-tube Foams

In this series of tests, the main objective was to study the effect of increasing the planar density of metal and composite tubes on the energy-absorbing response of these structures. Tests were conducted on three densities of foam, these being P1 (15.6 kg/m^3), P4 (90.4 kg/m^3) and P6 (224 kg/m^3). Here, between one and five tubes were embedded in square blocks of 20 mm thick foam, the dimensions are as shown in Figure 3.6. In the case of the composite tubes, the tubes were positioned alternately with chamfer facing both upwards and downwards in each of the foam panels to minimise the interaction between tubes. The samples were tested at quasi-static rates as outlined in Section 3.3.3.

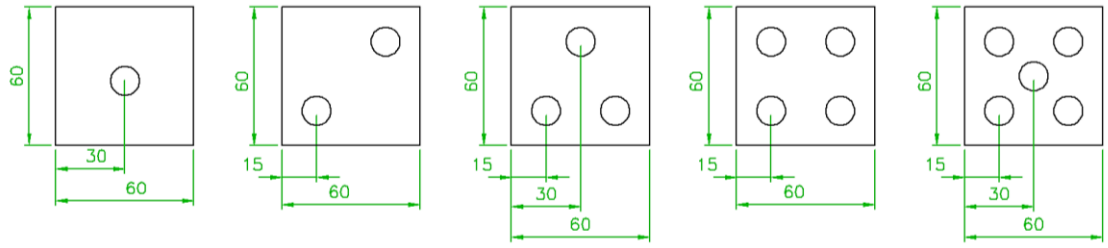

(a)

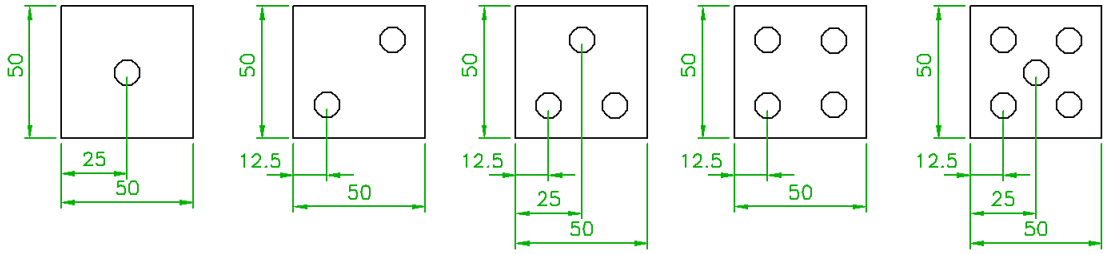

(b)

Figure 3.6 The positioning of the (a) metal and (b) composite tubes in the multi-tube samples of 20 mm thickness.

3.2.6 Blast Tests on Tubes Reinforced Foam Panels

Blast tests were conducted on 20 mm thick, 105 mm square P3 foam blocks with a density of 56 kg/m^3. Nine holes with diameters similar to the tubes were drilled into each foam sample. The CFRP, aluminium and steel tubes, with diameters of approximately 12.7 mm, were inserted into them to yield the reinforced array shown in Figure 3.7(a). As before, in order to minimise interaction between the CFRP tubes during the crush process, the tubes were positioned alternately facing upwards and downwards. A total of 15 blast tests were carried out on four types of structure, including the plain P3 foam, an array of nine CFRP tubes embedded in the P3 foam, an array of nine aluminium tubes embedded in the P3 foam and nine steel tubes embedded in the P3 foam.

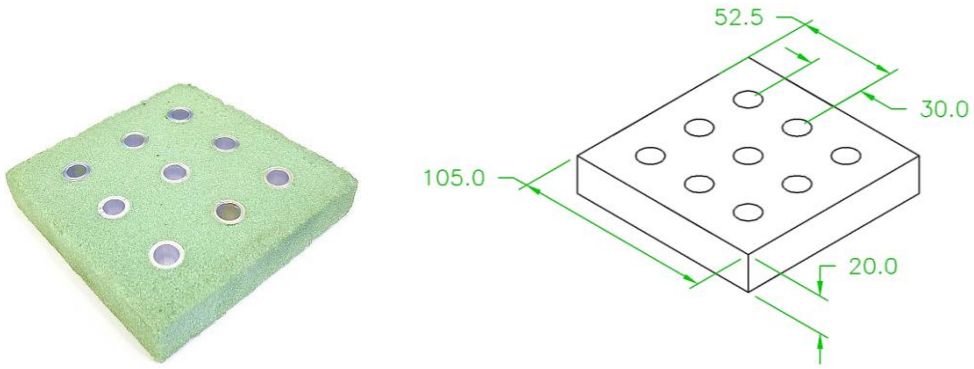

(a) (b)

Figure 3.7 (a) Photograph of the aluminium tube-reinforced foam structure and (b) the dimensions of the test specimen.

3.3 Test Method

3.3.1 Tensile Tests on Tube Materials

Tensile tests were carried out in accordance with BS EN 10002-1:2001, Materials Tensile Testing [130]. The shape of the test piece for tensile testing on tube specimen can be either a length of a tube or a strip cut from in the longitudinal or transverse direction from a section of the wall tube. In this study, a length of tube was selected as the shape for tensile test and determination of dimensions were based on the tube diameter and thickness, and this is represented in Figure 3.8. Before attaching the specimen to the machine, three readings of the outer diameter and thickness were taken and the average values were calculated. These values are important in computing the initial cross-sectional area of the tube before the tube is tested under tensile loading.

A steel rod of 30 mm long with the outer diameter that is approximately the same as the inner diameter of tube specimens was inserted at both ends of a tube to assist the gripping process. These steel rods act as reinforcement to the tube by preventing the tube from deforming due to the force from the grips. The specimen was then gripped at both ends by serrated wedges grips. The test specimen was aligned to avoid a bending force on the specimen. Next, an extensometer as shown in Figure 3.9 was attached to the specimen and was set to a gauge length of 50 mm. A mechanical clip-on extensometer was attached to the sample with the purpose of measuring strain. The free length of the samples was 80 mm and the crosshead displacement rate was 0.5 mm/minute up to 1% strain, then 1 mm/minute to 3% strain and 2 mm/min until fracture.

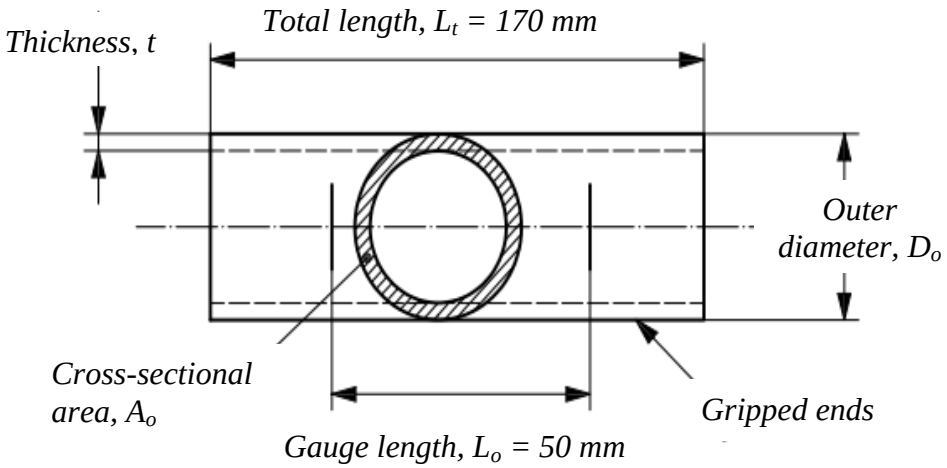

Figure 3.8 Test piece comprising a length of tube for tensile testing.

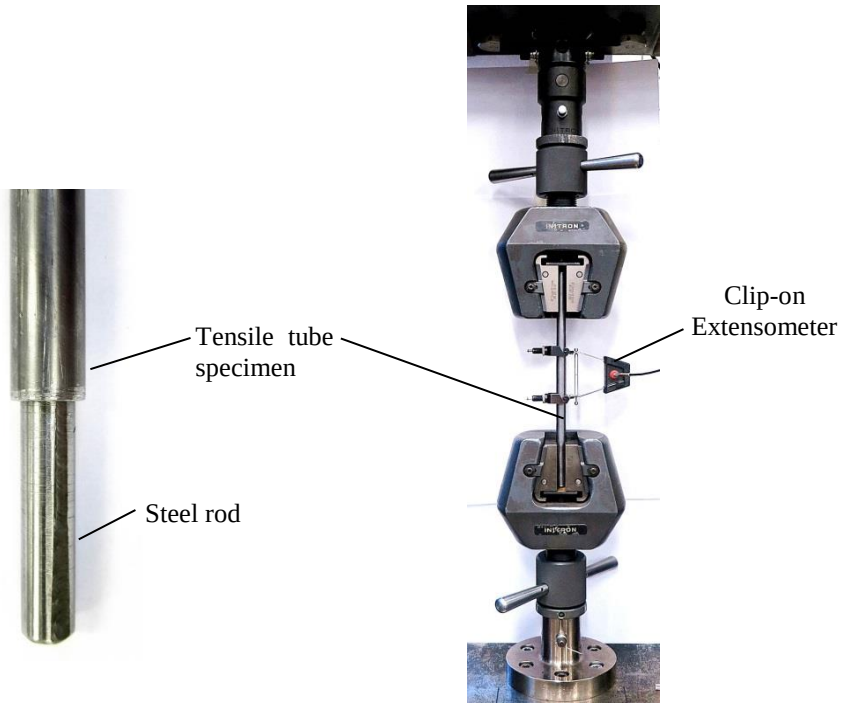

Figure 3.9 Steel rod was inserted into the grip ends of the tensile tube specimen. For clarity, the rod has not been fully inserted.

The tests were carried out using a Universal Testing Machine Instron 4505 and the force data were measured by a 100 kN load cell. For each of the test configurations, at least three specimens were tested. The raw data were used to plot engineering stress-strain curves and used to determine the mechanical properties of the materials. The tensile engineering stress which is defined as the ratio of applied tensile force and cross section area was calculated using:

$$\sigma_t = \frac{F}{A_\circ} \tag{3.2}$$

where σ_t is the tensile engineering stress [MPa], F is the applied tensile force [N] and A_o is the original cross-sectional area of the specimen [m^2].

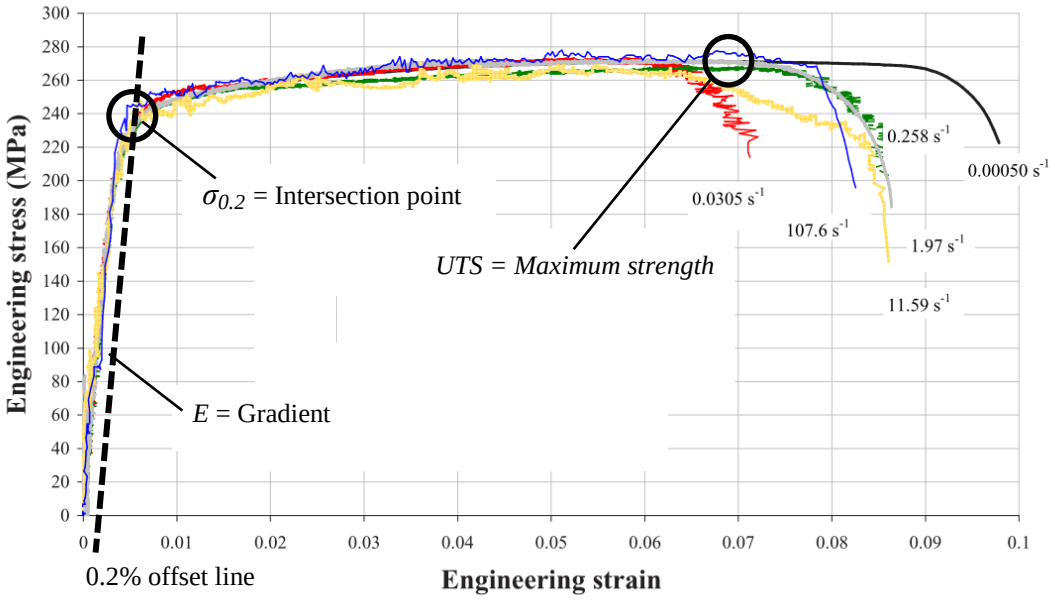

Figure 3.10 Properties obtained from the engineering stress-strain curve [67].

The tensile engineering strain which is defined as deformation of a solid due to tensile stress was calculated by applying:

$$\varepsilon_t = \frac{dL}{L_\circ} \tag{3.3}$$

where, ε_t represents the tensile engineering strain which is unitless, dL is the change of length [m] and $L_\circ$ is the original length [m]. Young's modulus, or elastic modulus, is a measure of the stiffness of a material, thus, it is one of the most important properties in engineering structural design. The unit of Young's modulus, E, is N/m^2 [Pa] but since metal materials are generally very stiff, it is commonly expressed in terms of GPa [131]. This value can be calculated from the slope of a tensile stress-strain curve:

$$E = \frac{\sigma_t}{\varepsilon_t} \tag{3.4}$$

The yield (proof) strength, $\sigma_{0.2}$, was determined from the stress-strain diagram by drawing a line parallel to the straight portion of the elastic region and at an offset of 0.2 % strain. The parallel line was extended to a point at which this line intersects the curve giving the proof strength. The ultimate tensile strength, *UTS*, can be obtained directly by reading the maximum stress value.

3.3.2 Burn-Off Tests

'Burn-off' tests were carried out on all of the composite tube specimens to determine the fibre and resin volume fractions. The detailed experimental procedure follows ASTM D2584, the Standard Test Method for Ignition Loss of Cured Reinforced Resins [132]. Three identical samples were repeated for each of the CFRP tube diameters to yield the average results. Initially, the mass of an empty crucible was recorded. A 20 mm unchamfered CFRP tube specimen was placed in the crucible and the total mass was determined. The crucible containing the sample was placed in a furnace which was then heated to a temperature up to 560°C and maintained at that temperature for forty five minutes.

Following this step, only the reinforcement material was left in the crucible with no visible resin remaining. The crucible was taken out of the furnace and left to cool to room temperature in a desiccator. The mass of sample together with crucible was recorded to the nearest 0.01 g. Using this information, the mass of the sample after the burn-off test was calculated by subtracting the mass of the crucible. Nomenclature for burn-off test are as follows [10]:

m_c	Mass of crucible [g]
m_{c+s}	Mass of crucible + sample [g]
m_s	Mass of sample before burn-off $m_{c+s} - m_c$ [g]
m_{c+f}	Mass of crucible + fibre residue after burn-off [g]
m_f	Mass of fibre $m_{c+f} - m_c$ [g]
m_m	Mass of matrix $m_{c+s} - m_{c+f}$ [g]
ρ_f	Fibre density [kg/m^3]

ρ_m Matrix density [kg/m^3]

W_m Weight fraction of matrix

W_f Weight fraction of fibre

V_m Volume fraction of matrix

V_f Volume fraction of fibre

Hence, with the obtained mass of fibre and matrix, the weight fractions of each sample were calculated using [10]:

$$\mathrm{W_f} = \frac{\mathrm{m_f}}{\mathrm{m_s}} \tag{3.5}$$

The weight fraction is expressed by:

$$\sum W_i = 1 \tag{3.6}$$

where W_i is the weight fraction of the constituent *i*. The weight fraction of the composite comprising the fibres and matrix can be described as:

$$W_f + W_m = 1$$

or $$W_m = 1 - W_f$$

The volume fraction is represented by:

$$\sum V_i = 1 \tag{3.7}$$

where, V_i is the volume fraction of the constituent *i*. The volume fraction of the composite containing fibre and matrix can be described as:

$$V_f + V_m = 1$$

or $$V_m = 1 - V_f$$

3.3.3 Quasi-static Tests

A series of compression axial quasi-static tests were conducted using conventional testing machine at a constant crosshead displacement rate. Each of the specimens with height of 20 mm was tested a constant crosshead speed of 1.0 mm/minute using a Universal Testing Machine Instron 4505 with a 100 kN load cell. The static test setup is as shown in Figure 3.11. For higher forces of up to 250 kN, a Dartec Universal Testing Machine was used, the test machine is shown in Figure 3.12. For this purpose, compression test was carried out in accordance to BS ISO 844:2001, Compression Test for Rigid Materials [133]. For each of the test configurations, at least three specimens were tested.

A specimen was placed on the lower platen and axially crushed between parallel steel flat platens. The crosshead was then lowered until the surface of the upper platen was in contact with the specimen. The quasi-static tests were continued beyond the starting point of densification of the specimen [35] or up to the bottoming-out displacement for tube materials [34]. For analysis purposes, the modes of failure were observed and photographs of the deformation process were taken throughout the tests. The force-displacement data were used to determine the energy absorption and specific energy absorption characteristics of the materials. The compressive engineering stress-strain curves were also plotted in order to determine the mechanical properties of the materials. The compressive engineering stress was calculated using Equation (3.2) and the compressive engineering strain was calculated using Equation (3.3).

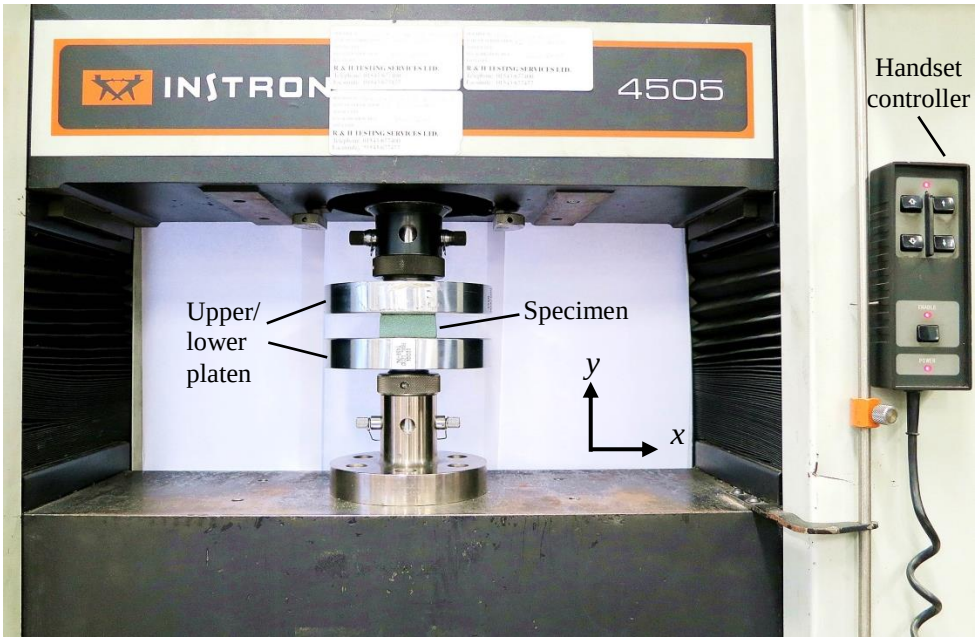

Figure 3.11 A specimen under compression loading using the Universal Testing Machine Instron 4505.

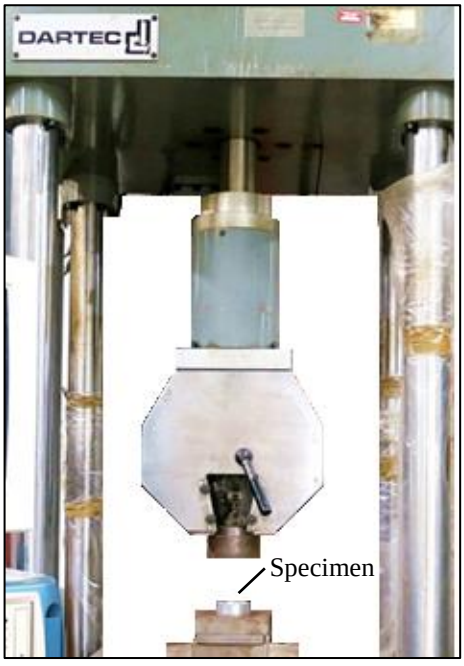

Figure 3.12 Dartec Universal Testing Machine was used for static loading up to 250 kN.

In an actual event of a crash, a structure dissipates energy through several mediums during the crush process. As many materials used in crashworthy structures are made of rate-sensitive materials, the energy absorption characteristics of these materials will depend on the crush speed [2]. Therefore, it is not sufficient to interpret data based solely on quasi-static testing when selecting materials for a crashworthy structure. Nevertheless, information from quasi-static testing can be used in preliminary design and selection before the sample is crushed dynamically. Since an impact test requires expensive equipment, such as a high-speed video camera, high frequency data loggers and load cells, data from quasi-static tests can be used in predicting the failure modes and the energy absorption characteristics of a sample to prevent potential damage of equipment.

3.3.4 Dynamic Loading Tests

The impact tests were undertaken using the drop-weight impact rig shown schematically in Figure 3.13(a). The energy was transferred by a free falling mass to the specimens, which were loaded axially. The mass and height of the impactor were adjusted to obtain the desired impact energy, E, based on test requirements. This can be calculated using the expression,

$$E = mgh \tag{3.8}$$

where, m is the mass in kg, g is the gravitational constant (9.81 m/s^2) and h is the height in metre. Prior to testing, the test specimens were placed on the impact plate and positioned parallel to the direction of the impactor as shown in Figure 3.13(b). Initially, a flat rectangular impactor, with dimensions of 120 mm x 80 mm was raised to a predefined level depending upon the velocity and impact energy. The movement of the impactor was guided by two greased steel rails with a ±0.5 mm clearance. Therefore, the contact between the impactor and rails was assumed to be frictionless. The impactor was released once the entire test configuration was ready. The dynamic compression tests were stopped when the specimens had been completely crushed and bottomed-out [35]. Load data were collected from piezoelectric load cell while the high speed video camera recorded the displacement during crushing. A load cell mounted beneath the impact plate measured the voltage-time histories during the impact event. The Kistler type 9363A load cell, with measuring range of 120 kN, was connected to a charge amplifier using an insulated co-axial cable.

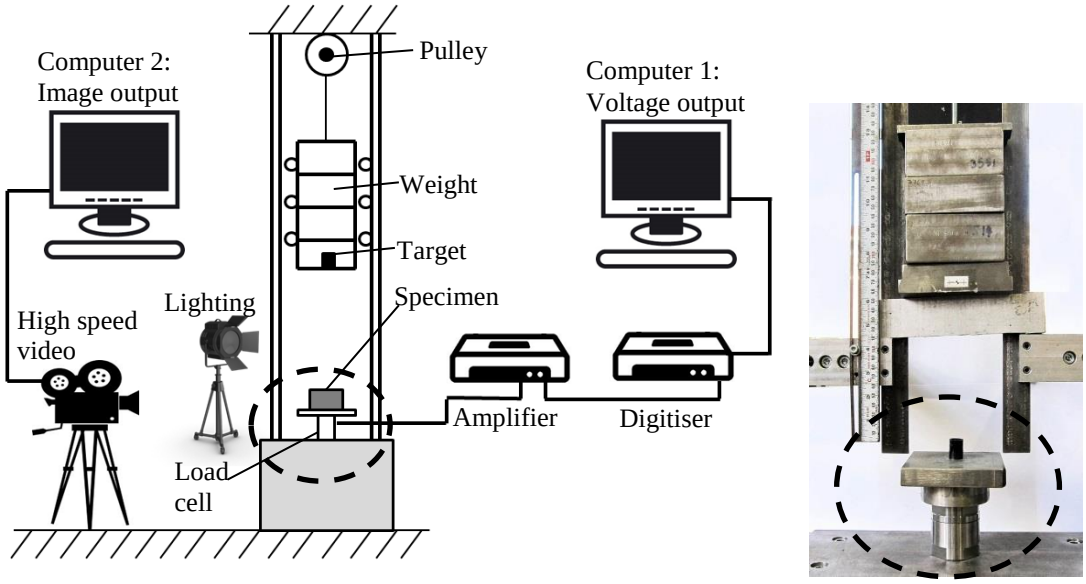

(a) (b)

Figure 3.13 Drop-weight impact test (a) schematic diagram of the set-up and (b) the specimen and the load cell.

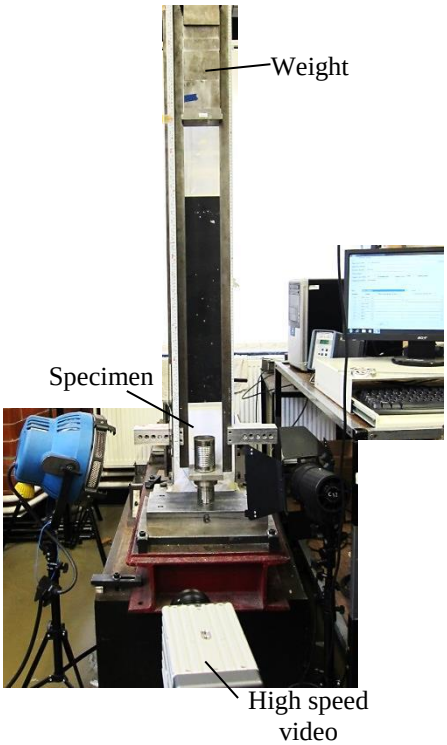

Camera-motionPro X4	Make: Integrated Design Tools, INC. M/N: X4C-U-4 S/N: 24-0507-0875
PROANALYST SOFTWARE	Make: Xcitex Edition: Professional Version: Workstation
Motion Pro software	Make: Redcake Alliance 24-0507-02075

Figure 3.14 The drop-weight test facility at the University of Liverpool and details of the high speed video camera.

During an impact event, the mechanical force was recorded by a pressure sensor in the load cell and converted to an electrical signal. Since the electrical signal is in order of millivolts, amplification of the signal was undertaken by a charge amplifier. A digitiser device was used to convert the analog signals into digital signals and these were recorded using a computer. Finally, the force (in Newtons) readings were obtained by converting the voltage using a scaling factor of 12,000 N/V which was found by conducting a static calibration on the Instron Machine [134].

The motion of the impactor was captured using a high speed video MotionPro X4, model no. X4CU-U-4 with a standard F/0.95-50 mm lens positioned in front of the impact rig, as shown in Figure 3.14. For all impact tests, the frequency of the high speed video was set to 10,000 frames per second. Before conducting the test, a target with a 15 mm scale was placed on the surface of impactor to enable the high speed video to track the motion.

The video file was captured and processed using MotionPro software, Version 2.30.0. This video file was then analysed and calibrated using the 15 mm scale and the motion analysis software, ProAnalyst, to produce the displacement data. The data from the piezoelectric load cell were filtered using the Impressions software package. A further analysis using Mathlab 2012a software was required to calibrate the force data to the displacement data.

3.3.5 Blast Tests

A limited number of blast tests were undertaken on a ballistic pendulum at the University of Cape Town, in the Blast Impact and Survivability Research Unit (BISRU). These tests were undertaken to evaluate the dynamic response of a more representative component (i.e. one with a greater number of tubes) subjected to one of the most severe forms of loading (blast). The blast tube arrangement, as shown in Figure 3.15(a), was used to generate a uniform loading condition on the tubes reinforced foam panels [135]. Here, tests were conducted on CFRP, aluminium and steel tubes reinforced 20 mm thick, 105 mm square P3 foam blocks with a density of 56 kg/m^3. The 20 mm thick foam squares were fixed using a double-sided adhesive tape, to a larger thick steel plate, which in turn was bolted to a ballistic pendulum. A steel plate with dimensions similar to those of the foam block was attached to the front of the core using the double-sided adhesive tape. The front steel plate was then positioned fully covering the inner end of the blast tube to prevent the blast wave from escaping.

Blast loading was applied to the specimens by detonating 33 mm diameter discs of PE4 explosive attached to the centre of a 100 mm square, 12 mm thickness polystyrene panel [136]. This panel was then fixed to the outer end of the blast tube to provide a stand-off distance of 150 mm from the front steel plate, Figure 3.15(b). The detonator with one gram of PE4 explosive, was positioned to the centre of the 33 mm diameter discs. The impulse was varied by increasing the mass of PE4 explosive. The impulse was determined from the measured swing of the pendulum using a method that was employed by Theobald and Nurick [137]. The final thickness was measured across the tube-reinforced foam panels to determine the average deformation.

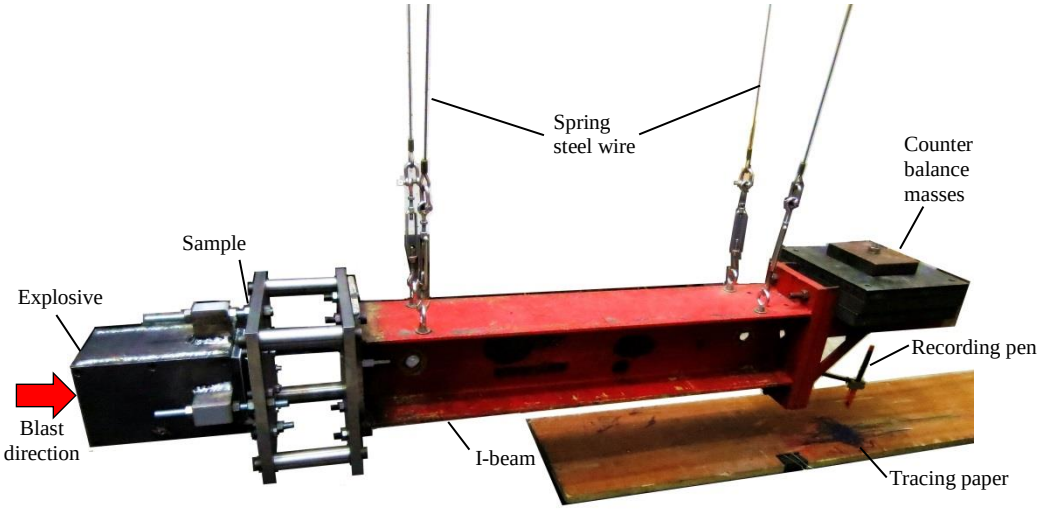

(a)

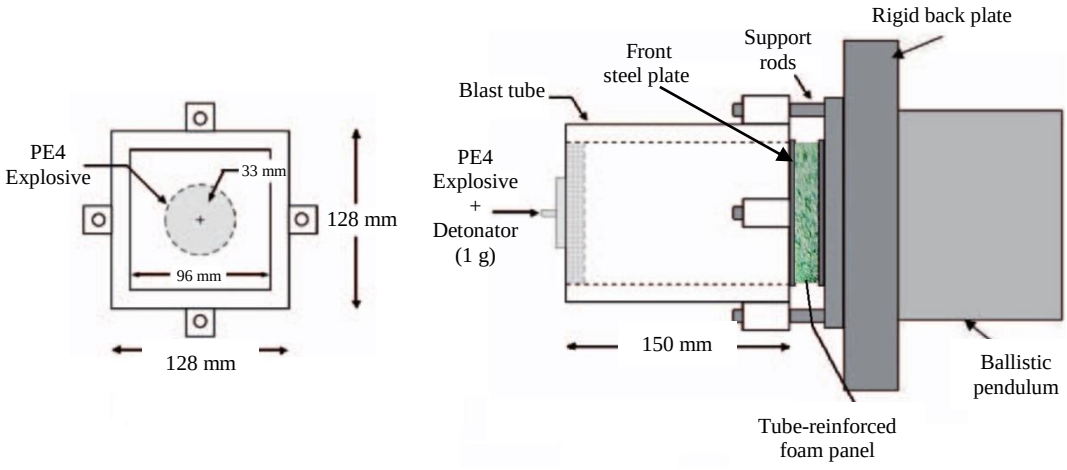

(b)

Figure 3.15 (a) Photograph of the ballistic pendulum used for conducting the blast tests and (b) schematic of the detonator and blast tube arrangement.

3.4 Summary

This chapter has presented the experimental details on metal tube and composite tube-reinforced foam structures. Firstly, it covers the preparation and configuration of the test specimens for various mechanical tests of the core materials, metal and composite tubes. This is followed by the detailed experimental set-up for various tests on quasi-static tension, resin burn-off, quasi-static compression, low-velocity impact and blast.

CHAPTER 4

RESULTS AND DISCUSSION

In this chapter, the experimental results obtained will be presented and discussed. Firstly, the mechanical response of each materials used were characterised through a series of compression and tensile tests. Subsequently, the influence of varying several parameters on the energy-absorbing metal and composite tube-reinforced foam structures is presented. This will be followed by a discussion based on the observations made from a series of blast tests on the metal and composite tube-reinforced foam structures. Finally, a comparison of the specific energy absorption (SEA) properties of the tube-reinforced foam structures with other energy absorbing core structures is presented.

4.1 Compressive Behaviour of Foam Materials

This section investigates the mechanical properties of the foam materials by conducting quasi-static compression tests on 6 different densities, ranging from 15.6 to 224 kg/m^3. The specimen size was 50 x 50 mm^2 with a thickness of 20 mm. Tests were undertaken at a crosshead displacement rate of 1 mm/min and the crushing process was interrupted when the crosshead had travelled at least 15 mm. All tests were performed at room temperature, i.e. 23^{o}C.

Details of the material properties of the foams, including the density, compressive yield stress, compressive modulus and sustained crushing stress are summarised in Table 4.1. From the test results, the sustained crushing stress of the foams was found to increase with increasing foam density. These findings agree with those of Lim et al. [47] and Thomas et al. [48].

Foam test ID	Density [kg/m^3]	Compressive yield stress [MPa]	Compressive modulus [MPa]	Sustained crushing stress [MPa]
P1	15.6	0.08	6	0.12
P2	38.3	0.45	37	0.47
P3	56.0	0.70	69	0.74
P4	90.4	1.29	97	1.43
P5	128.0	2.34	160	2.44
P6	224.0	4.19	280	4.13

Table 4.1 Summary of the mechanical properties of the foam materials.

Figure 4.1 shows a typical load-displacement curve following quasi-static testing on the P3 foam with a density of 56.0 kg/m^3. The data obtained from load-displacement curve were used to develop a stress-strain curve by utilising the equations discussed in the previous chapter.

A typical stress-strain curve following quasi-static test on the P3 foam with a density of 56.0 kg/m^3 is shown in Figure 4.2. There are three distinct phases during the compression process. Initially, a linear-elastic region occurs up to approximately 5% before collapse occurs. This obeys the Hooke's law, where the strain is directly proportional to the stress applied. Next, the crushing process is followed by an almost constant stress, forming the plateau stress region. Finally, the densification region starts at the point where the force increases rapidly with little deformation. This figure shows that foam material offer unique characteristics, whereby they can deform extensively while sustaining low levels of stress, before reaching the densification region [21].

The deformation process of the closed-cell foams in the linear region is related to the stretching of the cell faces [21]. The gradient of initial linear region of the diagram was used to calculate the compressive modulus of elasticity. The compressive yield stress is determined at the highest stress point at the end of the elastic region. After initial collapse, the plateau region starts and the magnitude of stress is related to the density of the foam [47]. The constant collapse process in the foam cells results in a sustained crushing load with increasing strain. The plateau state is the most interesting characteristic, as the majority of the energy is absorbed in this region.

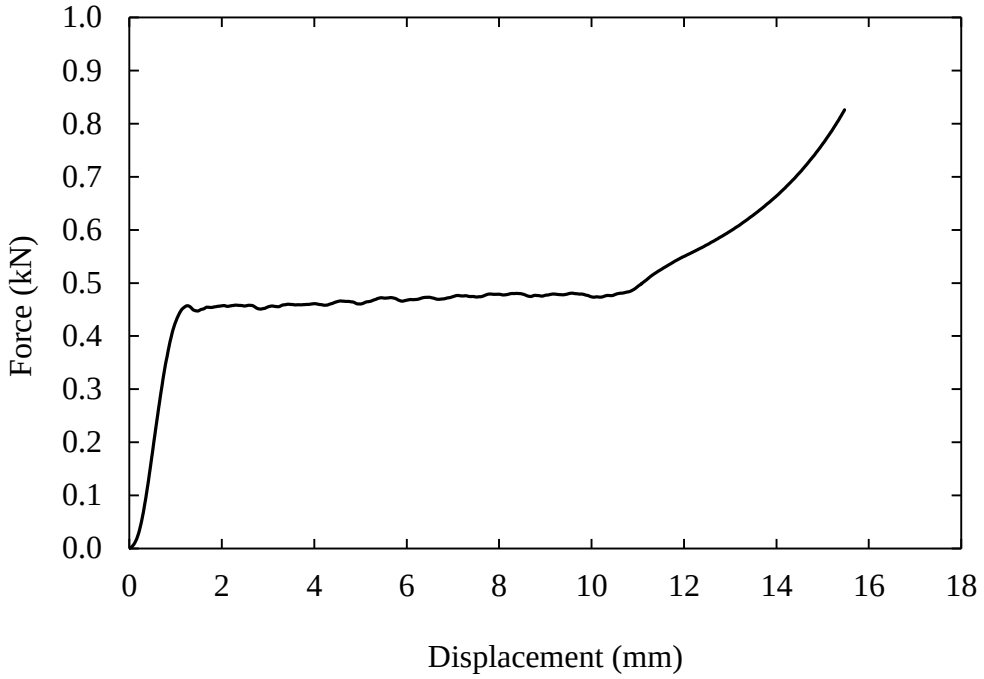

Figure 4.1 A typical load-displacement curve following a quasi-static test on P3 foam with a density of 56.0 kg/m^3.

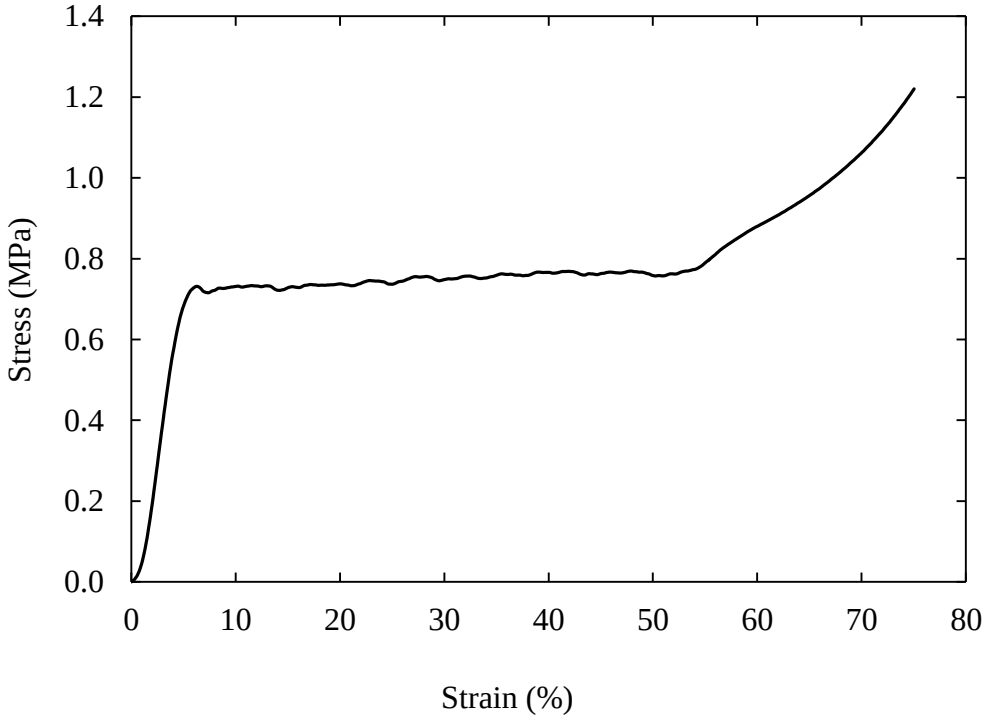

Figure 4.2 A typical stress-strain trace following a quasi-static test on P3 foam with a density of 56.0 kg/m^3.

Finally, the plateau region gradually ends as stiffening occurs when the cell walls collapse and started to interact with the neighbouring cell walls of the foam. This continuous interaction condition results in a rapidly increasing strain. In the figure, it can be seen that an increase in density will also increase the compressive modulus, the compressive stress and the sustained crushing stress. For an example, an increase in density from 56 to 128 kg/m^3 resulted in 300 percent increase in the compressive yield stress (0.7 to 2.34 MPa). The values obtained from experimental testing are similar to the mechanical properties supplied by the manufacturer [122], [123], as presented previously in Chapter 3.

4.2 Metal Tube-reinforced Foam Structures

4.2.1 Tensile Tests on the Aluminium and Steel Tubes

This section presents the mechanical properties of the aluminium and steel tubes before undertaking any further mechanical testing. The engineering stress-strain curves were obtained by conducting standard tensile testing on the aluminium and metal tubes. Figure 4.3 compares the quasi-static engineering tensile stress-strain curves for the aluminium and steel materials. From the figure, it can be seen that the mild steel has an ultimate tensile strength of almost twice that of aluminium, while its yield stress is only about one-quarter higher than that of aluminium. The results obtained from the stress-strain curves, such as the tensile strength, tensile modulus and yield strength, are compiled in Table 4.2.

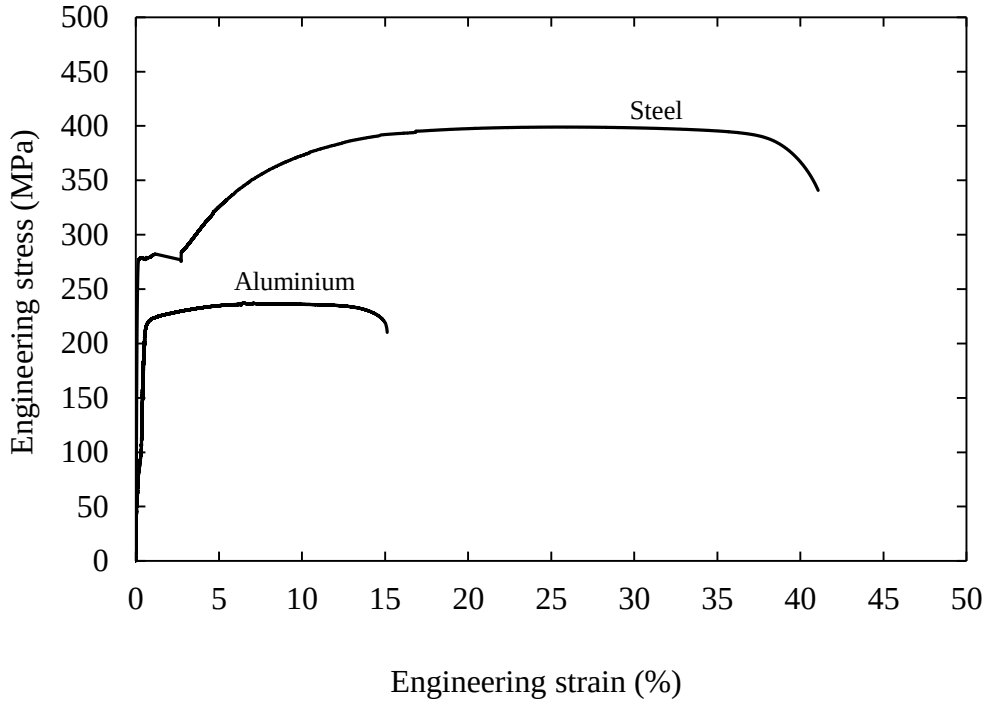

Figure 4.3 Engineering stress-strain curves following tensile tests on 12.62 mm diameter (a) aluminium (D/t = 5.21) and (b) steel (D/t = 5.51) tubes.

Material	Circular aluminium tube	Circular steel tube
Outer diameter, D_o [mm]	12.62	12.62
Thickness, t [mm]	1.75	1.68
Density [kg/m^3]	2543	7966
Tensile strength [MPa]	237	399
Tensile modulus [GPa]	70.4	200
0.2% Yield stress [MPa]	218	277

Table 4.2 Summary of the mechanical properties of the circular aluminium and steel tubes.

It is apparent that the steel tested is more ductile than the aluminium, with the engineering strains being 34% and 9% respectively. This behaviour is related to the fracture of the tubes as shown in Figure 4.4. The point of final fracture of the samples gives an indication of the level of ductility [67]. For both materials, fracture occurred approximately at the middle of the total gauge length and the location of the fracture surface was observed to be perpendicular to the tensile axis.

A visual inspection of the cross-section of the steel tube specimen after tensile failure reveals that it experienced significant necking prior to fracture. This resulted in a cup and cone fracture appearance, as shown in Figure 4.4(b). In contrast, the cross-section of the aluminium tube in Figure 4.4(a) shows little necking deformation and sharp edges, indicating that the material has undergone less plastic deformation during the tensile test [131].

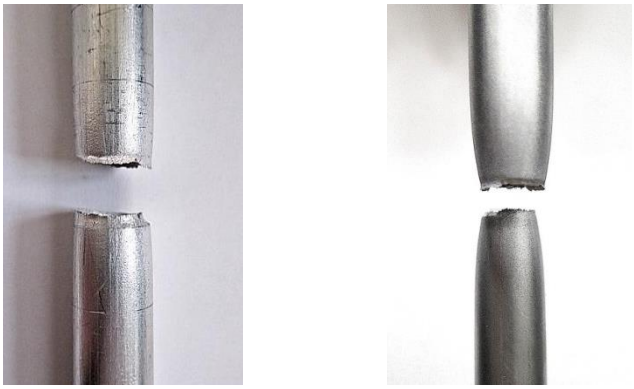

(a) (b)

Figure 4.4 Photographs following tensile tests on (a) the aluminium and (b) the steel tubes.

4.2.2 The Effect of the Length of the Aluminium and Steel Tubes on SEA

Initially, the influence of tube length on the energy-absorbing characteristics of the individual metal tubes was investigated through a series of tests on the aluminium and steel tubes with lengths of 15, 20, 25, 30 and 40 mm. Table 4.2 summarises the mechanical properties of the steel and aluminium samples following tensile loading on samples with an outer diameter of 12.62 mm.

Figure 4.5 shows typical load-displacement traces following static compression tests on the two types of metal tubing. All traces respond in a linear elastic manner, before yielding occurs at a force of approximately 15 kN. The ensuing response of the 15 mm long aluminium alloy sample differs significantly from that of its longer counterparts, Figure 4.5(a). Here, the slope of the post-yield region of the force-displacement trace of the sample is much higher than that associated with the longer samples, an affect associated with the greater level of constraint applied by the loading platens.

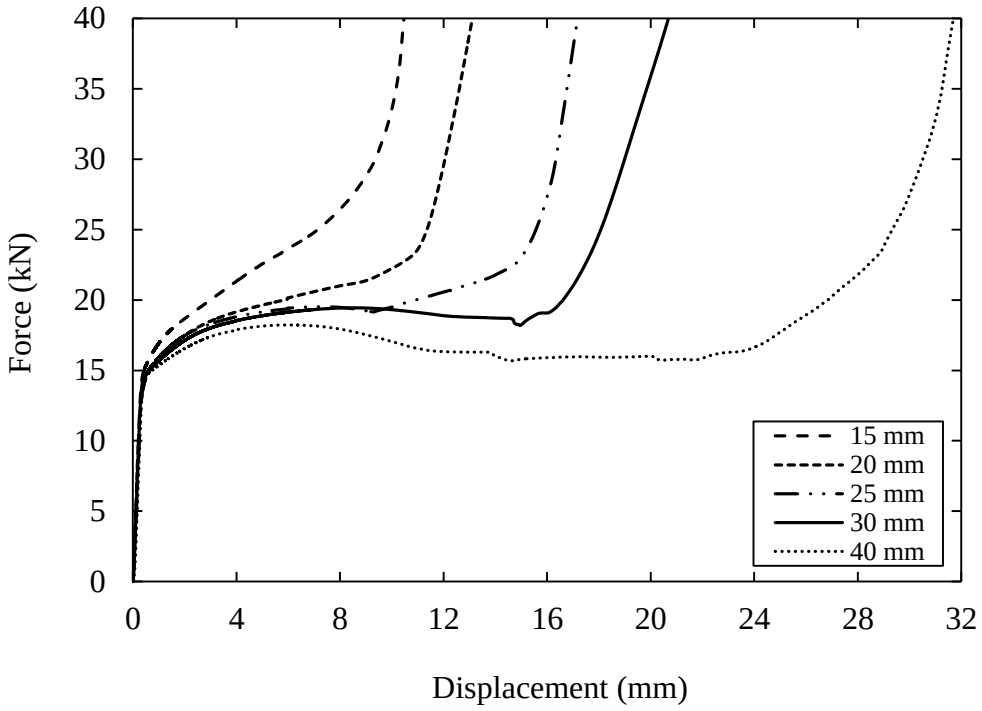

(a)

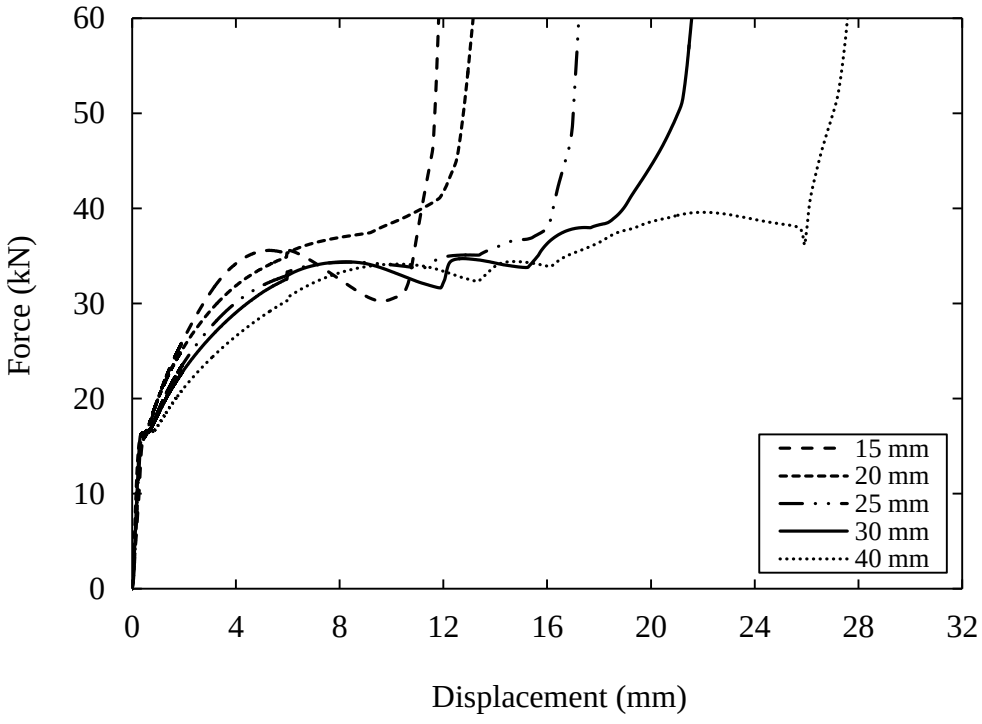

(b)

Figure 4.5 Typical load-displacement traces following tests on tubes of different length (a) 12.62 mm outside diameter , t=1.75mm (D/t = 5.21) aluminium alloy (b) 12.62 mm outside diameter, t =1.68mm (D/t = 5.51) steel.

During the latter stages of the test, the measured force begins to increase rapidly as the specimen is flattened between the platens (known as bottoming-out). The 20 mm and 25 mm long samples exhibit a slight drop in slope prior to a subsequent rapid increase and a relatively smooth trace up to high strains. Increasing the tube length to 30 mm and 40 mm resulted in a distinct change in response, with the load magnitude dropping after the sample yielded. This behaviour was associated with buckling failure, or the formation of wrinkles, in the tube and will be discussed in further detail below.

There are distinct differences between the load-displacements traces for the individual steel samples, Figure 4.5(b). All curves exhibit a similar slope during initial elastic loading. Following initial yield, the trace for the 15 mm sample rises to a maximum of approximately 35 kN before dropping rapidly during the latter stages of the test. The 20 mm long sample offers the highest peak load, approximately 37 kN and subsequently rising sharply as the sample is crushed. The remaining, longer samples all display a series of distinct peaks as well-defined wrinkles appear in the tubes during the compression process.

Figure 4.6 shows photos of the aluminium and steel tubes following testing. The shortest aluminium sample has clearly been compressed into a simple ring structure. Closer examination of the sample highlights the presence of small vertical cracks on the outer surface of the test sample. This form of localised failure is associated with the presence of large circumferential tensile stresses during the collapse process. The post-yield load-displacement trace for this specimen was relatively smooth as discussed previously.

(i) 15 mm

(ii) 20 mm

(iii) 25 mm

(iv) 30 mm

(v) 40 mm

(a)

(i) 15 mm

(ii) 20 mm

(iii) 25 mm

(iv) 30 mm

(v) 40 mm

(b)

Figure 4.6 Photographs of failed samples (a) Aluminium 12.62 mm (D/t = 5.21) and (b) Steel 12.62 mm (D/t = 5.51). The initial tube lengths are indicated on each figure.

The 20 mm long aluminium sample exhibits two distinct bulges as well as the previously-discussed tensile cracking. The 25 mm long sample is similar in appearance to that of the 20 mm long specimen and once again there is a small instability in the load-displacement trace at an intermediate displacement.

In contrast, the 30 mm aluminium sample exhibits a more complex buckling and cracking mode and lacks the axial symmetry observed in the previous samples. The load-displacement traces for this sample was relatively smooth up approximately 16 mm, at which point two small load-drops are apparent. Finally failure in the 40 mm long sample is complex, being associated with a more global buckling-type of failure. The load-displacement trace for this sample exhibited a significant drop in force at higher displacements, due to this global mode of buckling failure.

Failure in the steel tubes occurred in a more controlled manner with formation of distinct bulges for all specimen lengths. The deformation is categorised as concertina mode by Andrews et al. [59]. As before, the shortest sample was compressed to a ring-like structure. In this case, the failure process did not involve the initiation of the microcracking process observed in the aluminium samples.

Failure in the 20 and 25 mm long samples involved the formation of two wrinkles, whereas the longest sample exhibited three distinct bulges following testing. Clearly, the above photographs highlight the importance of the wrinkling mechanism in the energy-absorbing process within these steel tubes. The formation of wrinkles in axially-crushed metal tubes is discussed in [34] for thin-walled tubes.

The axial length of a tube which is available for the development of wrinkles is *L*, which when divided by 2*l*, gives the number (*n*) of wrinkles (and any partly formed wrinkles) when the tube is fully crushed to the bottoming-out displacement [34]:

$$n = \frac{L}{1.905\sqrt{D_m t}} = \frac{1}{1.905}\left(\frac{L}{D_m}\right)\left(\frac{D_m}{t}\right)^{\frac{1}{2}} \tag{4.1}$$

or,

$$n = \frac{L}{1.76\sqrt{D_m t}} = \frac{1}{1.76}\left(\frac{L}{D_m}\right)\left(\frac{D_m}{t}\right)^{\frac{1}{2}} \tag{4.2}$$

where D_m is the mean tube diameter and the actual circumferential strain is used, instead of a mean value and where 2*l* is the axial length of a tube necessary for the development of a complete wrinkle and is valid for $10 \leq D_m/t \leq 60$, approximately. This equation suggests that the number of wrinkles in the tube should scale with the length of the tube and should be independent of the material properties (i.e. identical steel and aluminium tubes should respond in a similar fashion).

The photographic evidence suggests that the number of wrinkles does indeed increase with tube length, although testing of a greater number of tubes is required to fully establish this. In terms of the influence of material properties, the steel and aluminium tubes behave in a similar fashion for small values of *L*, however this breaks down for the longer aluminium tubes where global buckling and fracture appear to become the predominant failure mechanisms.

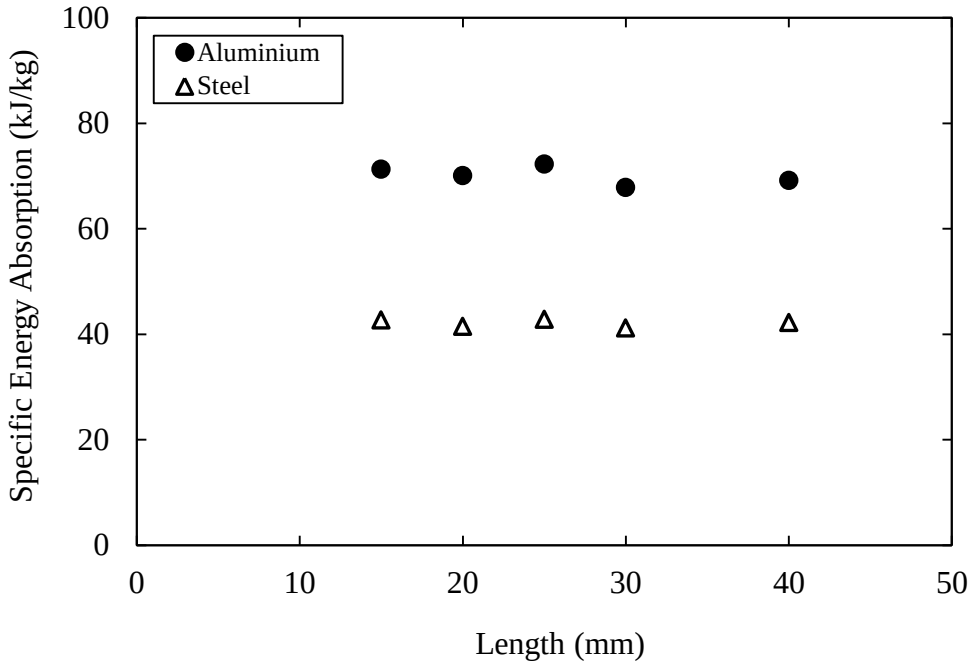

Figure 4.7 The influence of tube length on the energy-absorbing characteristics of the 12.62 mm outside diameter (D/t = 5.21) aluminium and 12.62 mm outside diameter (D/t = 5.51) steel tubes.

Figure 4.7 shows the variation of the specific energy absorption with tube length. The initial outer diameters of the aluminium and steel tubes were 12.62 mm (D/t = 5.21) and 12.62 mm (D/t=5.51), respectively. An examination of the figure indicates that the aluminium alloy clearly out-performs its steel counterpart. For example, the average value of SEA for the aluminium tube is almost fifty percent greater than that measured on a comparable steel tube. From the figure, it is clear that the value of SEA do not vary significantly with tube length. Indeed, it is anticipated that the SEA will remain constant for sufficiently long thin-walled tubes which deform in a ductile manner without any fracture. Finally, it is interesting to note that the level of scatter is much lower in those samples that fail in a controlled manner (i.e. all of the steel samples and the three shortest aluminium tubes) than in those that fail due to global buckling or fracture.

4.2.3 The Effect of the Diameter of the Aluminium and Steel Tubes on SEA

The effect of varying the ratio of the inner diameter of the metal tubes to its thickness, D/t, on energy absorption was investigated by conducting compression tests, details of which are given in Tables 4.3 and 4.4. Here, five different sizes of tubing were considered, with outer diameters ranging from approximately 12.6 mm to 25.4 mm. The values of D/t for the tubes ranged from 5.2 to 13.1 for the aluminium alloy tubes and 5.5 to 13.1 for the steel tubes.

Figure 4.8 shows typical load-displacement traces following compression tests on 20 mm long aluminium and steel tubes having different D/t ratios. From the two graphs, it is clear that varying this ratio has a significant effect on the mechanical response of the tubes. For example, the load-displacement traces for the tubes with the lowest D/t ratio show a steady increase until a constant plateau value is achieved. Increase in the D/t ratio results in a trace that exhibits a maximum load before reducing rapidly with increasing crosshead displacement. The displacement at peak load clearly increases as the D/t ratio is increased and these effects are more pronounced in the steel tubes than in their aluminium counterparts. Interestingly, the trace for the steel tube with the largest D/t ratio rises almost linearly to a peak value before dropping rapidly. Figure 4.9 shows the variation of SEA with the tube D/t ratio for both the aluminium and steel tubes. Here, it is clear that the energy-absorbing capability of the tubes decreases rapidly with increasing D/t. For example, the SEA of the aluminium tubes decreases from 70.0 to 52.9 kJ/kg (a reduction of 25%) and that of the steel from 41.5 to 24.1 kJ/kg (a reduction of 42%). As before, the aluminium tubes outperform their steel counterparts with the relative difference between the two increasing with D/t. Indeed, the value of SEA for the largest aluminium tubes was more than 220% that of the largest steel tube.

Tube ID	Outer diameter, D_o [mm]	Mean diameter, D_m [mm]	Inside diameter, D [mm]	Thickness, t [mm]	D/t ratio	SEA quasi-static [kJ/kg]	SEA dynamic [kJ/kg]
TAL12	12.62	10.87	9.12	1.75	5.21	70.07	71.76
TAL16	16.00	14.18	12.36	1.82	6.79	63.47	64.63
TAL19	19.10	17.35	15.60	1.75	8.91	58.28	60.06
TAL22	22.40	20.70	19.00	1.70	11.18	56.08	56.65
TAL25	25.40	23.72	22.04	1.68	13.12	52.96	53.53

Table 4.3 Summary of the geometrical and specific energy absorbing characteristics of the 20 mm long aluminium tubes.

Tube ID	Outer diameter, D_o [mm]	Mean diameter, D_m [mm]	Inside diameter, D [mm]	Thickness, t [mm]	D/t ratio	SEA quasi-static [kJ/kg]	SEA dynamic [kJ/kg]
TST12	12.62	10.94	9.26	1.68	5.51	41.46	45.73
TST16	15.78	14.10	12.42	1.68	7.39	36.94	39.82
TST19	19.05	17.37	15.69	1.68	9.34	31.22	34.73
TST22	22.22	20.54	18.86	1.68	11.23	27.97	31.33
TST25	25.40	23.72	22.04	1.68	13.12	24.12	26.50

Table 4.4 Summary of the geometrical and specific energy absorbing characteristics of the 20 mm long steel tubes.

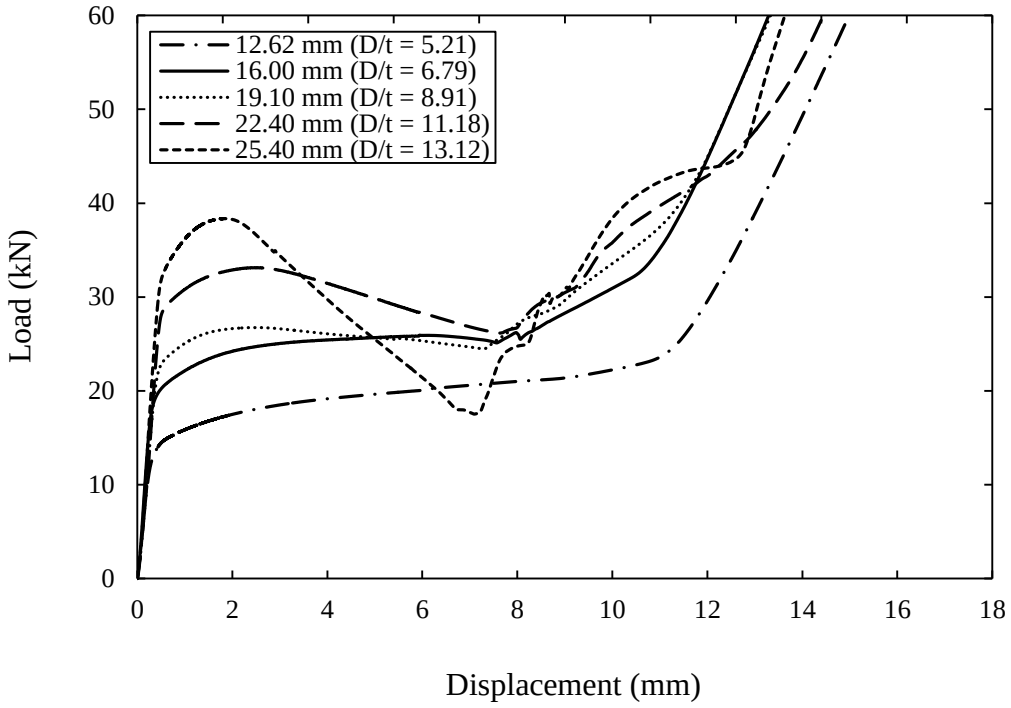

(a)

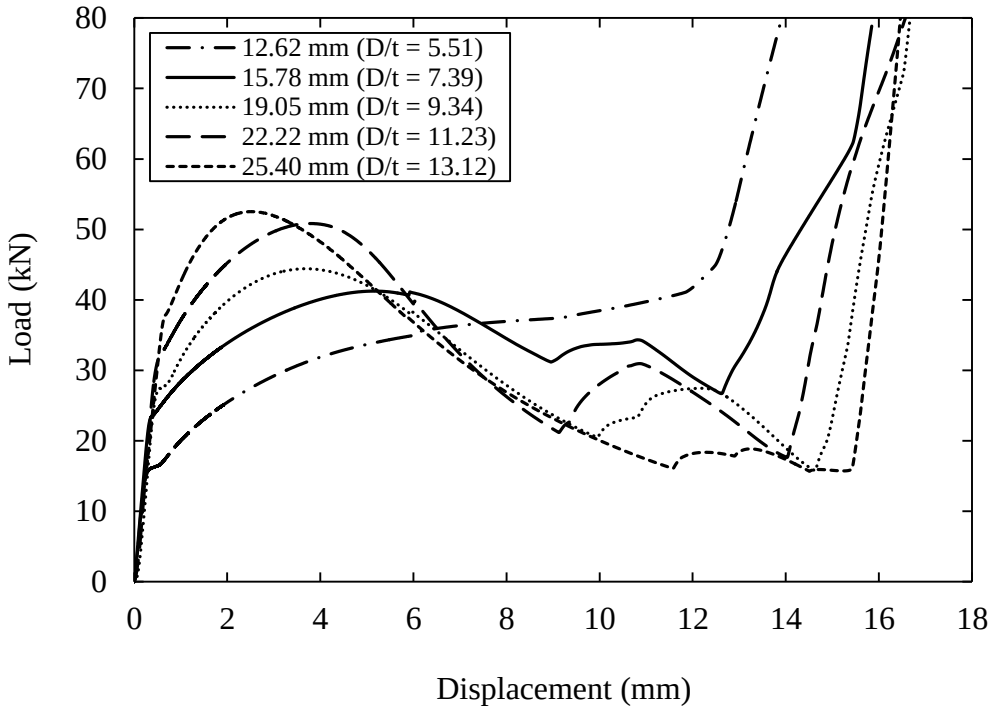

(b)

Figure 4.8 Load-displacement traces following crush tests on 20 mm long tubes with different values of D/t (a) aluminium (b) steel.

As mentioned previously, the specific energy absorption capacity of the tubes was determined from the area under the load-displacement trace up to the point at which the force begins to increase rapidly (the bottoming-out displacement) [35]. The SEA can also be predicted by considering the samples as thin-walled tubes. The quasi-static mean axial crushing force of a thin-walled cylindrical tube, P_m, can be approximated by [34]:

$$P_m = Kt\sigma_o(tD_m)^{\frac{1}{2}} \tag{4.3}$$

where,

$$K = \frac{2\pi^{\frac{3}{2}}}{3^{\frac{1}{4}}\sqrt{2}} = 5.984$$

and D_m is the mean tube diameter.

For simplicity, by assuming that the effective crushing displacement is taken as $0.75L$, where L is the initial tube length, then the work done by this force up to the bottoming-out displacement is approximately $P_m \times 0.75L$.

Thus, the specific energy absorption is given as:

$$SEA = \frac{P_m \times 0.75L}{M} \tag{4.4}$$

where, the tube mass is $M = \pi D_m tL\rho$, for a thin-walled tube, giving:

$$\mathrm{SEA} = \mathrm{k}\left(\frac{\sigma_o}{\rho}\right)\left(\frac{\mathrm{t}}{\mathrm{D_m}}\right)^{\frac{1}{2}} \tag{4.5}$$

where ,

$$k = \frac{0.75K}{\pi} = 1.428$$

This equation indicates that the SEA decreases as the ratio D_m/t (and D/t) increases for given values of σ_o and ρ, as indicated in Figure 4.9. The equation also suggests that the SEA should be independent of tube length, as indicated by the experimental results in Figure 4.7 suggesting that the assumption regarding the effective crushing length, based on thin-walled tubes, might not be reasonable for the thicker tubes studied here.

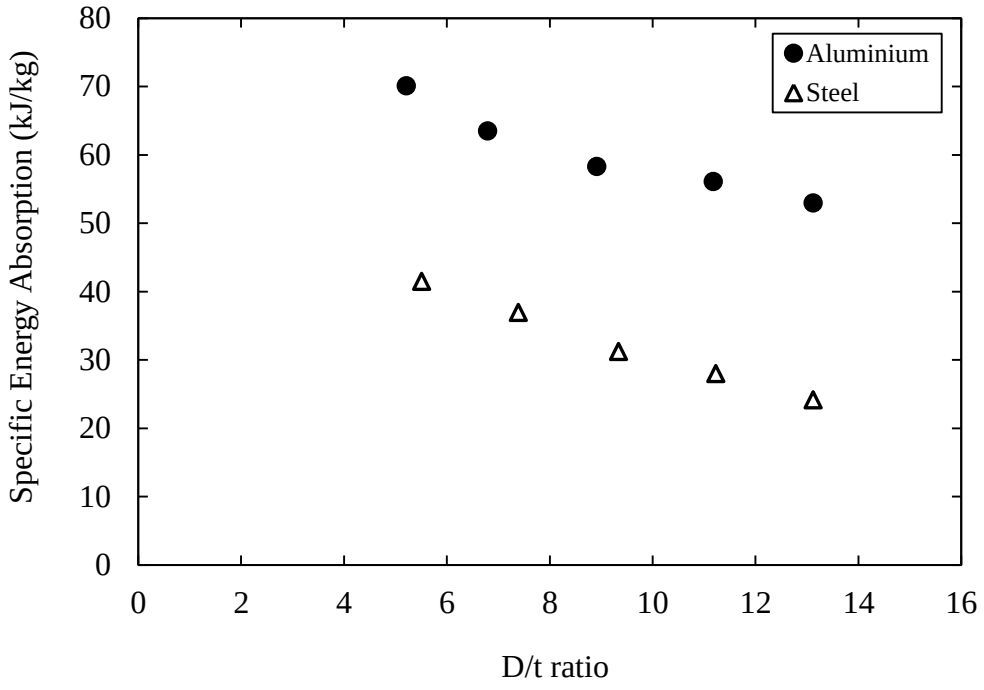

Figure 4.9 Variation of the quasi-static values of SEA with D/t ratio for 20 mm long aluminium and steel tubes.

Figure 4.10 shows images of crushed 20 mm long aluminium and steel tubes based on a range of initial D/t ratios. It is clear that the tubes with the lowest values of D/t exhibit distinct wrinkles, whereas samples with larger values of D/t tend to display a single bulge. The exception to this observation is the aluminium tube with a D/t value of 13.12, which appears to exhibit and large and a small wrinkle.

Indeed, Equations (4.1) and (4.2) suggest that the number of wrinkles should decrease as the tube diameter increases. For example the value of n for the smallest steel tube is 2.45 (i.e. two wrinkles), whereas that for its largest counterpart is 1.66 (one wrinkle).

The dynamic energy-absorbing characteristics of the aluminium and steel tubes were assessed through a series of drop-weight impact tests on the tubes. Figure 4.11 shows the variation of SEA with the tube D/t ratio under dynamic loading conditions. The trends in the experimental data are similar to those observed following the quasi-static tests on the tubes (Figure 4.9). Once again, the SEA reduces as the D/t ratio increases. The dynamic values of SEA for the aluminium tubes are very similar to the quasi-static data, highlighting a lack of any rate-sensitivity in this material system. In contrast, the steel tubes exhibit a distinct rate-sensitivity, with the dynamic enhancement factor (dynamic SEA divided by the quasi-static value) being approximately 10%.

It is evident from Equation (4.5) that the SEA is proportional to the flow stress, σ_o. This equation is based on simple models proposed elsewhere in the literature for thinner tubes and shows that the SEA decreases with D/t, but is independent of L. Thus, the SEA will increase if the material is strain-rate sensitive. The material strain-rate properties of steel can be significant and a large number of articles have been published which reveal that the enhancement at smaller strains is much larger than that at large strains [34]. On the other hand, the material strain-rate properties for aluminium alloys are generally much less than those for steel and, in fact, are often taken as strain-rate insensitive, at least for strain-rates up to about 1000 sec^{-1} [34].

(i) 12.62 mm (D/t = 5.21)

(ii) 16.00 mm (D/t = 6.79)

(iii) 19.10 mm (D/t = 8.91)

(iv) 22.40 mm (D/t = 11.18)

(v) 25.40 mm (D/t = 13.12)

(a)

(i) 12.62 mm (D/t = 5.51)

(ii) 15.78 mm (D/t = 7.39)

(iii) 19.05 mm (D/t = 9.04)

(iv) 22.22 mm (D/t = 10.99)

(v) 25.40 mm (D/t = 13.12)

(b)

Figure 4.10 Photos of failed 20 mm long aluminium and steel tubes with different initial D/t values.

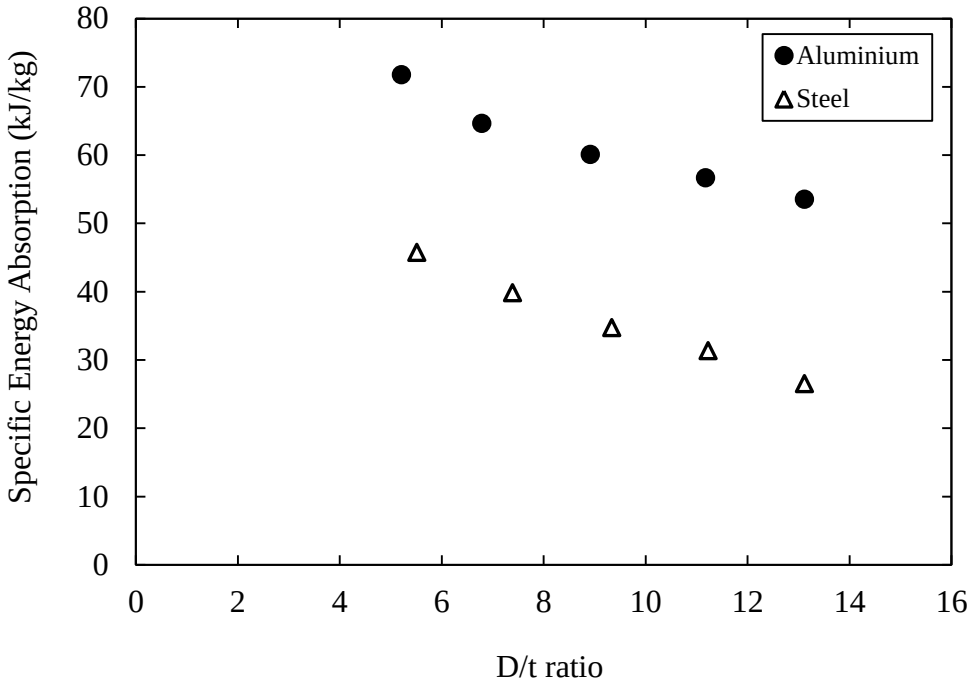

Figure 4.11 Variation of dynamic SEA with D/t ratio for the 20 mm long aluminium and steel tubes.

4.2.4 The Effect of the Foam Density on SEA for Systems with Embedded Tubes

Individual tubes were then embedded into foams with densities ranging from 15.6 to 224 kg/m^3. Details of the aluminium and steel tube-reinforced foam systems are given in Tables 4.5 and 4.6 respectively. Figure 4.12 shows a typical load-displacement trace for a compression test on an aluminium tube + foam combination. In this figure, a trace following a test on a 12.62 mm outer diameter aluminium tube embedded in a 38.3 kg/m^3 density foam is shown. Also included in the figure are the load-displacement traces for an individual tube as well as that for a polymer foam sample of similar volume to that of the combined tube + foam specimen. As expected, the aluminium tube dominates the response of the embedded foam. The performance of the reinforced foam is roughly equal to that of the sum of the individual foam and tube.

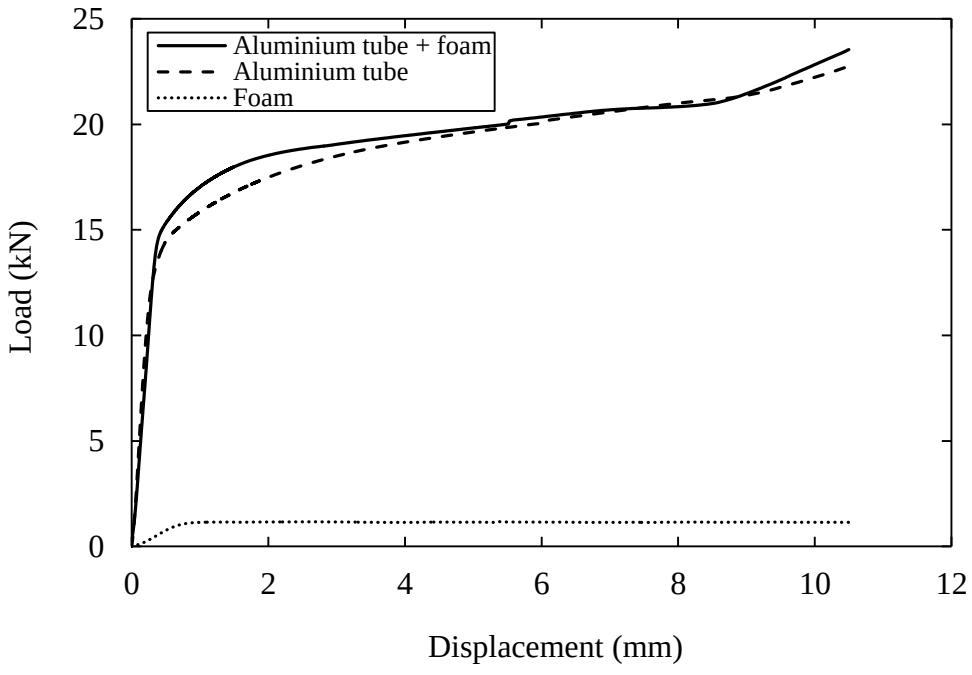

Figure 4.12 Load-displacement curves following tests on the 20 mm long aluminium tube (diameter = 12.62 mm, D/t = 5.21), the 38.3 kg/m^3 foam and the tube + foam combination.

Tube Embedded foam ID	Foam Density [kg/m^3]	Foam Modulus [MPa]	Quasi-static SEA of tube [kJ/kg]	Dynamic SEA of tube [kJ/kg]
TAL12	0 (no foam)	0 (no foam)	70.1	71.8
T1ALP1	15.6	6	70.6	71.1
T1ALP2	38.3	37	68.4	71.1
T1ALP3	56.0	69	68.6	69.4
T1ALP4	90.4	97	69.1	70.1
T1ALP5	128.0	160	69.4	71.5
T1ALP6	224.0	280	69.5	71.5

Table 4.5 Summary of the SEA values following tests on the 20 mm long aluminium tubes (diameter = 12.62 mm, D/t = 5.21) with foam densities.

Tube Embedded foam ID	Foam Density [kg/m^3]	Foam Modulus [MPa]	Quasi-static SEA of tube [kJ/kg]	Dynamic SEA of tube [kJ/kg]
TST12	0 (no foam)	0 (no foam)	41.5	45.7
T1STP1	15.6	6	41.8	45.5
T1STP2	38.3	37	41.2	45.3
T1STP3	56.0	69	43.1	46.3
T1STP4	90.4	97	43.9	48.1
T1STP5	128.0	160	42.3	46.3
T1STP6	224.0	280	40.2	44.8

Table 4.6 Summary of the SEA values following tests on the 20 mm long steel tubes (diameter = 12.62 mm, D/t = 5.51) with foam densities.

There is no evidence of any enhancement in the response of the aluminium tube associated with the small degree of additional support due to the presence of the low density foam. Figure 4.13 shows the aluminium and steel tubes following removal from the foam. A comparison of these images with those shown previously in Figure 4.6 indicates that the modes of deformation and failure are similar in both the individual tubes and those that have been removed from the foam, indicating that the foam does not modify the response of the tube. This evidence supports the view that the foam merely acts as a support for the metal tubes and its density should be as low as possible.

(a)

(b)

Figure 4.13 Photos of compressed (a) aluminium (diameter = 12.62 mm, D/t = 5.21) and (b) steel (diameter = 12.62 mm, D/t = 5.51) tubes following compression testing in the 38.3 kg/m^3 foam.

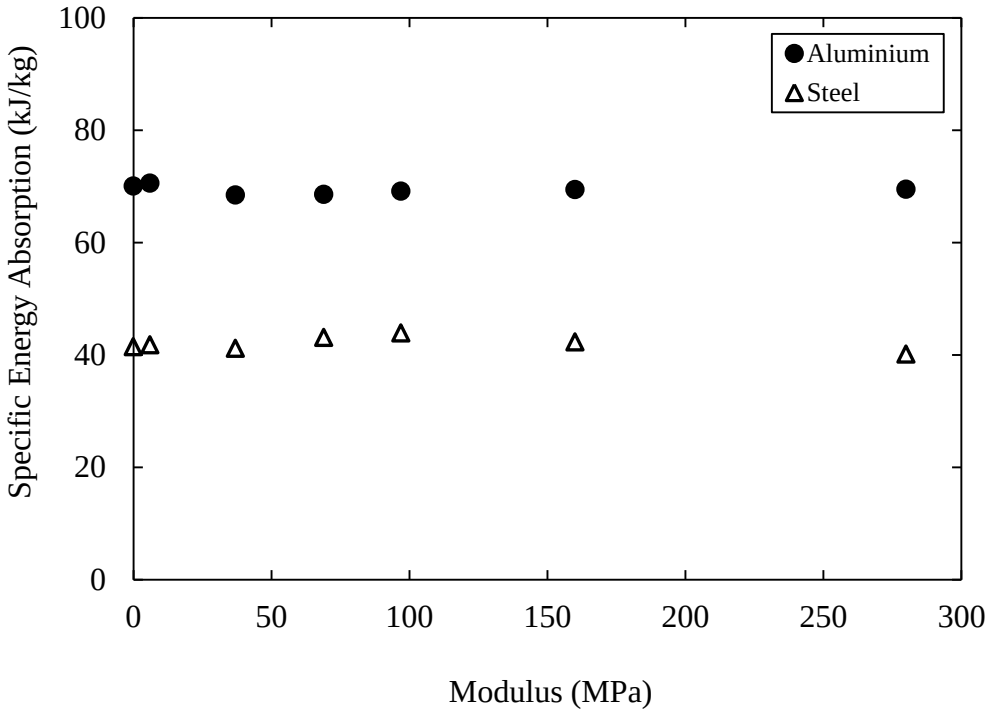

Figure 4.14 Variation of SEA at quasi-static rates of loading with foam modulus for the 20 mm long aluminium (diameter = 12.62 mm, D/t = 5.21) and steel (diameter = 12.62 mm, D/t = 5.51) tubes.

Tests were then undertaken on foams with nominal densities ranging between 15.6 and 224 kg/m^3. The energy absorbed by the embedded tubes was estimated by determining the energy under the load-displacement trace for the foam on its own and then subtracting this value from the energy under the load-displacement trace of the tube + foam combination. The energy was then normalised by the mass of the metal tube to yield an equivalent SEA value.

The resulting estimations for SEA for the two types of tubing are shown as a function of foam modulus in Figure 4.14. Also included in each figure are the values associated with the tests on the plain tubes (i.e. those not embedded in a foam). These data points are shown as being embedded in a foam having a modulus of zero.

From the figure, it is clear that the values of SEA of both the aluminium and steel tubes do not vary with foam modulus, indicating the foam serves only to maintain the tubes in place and not to modify or enhance their performance.

Figure 4.15 shows typical load-displacement traces following impact tests on the tube/38.3 kg/m^3 foam combination as well as the individual constituents (i.e. the tube and the unreinforced 38.3 kg/m^3 foam). Clearly, the response of the tube and the tube plus foam combination are oscillatory, due to ringing in the load cell following impact of the steel impactor on the stiff aluminium tube. It is clear that the tube is responsible for absorbing most of the energy in these reinforced structures.

As before, the energy absorbed by the metal tube was estimated by removing the energy absorbed by the foam (as determined from the dynamic compression test on the plain foam) and these values are presented as a function of foam modulus in Figure 4.16. The figure also includes the quasi-static data presented earlier as well as the SEA values for unsupported tubes (i.e without foam).

Again, it is clear that the properties of the foam do not have any effect on the energy absorbing behaviour of the metal tubes. This suggests that a simple rule of mixtures approach could be used to predict the energy-absorbing capability of foams reinforced with a multitude of metal tubes. In addition, there is a lack of rate-sensitivity in the response of the aluminium tubes, given that the dynamic values of SEA are almost identical to those measured at quasi-static rates. However, closer inspection of the steel values indicates that the dynamic values are higher than their quasi-static counterparts highlighting a rate-sensitive response.

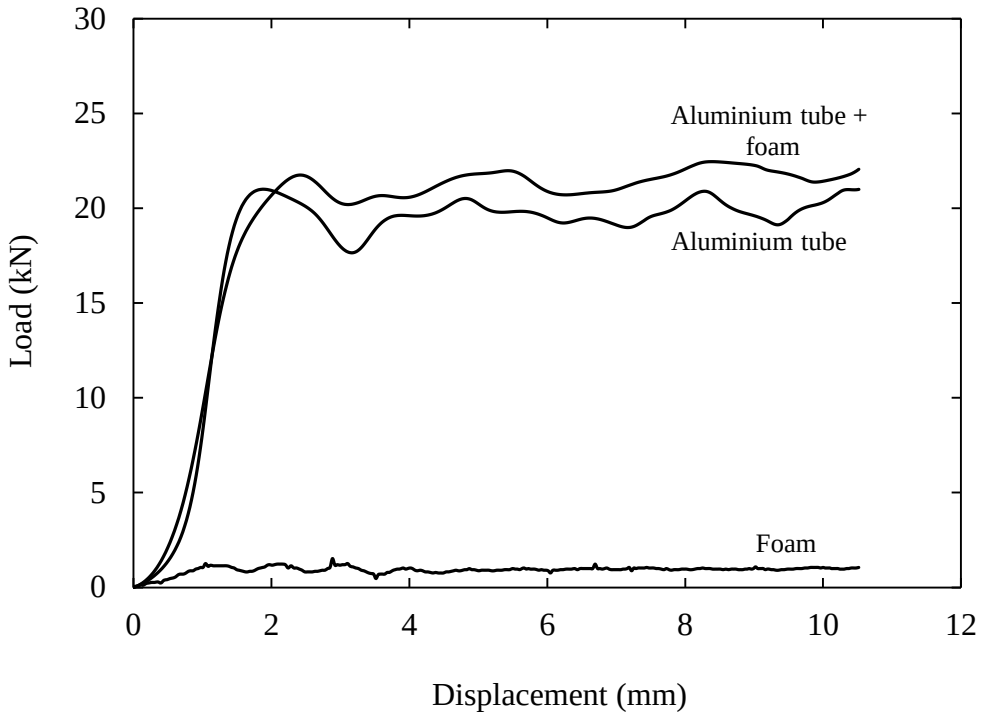

Figure 4.15 Dynamic load-displacement traces for the 20 mm long aluminium (D_o = 12.62 mm, D/t = 5.21) tube, foam (density = 38.3 kg/m^3) and foam+aluminium tube.

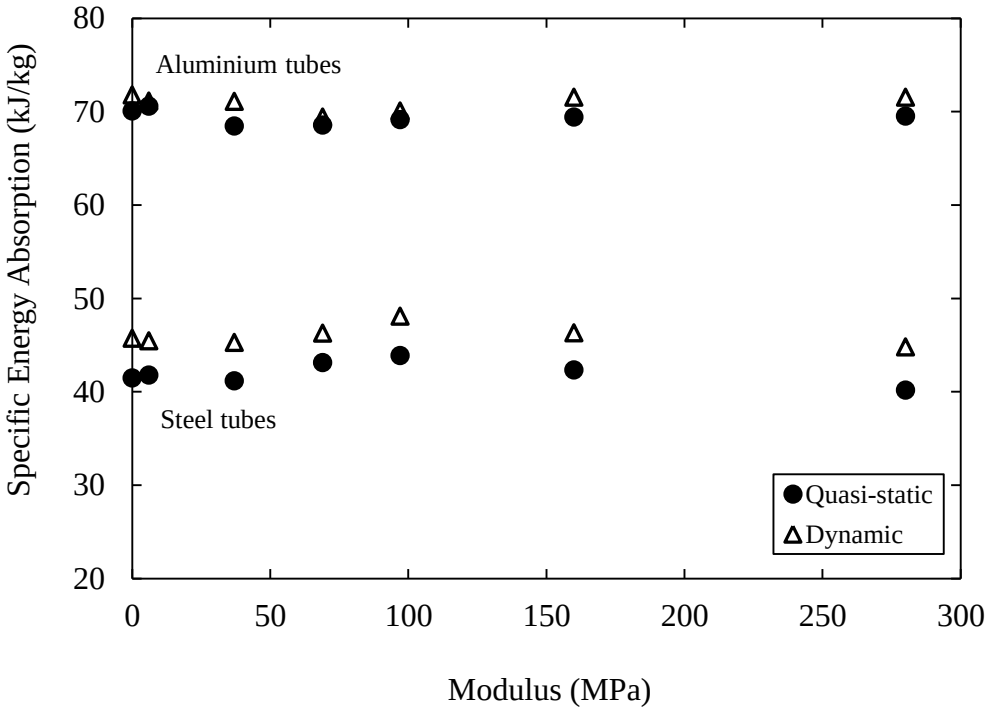

Figure 4.16 The variation of quasi-static and dynamic SEA with foam density for the 20 mm long aluminium (D_o = 12.62 mm, D/t = 5.21) and steel (D_o = 12.62 mm, D/t = 5.51) tubes.

4.2.5 Tests on the Metal Multi-tube Foams

This section investigates the effect of increasing the planar density of metal tubes on the quasi-static energy-absorbing response of these reinforced foam structures. Here, between one and five 12.6 mm diameter metal tubes were embedded into 20 mm thick, 60 mm square foam blocks with densities of 15.6, 90.4 and 224 kg/m^3. Details of the total density and SEA are given in Tables 4.7 and 4.8.

No of tubes in foam	Density [kg/m^3]			SEA [kJ/kg]		
	P1	P4	P6	P1	P4	P6
1	51.6	126.3	220.8	57.5	29.9	26.3
2	93.5	166.7	256.9	60.2	39.2	32.9
3	135.4	206.9	311.1	62.1	43.6	35.9
4	177.2	248.6	347.2	63.1	46.9	40.5
5	219.1	286.1	384.7	65.3	50.3	42.6

Table 4.7 Summary of the total density for the aluminium tubes plus foam and the specific energy absorption of the samples.

No of tubes in foam	Density [kg/m^3]			SEA [kJ/kg]		
	P1	P4	P6	P1	P4	P6
1	133.3	212.5	305.6	42.5	30.2	26.7
2	256.9	338.9	429.2	42.1	32.1	31.3
3	380.6	463.9	551.4	41.1	34.5	32.9
4	505.6	586.1	677.8	41.7	35.5	34.0
5	627.8	716.7	794.4	41.5	37.1	34.4

Table 4.8 Summary of the total density for the steel tubes plus foam and the specific energy absorption of the samples.

Figure 4.17 shows the variation of SEA with core density (the density of the core was based on the foam and metal combined). Included in the figure are the values associated with the tests on the 12.6 mm diameter single tubes, presented previously in Figure 4.9. The resulting SEA values were calculated based on the total mass of the test samples, that is, no attempt was made to remove the contribution associated with the foam.

Figure 4.17(a) shows that the SEA of the aluminium-P1 foam (density = 15.6 kg/m^3) system increases slightly from 58 to 65 kJ/kg as the number of tubes is increased from one to five. Similar trends are apparent in the 224 kg/m^3 foam, where increasing the number of tubes serves to increase the SEA from 26 to 43 kJ/kg. It is interesting to note that the SEA of the P1 structure containing five tubes for both metals is similar to that of the plain tube, suggesting that the response of the metal tubes completely masks that of the foam.

It is anticipated that increasing the number of metal tubes in the foams serves to increase the overall SEA of the structure. However, this is true for all of the samples tested except for those steel tubes in P1 foam, Figure 4.17(b). The SEA value regardless any number of steel tubes in P1 foam was observed to be almost similar to the SEA of individual steel tubes tested. This is related to the much lower density of the foam that has insignificant effect to the total SEA of the structures. A closer inspection of the aluminium and steel tubes following removal from the foam multi-tube foams structures shows that the buckling response is similar to that of individual tubes as previously shown in Figure 4.13. The experimental evidence suggests that the foam does not modify the response of the tube and that that a simple rule of mixtures approach could be used to estimate the energy-absorbing capability of foams reinforced with a multitude of metal tubes.

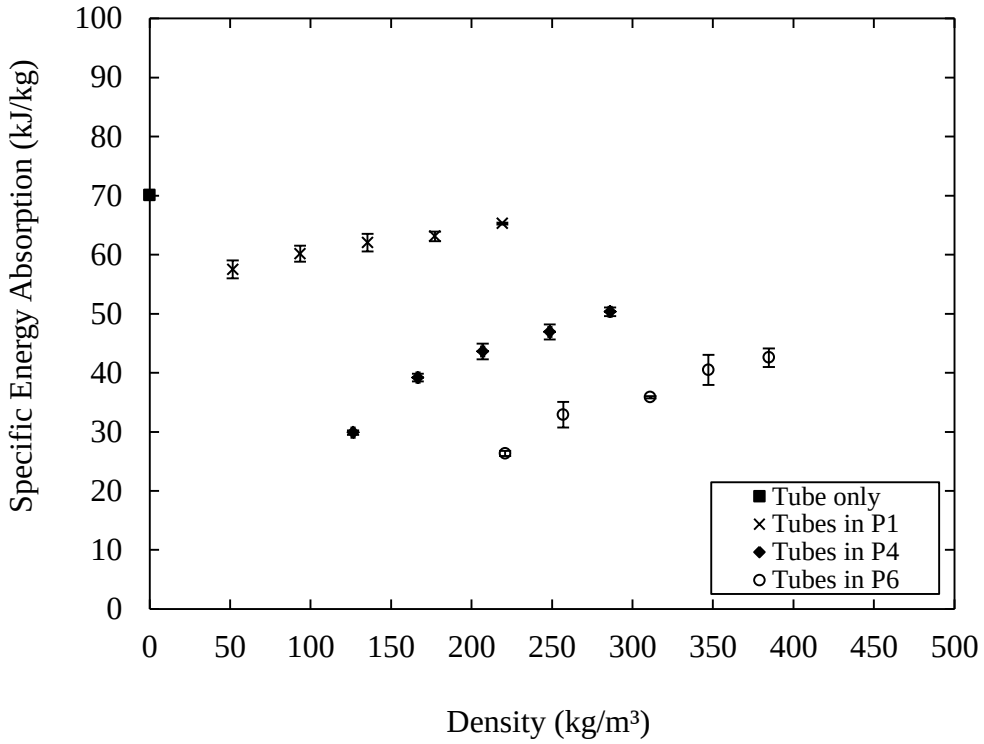

(a)

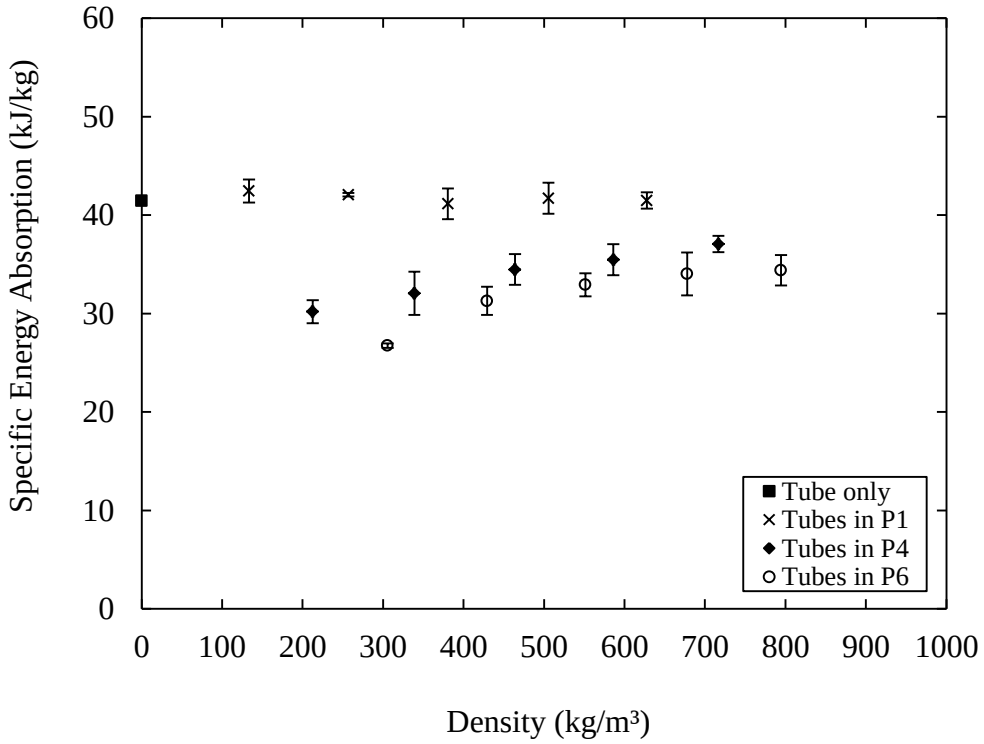

(b)

Figure 4.17 Variation of the quasi-static SEA with total tube plus foam density for the 20 mm long (a) aluminium (diameter = 12.62 mm, D/t = 5.21) and (b) steel (diameter = 12.62 mm, D/t = 5.51) tubes.

4.3 CFRP Tube-reinforced Foam Structures

4.3.1 Resin Burn-off Tests on the CFRP Tubes

A burn-off test is a common test to identify the volume fraction of individual constituent of a composite material. The composite materials investigated in this research were based on readily-available tubes supplied by Easy Composite Ltd. Six different sizes of tubing were investigated, with outer diameters ranging from approximately 10.2 mm to 63.6 mm and values of the ratio of internal diameter to thickness (D/t) ranging from 6.3 to 32.6. The tubes were based on a unidirectional T700 carbon fibre-reinforced epoxy wrapped with unidirectional E-glass fibres and produced using a roll-wrapping procedure [129].

The weight fraction of fibres in the composite tubes was determined by burning off the resin in a furnace at a temperature of 560^{o}C [138]. A total of 18 samples were tested and analysed to determine the fibre weight fraction values of the composite. Figure 4.18 shows photographs the before and after resin burn-off of a 12.7 mm specimen. After the burning process, the resin was completely removed from composite specimen and the remaining fibres are apparent. It is clear that the carbon fibres are unidirectional and oriented along the 0^{o} direction while the glass fibres are oriented at 90^{o}.

(a) (b)

Figure 4.18 Specimen with diameter of 12.7 mm CFRP tubes (a) before and (b) following resin burn-off in a furnace.

Table 4.9 gives a summary of the CFRP tubes following burn-off tests. From this test, parameters such as the weight fraction, W, volume of the sample, v_s, volume fraction, V, density, ρ_s, and longitudinal modulus, E_1, were determined. For example, by considering the CF12A sample, the weight fraction of the carbon fibre, glass fibre and epoxy resin matrix are given by [10]:

$$1 = W_{fc} + W_{fg} + W_m \tag{4.6}$$

$$W_{fc} = \frac{m_{fc}}{m_s} = \frac{0.65}{1.60} = 0.40$$

$$W_{fg} = \frac{m_{fg}}{m_s} = \frac{0.38}{1.60} = 0.24$$

$$W_m = \frac{m_m}{m_s} = \frac{0.57}{1.60} = 0.36$$

$$\therefore \quad W_f = W_{fc} + W_{fg} = 0.40 + 0.24 = 0.64$$

The results presented in Table 4.9 show that the fibre weight fraction varied from 0.58 to 0.65 across the range of tube diameters with the average being 0.62. Such variations in the fibre weight fraction are linked to difficulties in accurately wrapping the fibres during the manufacturing process.

Outer diameter, D_o [mm]	Sample ID	Mass sample, m_s [g]	Mass Fibre, m_f [g]	Mass carbon fibre, m_{fc} [g]	Mass glass fibre, m_{fg} [g]	Mass Matrix, m_m [g]	Fibre weight fraction, W_f	Longitudinal modulus, E_1 [GPa]	Predicted density [g/cm^3]
10.20	CF10A	1.00	0.59	0.37	0.22	0.41	0.59	82.73	1.50
	CF10B	0.99	0.57	0.36	0.21	0.42	0.58	80.14	1.49
	CF10C	0.94	0.54	0.34	0.20	0.40	0.57	79.88	1.49
	Average	0.98	0.57	0.36	0.21	0.41	0.58	80.91	1.50
12.70	CF12A	1.60	1.03	0.65	0.38	0.57	0.64	92.95	1.56
	CF12B	1.60	1.04	0.66	0.38	0.56	0.65	94.18	1.56
	CF12C	1.49	0.95	0.65	0.30	0.54	0.64	96.22	1.54
	Average	1.56	1.01	0.65	0.36	0.56	0.64	94.45	1.55
29.40	CF29A	4.44	2.62	1.65	0.97	1.82	0.59	82.75	1.50
	CF29B	4.27	2.59	1.63	0.96	1.68	0.61	85.80	1.52
	CF29C	4.30	2.66	1.68	0.98	1.64	0.62	88.08	1.53
	Average	4.34	2.62	1.65	0.97	1.71	0.61	85.54	1.52
40.90	CF40A	5.71	3.94	2.48	1.46	1.77	0.69	102.33	1.61
	CF40B	5.85	3.75	2.36	1.39	2.10	0.64	92.41	1.55
	CF40C	6.37	3.92	2.47	1.45	2.45	0.62	87.47	1.53
	Average	5.98	3.87	2.44	1.43	2.11	0.65	94.07	1.56
50.40	CF50A	7.61	4.79	3.02	1.77	2.82	0.63	90.16	1.54
	CF50B	7.50	4.67	2.77	1.90	2.83	0.62	85.85	1.55
	CF50C	7.73	4.79	2.89	1.90	2.94	0.62	86.12	1.54
	Average	7.61	4.75	2.89	1.86	2.86	0.62	87.37	1.54
63.60	CF63A	11.33	6.77	4.27	2.50	4.56	0.60	84.12	1.51
	CF63B	11.50	7.00	4.41	2.59	4.50	0.61	86.20	1.52
	CF63C	11.52	7.16	4.56	2.60	4.36	0.62	89.19	1.53
	Average	11.45	6.98	4.41	2.56	4.47	0.61	86.51	1.52
						Average	0.62	88.14	1.53

Table 4.9 Summary of the CFRP tubes with various diameters following burn-off tests.

The volume of a sample is related to the density of the constituents, as listed in Table 4.10. The volume for the CF12A sample can be determined by:

$$v_s = v_{fc} + v_{fg} + v_m \tag{4.7}$$

$$v_{fc} = \frac{m_{fc}}{\rho_{fc}} = \frac{0.65}{1.80} = 0.36\ cm^3$$

$$v_{fg} = \frac{m_{fg}}{\rho_{fg}} = \frac{0.38}{2.56} = 0.15\ cm^3$$

$$v_m = \frac{m_m}{\rho_m} = \frac{0.57}{1.10} = 0.52\ cm^3$$

$$\therefore \quad v_s = 1.03\ cm^3$$

Volume fraction which refers to the fibre content is given by:

$$1 = V_{fc} + V_{fg} + V_m \tag{4.8}$$

$$V_{fc} = \frac{v_{fc}}{v_s} = \frac{0.36}{1.03} = 0.35$$

$$V_{fg} = \frac{v_{fg}}{v_s} = \frac{0.15}{1.03} = 0.14$$

$$V_m = \frac{v_m}{v_s} = \frac{0.52}{1.03} = 0.50$$

The density of the sample is obtained from the relationship:

$$\rho_s = \rho_{fc}V_{fc} + \rho_{fg}\,V_{fg} + \rho_m V_m \tag{4.9}$$

$$\rho_s = (1.80)(0.35) + (2.56)(0.14) + (1.10)(0.50)$$

$$\therefore \quad \rho_s = 1.56\ g/cm^3$$

The carbon fibres that are stronger and stiffer dominate the longitudinal properties of the tube. By assuming a perfect bond between fibres and matrix, the longitudinal strains are equal throughout the length of the tube. The longitudinal modulus is given by:

$$E_1 = E_{1fc}V_{fc} + E_{1fg}\,V_{fg} + E_{1m}V_m \tag{4.10}$$

$$E_1 = (230)(0.35) + (72.40)(0.14) + (3.50)(0.50)$$

$$\therefore \quad E_1 = 92.95\ GPa$$

The relation presented above is known as a rule of mixtures for the longitudinal modulus associated with the moduli of the constituents and volume fractions. The density and longitudinal modulus values provide a comparison between the analytical values and those supplied by the manufacturer. Verification of these values is important and useful when undertaking finite element modelling.

Property	Carbon fibre T700 [139]	E-glass fibre [10], [140]	Epoxy resin [141]	CFRP tube [129]
E_1 [GPa]	230	72.4	3.5	90
E_2,E_3 [GPa]	19	72.4	3.5	19
G_{12},G_{13} [GPa]	27.6	30.2	1.29	4.6
G_{23} [GPa]	7.04	30.2	1.29	4.6
ν_{12}, ν_{13}	0.2	0.2	0.35	0.14
ν_{23}	0.35	0.2	0.35	0.14
Density [g/cm^3]	1.80	2.56	1.10	1.60

Table 4.10 The elastic properties of the tube constituents and the CFRP tube properties as provided by the manufacturer.

By referring to Tables 4.9 and 4.10, the average predicted density (1.53 g/cm^3) was found to be very close to the value given by the supplier (1.60 g/cm^3). While the average calculated longitudinal modulus (88.14 GPa) differs only by 2% from the given value (90GPa). In this case, some of the differences were related to uncertainties in the measurements and imperfections caused during manufacturing process. Another aspect may also be due to the nature of variations in the microstructure within the tube constituents. Nevertheless, the predictions from the rule of mixtures are considered reliable and in a good agreement with the expected values. This indicates that the mechanical properties are valid for the finite element analysis in Chapter 5.

4.3.2 Tensile Tests on the CFRP Tubes

CFRP tubes with an outer diameter of 12.7 mm were tested under tensile loading. Generally, grips are clamped onto the flat ends of a specimen and a tensile force is applied through shear at the specimen grip surfaces, generating tensile stresses within the specimen [131]. The greatest challenge in conducting a tensile test on a composite tube is to grip the specimen without generating high stress concentrations that can cause the tube to fracture at the grip. Hence, a steel rod was inserted into the tube ends to prevent the tube from breaking, due to the clamping force applied.

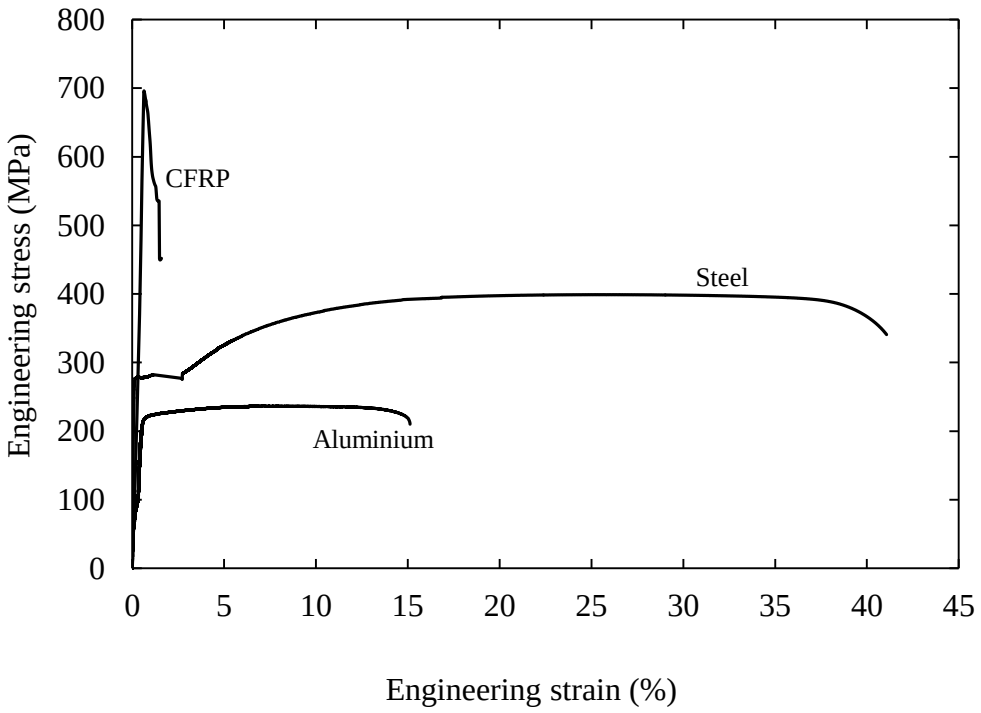

Figure 4.19 Stress-strain curve following a tensile test on a 12.7 mm diameter (D/t = 7.4) CFRP tube. (The figure includes the stress-strain curve for aluminium and steel).

The stress-strain curve for the CFRP tube is shown in Figure 4.19 and the related data are summarised in Table 4.11. For comparison purposes, the stress-strain curves for the aluminium and steel are also included in the figure. The stress-strain curve for the carbon fibre-reinforced polymer was virtually linear. The stress increased steeply up to approximately 700 MPa and fracture occurred. This is a characterisation of brittle materials due to the fact that abrupt rupture occurs without any visible indication [18]. The elongation at rupture was approximately 0.5%. This is relatively very small compared to aluminium and steel, which fractured at strains of approximately 15% and 40% respectively. In this case, the CFRP is inherently brittle and exhibits extremely low ductility, whereas the steel material, which is the most ductile material, offers the highest strain to failure.

Material	Circular CFRP tube
Outer diameter, D_o [mm]	12.7 mm
Thickness, t [mm]	1.35 mm
Density [kg/m^3]	1590 kg/m^3
Tensile strength [MPa]	691
Tensile modulus [GPa]	87

Table 4.11 Summary of the mechanical properties of the circular CFRP tube.

The tensile test results show that the CFRP material offers a superior tensile strength (691 MPa) than the aluminium and steel. The tensile strength of the CFRP is approximately 3.5 and 1.5 times greater than the aluminium and steel materials respectively. As for the tensile modulus, the value obtained from the test on the CFRP tube is 87 GPa. The CFRP tube is the lightest, a density of about 40% lower than the aluminium and 80% lower than the steel. The properties obtained from tensile tests were compared to the previous values calculated using the rule of mixtures. Agreement between the analytically-predicted (Table 4.9) and the measured (Table 4.11) values for the CFRP samples are generally good.

4.3.3 The Effect of the Length of the CFRP Tubes on SEA

The primary aim of this research study was to investigate the specific energy absorbing characteristics of the CFRP tube-reinforced foams as shown in Figure 4.28. However, prior to testing the reinforced foams, attention focused on establishing the influence tube length of individual CFRP tubes on their resulting energy absorbing characteristics. The influence of tube length was investigated by conducting compression tests on 10.2 mm and 12.7 mm diameter CFRP tubes with lengths of 15, 20, 25, 30 and 40 mm.

Figure 4.20 shows typical load-displacement traces following static compression tests on the 10.2 and 12.7 diameters of CFRP tubing. All traces in the 10.2 mm and 12.7 mm diameters of CFRP tubes respond in an initial linear elastic manner before failure occurs at forces of approximately 7 and 11 kN respectively. Beyond the initial failure point, constant crushing can be observed for both diameters, at average forces of 6 kN for the 10.2 mm diameter and 10 kN for the 12.7 mm tube diameter. This behaviour was associated with progressive crushing in the tube and will be discussed in further detail in the next part. It is clear that when the diameter of the structure is increased from 10.2 to 12.7 mm, the stable crushing force increased by approximately 60%.

In general, the crush length increased with increasing tube length from 15 to 40 mm. The crushing process proceeds in a stable manner up to approximately 70% of the total tube length, before the onset of densification [25]. Prior to densification of the structure, final collapse of the tube wall was indicated by an abrupt drop in force that was observed in all samples.

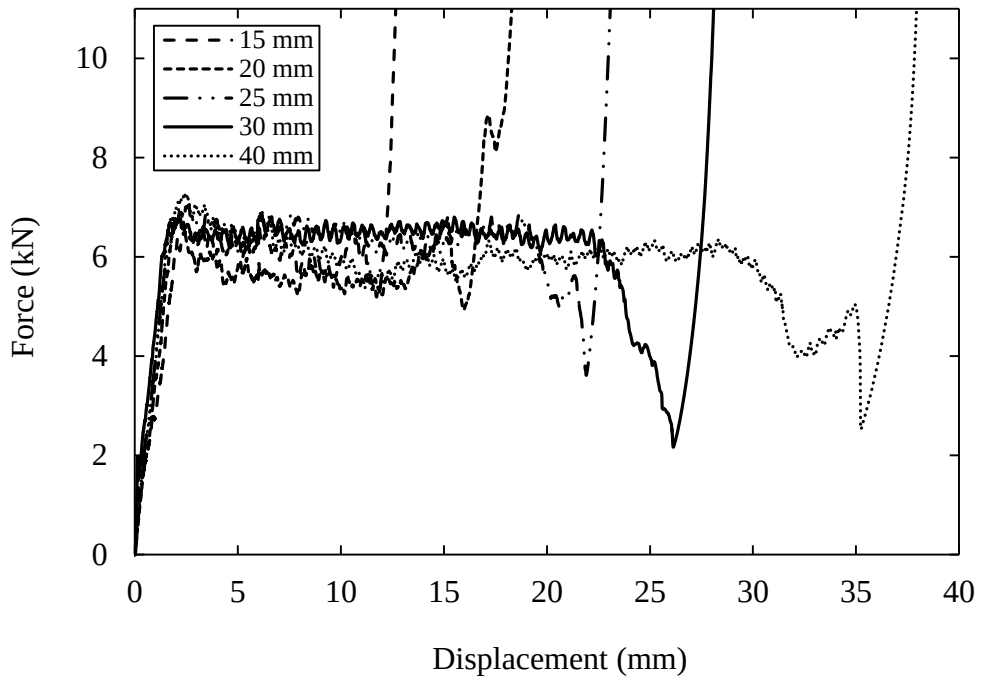

(a)

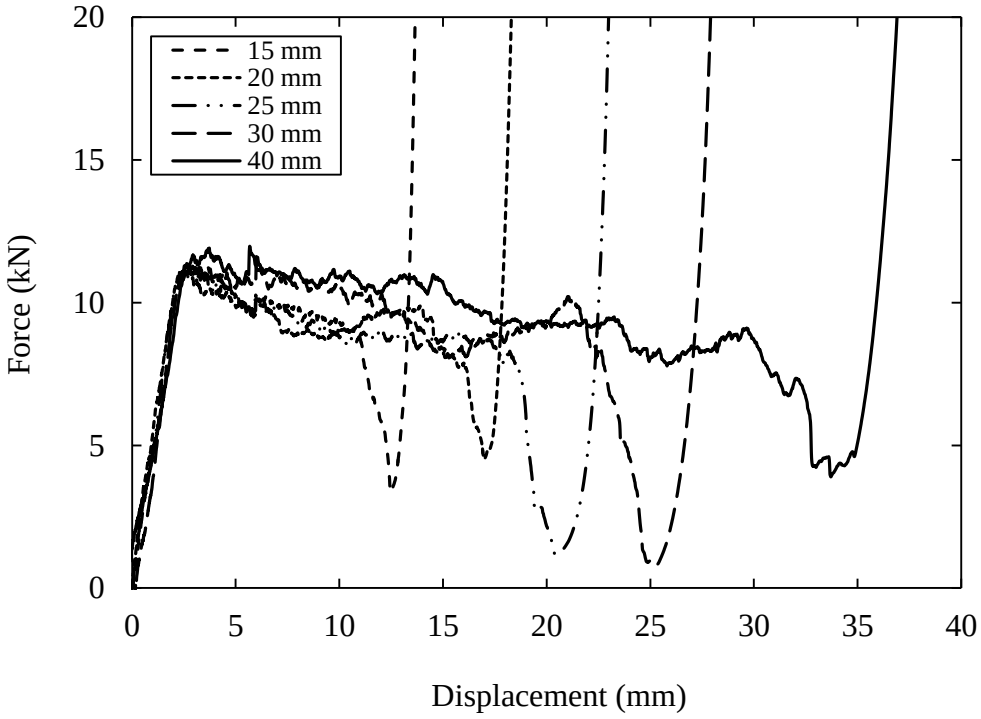

(b)

Figure 4.20 Load displacement traces following quasi-static tests on (a) 10.2 mm diameter (D/t = 6.3) and (b) 12.7 mm diameter (D/t = 7.4) CFRP tubes of different length.

Figure 4.21 shows photos of the remnants of the composite tubes following quasi-static tests on different lengths of 12.7 mm diameter tubes. All lengths of the 12.7 mm diameter tube failed in delamination along its mid-plane by forming outwards and inwards fronds. The CFRP tubes have been clearly compressed by longitudinal splitting mode, leaving long fibre strands of similar length to that of the original tube.

Closer examination of the samples in Figure 4.21 highlights the presence of residual debris. The unidirectional carbon fibres are supported by the hoop glass fibres that determined the bending radius of the unidirectional carbon fibres during crushing process. A small bending radius yields a greater bending stresses, which leads to an increase in the number of fractures in the composite layers [105]. More debris can be observed in Figure 4.21(c) compared to Figure 4.21(a) as the crushing process was longer which produced additional fractures. Clearly, the photographs highlight the importance of progressive crushing mechanism in the energy-absorbing process within the CFRP tubes.

(a) (b) (c)

Figure 4.21 Remnants of the composite tubes following quasi-static tests on 12.7 mm (D/t = 7.4) CFRP tubes of (a) 15 mm, (b) 30 mm and (c) 40 mm long.

Figure 4.22 shows the variation of the specific energy absorption of 10.2 mm and 12.7 mm diameter CFRP tubes with lengths of 10, 20, 25, 30 and 40 mm. An examination on the figure indicates that the smaller tube clearly out-performs its larger diameter counterpart by approximately 8%. Interestingly, even though the stable crushing force of the 12.7 mm diameter tube is higher by 60% compared to the 10.2 mm diameter, the SEA of the smaller tube was found to be higher than its larger diameter. The data indicate that the variation of the specific energy absorption of the tubes with tube length is roughly constant for both tube diameters. This suggests that the tube length has an insignificant effect on the CFRP tubes tested, an observation that agrees with the findings of Fairfull [94]. The evidence agrees with the observations evident in Figure 4.21, where the remnants of the composite tubes showing similar crushing mode with longer strands and more debris as the tube length is increased from 15 to 40 mm.

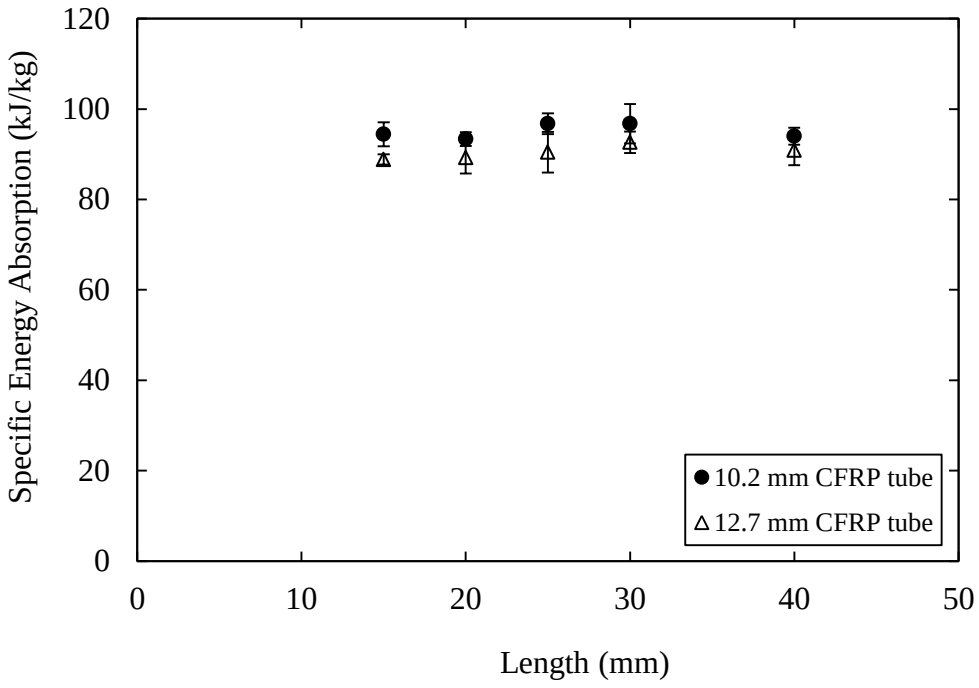

Figure 4.22 SEA of 10.2 mm and 12.7 mm diameter CFRP tubes with length of 10, 20, 25, 30 and 40 mm.

4.3.4 The Effect of the Diameter of the CFRP Tubes on SEA

This study focused on investigating the crush behaviour of the individual composite tubes and assessing the influence of the tube diameter to thickness (D/t ratio) on their energy-absorbing capability, details are given in Table 4.12. Here, six different sizes of tubing were considered, with outer diameters ranging from approximately 10.2 mm to 63.6 mm. The values of D/t ranged from 6.3 to 32.6 for the composite tubes.

Tube ID	Outer dia., D_o [mm]	Inner dia., D [mm]	Thickness, t [mm]	D/t	Mass, m [g]	Fibre weight fraction	SEA static [kJ/kg]	SEA dynamic [kJ/kg]
TCF10	10.20	7.74	1.23	6.3	0.95	0.58	93.3	88.2
TCF12	12.70	10.00	1.35	7.4	1.50	0.64	89.2	79.0
TCF29	29.40	26.28	1.56	16.9	3.90	0.61	81.4	67.1
TCF40	40.90	37.54	1.68	22.4	5.20	0.65	76.7	58.9
TCF50	50.40	47.04	1.68	28.0	6.50	0.62	58.5	51.9
TCF63	63.60	59.92	1.84	32.6	9.90	0.61	48.1	42.7

Table 4.12 Summary of the geometrical and specific energy absorbing characteristics of 20 mm long CFRP tubes.

Figure 4.23(a) shows typical load-displacement traces for tubes with diameters of 10.2, 12.7 and 29.4 mm (D/t values between 6.3 and 16.9) under quasi-static loading. All three traces exhibit similar characteristics, with failure occurring in a stable manner at an approximately constant force. The largest diameter tube displays an initial, albeit broad, peak in spite of the fact that it contained a trigger mechanism.

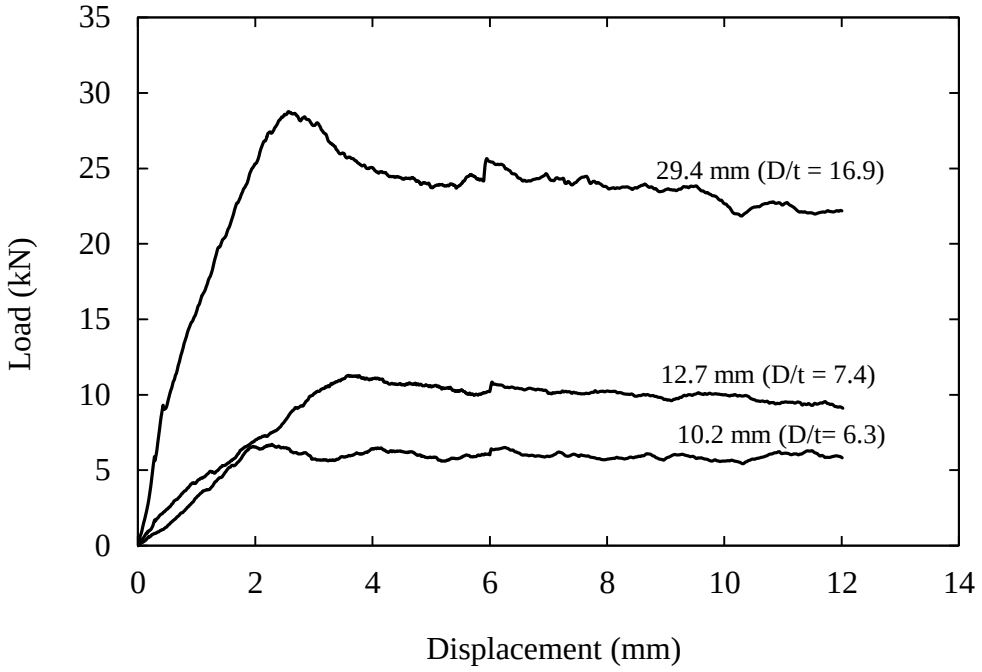

(a)

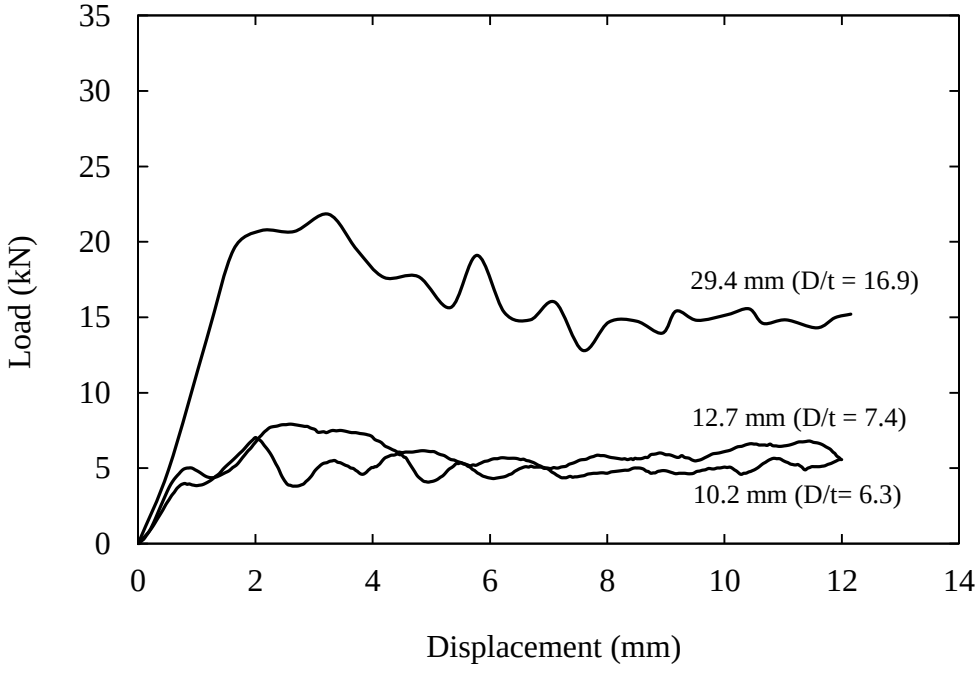

(b)

Figure 4.23 Typical load-displacement traces following crush tests on tubes with different values of D/t (a) quasi-static test (b) dynamic test.

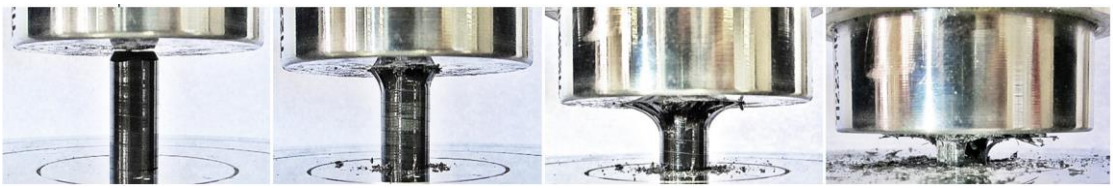

(a) 10.2 mm

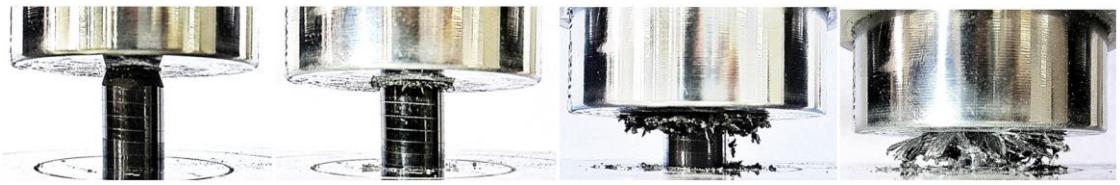

(b) 12.7 mm

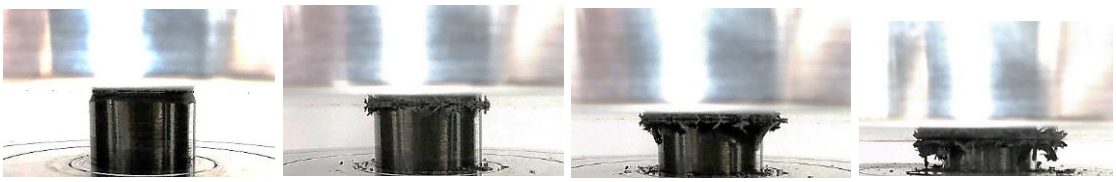

(c) 29.4 mm

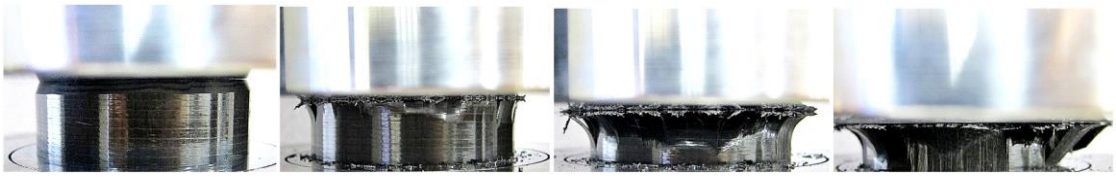

(d) 63.6 mm

Figure 4.24 The quasi-static crushing process in tubes with diameters of (a) 10.2 (D/t = 6.3) , (b) 12.7 (D/t = 7.4) and (c) 63.6 mm (D/t = 32.6).

Figure 4.24 shows photos of the crushing process in the tubes. An examination of the 10.2 mm and 12.7 mm diameter tubes highlights the presence of a distinct crush front, in which the fibres splay outwards against the moving platen. Closer inspection of the lower platen suggested that the failure process generated a significant number of small fragments, suggesting that a large number of fibres had been fractured during the crush process. In contrast, the larger diameter tube failed in a delamination mode, with the composite fracturing vertically in an interlaminar mode along its mid-thickness.

Figure 4.25(a) shows the remnants of the test samples following these quasi-static tests. An examination of the figure highlights very different failure modes in the three specimens. The smallest tube was reduced to fine particles and fragments, with there being little or no evidence of the original unidirectional structure. The 12.7 mm diameter tube failed in delamination along its mid-plane as well as in a longitudinal splitting mode, leaving long fibre strands of similar length to that of the original tube. In addition, a limited amount of residual powder was in evidence following failure.

Finally, fracture of the large 63.6 mm tube resulted in the formation of relatively large plate-shaped structures, with there being little evidence of the aforementioned residual dust on the lower platen. Closer examination of the test indicated that these platelets formed as a result of the downward propagation of large planes of delamination during compression. During failure, the innermost layers of composite collapsed inwards, whilst the outer layers fractured and fell onto the steel platen. A comparison of the three images in Figure 4.25 clearly gives qualitative evidence for the higher specific energy absorption of the smaller diameter tubes.

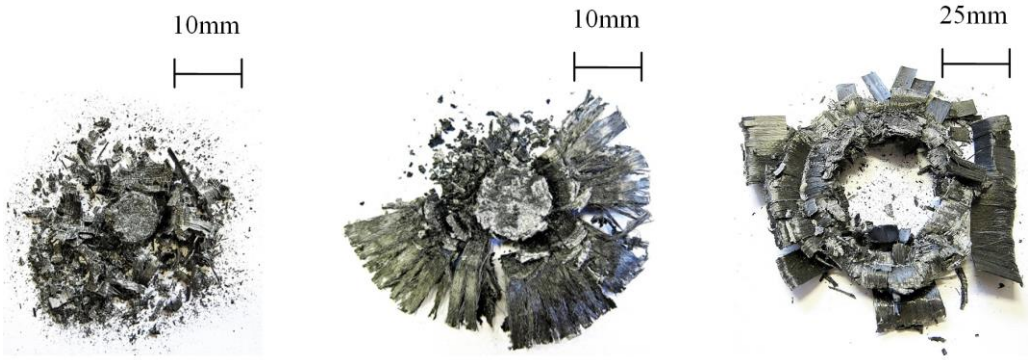

10.2 mm (D/t = 6.3) 12.7 mm (D/t = 7.4) 63.6 mm (D/t = 32.6)

(i) (ii) (iii)

(a)

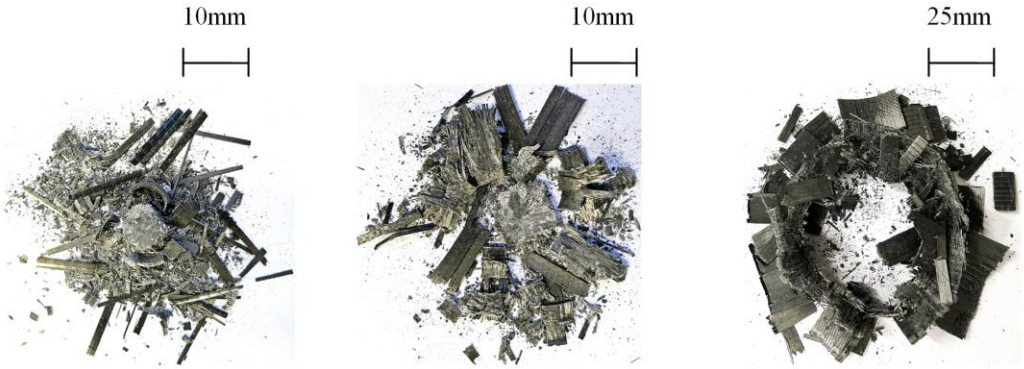

10.2 mm (D/t = 6.3) 12.7 mm (D/t = 7.4) 63.6 mm (D/t = 32.6)

(i) (ii) (iii)

(b)

Figure 4.25 Remnants of the composite tubes following (a) testing at 1mm/minute (b) testing at 5 m/s.

Figure 4.26 shows the variation of SEA with D/t for the six tube diameter tested here. From the figure, it is clear that the SEA of the composite tubes increases with decreasing D/t, an observation that agrees with the findings of Farley [90]. For example, the value of SEA passes from approximately 50 kJ/kg for a D/t ratio of 32.6 to 93.3 kJ/kg when D/t equals 6.3. A comparison of Figures 4.25 and 4.26 indicates that those tubes that fragment into very small particles absorb significantly more energy than those that fail in a macroscopic manner. Farley conducted static crushing tests on CFRP tubes with values of D/t between 3.8 and 120 and observed increasing values of SEA with decreasing D/t [90].

This increase in energy absorption was related to a reduction in interlaminar cracking in the crushed region of the tube and a non-linear increase in the force required to buckle a ply. In early work on energy-absorption in metal tubes, Alexander [56] observed that failure occurred as a result of local wrinkling or buckling of the tube walls. It was shown that the mean crushing force P_m, associated with this type of failure is related to D, t and the materials flow stress, σ_o, through:

$$P_m = 2(\pi t)^{3/2} \left(\frac{D}{2}\right)^{1/2} \sigma_0 / 3^{1/4} \tag{4.11}$$

Assuming that this force acts over the length of crush, it can be shown that the SEA of such a tube is proportional to $(t/D)^{1/2}$. Clearly, composite tubes do not fail in the same way as do their metal counterparts. However, it is likely that failure in both types of material involves local buckling (either of the metal walls or the composite plies) and therefore this equation highlights a geometrical dependency that may be more broadly applicable.

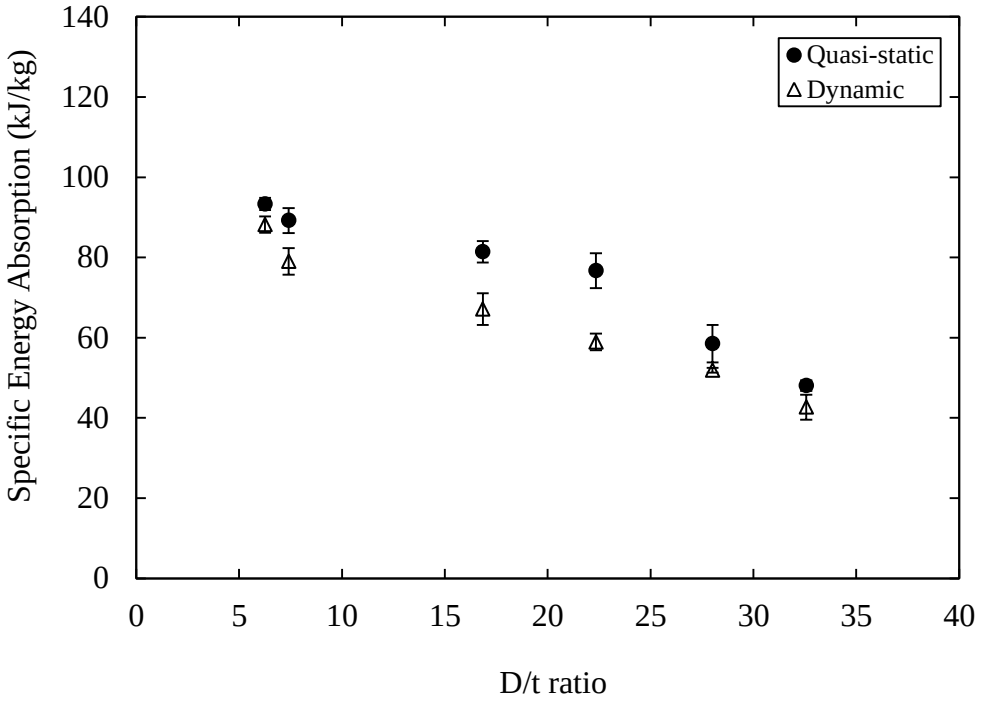

Figure 4.26 The variation of the specific energy absorption of the composite tubes at quasi-static and dynamic rates with diameter to thickness ratio.

Figure 4.23(b) shows typical load-displacement traces following dynamic tests on the composite tubes. A comparison of the load-displacement traces in Figures 4.23(a) and (b) indicates that the average crush loads are lower at dynamic rates of loading, which in turn is indicative of a lower energy absorption. The resulting values of SEA are compared with the quasi-static data in Figure 4.26. Here, it is indeed clear that the dynamic values of energy absorption are lower than the quasi-static data suggesting a pronounced rate-sensitivity. The figure indicates that differences between the quasi-static and dynamic values are greatest at intermediate values of D/t, possibly as a result of a change in failure mechanism with increasing rate.

The trends in Figure 4.26 agree with the findings reported by Schmueser and Wickliffe [95], who observed sizeable reductions in SEA at dynamic rates of loading. Figure 4.25(b) shows the composite tubes after impact testing. A comparison of the two sets of specimens does not highlight any significant differences between the samples, although the qualitative evidence does suggest that there are larger fragments in the dynamically-loaded samples. Given that delamination-type failure has been observed in the intermediate and larger diameter tubes, the reduction in SEA may be associated with a drop in the Mode I interlaminar fracture toughness of the composite at higher rates.

4.3.5 The Effect of the Foam Density on SEA for Systems with Embedded Tubes

The next stage of this research study investigated the behaviour of the composite tubes when embedded in a foam core. Single 20 mm long tubes, with a diameter of 10.2 mm, were inserted in 20 mm thick foams with densities ranging from 15.6 kg/m^3 to 224 kg/m^3. The energy absorbed by the embedded tubes was estimated by subtracting the energy value from the foam as previously discussed in Section 4.2.4. Table 4.13 summarises the results in terms of quasi-static and dynamic specific energy absorption.

Tube Embedded foam ID	Foam Modulus [MPa]	Foam Density [kg/m^3]	Quasi-static SEA of tube [kJ/kg]	Dynamic SEA of tube [kJ/kg]
TCF10	0 (no foam)	0 (no foam)	93.3	88.2
T1CFP1	6	15.6	93.2	90.6
T1CFP3	69	56.0	106.0	100.3
T1CFP4	97	90.4	107.3	99.6
T1CFP5	160	128.0	120.5	105.4
T1CFP6	280	224.0	155.8	133.0

Table 4.13 Summary of the specific energy absorption of the 10.2 mm (D/t = 6.3) diameter tubes with the energy absorbed by the foam removed.

Figure 4.27(a) shows typical load-displacement traces following quasi-static tests on the tube-reinforced P3 foam (density of 56 kg/m^3). Also included in the figure are the corresponding traces for the plain tube and the equivalent unreinforced foam. An examination of the figure indicates that the stabilised crushing load for the tube-foam system is approximately 9.2 kN, suggesting that the reinforced foam structure offers a response that is slightly higher than the sum its individual components (6.25 kN for

the tube and 1.8 kN for the foam). This difference became more pronounced as the foam density increased. For example, the 224 kg/m^3 system exhibited an average force that was approximately 10 kN higher than the sum of its individual components, as shown in Figure 4.27(b).

Figure 4.28 shows the corresponding hybrid structures following testing. A closer inspection on the P3 foam in Figure 4.28(a)ii shows a slight lateral fracture around the perimeter of the tube, whereas this was not observed in the denser P6 foam. Here, the composite has been crushed without spreading laterally beyond its initial diameter. A comparison of Figures 4.28(a)ii and 4.24(a) suggests that the foam serves to constrain the splaying process, possibly resulting in greater levels of crushing within the embedded tube. Indeed, subsequent removal of the tube from the core indicated that the composite had been reduced to an even finer particle size as the foam density increased.

Given that the composite is likely to be principal energy-absorbing material in these bi-material systems (particularly at low foam densities) the SEA of the embedded tubes was estimated by removing the energy absorbed by the foam from the combined tube/foam trace. Here, it was assumed that the foam absorbed an amount of energy equivalent to that of a block containing the same volume of material.

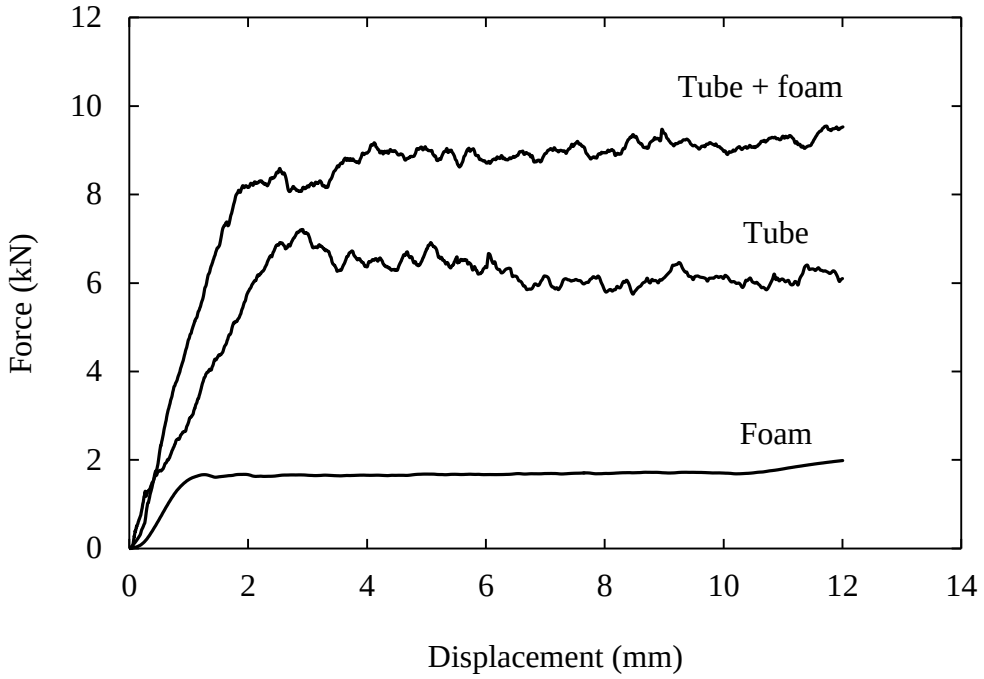

(a)

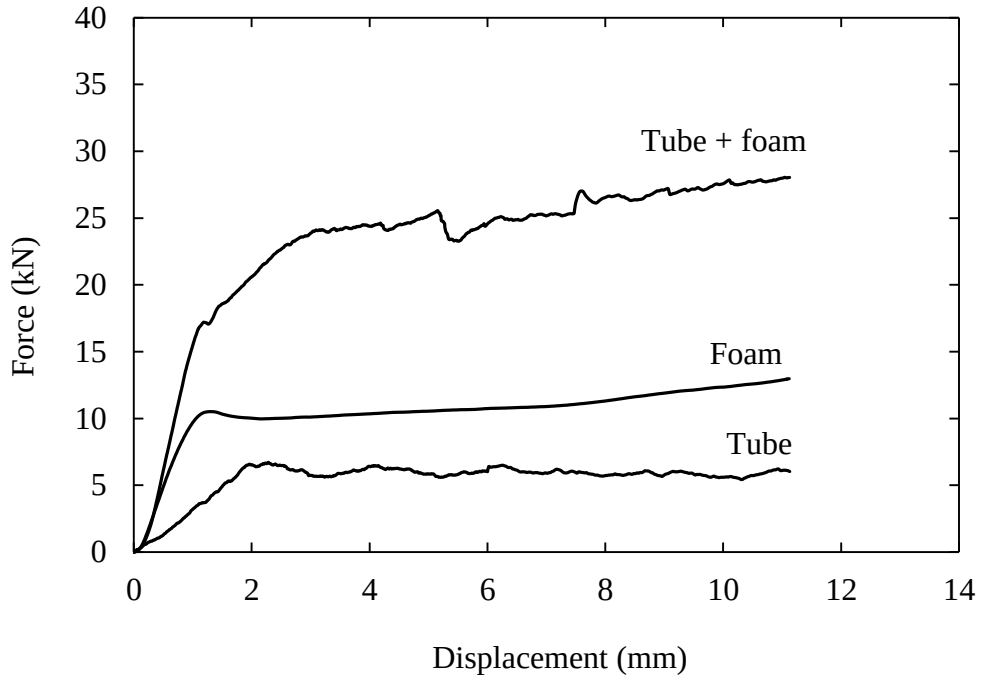

(b)

Figure 4.27 Load-displacement traces following quasi-static tests on the tube-reinforced structures (tube diameter = 10.2 mm) on the (a) P3 structures (foam density = 56 kg/m^3) and (b) P6 structures (foam density = 224 kg/m^3).

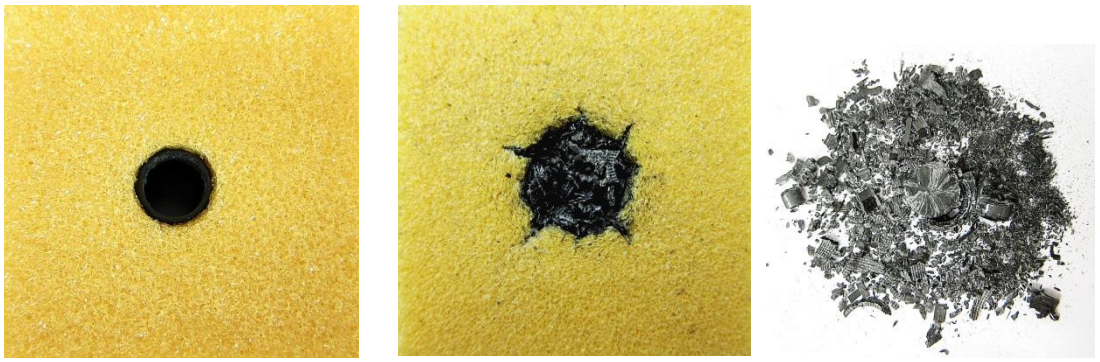

(i) (ii) (iii)

(a)

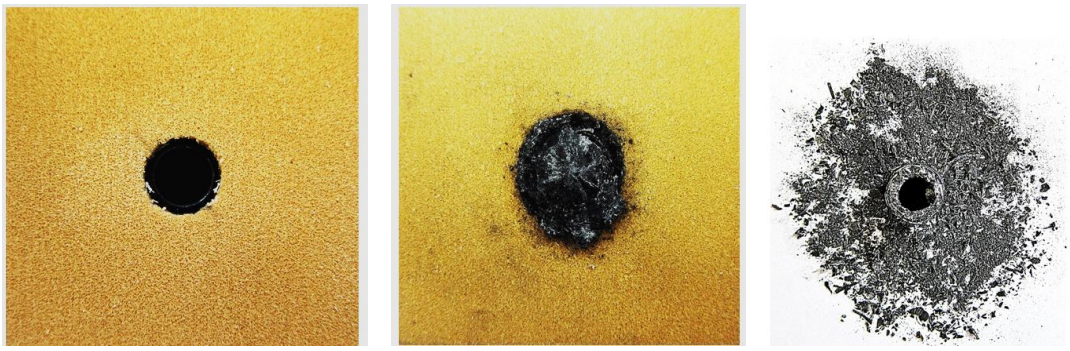

(i) (ii) (iii)

(b)

Figure 4.28 (i) An untested foam-tube sample (ii) the sample following testing (iii) the remnants of the 10.2 mm (D/t = 6.3) tube following testing on 10.2 mm tube-foam combination of (a) P3 foam (foam density = 56.0 kg/m^3) and (b) P4 foam (foam density = 224 kg/m^3).

Figure 4.29 shows the variation of the resulting estimates for the SEA of the individual tubes as a function of foam modulus. Included in the figure is the value associated with crushing the plain, unsupported tube (i.e. corresponding to the case where the foam modulus equals zero). From the figure, it is clear that increasing the density of the foam results in a greater absorption of energy within the individual tubes. The data suggest a linear relationship between SEA and modulus, with the energy absorption value associated with the tube reaching approximately 155 kJ/kg in the highest density foam.

Figure 4.30 shows the load-displacement traces following impact tests on the 56 kg/m^3 system. Here, the force for the tube + foam rises steadily to a maximum of 10 kN before oscillating around a value of approximately 9 kN. Such oscillatory behaviour is likely to be due to dynamic effects in the load cell and drop-weight carriage, as well as instabilities in the fracture process (possibly in the previously-reported delamination mode of failure). The load-displacement trace for the plain foam is slightly higher than its quasi-static counterpart, due to rate effects in the polymer. The average SEA of the tube in this tube-foam combination was found to be approximately 100 kJ/kg, this being slightly lower (6%) to its quasi-static value reported in Table 4.13.

Figure 4.29 includes the SEA values resulting from the dynamic tests on the tube-foam hybrids. As before, the contribution of the foam has been removed in order to establish the SEA of the individual tubes. Once again the contribution of the tube increases with foam modulus, although the effect of foam density is less than that observed following the quasi-static tests. It is interesting to note that the difference between the quasi-static and dynamic values increases with foam density.

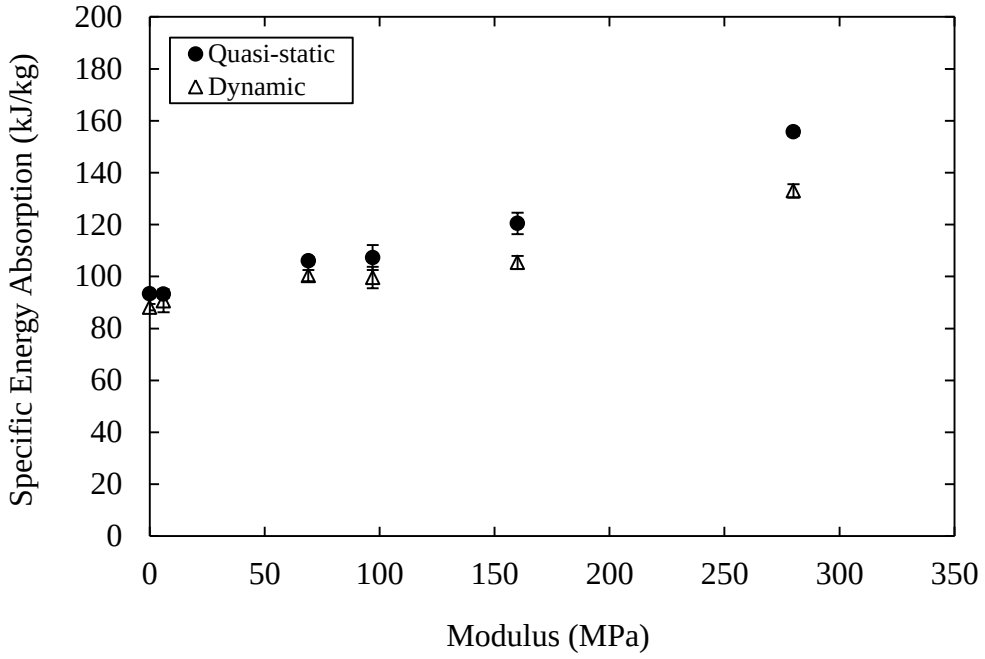

Figure 4.29 The variation of the specific energy absorption of the 10.2 mm diameter tubes with foam density.

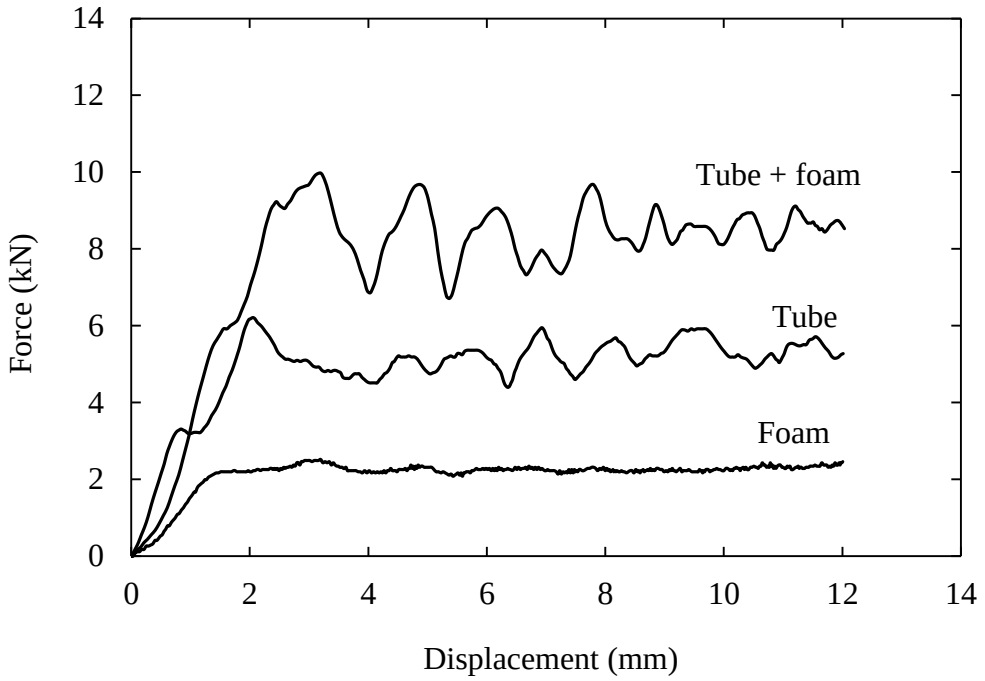

Figure 4.30 Load-displacement traces following tests on the tube-reinforced structures (tube diameter = 10.2 mm) following dynamic-tests on the 56 kg/m^3 structures.

4.3.6 Tests on the CFRP Multi-tube Foams

The next stage of this investigation focused on studying the effect of increasing the planar density of the tubes on the energy-absorbing response of these structures. Here, between two and five 10.2 mm diameter tubes were embedded in 50 mm square blocks of 20 mm thick foam. Table 4.14 lists the measured total density and calculated SEA results of the crushing tests. The resulting SEA values were calculated based on the total mass of the test samples (i.e. no attempt was made to remove the contribution of the foam).

No of tubes in foam	Density [kg/m^3]			SEA [kJ/kg]		
	P1	P4	P6	P1	P4	P6
1	34.0	106.5	235.7	54.0	27.6	21.9
2	52.5	122.5	247.5	66.8	41.4	33.1
3	71.0	138.6	259.2	76.1	51.5	42.3
4	89.5	154.7	270.9	78.9	58.7	49.5
5	107.8	170.7	282.7	86.1	66.4	60.1

Table 4.14 Summary of the total density for the CFRP tubes plus foam and the specific energy absorption of the samples.

Figure 4.31 shows the variation of SEA with core density (the density of the core was based on the foam and composite combined). Included in the figure are the values associated with the tests on the single tubes, presented previously in Figure 4.29. As expected, increasing the number of tubes in the foams serves to increase the overall SEA of the structure. For example, the SEA of the P1 (density = 15.6 kg/m^3) system increases from 54 to 86 kJ/kg as the number of tubes in the 50 mm square blocks is increased from one to five.

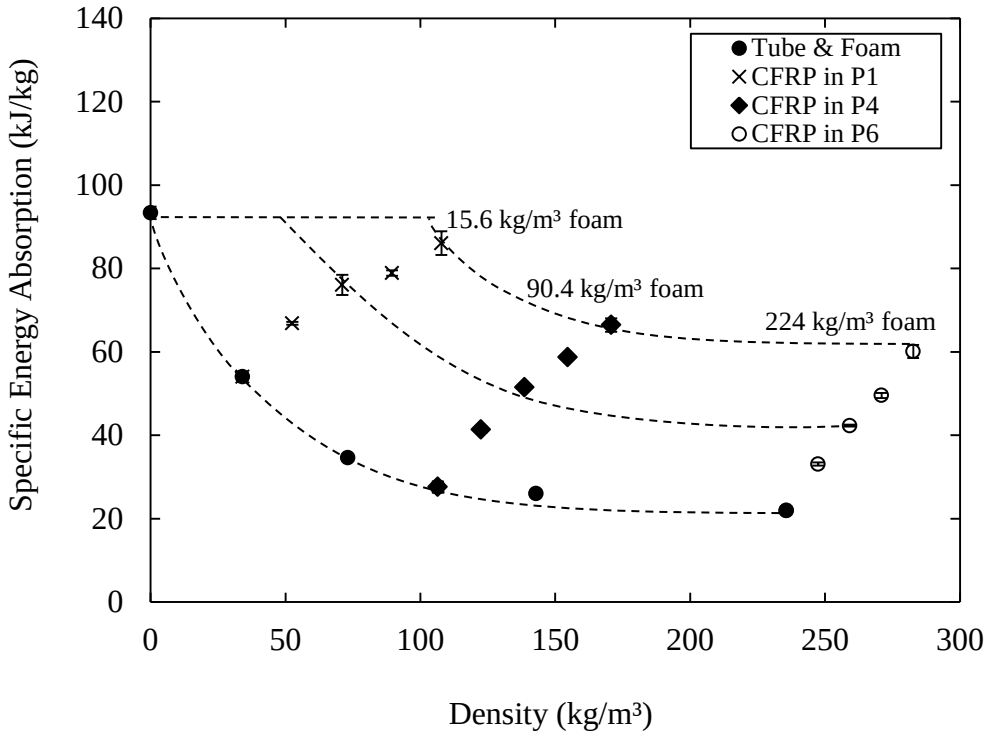

Figure 4.31 Specific energy absorption values for the tube-reinforced foams as a function of core density (including the contribution of the tubes).

Similar trends are apparent in the 224 kg/m^3 foams where increasing the tube density leads to significant increases in SEA. It is interesting to note that the SEA of the five tube-P1 foam structure is similar to that of the plain tube, suggesting that the contribution of the foam is negligible. It is believed that lower foam densities would be required to achieve a similar condition in the two, three and four tube systems. For example, consider the data points associated with the three tube systems. If the trendline that passes through these points is extended to lower densities (see figure), it appears that a (core + foam) density of approximately 50 kg/m^3 would yield a value of energy absorption similar to that of an individual tube. As mentioned previously, the highest SEA recorded during these tests is approximately 86 kJ/kg,

recorded on the five tube/P1 foam structure and this value will be compared with data from tests on other core materials in the final part of this chapter.

Figure 4.32 shows the crushed multi-tube foam structures consisting of two and four number of tubes. It is interesting to note that the interaction between the neighbouring tubes during the crushing process was minimised by placing the chamfered ends alternately facing up and down. A closer inspection of the composite tubes following removal from the foam multi-tube foams structures shows that the crushing response are similar to that of tubes as previously discussed in Section 4.3.5. This suggests that the neighbouring tubes do not affect the response of the tubes in the foams reinforced with a multitude of composite tubes.

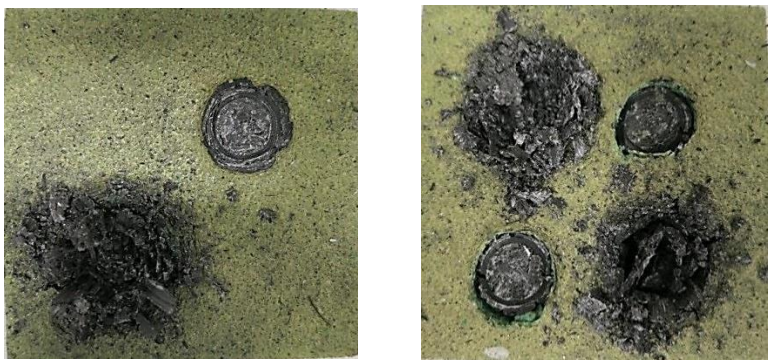

Figure 4.32 Composite tubes embedded in the P4 foam following compression tests.

4.4 Blast Tests on the Tube-reinforced Foam Structures

Preliminary blast tests were conducted on a limited number of sandwich panels based on 105 x 105 mm of 20 mm thick plain P3 foam (density = 56 kg/m^3) and P3 foam reinforced with nine tubes of the CFRP, aluminium and steel. The explosive (PE4) mass used and blast results are presented in Table 4.15. The number of blast tests conducted was limited due to inadequate amount of the explosive material. The explosive mass of PE4 consists of the mass of explosive directly applied to the explosive disc plus the mass of explosive applied to the detonator.

Sample	Sandwich Panel ID	Explosive mass, PE4 [g]	Impulse [Ns]	Approximate Crush Level [%]
P3 foam only	P3P1	10+1	20.7	85
	P3P2	15+1	26.6	85
	P3P3	20+1	31.4	85
P3 foam + CFRP tubes	P3CF1	10+1	21.4	30
	P3CF2	15+1	34.4	55
	P3CF3	20+1	37.9	60
	P3CF4	25+1	41.3	68
	P3CF5	30+1	46.4	70
P3 foam + Aluminium tubes	P3AL1	10+1	23.1	4
	P3AL2	30+1	46.7	25
	P3AL3	40+1	61.9	50
	P3AL4	50+1	71.2	52
P3 foam + Steel tubes	P3ST1	10+1	21.5	1
	P3ST2	30+1	52.9	5
	P3ST3	40+1	78.4	12

Table 4.15 Summary of the blast conditions on the sandwich panels.

The level of crush in the foam, CFRP, aluminium and steel structures was plotted against the blast impulse as shown in Figure 4.33. The approximate crush level was determined from the average deformation of the tubes and foam sample [142]. Clearly, the crush level shows a linear relationship up to the densification where the points reach a plateau for all materials except for steel. Up to the highest impulse tested (78.4 Ns), the maximum deformation of steel tubes is approximately 12%.

Figure 4.34 shows the top surface and cross-section view of the CFRP and aluminium tubes-reinforced foam sample subjected to blast impulse of 41.3 and 71.2 Ns respectively. It is worth reiterating that five of the CFRP tubes were facing upwards and four downwards, as shown in Figure 4.34(a). An inspection of the panel clearly illustrates that the five upwards facing tubes CFRP tubes have undergone crushing of approximately 68% during the failure process. Observation of the sample shows that the CFRP tubes failed by localised crushing of the chamfered ends and lateral splaying. This evidence indicates that the tubes have failed in a similar manner to that observed following quasi-static tests. An examination of the cross-section indicates that the downward facing tubes have also failed in crushing. Increasing the impulse to 46.4 Ns for the CFRP sample resulted in approximately similar crushing level as before but with more extensive damage of the foam.

The aluminium tubes which failed by buckling mode were observed to deformed approximately 52%, Figure 4.34(b). The cross-section images show that the most of the deformation occurred at the tubes closer to the outer edges. This could be due to the force concentration at the edges inside of the blast tube. Similar failure modes were also observed in the remaining panels subjected to different levels of applied impulse. Hence, this evidence suggests that composite and metal tube-reinforced foams do offer potential for use in blast-resistant designs.

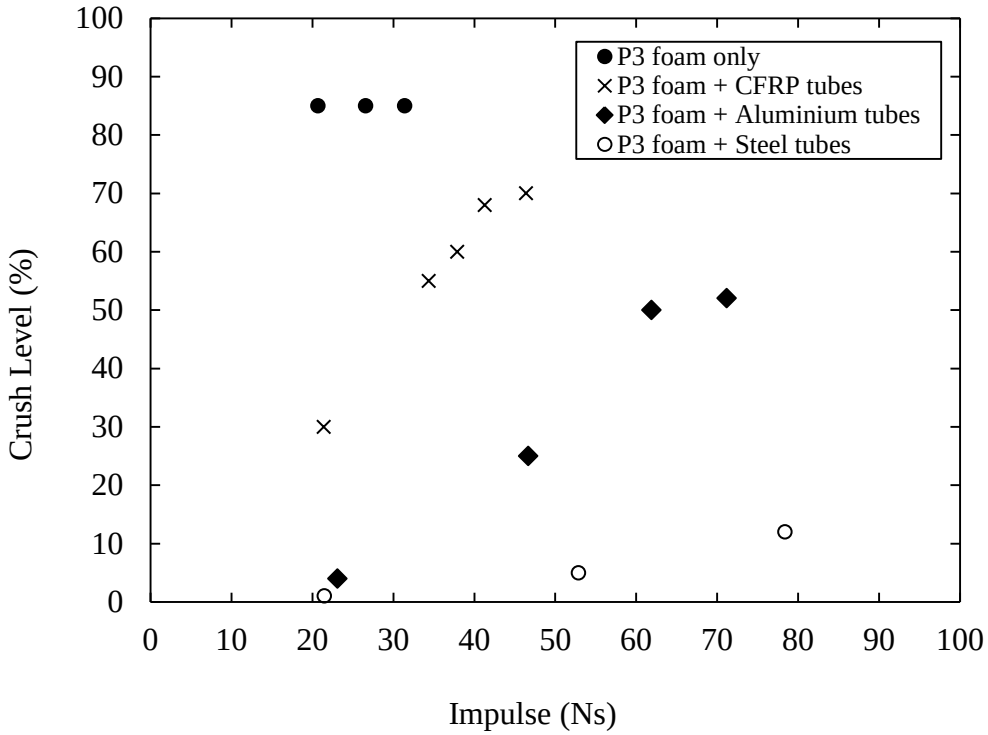

Figure 4.33 The variation of the crush level with the applied blast impulse.

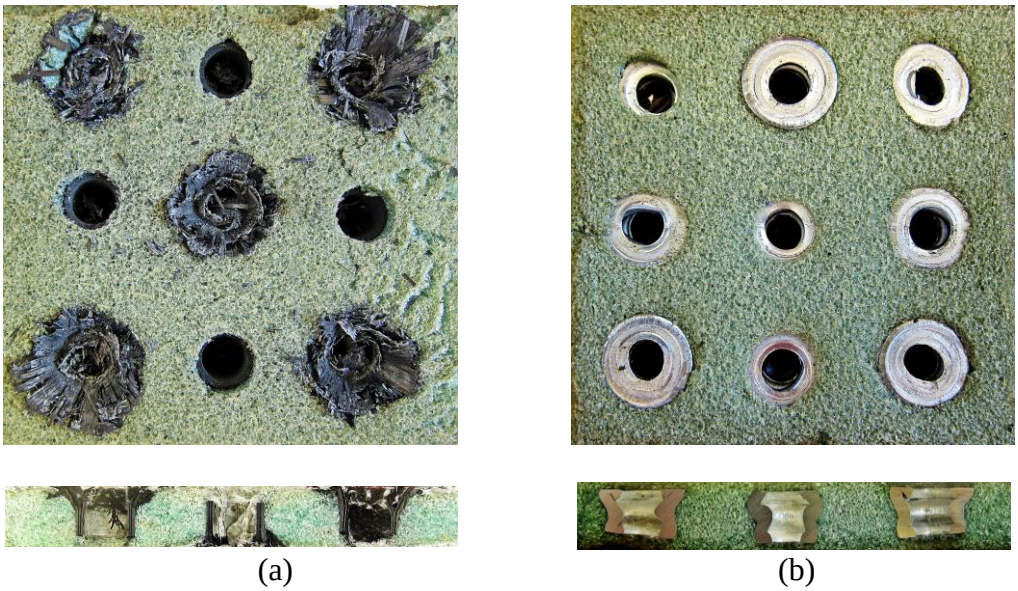

(a) (b)

Figure 4.34 The top and cross-sectional views of blast-loaded specimens of (a) CFRP-foam (Impulse = 41.3 Ns) and (b) aluminium-foam (Impulse = 71.2 Ns) structures.

4.5 Comparison with other Energy-absorbing Cores

Quasi-static compression tests were carried out on commonly used energy absorber structures to benchmark the energy absorbing performance of the systems tested here. The relative performance of the tube-reinforced foams investigated during the course of this study was assessed by undertaking additional tests on a 20 mm thick aluminium honeycomb structure (wall to wall distance of the honeycomb core was 7 mm) with a density of 40 kg/m^3, a 20 mm thick aluminium foam with a nominal density of 313 kg/m^3, a polypropylene (PP) honeycomb (wall to wall distance 8 mm) with a density of 40 kg/m^3 and 80 kg/m^3. These tests were undertaken at a crosshead displacement rate of 1 mm/minute and continued until the measured strain exceeded the densification threshold.

A typical load-displacement curve for an aluminium honeycomb tested at a quasi-static loading rate is shown in Figure 4.35. In this figure, the general response of the load–displacement is in agreement with those described by previous researchers [21], [39], [143], [144]. Initially, the load increases rapidly in the elastic region, which reflects the stiffness of the aluminium material, as the displacement increases. The load reaches a peak at approximately 3.2 kN and drops abruptly to a value of about 2 kN. This is followed by oscillatory crushing at a nearly constant value as the displacement increases. The peak load is termed the bare compressive strength and the plateau stress is known as the crush strength of aluminium honeycomb [143]**.** The plateau region suggests that the aluminium honeycomb is absorbing energy by propagation of localised folding of cell walls as the displacement increases [21]. As the crushing proceeds, the honeycomb acts as a solid material and the load increases sharply due to densification of the structure. The specific energy absorption determined up to densification for aluminium honeycomb is 16.4 kJ/kg.

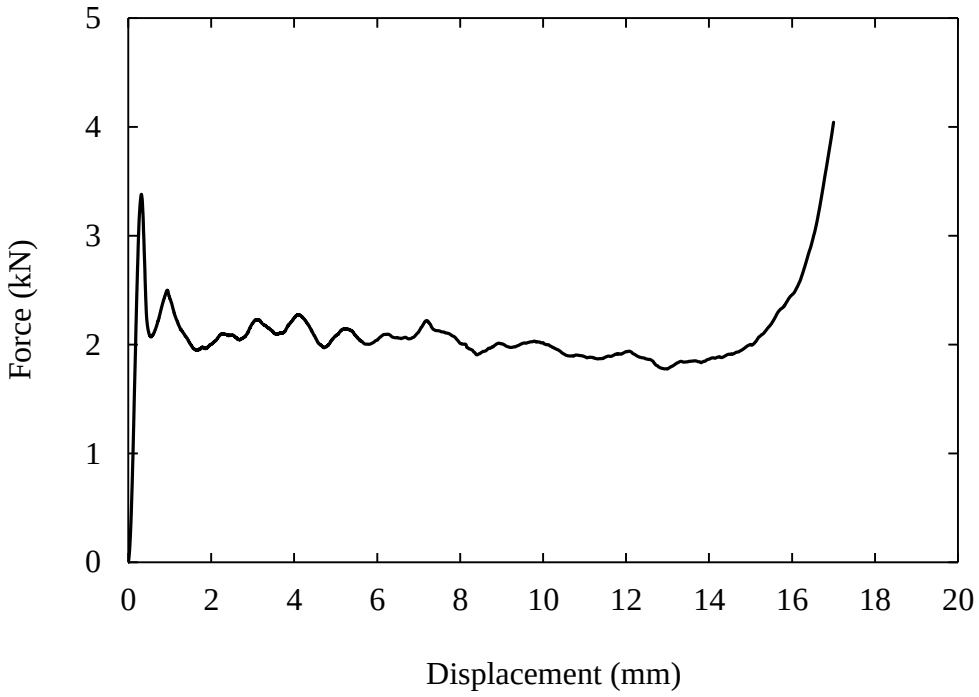

Figure 4.35 A load-displacement curve for the aluminium honeycomb following quasi-static testing.

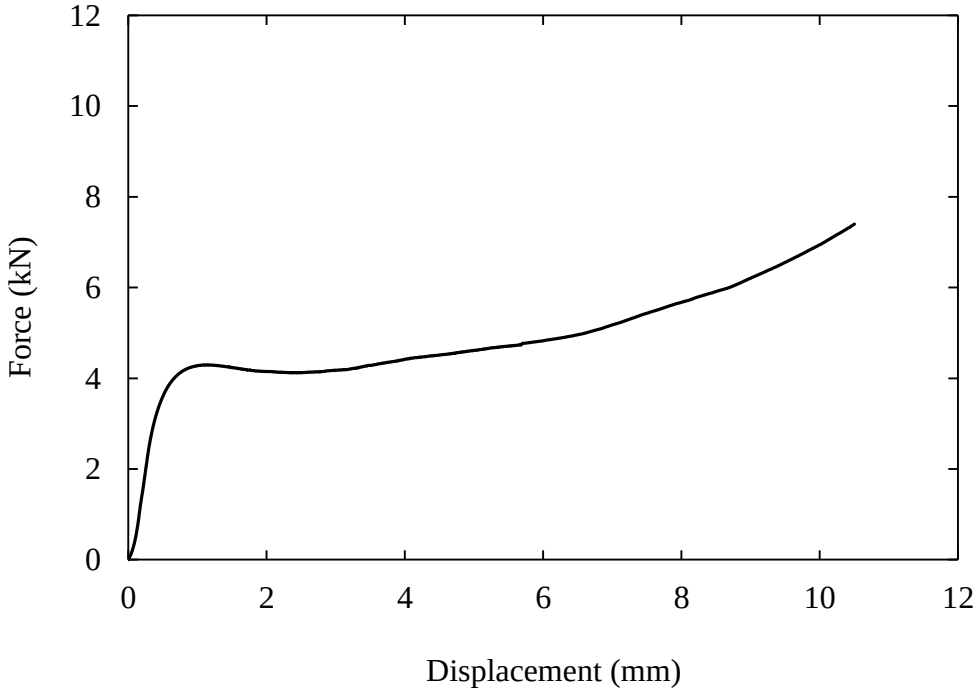

Figure 4.36 A load-displacement curve for an aluminium foam with a density of 313 kg/m^3 following quasi-static testing.

The typical load-displacement curve for an aluminium foam with a density of 313 kg/m^3 under quasi-static loading is presented in Figure 4.36. The load-displacement curve consists of three distinct regions. Firstly, the load increased in the elastic region until the aluminium foam reached a peak force at approximately 4.2 kN. Then, the material continued to crush in the plateau region by collapsing of cell walls up to densification point. Beyond this point, densification was completed and force increased continuously with increasing displacement. The specific energy absorption computed from load-displacement curve of this structure is 4.98 kg/m^3.

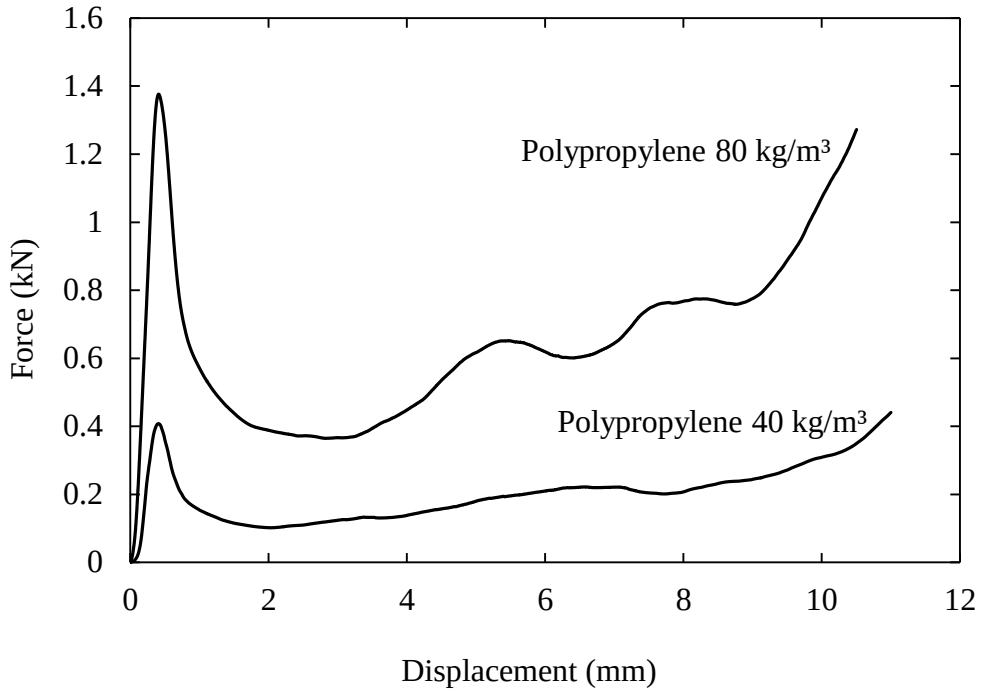

Figure 4.37 Quasi-static load-displacement traces for polypropylene honeycombs with densities of 40kg/m^3 and 80 kg/m^3.

The load-displacement responses of the 40 and 80 kg/m^3 polypropylene honeycombs at a quasi-static loading rate are shown in Figure 4.37. For both 40 and 80kg/m^3 PP honeycombs, the structure exhibits an initial linear response before reaching a peak load of approximately 0.4 and 1.4 kN respectively.

After this point, a large drop was observed due to cell wall collapse through bending and local buckling. Following this, the load continued to increase gradually which is related to compaction of the folded cell walls.

In Figure 4.37, it is clear that the denser structure of the polypropylene honeycomb exhibits a higher peak load and plateau load. It was found that when the density of the structure is increased from 40 to 80 kg/m^3, the peak load and the plateau stress increases by approximately 250% and 200% respectively. In terms of specific energy absorption, the 80 kg/m^3 (5.2 kJ/kg) density of PP honeycomb exhibits about 70% higher than 40kg/m^3 (3.1 kJ/kg) density structure. The experimental data obtained from the quasi-static tests on the aluminium honeycomb, aluminium foam and polypropylene honeycomb structures are summarised in Table 4.16.

The resulting values of SEA are compared with that for a 50 mm square, 20 mm thick P1 foam (density = 15.6 kg/m^3) containing five CFRP, aluminium and steel tubes. Also included in the table are published data following tests on various aluminium, polypropylene and Nomex honeycombs, a number of polymer and aluminium foams, a variety of folded (origami-type) composite cores as well as other types of core material [16], [145]–[150].

An examination of Table 4.16 shows that the value of SEA measured here on the 40 kg/m^3 aluminium honeycomb (16.4 kJ/kg) is significantly higher than those measured on the aluminium foam (4.98 kJ/kg) and on a polypropylene honeycomb (3.1 kJ/kg). It should be noted, however, that the aluminium honeycomb suffered the disadvantage in that it exhibited a large initial force peak prior to initial collapse of the cell walls.

Heimbs [16] reported SEA values for a range of honeycombs, foams and other types of lightweight core. Quoted values for honeycomb-type structures varied from approximately 9 to 45 kJ/kg. Values for polymer foams varied from approximately 1.5 kJ/kg for a polyethylene system (density = 69 kg/m^3) to 18 kJ/kg for a high density PMI foam. Additionally Heimbs quoted data from tests on a number of carbon (Figure 4.38(a)) and Kevlar-based foldcore structures, where energy absorption values between 2 and 22.5 kJ/kg were noted [16].

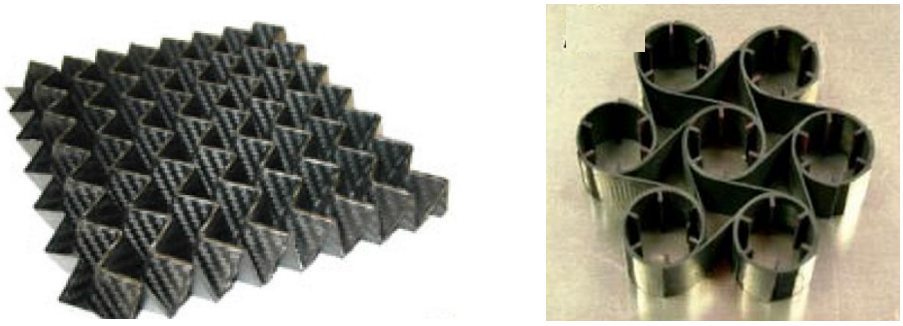

(a) (b)

Figure 4.38 Energy-absorber structures of (a) carbon foldcore [16] and (b) composite chiral unit [145].

Airoldi et al. [145] manufactured and tested chiral honeycomb structures based on a (0^o,+-45^o) carbon fibre-reinforced plastic and reported values as high as 96.5 kJ/kg, as shown in Figure 4.38(b). Observation of the chiral structures during failure identified the development of a progressive crushing mode similar to that observed here during tests on plain composite tubes. Although these values for SEA are clearly impressive, it is likely that the cost associated with producing these elegant, if somewhat complex structures, would be significant, potentially outweighing their attractive energy-absorbing characteristics.

Tarlochan and co-workers [148] developed a concept in which woven glass fibre/epoxy composite tubes were embedded within larger composite tubes and held in place using an expanded polystyrene foam. Although not a core material in the conventional sense, these systems offered attractive energy-absorbing characteristics, with values of SEA ranging from 17.7 to 32.6 kJ/kg.

In a parallel study Tarlochan and Ramesh [149] grouped up to six quadrilateral glass or carbon/epoxy composite tubes with foam centres to form what was termed a nested design. The primary mode of failure in these structures was progressive crushing, resulting in values of SEA of up to 47.1 kJ/kg for an optimised carbon fibre system. Tao and Zhao [147] manufactured a range of syntactic foams based on an aluminium matrix and obtained values as high as 50 kJ/kg. However, these relatively high values are somewhat negated by the high density of these core materials (in excess of 1600 kg/m^3).

The evidence from the tests conducted here and the review of many systems in the literature highlights the greater performance of the tube-reinforced foams investigated here, particularly of the P1 foam (15.6 kg/m^3) containing five CFRP tubes system. Here, approximately 1.3 kg of a composite tube-foam structure is required to absorb the energy of a 1000 kg car travelling at 15.5 m/s (35 mph). Clearly, selecting a low density foam (15.6 kg/m^3) and positioning the tubes in close proximity has yielded a lightweight material with a very high value of SEA. Indeed, it is likely that this impressive value of SEA could be further improved by employing an optimised fibre stacking sequence and/or by using a tougher thermoplastic matrix, such as carbon fibre-reinforced PEEK.

Material	Density [kg/m^3]	SEA [kJ/kg]	Reference
Five CFRP tubes in P1 foam	107.8	86.1	Section 4.3.6
Five aluminium tubes in P1 foam	219.1	65.3	Section 4.2.5
Five steel tubes in P1 foam	627.8	41.5	Section 4.2.5
Aluminium honeycomb	40	16.4	Section 4.5
	27 - 192	9 - 45	[16]
Polypropylene honeycomb	40	3.1	Section 4.5
	80	5.2	
Aluminium foam	313	4.98	Section 4.5
	270	5.5	[146]
Carbon foldcore	103 - 114	4.5 - 22.5	[16]
Kevlar foldcore	48 - 113	2 - 7.5	[16]
Nomex honeycomb	29 - 48	8 -18	[16]
PMI foam	52 - 160	11 - 18	[16]
PVC foam	70-250	11 - 12.5	[16]
Chiral CFRP honeycomb	n/a	96.5	[145]
Concentric GFRP tubes supported by PS foam	n/a	17.7 - 32.6	[148]
Aluminium matrix syntactic foam	1640	50.6	[147]
Carbon fibre composite sandwich panels with a with pyramidal truss cores.	20 - 35	0.75 – 8.0	[150]

Table 4.16 Comparison of the SEA values of the best-performing tube-reinforced foam with those of other types of core material.

4.6 Summary

Chapter 4 presented the experimental results and discussion for metal and composite tube-reinforced foam structures. Initially, the mechanical properties of the foam and tubes were characterised by performing compression and tensile tests. The weight fraction of the composite tubes was determined by conducting resin burn-off test. The general summary of the influence of the parameters on the metal and composite tube-reinforced foam structures is divided into metal and composite tube-reinforced foam structures.

The energy-absorbing characteristics of foams reinforced with relatively thick metal tubes have been investigated at quasi-static and dynamic rates of loading. Initial tests on the plain aluminium and steel tubes have shown that the specific energy absorption (SEA) is virtually independent of tube length (up to a value of L/D = 2) and the SEA increases as decreasing values of D/t (inner diameter to thickness).

Tubes with low values of D/t were embedded in a range of polymer foams with a view to developing lightweight energy-absorbing structures. The results show that the foam does not modify the energy-absorbing capability of the embedded tubes and the aluminium-based systems offer superior properties to the steel-based materials. Given that the metal tubes absorb much greater levels of energy than the foams in which they are embedded, the density of the latter should be set as low as possible, ensuring that the metal reinforcements are held in place during the loading process.

A tube-reinforced sandwich core structure has been developed in which chamfered CFRP tubes are embedded in low density core materials. Initial tests on plain composite tubes have shown that their specific energy absorption characteristics are

independent of tube length. As before, the SEA increases with decreasing inner diameter to thickness (D/t) ratio.

Here, significant changes in failure modes have been observed, with larger diameter tubes failing in delamination and smaller tubes failed in a combination of splaying and fragmentation modes. This principle has then been applied to develop reinforced foams based on low D/t tubes. Compression tests on these modified foams have shown that the composite tubes absorb greater levels of energy with increasing foam density, again due to increased levels of fragmentation. Varying the planar density of the tubular arrangement in a foam has shown that values of SEA as high as 86 kJ/kg can be achieved using a low density foam in conjunction with dense packing of tubes.

The observation on samples following blast tests highlighted similar failure modes to those observed in compression suggest that tube-reinforced foams represent an attractive option for use in dynamically-loaded structures. The SEA values of these structures compare very favourably with data from tests on a wide range of honeycombs, foams and foldcore structures.

CHAPTER 5

FINITE ELEMENT MODELLING

The finite element (FE) theories and techniques considered in modelling the response of individual tubes and tube-reinforced foam structures subjected to compression loading are presented. The FE modelling results are verified and compared with the experimental results previously presented in Chapter 4. A summary is presented at the end of this chapter to highlight the main findings.

5.1 Constitutive Models

Numerical models were developed to simulate the mechanical response of the individual tubes, as well as the tubes embedded in foams subjected to compression loading. Here, four materials are considered, these being the aluminium alloy, mild steel, composite tube and polymer foam. The aluminium and steel tubes exhibited similar buckling modes when loaded in compression. The composite tubes exhibit fibre and matrix fracturing modes, whereas the foams are deformed and compacted during compression. Given these different responses, different constitutive models are required to predict their respective behaviour. The material models described below were implemented in Abaqus/Explicit and the predictions of the load-displacement responses and the associated failure modes were compared to experimental results.

5.1.1 Metal Tubes

An isotropic elastic-plastic material model was employed to simulate the mechanical response of the metallic tubes [151]. The total strain-rate, $\dot{\varepsilon}$, can be decomposed into an elastic component, $\dot{\varepsilon}^{el}$, and a plastic component, $\dot{\varepsilon}^{pl}$, such that:

$$\dot{\varepsilon} = \dot{\varepsilon}^{el} + \dot{\varepsilon}^{pl} \tag{5.1}$$

The rate-dependent material is assumed to obey a uniaxial plastic flow rule and the relationship of the equivalent plastic strain-rate, $\dot{\bar{\varepsilon}}^{pl}$, is given as:

$$\dot{\bar{\varepsilon}}^{pl} = h(\bar{\sigma}, \bar{\varepsilon}^{pl}) \tag{5.2}$$

where h represents the strain-hardening function, $\bar{\sigma}$ is the equivalent stress and $\bar{\varepsilon}^{pl}$ is the equivalent plastic strain.

Temperature is not considered here as both testing and modelling are conducted at an ambient condition. The uniaxial plastic strain, ε^{pl}, which is based on recoverable elastic strain, can be calculated using the following equation:

$$\varepsilon^{pl} = \varepsilon_{total} - \frac{\sigma_{total}}{E} \quad \sigma_{total} > \sigma^{o} \tag{5.3}$$

where σ_{total} is any stress level exceeding the initial yielding point, ε_{total} is the total strain corresponding to σ_{total}, E is modulus of elasticity and σ^{o} is the initial yield stress. For the aluminium alloy and steel materials used in this research, the isotropic hardening data were determined using data from the uniaxial tensile tests presented in Chapter 4. The mechanical and elastic properties determined from these engineering stress-strain curves are presented in Table 5.1. Note that since there is a slight (6%) difference in the value of density measured experimentally to the density provided by the manufacturer, this may affect the simulation result. However, the sensitivity studies showed that the simulations are not sensitive to the slightly varied densities used.

The rate-dependent hardening curves in the static relation, are given by:

$$\bar{\sigma}(\bar{\varepsilon}^{pl}, \dot{\bar{\varepsilon}}^{pl}) = \sigma^{o}(\bar{\varepsilon}^{pl}) R(\dot{\bar{\varepsilon}}^{pl}) \tag{5.4}$$

where σ^{o} is the static yield stress and R is a stress ratio ($R = \bar{\sigma}/\sigma^{o}$). In the quasi-static case, R = 1 at $\dot{\bar{\varepsilon}}^{pl}$= 0 and $\bar{\sigma} = \sigma^{o}$. The ductile damage model is based on the equivalent fracture strain as a failure criterion.

The initiation of damage in a ductile metal is due to the growth and nucleation of voids, which assumes that the equivalent plastic strain at the onset of damage, $\bar{\varepsilon}_{D}^{pl}$, is a function of stress triaxiality and equivalent plastic strain-rate [151], [152]:

$$\bar{\varepsilon}_D^{pl}(\eta, \dot{\bar{\varepsilon}}^{pl}) \tag{5.5}$$

where $\dot{\bar{\varepsilon}}^{pl}$ is the equivalent plastic strain-rate, η is the material stress triaxiality $\left(\eta = -\frac{p}{\bar{\sigma}}\right)$, p is the pressure stress and $\bar{\sigma}$ is the equivalent stress.

The material is predicted to undergo ductile failure when the following is satisfied:

$$\omega_D = \int_0^{\bar{\varepsilon}_D^{pl}} \frac{d\bar{\varepsilon}^{pl}}{\bar{\varepsilon}_D^{pl}(\eta, \dot{\bar{\varepsilon}}^{pl})} = 1 \tag{5.6}$$

where ω_D is defined as a state (damage) variable which increases with plastic deformation. The damage variable will affect all stiffness components, which gives degraded stress components as $(1 - \omega_D)\bar{\sigma}$ ($\bar{\sigma}$ is the equivalent or undamaged stress tensor). The accumulation of damage is based on its incremental form, $\Delta\,\omega_D$, which can be expressed as:

$$\Delta\omega_D = \frac{\Delta\bar{\varepsilon}^{pl}}{\bar{\varepsilon}_D^{pl}(\eta, \dot{\bar{\varepsilon}}^{pl})} \geq 0 \tag{5.7}$$

The process of manufacturing metal tubes by extrusion leads to some form of "minor defect" or geometric imperfections in the finished product. This may have an effect on the deformation response of the metal tube, despite the fact that percentage of these imperfections is very small. Hence, a geometrical imperfection pattern was introduced in the "perfect" cylindrical model in order to trigger a buckling response before the critical load associated with failure of the material is reached.

The geometrical imperfection pattern, or buckling modes, were obtained from the initial *Buckle Linear Perturbation step executed within Abaqus/Standard [151]. Abaqus/Explicit [151] was then used to perform a further postbuckling analysis to account for the complex interactions introduced during progressive failure relating to the buckling collapse of the tube wall. Here, the predicted buckling modes were applied to the numerical model by introducing a geometrical imperfection through the tube wall, which is given by:

$$\Delta x_i = \sum_{i=1}^{M} \omega_i \phi_i \tag{5.8}$$

where ϕ_i represents the ith mode shape and ω_i is the related scale factor. Variations in the thicknesses of the tubes (from measurements) were used to perturb the mesh and the scale factor, which reflects the imperfection, being set to 5% of the tube thickness. An imperfection was then introduced to a tube geometry by including the *Imperfection parameter in the Keywords Editor. The appropriate time step in this analysis was set to 0.1 seconds, which was ascertained through a series of numerical studies conducted with different durations, until dynamic effects were insignificant [36].

Property	Aluminium alloy		Mild steel	
Density, ρ [kg/m^3]	2543		7966	
Young's modulus, E [GPa]	70.4		200	
Poisson's ratio, υ	0.33		0.33	
Plasticity properties	Yield stress [MPa]	Plastic strain	Yield stress [MPa]	Plastic strain
	220	0	278	0
	264	0.01	300	0.01
	273	0.02	305	0.02
	277	0.03	345	0.04
	281	0.04	385	0.06
	286	0.06	425	0.10
	288	0.07	462	0.16
	289	0.08	480	0.24

Table 5.1 Summary of the material properties of the aluminium and steel tubes.

5.1.2 Composite Tubes

Modelling the failure behaviour of composite materials is a very complex process due to factors such as the variation of fibres and matrices materials, types of ply for instance unidirectional or fabrics and orientation ply angle [114]. Thus, currently there are no universally accepted material constitutive models for crash simulations of composite materials. A comprehensive literature review on the classification of composite crushing models is explained in Chapter 2.

Layer	Material	Thickness [mm]	Orientation
1st layer	Carbon fibre/epoxy	0.27	0^o
2nd layer	Glass fibre/epoxy	0.27	90^o
3rd layer	Carbon fibre/epoxy	0.27	0^o
4th layer	Glass fibre/epoxy	0.27	90^o
5th layer	Carbon fibre/epoxy	0.27	0^o

Table 5.2 Layup sequence of the composite tube.

In this study, the composite tubes are based on five plies, consisting of three layers of T700 unidirectional pre-preg carbon fibre reinforced epoxy, oriented at 0^o and two layers of unidirectional E-glass oriented at 90^o, as indicated in Table 5.2. As such, the tubes response differently subjected to the loading direction applied. With reference to this information, it is required to model discrete layers of carbon and glass fibre pre-preg in order to simulate the overall response of the composite tube subjected to axial crushing. Table 5.3 presents the elastic properties for carbon fibre/epoxy and glass fibre/epoxy composite used in the FE analysis.

The composite tubes were modelled as orthotropic elastic with Hashin's failure criteria for the unidirectional laminates [153]. The failure model is related to brittle properties which degraded by micro-cracking. A key assumption here is that the material properties were based on carbon and glass pre-preg laminates, where the fibre and resin constituents were not considered separately.

Symbol	Carbon fibre/epoxy	Glass fibre/epoxy	Parameters
ρ [kg/m^3]	1550	1970	Density
E_1 [GPa]	147	41	Young's modulus in longitudinal direction
E_2 [GPa]	10.3	10.4	Young's modulus in transverse direction
E_3 [GPa]	10.3	10.4	Young's modulus in thickness direction
G_{12} [GPa]	7.0	4.3	In-plane shear modulus
G_{13} [GPa]	7.0	4.3	Out-of-plane shear modulus
G_{23} [GPa]	3.7	3.5	Out-of-plane shear modulus
υ_{12}	0.27	0.28	Major in-plane Poisson's ratio
υ_{13}	0.27	0.28	Out-of-plane Poisson's ratio
υ_{23}	0.54	0.50	Out-of-plane Poisson's ratio

Table 5.3 Summary of the elasticity properties of the carbon [150], [10] and glass fibre/epoxy materials [10].

The Hashin's damage model [153] consists of interaction of more than one stress components in evaluating failure modes. Hashin's damage initiation assumes that the response of the undamaged material is linearly elastic with the point stress calculations involving four failure modes. The failure modes are (i) fibre rupture in tension, (ii) fibre buckling and kinking in compression, (iii) matrix cracking under

transverse tension and shearing and (iv) matrix crushing under transverse compression and shearing. By considering $\hat{\sigma}_{11}, \hat{\sigma}_{22}$ and $\hat{\tau}_{12}$ as the longitudinal, transverse and shear effective stresses, Hashin's damage initiation criteria take the general form as follows [153]:

(a) Tensile fibre failure for ($\hat{\sigma}_{11} \geq 0$):

$$F_f^t = \left(\frac{\hat{\sigma}_{11}}{X^T}\right)^2 + \alpha\left(\frac{\hat{\tau}_{12}}{S^L}\right)^2, d_f = 1 \tag{5.9}$$

(b) Compressive fibre failure for ($\hat{\sigma}_{11} < 0$):

$$F_f^c = \left(\frac{\hat{\sigma}_{11}}{X^C}\right)^2, d_f = 1 \tag{5.10}$$

(c) Tensile matrix failure for ($\hat{\sigma}_{22} \geq 0$):

$$F_m^t = \left(\frac{\hat{\sigma}_{22}}{Y^T}\right)^2 + \left(\frac{\hat{\tau}_{12}}{S^L}\right)^2, d_m = 1 \tag{5.11}$$

(d) Compressive matrix failure for ($\hat{\sigma}_{22} < 0$):

$$F_m^c = \left(\frac{\hat{\sigma}_{22}}{2S^T}\right)^2 + \left[\left(\frac{Y^C}{2S^T}\right)^2 - 1\right]\frac{\hat{\sigma}_{22}}{Y^C} + \left(\frac{\hat{\tau}_{12}}{S^L}\right)^2, d_m = 1 \tag{5.12}$$

where, X^T and X^C denote the tensile and compressive strength components in longitudinal direction by superscripts *T* and *C*, respectively. Similarly, Y^T and Y^C denote the tensile and compressive strengths in transverse direction, S^L *and* S^T are the longitudinal and transverse shear strengths. Table 5.4 gives a summary of the damage initiation data for carbon/epoxy and glass fibre/epoxy. In Equation (5.9), α is a coefficient that determines shear stress contribution to the fibre tensile initiation criterion. In this case, $\alpha = 1$ as the shear stress contribution was taken into account.

Symbol	Carbon fibre/epoxy	Glass fibre/epoxy	Parameters
X^T [MPa]	2280	1140	Longitudinal tensile strength
X^C [MPa]	1725	620	Longitudinal compressive strength
Y^T [MPa]	57	39	Transverse tensile strength
Y^C [MPa]	228	128	Transverse compressive strength
S^T [MPa]	76	89	Transverse shear strength
S^L [MPa]	76	89	Longitudinal shear strength
G_{ft}^C [kJ/m^2]	91	50	Fibre tension
G_{fc}^C [kJ/m^2]	79	45	Fibre compression
G_{mt}^C [kJ/m^2]	91	50	Matrix tension
G_{mc}^C [kJ/m^2]	79	45	Matrix compression

Table 5.4 Summary of the damage initiation and fracture energy data of the carbon and glass fibre/epoxy materials [10], [154], [155].

Once the damage criteria are satisfied within all of the element integration points, a failed element was removed from the mesh and the element status in field output variable was set from one to zero. At this point, the stress of the element contributes no resistance to the model stiffness in the subsequent deformation. For a shell model, element deletion can occur from both tensile and compressive damage. In contrast, element deletion for solid model is only possible as a result of fibre tensile damage [151]. A linear damage evolution law was specified in terms of fracture energy per unit area in the numerical model. Table 5.4 presents the fracture energies for fibre and matrix failure mode.

5.1.3 Foams

The foams were modelled using isotropic linear elasticity and crushable foam plasticity to describe their elasto-plastic behaviour. The response of the foams was characterised by conducting compressive tests on blocks with dimensions of 50 x 50 x 20 mm^3 and the elastic properties of foam materials are presented in Table 5.5. The material input data required in the elastic region are the Young's modulus and the Poisson's ratio, where the latter was assumed to be 0.32 for all of the foams since the sensitivity studies showed that the simulations are not sensitive to Poisson's ratios in the range from 0.25 to 0.35. The yield surface for a closed-cell foam material, as described by Deshpande and Fleck [156], is given as:

$$\phi \equiv \frac{1}{\left[1+\left(\frac{\alpha}{3}\right)^2\right]}[\bar{\sigma}^2 + \alpha^2\sigma_m^2] - \sigma_y^2 \leq 0 \tag{5.13}$$

where $\bar{\sigma}$ is the equivalent stress, σ_y is the uniaxial yield strength of the foam in tension or compression and σ_m is the mean stress. The term α defines the shape of the yield surface, which is given by:

$$\alpha = \frac{3k}{\sqrt{(3k_t + k)(3 - k)}} \tag{5.14}$$

where k and k_t are related to the ratios of the initial uniaxial yield stress in compression, σ_c^o, and the hydrostatic tensile yield stress, p_t, to the hydrostatic compressive yield stress, p_c^o, respectively. The uniaxial yield strength in hydrostatic compression, p_c, describes the growth of the size of the yield surface and is defined as:

$$p_c\left(\varepsilon_{vol}^{pl}\right) \equiv \frac{\sigma_c\left(\varepsilon_{axial}^{vol}\right)\left[\sigma_c\left(\varepsilon_{axial}^{pl}\right)\left(\frac{1}{\alpha^2}+\frac{1}{9}\right)+\frac{p_t}{3}\right]}{p_t+\frac{\sigma_c\left(\varepsilon_{axial}^{pl}\right)}{3}} \tag{5.15}$$

where ε_{vol}^{pl} is the plastic volumetric strain in the volumetric hardening model, which is set to be equal to the uniaxial compressive plastic strain, ε_{axial}^{pl}, σ_c is the uniaxial compressive stress in the strain hardening stage. Hence, the term p_c can be determined by conducting compression tests on the foam. It is assumed that the response of a rate-dependent solid follows a uniaxial flow rule, as given in Equation (5.2) and rate-dependent hardening curves is as in Equation (5.4) for the foam material. Damage development in the foam material was modelled by implementing both the ductile damage and the shear damage criteria with the similar form shown in Equation (5.5) available in Abaqus [151]. Table 5.6 presents the yield stress and plastic strain of foam with various densities.

Foam ID	Foam density [kg/m^3]	Foam modulus [MPa]	Poisson ratio
P1	15.6	6	0.32
P2	38.3	37	0.32
P3	56.0	69	0.32
P4	90.4	97	0.32
P5	128.0	160	0.32
P6	224.0	280	0.32

Table 5.5 Elastic properties of foam with various densities.

P1	Yield stress [MPa]	0.0197	0.0566	0.095	0.1100	0.1500	0.1700	0.1900	0.2000
	Plastic strain	0	0.16	0.40	0.50	0.62	0.72	0.78	0.86
P2	Yield stress [MPa]	0.4981	0.5024	0.5109	0.5131	0.5152	0.5194	0.5727	0.6350
	Plastic strain	0	0.16	0.40	0.50	0.62	0.72	0.80	0.86
P3	Yield stress [MPa]	0.7116	0.7177	0.7299	0.7329	0.7360	0.7421	0.8181	0.9072
	Plastic strain	0	0.16	0.40	0.50	0.62	0.72	0.80	0.86
P4	Yield stress [MPa]	1.3291	1.3405	1.3632	1.3689	1.3746	1.3859	1.5279	1.6756
	Plastic strain	0	0.16	0.40	0.50	0.62	0.72	0.80	0.86
P5	Yield stress [MPa]	2.3422	2.3671	2.4034	2.4109	2.4202	2.4480	2.6909	2.9505
	Plastic strain	0	0.16	0.40	0.50	0.62	0.72	0.80	0.86
P6	Yield stress [MPa]	4.7904	4.8314	4.9133	5.0500	5.1607	5.4033	5.7364	6.1909
	Plastic strain	0	0.16	0.40	0.50	0.62	0.72	0.80	0.86

Table 5.6 Material properties of foam with various densities.

5.2 Geometrical Model and Contact Conditions

Due to geometrical symmetry, quarter models of each metal tube were constructed by applying suitable boundary conditions along each edge of the model in the x-axis and z-axis directions, as shown in Figure 5.1(a). This approach serves to reduce computational time and has been used by previous researchers when modelling the crushing response of square and circular cross-sections of steel tubes [74].

In the first stage of the modelling process, three tube diameters were simulated and validated against the experimental results, as shown in Tables 5.8 and 5.9. The tubes were modelled using 8-noded solid elements with reduced integration. Two 40 mm square plates with thicknesses of 1 mm, to represent the upper and lower platens, were defined as 3-D discrete rigid bodies, as shown in Figure 5.2. The axial crushing process was modelled by displacing the top plate downwards in the y-direction (Figure 5.2) with the bottom plate being held stationary. The top and bottom ends of the tube were allowed to deform freely in all directions.

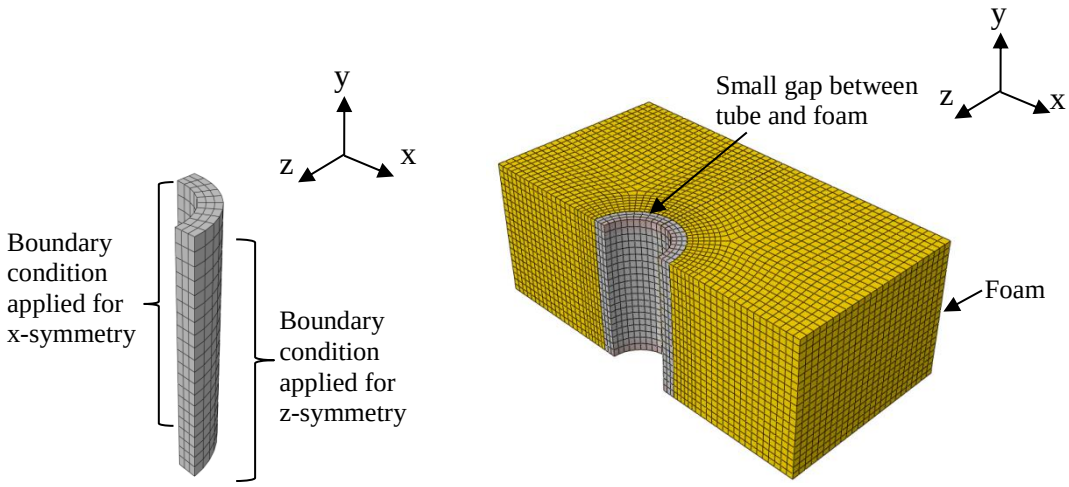

(a) (b)

Figure 5.1 (a) A quarter model of a tube and (b) the cross-sectional view (shown this way simply for clarity) of a 12.62 mm metal tube in a foam block. Note that a small gap of 0.1 mm has been introduced between the tube and the foam.

In a subsequent part of this research program, one metal tube, with a diameter 12.62 mm, was inserted into a number of foams based on different densities, details of which are given in Tables 5.10 and 5.11. The foam materials were modelled using 8-noded solid elements with reduced integration. A small gap of 0.1 mm (Figure 5.1(b)) was introduced between the tube and the foam to avoid convergence problems.

Figure 5.2 shows the contact condition for crushing of the metallic tubes. Due to the observed folding action of the tube, a frictional contact constraint was added to both the interior and exterior surfaces in order to prevent the tube wall from penetrating into itself [74]. In order to model the metal tubes embedded in the foams, a further contact condition between the tube and the foam has to be considered. A coefficient of friction of 0.1 [157] was used between the tube and the rigid platens to achieve satisfactory agreement with the experimental results.

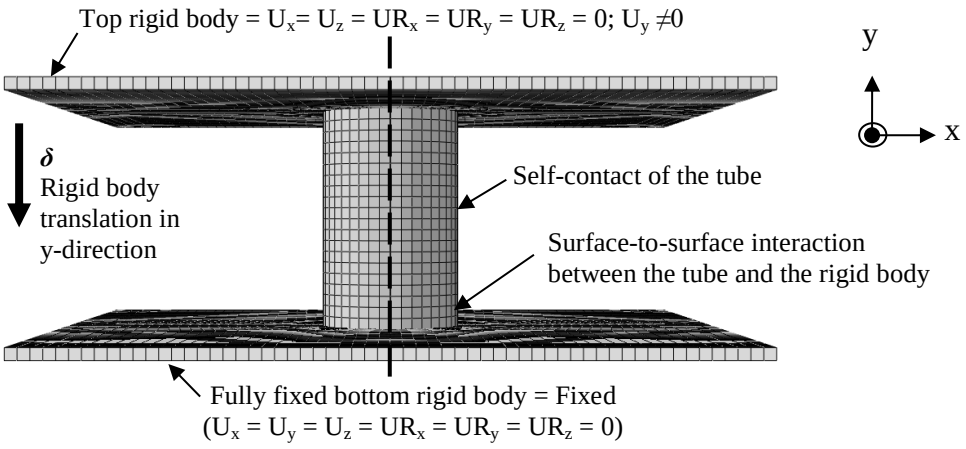

Figure 5.2 Loading and boundary conditions adopted in the finite element model.

The composite tubes were modelled by a single layer of 4-noded, reduced integration shell elements (S4R) consisting of one element through the tube thickness. Quarter

models of each composite tube were constructed by applying boundary conditions along x-axis and z-axis edges, similar to the metal tube models. Two 40 mm square upper and lower platens were defined as 3-D discrete rigid bodies and the tube model was assembled in between the platens. As before, the axial crushing process was simulated by moving the top plate downwards in the y-direction and the bottom plate being held stationary. The top and bottom ends of the composite tube were allowed to deform freely in all directions.

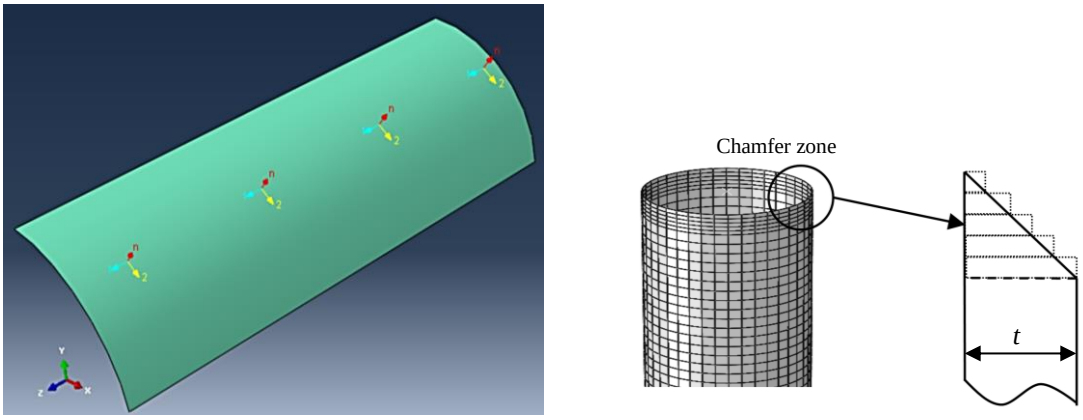

(a) (b)

Figure 5.3 (a) A local cylindrical coordinate system for the composite tubes and (b) detailed view of the chamfer zone.

Here, the material properties of the carbon and glass fibres in principal directions were defined by introducing a discrete cylindrical coordinate system for circular tubes. Figure 5.3(a) shows the definition of direction-1 and direction-2, which were oriented along the tube length and around the section of the tube respectively. Also shown in this figure is the normal direction which was defined in the thickness direction of the tube.

In order to trigger crushing process, forty five degree chamfer was modelled by reducing the thickness of the trigger zone as shown in Figure 5.3(b). The modelling technique adopted for composite tubes in Abaqus was based on composite layup for conventional shell elements. Figure 5.4 shows the composite layup for a tube with outer diameter of 10.2 mm. It was assumed that the thickness of each individual layer is 0.27 mm as the total thickness of the tube is 1.35 mm. The corresponding material section and its orientation were assigned to the shell elements. The tube consists of a total of five carbon and glass fibre pre-preg layers oriented in direction-1 (0^o) and direction-2 (90^o) respectively. In modelling the CFRP tubes, the number and orientation of layers defined in the material model are the key features as these factors have a great influence on the results.

Two different friction coefficients were implemented in order to model the contact during the crushing process. A coefficient of friction of 0.3 was used for the contact friction between the tube and rigid platens. The second contact coefficient value for self-contact of the deformed tube was set to 0.65. These values were chosen based on contact coefficients employed in previous literature [106]. In order to validate the modelling and its approaches, the simulation results of chamfered tubes were compared with the experimental data.

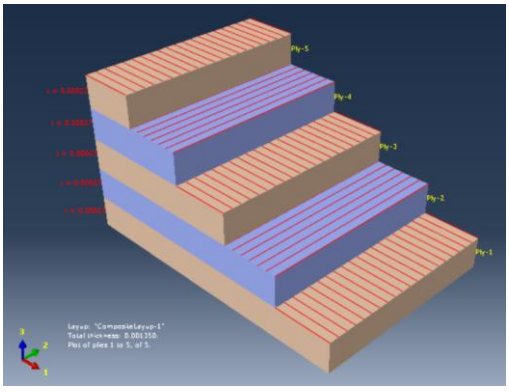

Figure 5.4 Composite layup for a CFRP tube with outer diameter of 10.2 mm.

5.3 Results and Discussion of the Metallic Tubes

5.3.1 Mesh Sensitivity Analysis

A mesh sensitivity analysis was performed using a model of an aluminium tube specimen with a diameter of 12.62 mm and a length of 20 mm. The finite element model was meshed using four different mesh sizes, these being 2 mm (coarse), 1 mm (medium), 0.8 mm (fine) and 0.5 mm (very fine). Another parameter that contributes to the overall number of elements within the model is the number of elements through the thickness of the tube. Results are shown in Table 5.7.

Here, six models were studied, with each containing 100, 150, 600, 900, 2400 and 4800 elements. Figure 5.5(a) summarises the findings of this mesh sensitivity analysis, where the relationships between the number of elements and the predicted specific energy absorption, bottoming-out displacement and CPU time are shown.

Number of Elements	Mesh size (mm)	Elements through tube thickness	CPU time (hour)	Densification point	SEA (kJ/kg)	Number of axial lobes
Experiment	-	-	-	11.03	70.07	2
100	2	2	0.18	14.58	101.28	1
150	2	3	0.22	14.24	77.59	1
600	1	3	0.75	10.97	70.89	2
900	0.8	3	1.13	10.94	69.79	2
2400	0.5	3	3.62	10.97	70.52	2
4800	0.5	6	8.42	10.98	70.13	2

Table 5.7 Details of mesh sensitivity analysis.

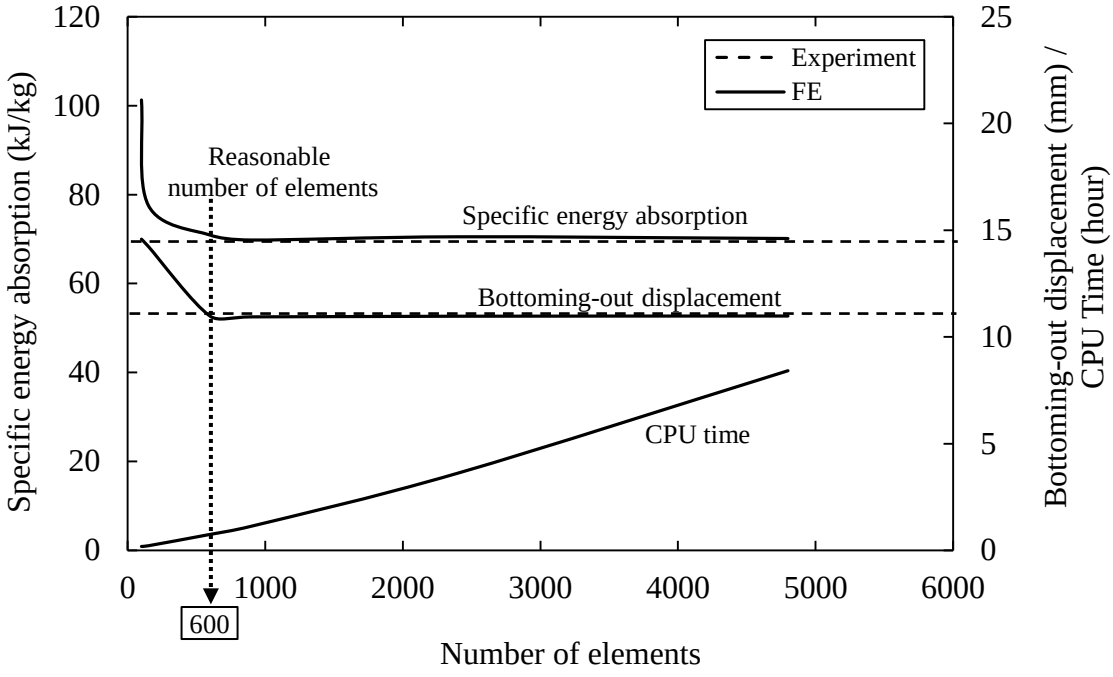

(a)

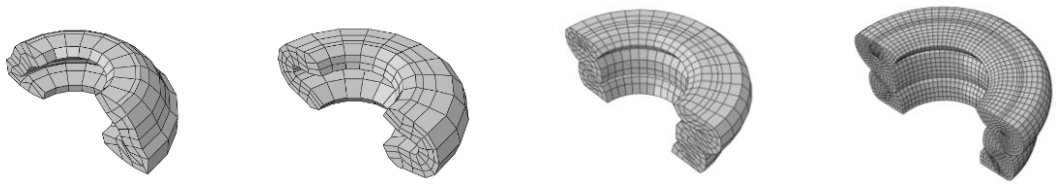

(b) (c) (d) (e)

Figure 5.5 (a) Mesh-sensitivity analysis showing the number of elements required for convergence of the FE model for an aluminium tube of diameter 12.62 mm. Deformed shapes of tubes based on (b) 100 elements (mesh = 2mm), (c) 150 elements (mesh = 2mm), (d) 600 elements (mesh = 1 mm) and (e) 4800 elements (mesh = 0.5 mm).

Clearly, the CPU time increases as the number of elements is increased. However, the bottoming-out displacement and the specific energy absorption values are very sensitive to the number of axial lobes. The symmetrical deformation modes of the models are shown in Figure 5.5, where Figure 5.5(b) and 5(c) indicate one lobe, whilst Figure 5.5(d) and 5(e) show two axial lobes. It is clear that a coarse mesh size of 2 mm (100 or 150 elements) is not suitable for this case, as the tubes were unable to form the two axial lobes observed experimentally. This resulted in errors in the predicted specific energy absorption of up to 45% (for the model with 100 elements).

Based on this observation, it is evident that increasing the number of elements from 600 to 4800 does not have a significant effect on the deformation shape, suggesting that mesh sizes in the range of 0.5 to 1 mm are appropriate for simulation. In the present study, 600 elements are used, since this value corresponds to the threshold at which the SEA and the force associated to bottoming-out tend to a constant value (see Figure 5.5(a)). Additionally, an element size of 1 mm was deemed to be appropriate, since it produces sufficiently accurate results in a short CPU time (45 minutes in the present case).

5.3.2 Influence of the D/t on SEA

The FE models were validated against the experimental data relating to the smallest, the largest and one of the intermediate-sized tube diameters, as given in Tables 5.8 and 5.9. Figure 5.6(a) compares the quasi-static experimental load-displacement curves for the 12.62 mm diameter aluminium and steel tubes with the predictions offered by the FE models. From the figure, it is evident that the load-displacement curves for the tubes show a steady increase in load until they reach the peak value. This is followed by a region of almost constant load, before the final bottoming-out of the sample at higher displacements. It should be noted that since perfect contact between the tube and the platens was assumed in all cases, the FE predictions slightly over-estimate the measured stiffness. Beyond the elastic region, it is clear that the FE predictions are in good agreement with the experimental results for both types of tube.

The predicted dynamic load-displacement curves for the 12.62 mm diameter aluminium and steel tubes are compared with their experimental counterparts in Figure 5.6(b). An examination of the numerical curves indicates that they are in close agreement with the experimental results for both types of tube. The FE models predict a smoother response than that associated with the test samples, since the latter exhibit an oscillatory response. This is due to ringing effects in the load-cell following impact of the steel impactor on the stiff metal tube [158]. Despite this, the level of agreement between the experimental and FE predicted SEA values are very good.

Tube ID	Outer diameter, D_o (mm)	Inner diameter, D (mm)	Thickness, t (mm)	D/t	SEA experimental (kJ/kg)	SEA numerical (kJ/kg)	FE/Exp difference (%)
TAL6	6.50	3.14	1.68	1.87	-	86.22	-
TAL9	9.53	6.17	1.68	3.67	-	77.11	-
TAL12	12.62	9.12	1.75	5.21	70.07	70.89	+ 1.2
TAL16	16.00	12.36	1.82	6.79	63.47	57.96	- 8.7
TAL19	19.10	15.60	1.75	8.91	58.28	-	-
TAL22	22.40	19.00	1.70	11.18	56.08	-	-
TAL25	25.40	22.04	1.68	13.12	52.96	48.08	- 9.2
TAL38	38.10	34.74	1.68	20.68	-	37.21	-

Table 5.8 Comparison of the quasi-static experimental and numerical SEA characteristics of 20 mm long individual aluminium tubes.

Tube ID	Outer diameter, D_o (mm)	Inner diameter, D (mm)	Thickness, t (mm)	D/t	SEA experiment (kJ/kg)	SEA numerical (kJ/kg)	FE/Exp difference (%)
TST6	6.50	3.14	1.68	1.87	-	57.02	-
TST9	9.53	6.17	1.68	3.67	-	43.65	-
TST12	12.62	9.26	1.68	5.51	41.46	40.75	- 1.7
TST16	15.78	12.42	1.68	7.39	36.94	33.50	- 9.3
TST19	19.05	15.69	1.68	9.34	31.22	-	-
TST22	22.22	18.86	1.68	11.23	27.97	-	-
TST25	25.40	22.04	1.68	13.12	24.12	21.78	- 9.7
TST38	38.10	34.74	1.68	20.68	-	17.18	-

Table 5.9 Comparison of the quasi-static experimental and numerical SEA characteristics of 20 mm long individual steel tubes.

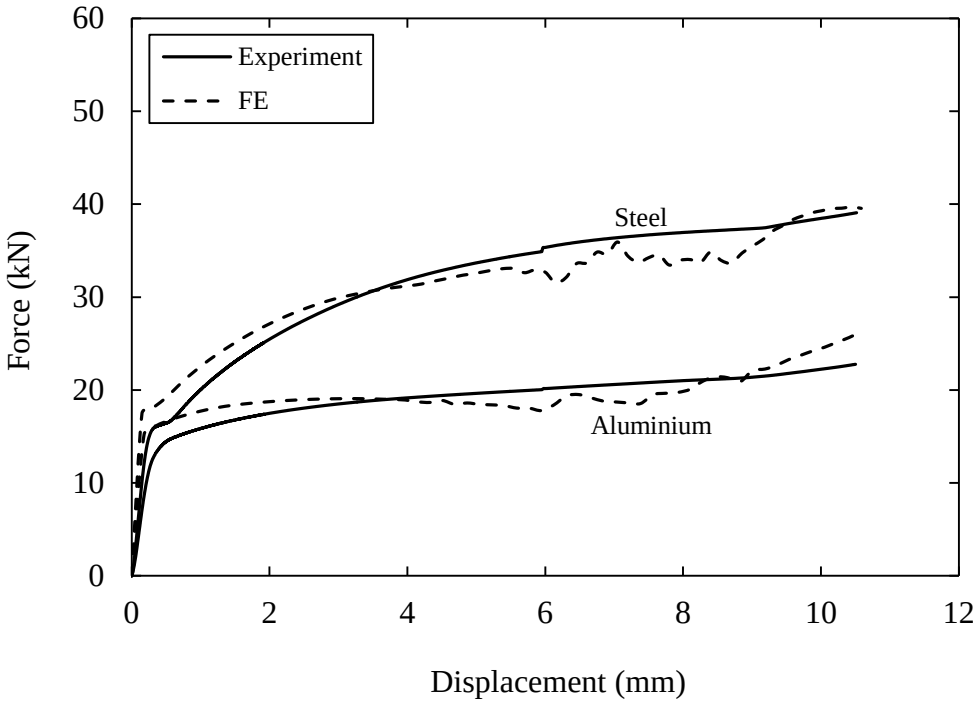

(a)

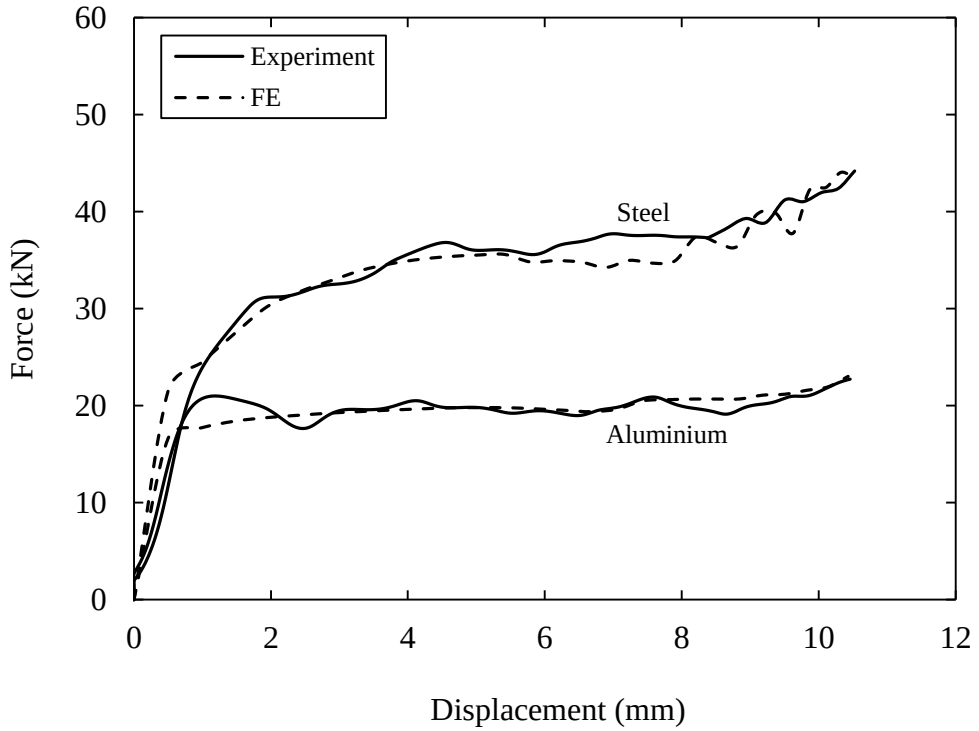

(b)

Figure 5.6 Experimental and numerical force-displacement traces for 20 mm long 12.62 mm diameter aluminium (D/t = 5.21) and steel (D/t = 5.51) tubes following (a) quasi-static and (b) dynamic loading.

The evidence in Figure 5.6 suggests that strain-rate effects are not significant for the aluminium. In contrast, an enhancement of approximately 10% is observed for the steel tubes, when tested under dynamic loading conditions. This evidence suggests that strain-rate effects are not significant for the aluminium alloy over the range of loading conditions tested here, whereas these findings indicate that it is important to define the strain-rate for accurate numerical modelling of the steel tubes.

Figure 5.7 shows the variation of SEA with inner diameter/thickness, D/t, for both the aluminium and steel tubes, where the dotted lines in the figure correspond to the FE predictions. From the figure, it is clear that the energy-absorbing capability of the tubes decreases rapidly with increasing D/t. The figure shows that the FE models yield predictions that are very similar (less than 10%) to the experimental values. This indicates that the models accurately predict the key aspects of the crushing response of these simple tubes.

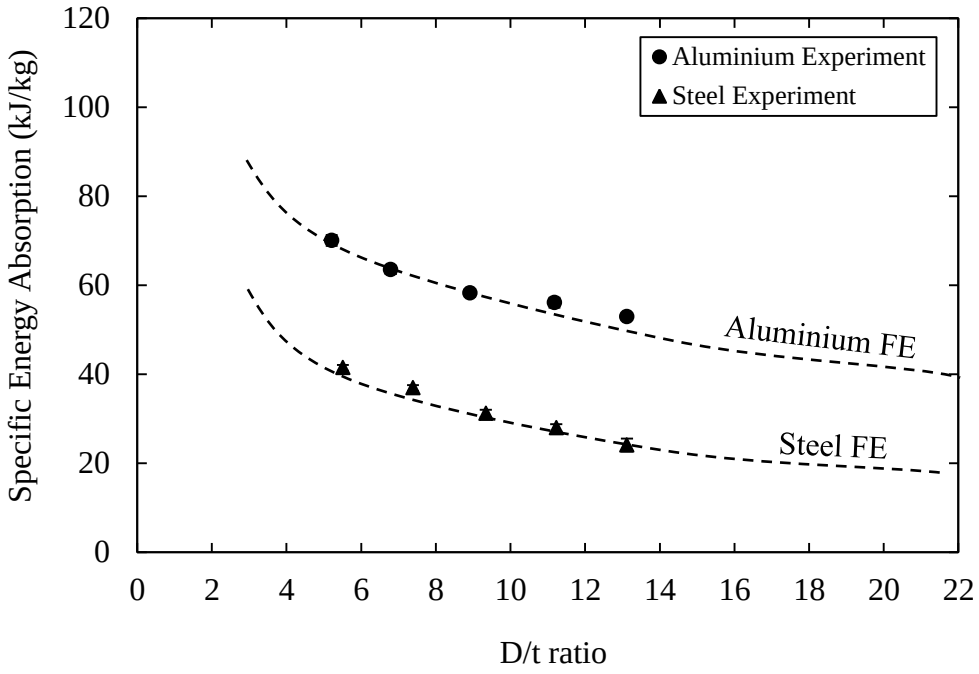

Figure 5.7 The variation of SEA with D/t for 20 mm long aluminium and steel tubes.

Figure 5.8 shows images obtained following experimental testing and FE modelling of the aluminium and steel tubes for a range of initial D/t values. It is clear that the deformation modes have been accurately predicted for all tube diameters, with buckling producing a ring shape, or what is often known as a concertina mode of collapse. These figures demonstrate that there is a very high level of agreement between the predicted and observed failure modes in the two types of tube.

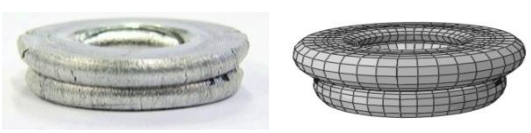

(i) 12.62 mm (D/t = 5.21)

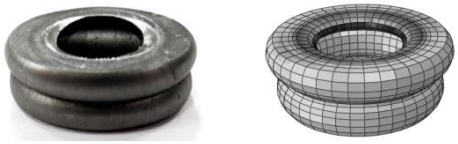

(i) 12.62 mm (D/t = 5.51)

(ii) 16.00 mm (D/t = 6.79)

(ii) 15.78 mm (D/t = 7.39)

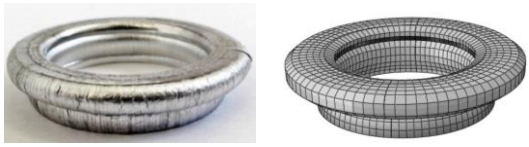

(iii) 25.40 mm (D/t = 13.12)

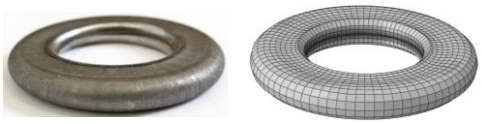

(iii) 25.40 mm (D/t = 13.12)

(a) (b)

Figure 5.8 Comparison of the photographs and FE simulations of 20 mm long metal tubes with different diameters following quasi-static compression for (a) aluminium and (b) steel tubes.

In the next stage of this research investigation, the FE models were used to further investigate the effect of varying the diameter to thickness ratio of the aluminium and steel tubes. Figure 5.9 shows the predicted load-displacement curves for steel tubes with diameters of 9.53 mm (D/t = 3.85) and 38.10 mm (D/t = 21.37). Also included in the figure are the corresponding deformation modes for both types of tube. The FE simulations predict that compression of the smaller tube will generate two wrinkles and that the larger diameter tube will exhibit a single wrinkle. This agrees well with findings reported by Jones [34], where it was observed that the number of wrinkles in a steel tube decreases with increasing tube diameter.

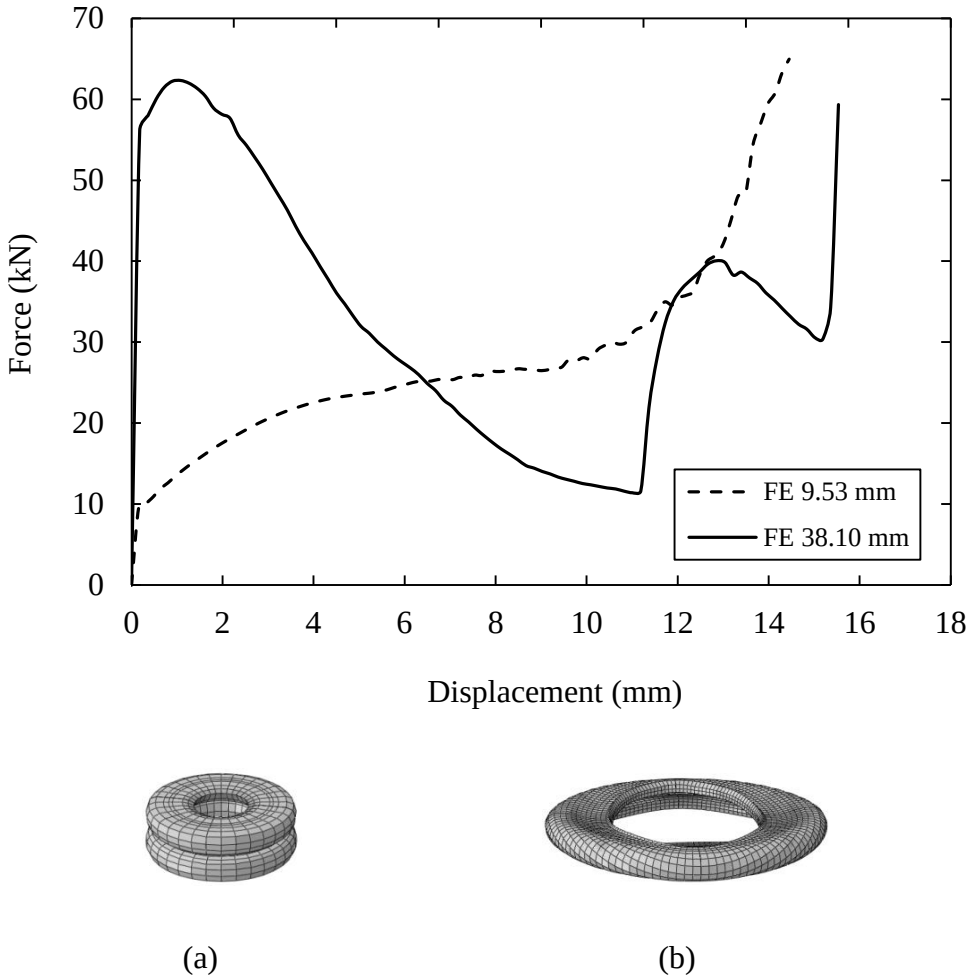

Figure 5.9 Predicted quasi-static load-displacement traces for 20 mm long steel tubes (a) 9.53 mm diameter (D/t = 3.85) and (b) 38.10 mm diameter (D/t = 21.37).

5.3.3 Influence of the Foam Density on SEA

This part of the study considered the effect of embedding single metal tubes in a polymeric foam, details are given in Tables 5.10 and 5.11. Figure 5.10 shows experimental and predicted load-displacement curves following compression tests on the aluminium and steel tubes embedded in a P6 foam with a density of 224 kg/m^3. Also included in the figure are the load-displacement curves for the individual tube, as well as that for a foam sample having a similar volume to that of the combined tube + foam specimen. Generally, agreement between the experimental results and the FE data is very good, with all of the main features being captured by the model, including similar values of initial stiffness, peak load, plateau stress and bottoming-out displacement.

In both the experimental and FE models, it is clear that the metal tubes dominate the response by absorbing most of the energy in these reinforced structures. At low and intermediate foam densities, the performance of the reinforced foam is roughly equal to that of the sum of the individual foam and tube in terms of SEA. In contrast, there is a small degree (<5%) of additional support due to the presence of the foam with a relatively high density, such as 224 kg/m^3 as shown in Figure 5.10(b). This suggests that the presence of the foam may modify the collapse behaviour of the tube.

Figure 5.11 shows the predicted cross-sections of the aluminium and steel tubes embedded in a P6 foam following compression testing at quasi-static rates of loading. Given that an imperfection was introduced along the longitudinal axis of the tube, it is possible that the tube could penetrate into the foam. This was prevented by introducing a small gap between the tube and the foam in FE models, as shown in Figure 5.1(b).

Sample ID	Foam density (kg/m^3)	Foam modulus (MPa)	SEA experimental (kJ/kg)	SEA numerical (kJ/kg)	FE/exp difference (%)
TAL12	0	0	70.07	70.89	+ 1.2
T1ALP1	15.6	6	70.58	71.11	+ 0.8
T1ALP2	38.3	37	68.43	71.49	+ 4.5
T1ALP3	56.0	69	68.56	70.74	+ 3.2
T1ALP4	90.4	97	69.15	70.76	+ 2.3
T1ALP5	128.0	160	69.42	67.58	- 2.6
T1ALP6	224.0	280	69.50	70.40	+ 1.3

Table 5.10 Summary of the quasi-static experimental and numerical values of SEA for individual 20 mm long aluminium tubes in foams of different density.

Sample ID	Foam density (kg/m^3)	Foam modulus (MPa)	SEA experimental (kJ/kg)	SEA numerical (kJ/kg)	FE/Exp difference (%)
TST12	0	0	41.5	40.7	- 1.7
T1STP1	15.6	6	41.8	40.7	- 2.5
T1STP2	38.3	37	41.2	40.3	- 2.1
T1STP3	56.0	69	43.1	42.5	- 1.4
T1STP4	90.4	97	43.9	44.3	+ 1.0
T1STP5	128.0	160	42.3	41.3	- 2.5
T1STP6	224.0	280	40.2	43.1	+ 7.3

Table 5.11 Summary of the quasi-static experimental and numerical values of SEA for individual 20 mm long steel tubes in foams of different density.

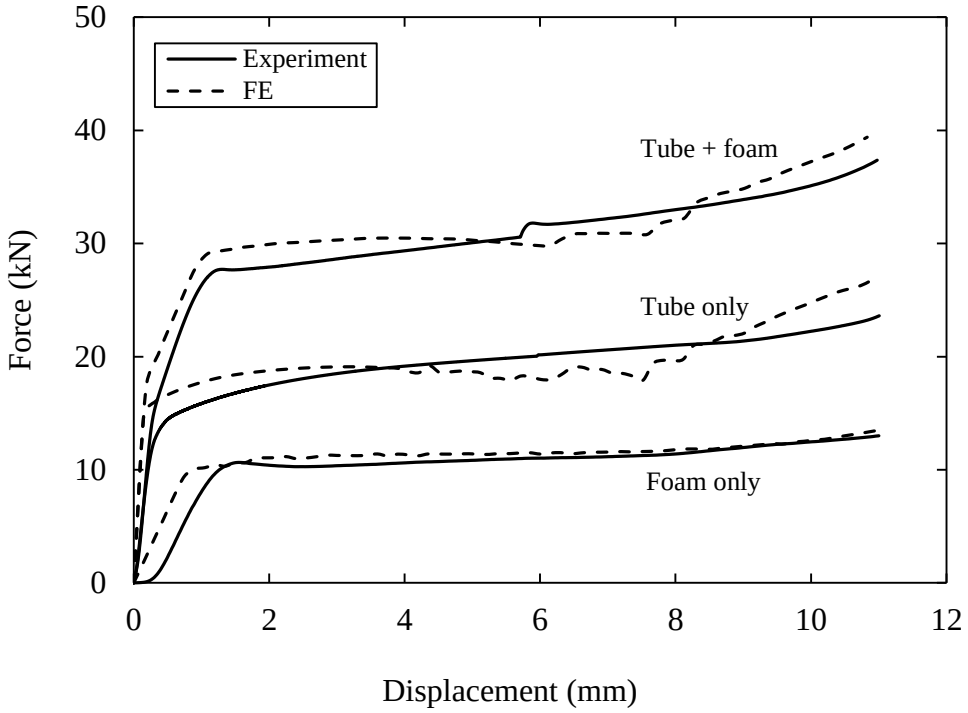

(a)

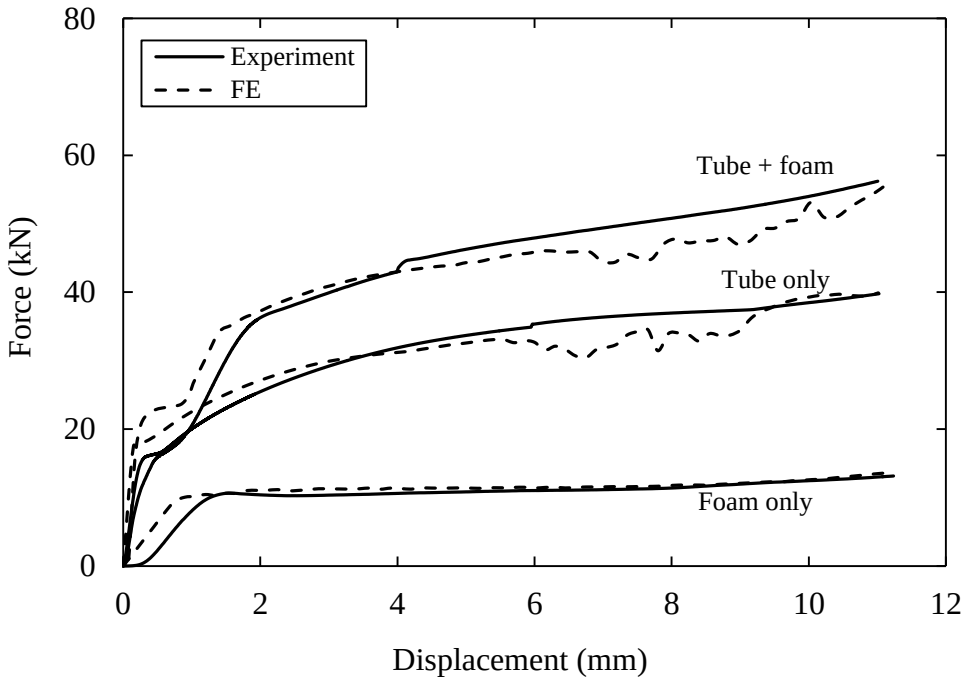

(b)

Figure 5.10 Experimental and numerical quasi-static load-displacement traces following tests on a 20 mm long, 12.62 mm diameter (a) aluminium tube (D/t = 5.21) and (b) steel tube (D/t = 5.51) in a foam with a density of 224 kg/m^3.

A comparison of these images with those shown previously in Figures 5.8(a)i and (b)i indicates that the modes of deformation and failure are similar for both the plain and embedded tubes. This suggests that the foam does not significantly modify the response of the tube and suggests that the former merely acts as a substrate to secure the position of the tubes. The density of the foam should therefore be as low as possible, whilst serving to hold the tubes in the required locations during loading.

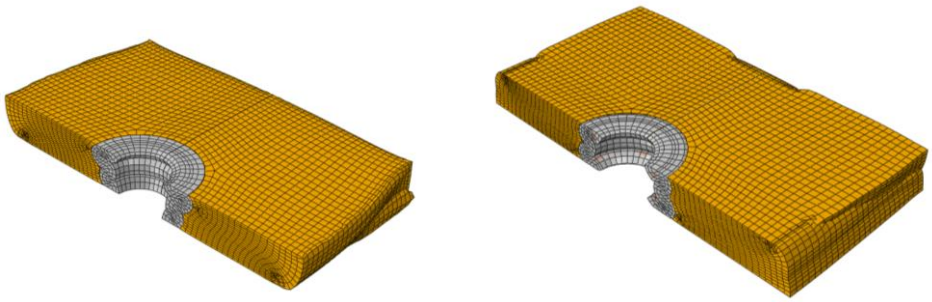

(a) (b)

Figure 5.11 Cross-sections of the deformed shapes of 20 mm long tubes (D_o= 12.62 mm) embedded in a P6 foam (224 kg/m^3) (a) aluminium tube (D/t = 5.21) and (b) steel tube (D/t = 5.51).

The experimental results and the FE predictions for the SEA of the tubes under quasi-static loading are given as a function of foam modulus in Figure 5.12. Here, the energy absorbed by the individual metal tube was estimated by removing the contribution associated with the foam [158]. The resulting value of energy was then divided by the mass of the metal tube to yield an effective SEA value for the tube on its own. Also included in the figure are the values resulting from the previously-reported tests on the individual metal tubes, that is, those tubes that were not embedded in a foam. These particular points are shown on the y-axis of the figure. From the figure, it is evident that the values of SEA for both types of tube do not

vary with foam modulus. Additionally, it is clear that the FE models accurately predict the SEA values of these embedded tubes, with the greatest error being approximately 8%. These results support the conclusion that the foam functions only to maintain the tubes in place during loading and that it does not significantly modify or improve their performance.

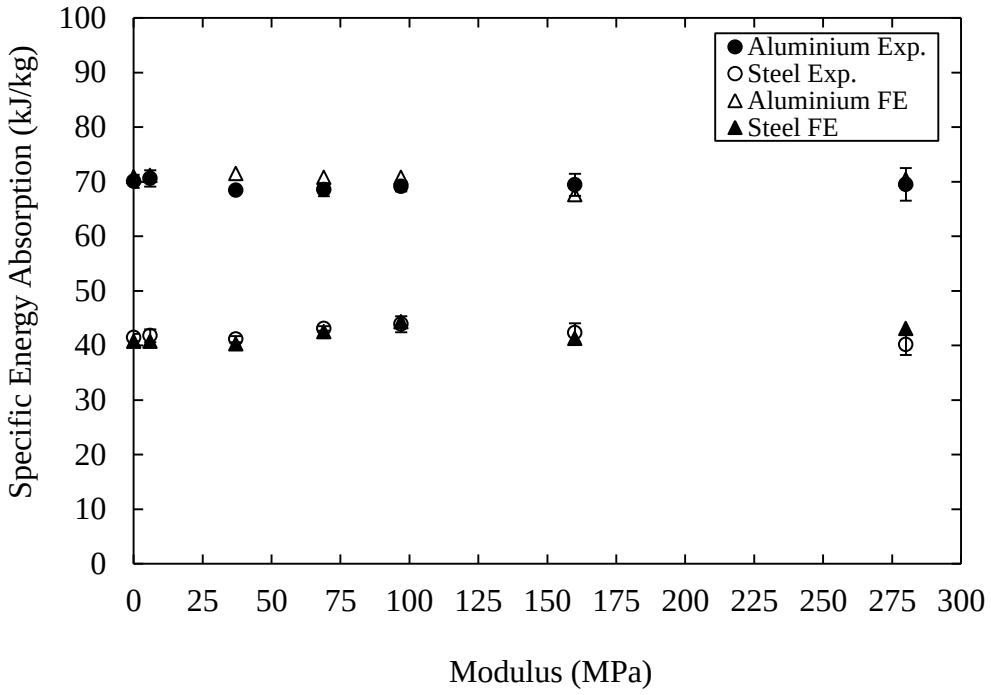

Figure 5.12 The variation of the quasi-static experimental and FE values of SEA for aluminium and steel tubes. The contribution of the foam has been removed.

Figure 5.13 compares the variation of the quasi-static and dynamic (experimental) values of SEA with foam density for the two types of tubes. Once again, the contribution of the foam has been removed in order to yield effective SEA values for the individual tubes. As before, the properties of the foam do not have a significant effect on the energy-absorbing characteristics of the metal tube. Here, it is evident that the SEA values exhibited by the aluminium tubes at dynamic rates are almost identical to their corresponding quasi-static values, indicating that there is a lack of

rate-sensitivity in the response of this material. In contrast, the steel tubes exhibit a small level of rate-sensitivity (approximately 10%) reflecting the trends observed previously in Figure 5.6. FE models were developed to predict the response of the aluminium and steel tubes embedded in foam at impact rates of loading. Figure 5.14 shows typical load-displacement curves (experimental and predicted) following impact tests on aluminium and steel tubes embedded in a P2 (38.3 kg/m^3) foam. Also included are the responses of the individual constituents, that is, the tube and the foam. Despite some small oscillations in the FE prediction during the later stages of the load-displacement curve, the predicted SEA values are again in a good agreement with the experimental results, where the average differences between the predicted and measured values for the aluminium and steel are approximately 4 and 7 % respectively.

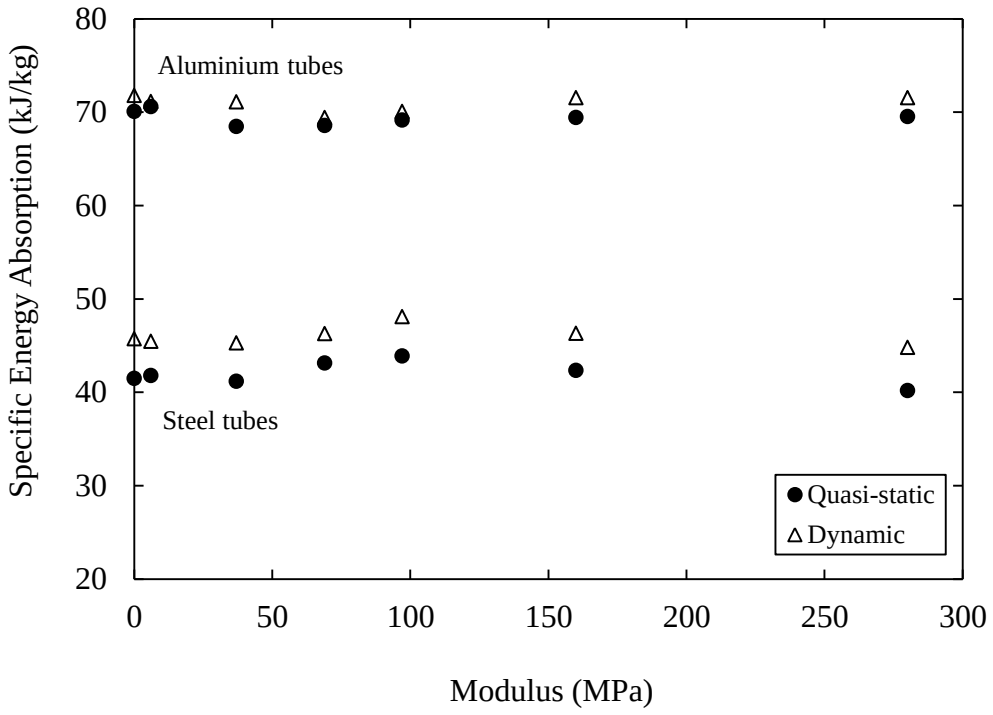

Figure 5.13 The variation of the experimentally-determined quasi-static and dynamic values of SEA with foam density. Aluminium (outside diameter = 12.62 mm, D/t = 5.21) and steel (outside diameter = 12.62 mm, D/t = 5.51).

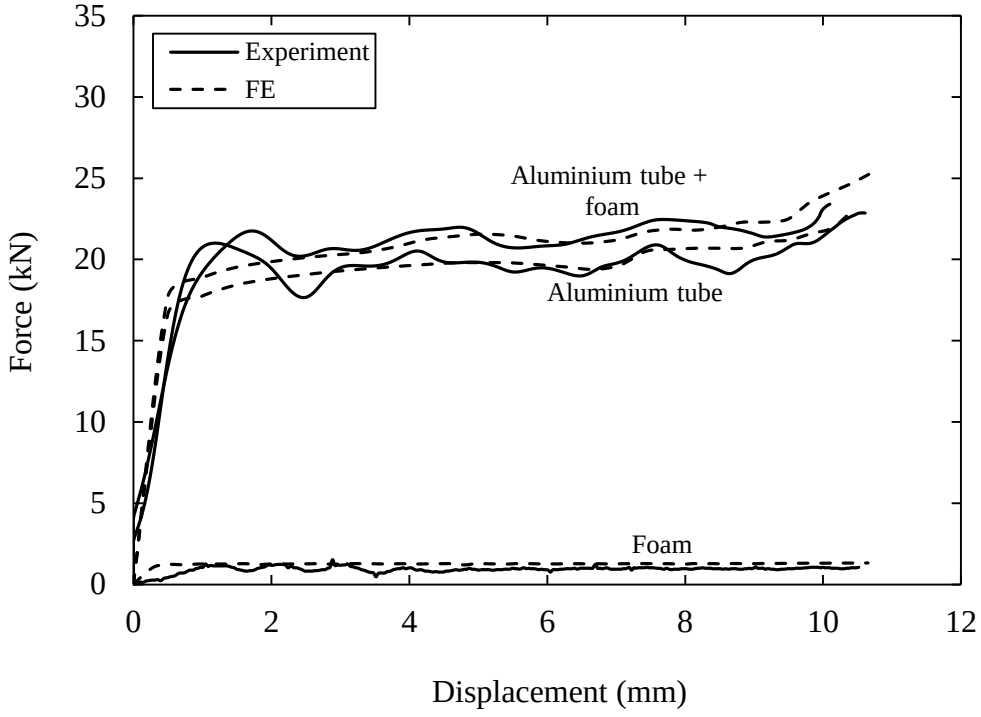

(a)

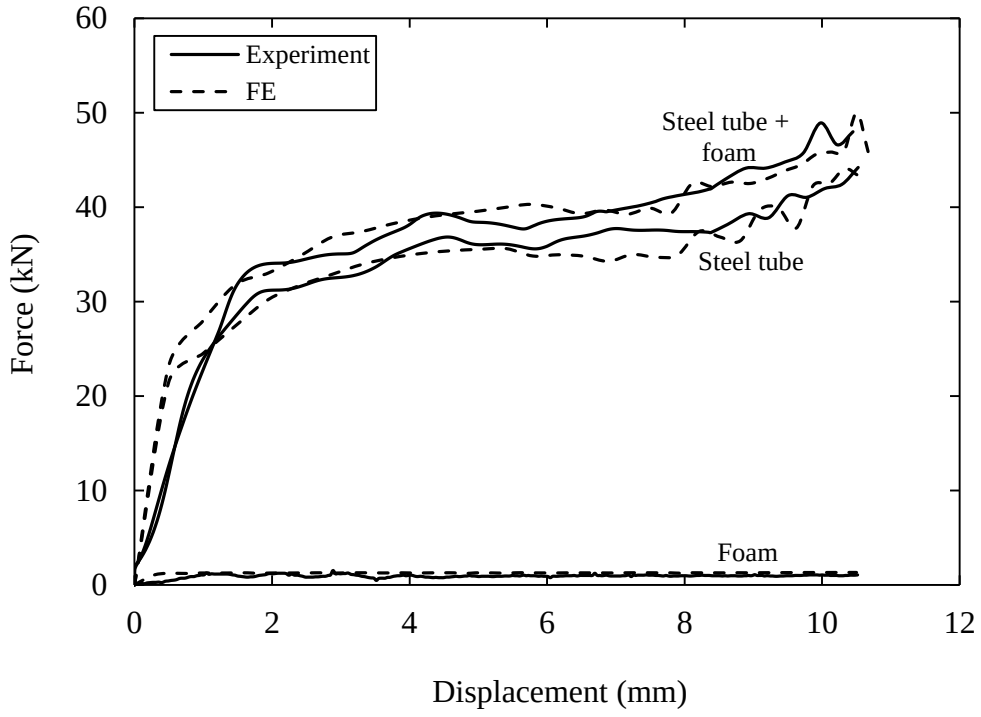

(b)

Figure 5.14 Predicted and measured dynamic load-displacement traces for the metal tubes, a low density foam (38.3 kg/m^3) and the combined tube plus foam: (a) Aluminium (D_o = 12.62 mm, D/t = 5.21) and (b) steel (D_o = 12.62 mm, D/t = 5.51).

The FE investigation continues with a study on the effect of increasing the number of tubes on the quasi-static energy-absorbing response of these reinforced foam structures. Here, between one and five 12.6 mm diameter metal tubes were embedded into 20 mm thick, 60 mm square foam blocks, details of which are given in Tables 5.12 and 5.13.

Figure 5.15 shows a series of measured and predicted load-displacement curves for multi-tube systems embedded in a P6 foam with a density of 224 kg/m^3. As before, the FE models over-estimate the initial stiffness in almost all cases, most particularly for the case of the aluminium systems. However, it can be seen that the overall trends in both the experimental and FE predictions are generally similar. Any differences between the experimental data and the model may, in part, be due to the fact that the buckling resistance of the tubes is very sensitive to the presence of imperfections within them.

The resulting SEA values were calculated based on the total mass of the test samples, that is, no attempt was made to remove the contribution associated with the foam. As expected, increasing the number of tubes in a foam sample serves to increase the overall SEA of the structure. For example, the SEA of the aluminium-P1 (density = 15.6 kg/m^3) system increases from 58 to 65 kJ/kg as the number of tubes is increased from one to five. Similar trends are apparent in the P6 (224 kg/m^3) foam, where increasing the number of tubes serves to increase the SEA from 26 to 43 kJ/kg. A closer inspection of Figure 5.16 shows that the buckling response of the multiple tubes embedded in the foam is similar to that of individual tubes, Figure 5.8(a)i and (b)i. It is interesting to note that the SEA of the P1 structure containing five tubes is similar to that of the plain tube, suggesting that the response of the metal tubes completely masks that of the foam.

No of tubes in foam	SEA experimental [kJ/kg]			SEA numerical [kJ/kg]			FE/Exp difference [%]		
	15.6 kg/m^3	90.4 kg/m^3	224.0 kg/m^3	15.6 kg/m^3	90.4 kg/m^3	224.0 kg/m^3	15.6 kg/m^3	90.4 kg/m^3	224.0 kg/m^3
1	57.5	29.9	26.3	58.7	29.2	25.3	+ 2.1	- 2.2	- 4.0
2	60.2	39.2	32.9	67.0	41.0	33.3	+ 11.3	+ 4.6	+ 1.3
3	62.1	43.6	35.9	68.0	47.0	37.0	+ 9.7	+ 7.7	+ 3.0
4	63.1	46.9	40.5	70.2	52.3	42.3	+ 11.2	+ 11.4	+ 4.4
5	65.3	50.3	42.6	69.5	56.0	46.4	+ 6.5	+ 11.3	+ 9.0

Table 5.12 Summary of the SEA values (experimental and numerical) for foams containing between 1 and 5 aluminium tubes.

No of tubes in foam	SEA experiment [kJ/kg]			SEA numerical [kJ/kg]			FE/Exp difference [%]		
	15.6 kg/m^3	90.4 kg/m^3	224.0 kg/m^3	15.6 kg/m^3	90.4 kg/m^3	224.0 kg/m^3	15.6 kg/m^3	90.4 kg/m^3	224.0 kg/m^3
1	42.5	30.2	26.7	40.6	28.2	25.8	- 4.3	- 6.7	+ 3.5
2	42.1	32.1	31.3	40.6	33.4	30.2	- 3.4	+ 4.2	- 3.4
3	41.1	34.5	32.9	42.1	34.8	33.5	+ 2.2	+ 1.0	+ 1.7
4	41.7	35.5	34.0	41.1	35.7	34.8	+ 1.4	+ 0.6	+ 2.2
5	41.5	37.1	34.4	41.2	36.2	35.4	- 0.6	- 2.3	+ 3.0

Table 5.13 Summary of the SEA values (experimental and numerical) for foams containing between 1 and 5 steel tubes.

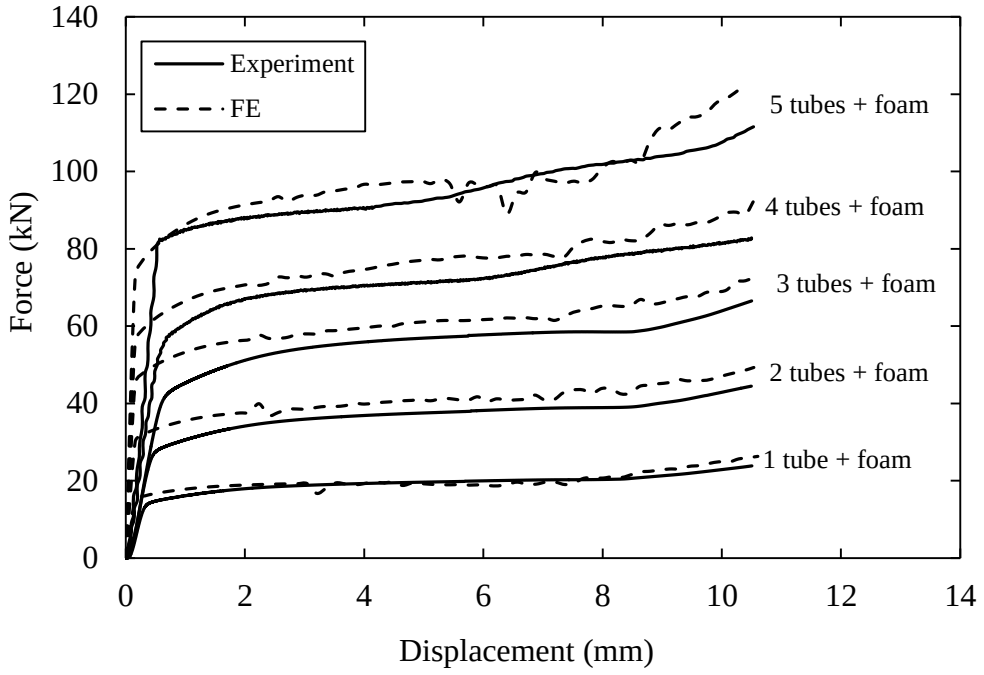

(a)

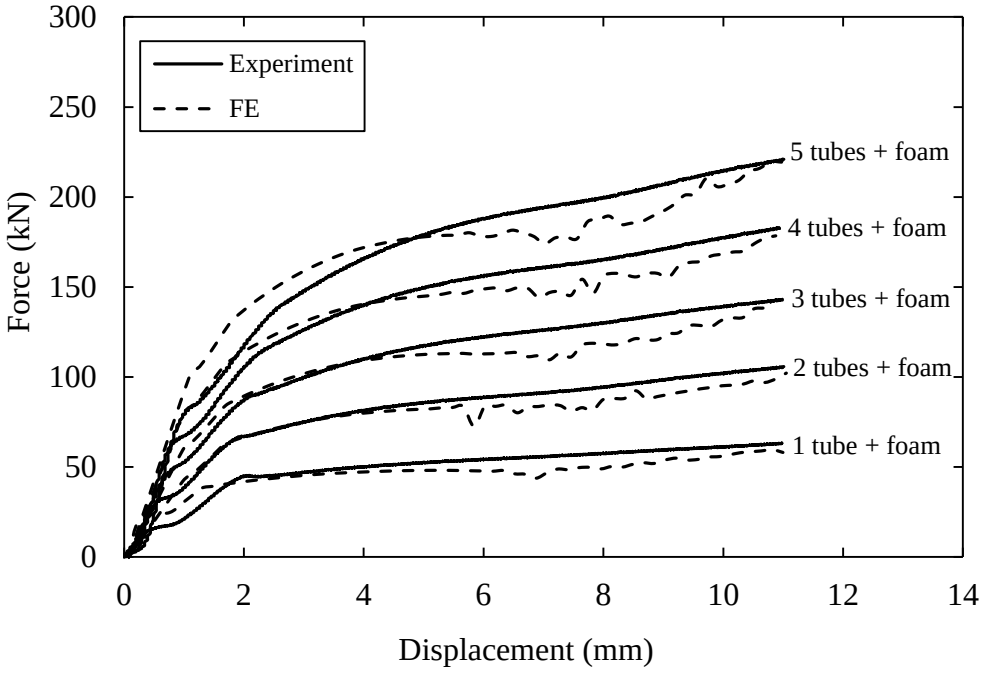

(b)

Figure 5.15 Predicted and measured force-displacement traces for increasing numbers of 12.62 mm diameter metal tubes in a P6 foam with a density of 224 kg/m^3 (a) aluminium tubes (D/t = 5.21) and (b) steel tubes (D/t = 5.51).

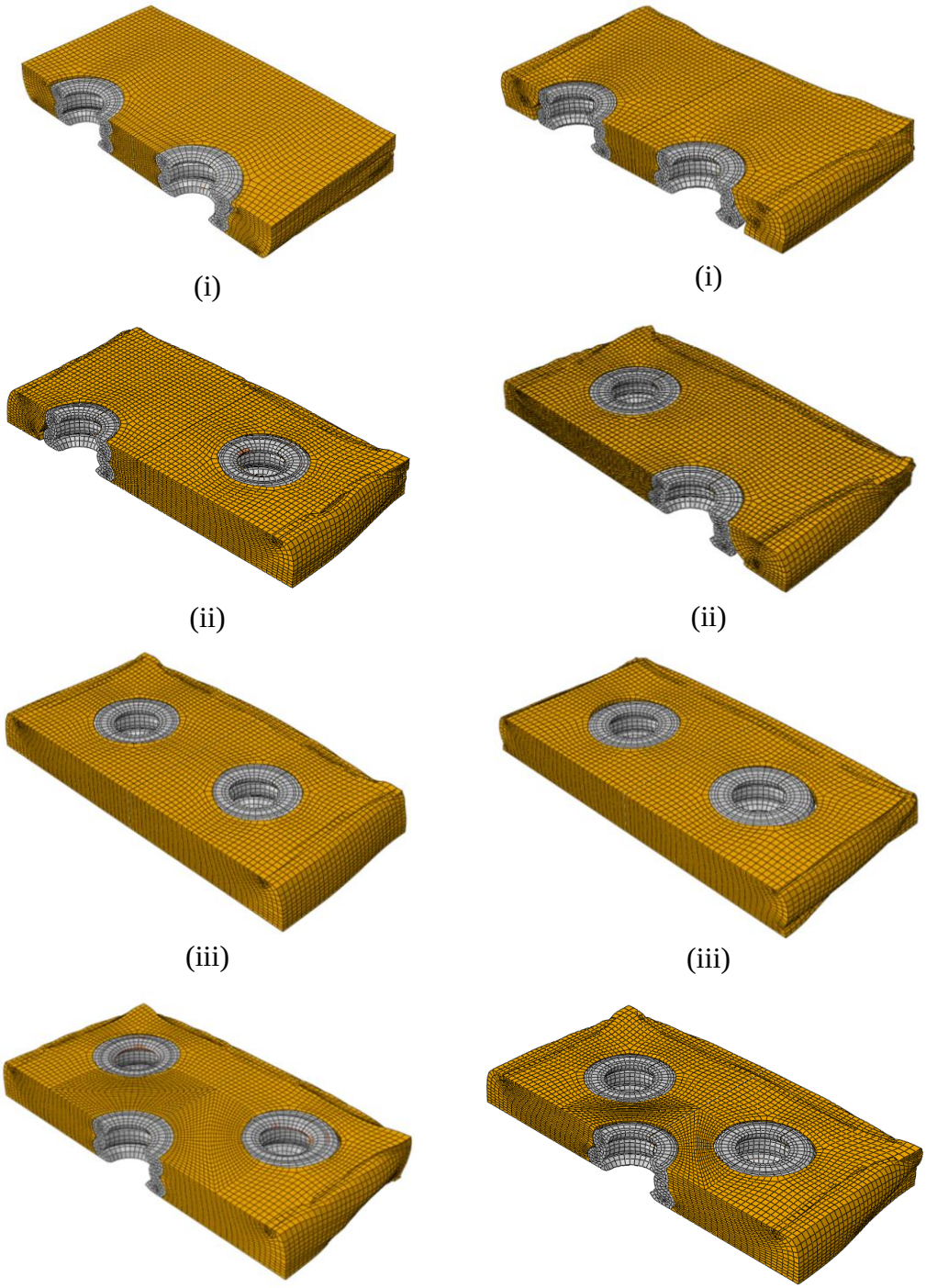

Figure 5.16 Cross-sections of deformed foam samples based on increasing numbers of tubes in a P6 (224 kg/m^3) foam (a) aluminium tubes (D/t = 5.21) and (b) steel tubes (D/t = 5.51).

5.4 Results and Discussion of the CFRP Tubes

5.4.1 Mesh Sensitivity Analysis

A mesh sensitivity analysis was performed using a model of a CFRP tube specimen with an outer diameter of 10.20 mm and a length of 20 mm. For verification purposes, the CFRP tubes previously subjected to quasi-static loading are used to validate the current FE models. The finite element model was meshed using four different mesh sizes, these being 2 mm (coarse), 1 mm (medium), 0.6 mm (fine) and 0.4 mm (very fine). Here, four models were studied, with each containing 56, 132, 340 and 800 elements. Results are shown in Table 5.14.

Figure 5.17(a) summarises the findings of the mesh sensitivity analysis, which comprises the relationships between the number of elements, predicted specific energy absorption and total CPU time. The reasonable number of elements was also indicated in the figure. As anticipated, the CPU time increases as the number of elements is increased. Similarly, the predicted SEA increases gradually as the number of elements increases and remains almost constant as it approaches the experimental value.

Number of Elements	Mesh size [mm]	CPU time [hour]	SEA [kJ/kg]	FE/exp difference [%]
Experiment	-	-	93.3	-
56	2.0	0.23	71.0	-23.9
132	1.0	0.50	79.8	-14.5
340	0.6	2.83	89.7	-3.9
800	0.4	5.37	90.2	-3.3

Table 5.14 Details of mesh sensitivity analysis.

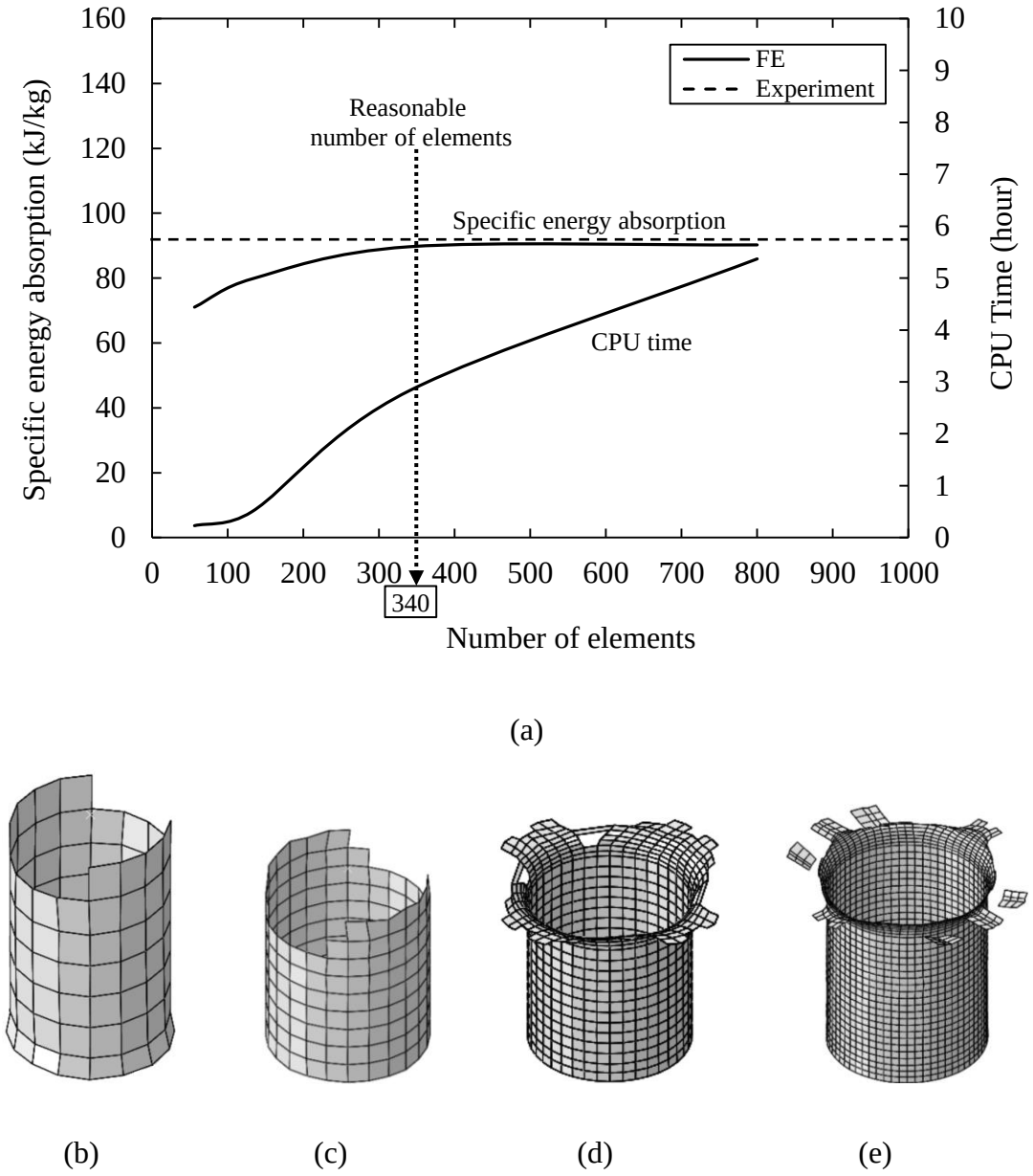

Figure 5.17 (a) Mesh-sensitivity analysis showing the number of elements required for convergence of the FE model for a CFRP tube of 10.2 mm diameter. Deformed shapes of tubes based on (b) 56 elements (mesh = 2 mm), (c) 132 elements (mesh = 1 mm), (d) 340 elements (mesh = 0.6 mm) and (e) 800 elements (mesh = 0.4 mm).

The deformations of the models with different number of elements are shown in Figures 5.17(b), (c), (d) and (e). All models show the occurrence of element deletion, where the element deletion condition is satisfied at all of the section points of an element. However, splaying mode can only be observed in models with finer mesh sizes of 0.4 and 0.6 mm (Figures 5.17(d) and (e)). In the finer mesh models, the splaying characteristic offers resistance to their subsequent deformation.

The load-displacement curves in Figure 5.18(a) show that the models with larger mesh sizes exhibit a higher fluctuation trend as compared to the models with finer mesh sizes in Figure 5.18(b). Consequently, the models with larger mesh sizes of 2 and 1 mm resulted in substantial errors of 23.9 and 14.5% respectively. This shows that finite element predictions involving composite fracture mechanisms are sensitive to the mesh size selected. It should be noted that since perfect contact between the tube and the platens was assumed in all cases, the FE predictions slightly over-estimate the measured stiffness.

Figure 5.18(b) shows that the model with 0.4 mm is less fluctuated as compared to the 0.6 mm model with minor errors of 3.9 and 3.3% respectively. In terms of practicality, the mesh size of 0.6 mm (2.83 hour) is used as it has a more reasonable runtime with almost half the duration of that 0.4 mm (5.37 hour) model. Although the predictions of both models are only with minor errors, model with 0.6 mm (2.83 hour) has a shorter runtime than model 0.4 mm (5.37 hour). Therefore, model 0.6 mm is deemed to be more appropriate because of its close agreement with the experimental results and shorter runtime.

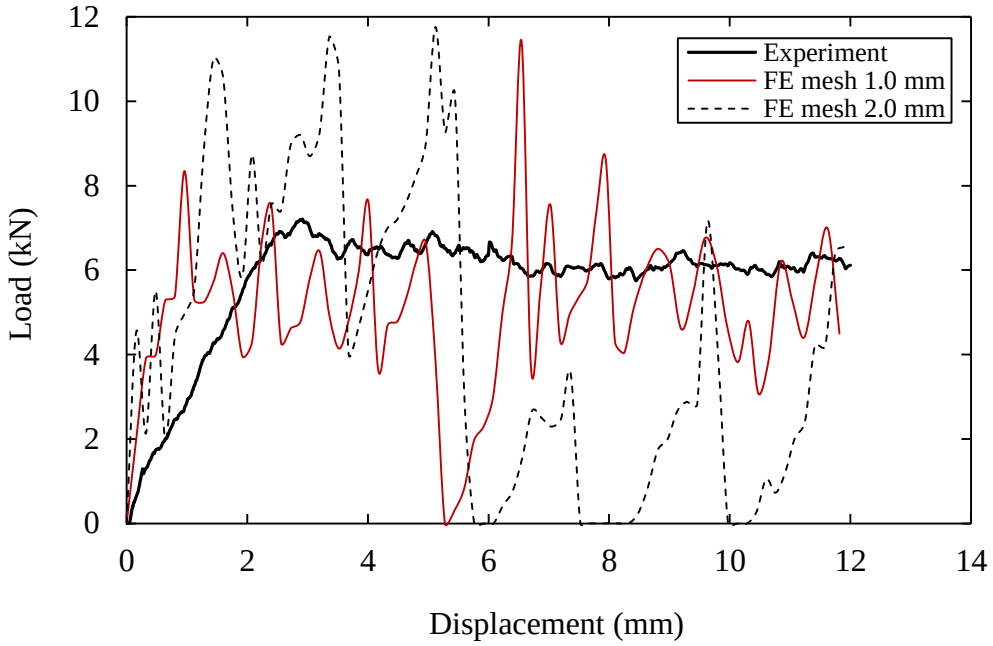

(a)

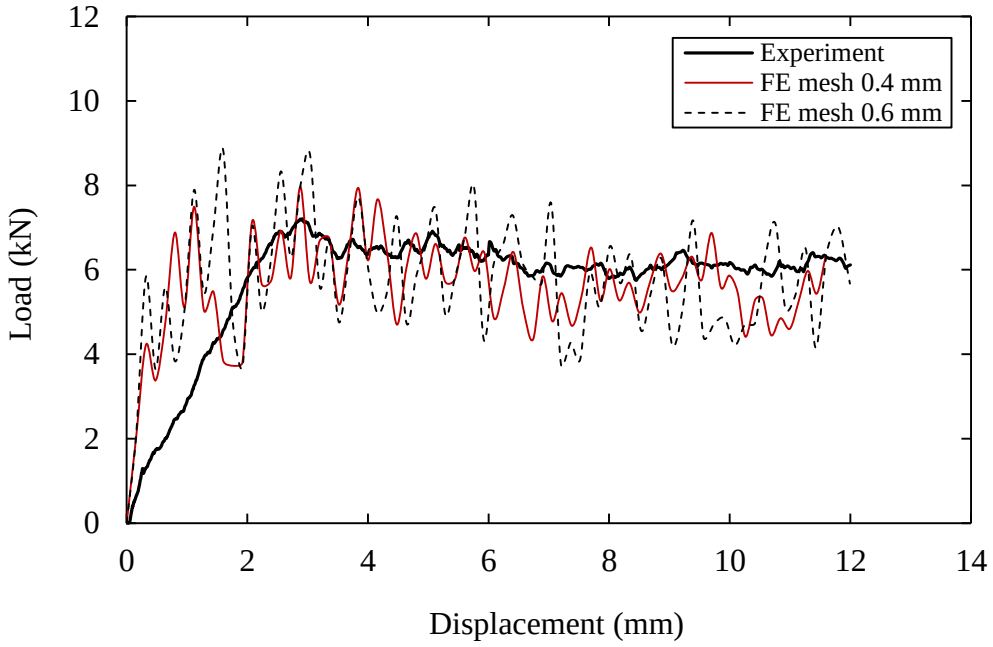

(b)

Figure 5.18 Experimental and numerical force-displacement traces for 20 mm long 10.2 mm diameter CFRP tube mesh sizes of (a) 1 mm, 2 mm, (b) 0.4 mm and 0.6 mm following quasi-static loading.

5.4.2 Influence of the D/t on SEA

Table 5.15 gives a summary of the experimental and numerical SEA characteristics of 20 mm long individual CFRP tubes. From the table, it is clear that the energy-absorbing capability of the tubes decreases rapidly with increasing D/t. For example, the SEA decreases by 48% from 93.3 to 48.1 kJ/kg over the range of values of D/t considered here. The table shows that the FE models yield predictions that are very close to the experimental values with difference of less than 8%.

Tube ID	Outer diameter, D_o [mm]	Inner diameter, D [mm]	Thickness, t [mm]	D/t	SEA experimental [kJ/kg]	SEA FE [kJ/kg]	FE/Exp difference [%]
TCF10	10.20	7.74	1.23	6.3	93.3	89.7	-3.9
TCF12	12.70	10.00	1.35	7.4	89.2	90.7	+1.7
TCF29	29.40	26.28	1.56	16.9	81.4	-	-
TCF40	40.90	37.54	1.68	22.4	76.7	-	-
TCF50	50.40	47.04	1.68	28.0	58.5	-	-
TCF63	63.60	59.92	1.84	32.6	48.1	51.7	+7.5

Table 5.15 Comparison of the quasi-static experimental and numerical SEA characteristics of 20 mm long individual aluminium tubes.

Figure 5.19 compares the experimental load-displacement traces for the 10.2, 12.7 and 63.3 mm diameter CFRP tubes with the predictions offered by the FE models. It is evident that all traces exhibit similar characteristics, with force rising to a maximum before dropping slightly and failure occurring in a stable manner at an approximately constant force. The exception to this observation is the largest diameter tube (D_o = 63.3 mm) with a D/t value of 32.6. Initially, the trace displays a linear response up to a peak load of approximately 65 kN. This is followed by a

substantial drop to approximately 30 kN before reaching a region of almost constant load. Again, as perfect contact between the tube and the platens was assumed in all cases, the FE predictions over-estimate the measured stiffness.

Figures 5.20 and 5.21 show images obtained following experimental testing and FE modelling of the CFRP tubes for a range of initial D/t values. The presence of a distinct crush front, in which the fibre splay outwards against the moving platen, can be observed in the experimental and FE images of 10.2 mm and 12.7 mm diameter tubes. Closer inspection of the lower platen in the experimental images of 10.2 mm and 12.7 mm diameter tubes suggested that the failure process generated a significant number of small fragments. However, the presence of fractured small fragments in FE models is immensely minimal, as the detached elements were removed from the model to avoid premature termination of the analysis. Finally, fracture of the large 63.6 mm tube resulted in the formation of relatively large plate-shaped structures, with there being little evidence of the aforementioned residual dust on the lower platen. It is clear that the numerical deformation modes correlate reasonably well for the large 63.6 mm tube.

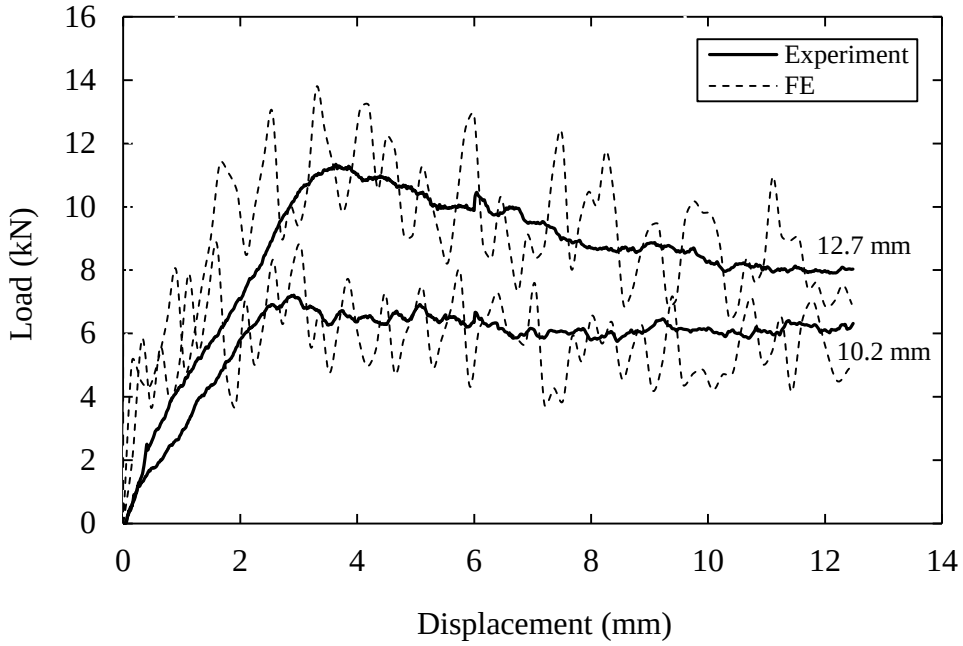

(a)

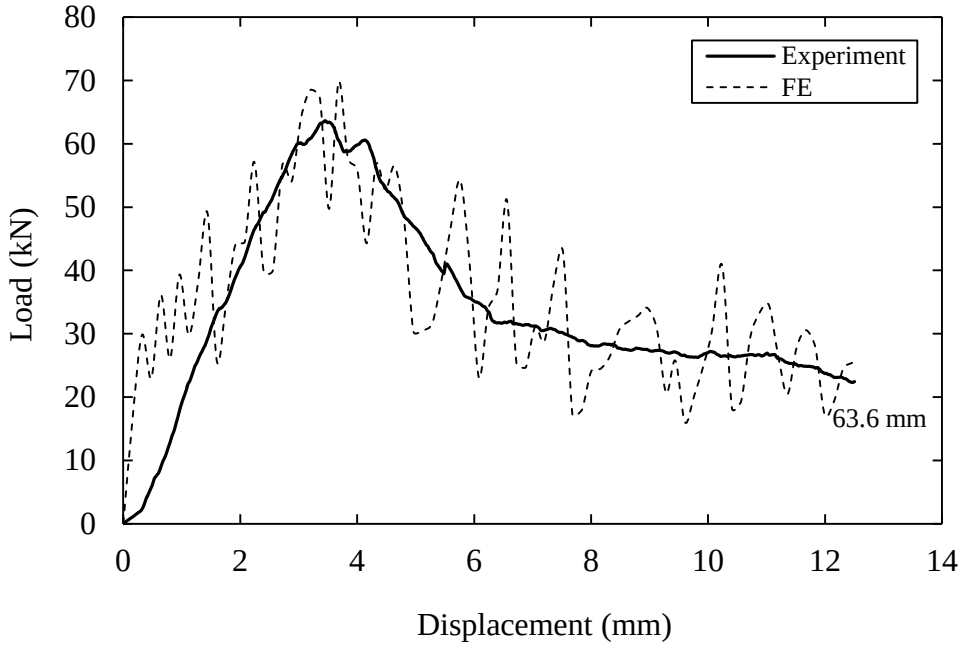

(b)

Figure 5.19 Experimental and numerical force-displacement traces for 20 mm long CFRP tubes of (a) 10.2 mm, 12.7 mm and (b) 63.6 mm diameters following quasi-static loading.

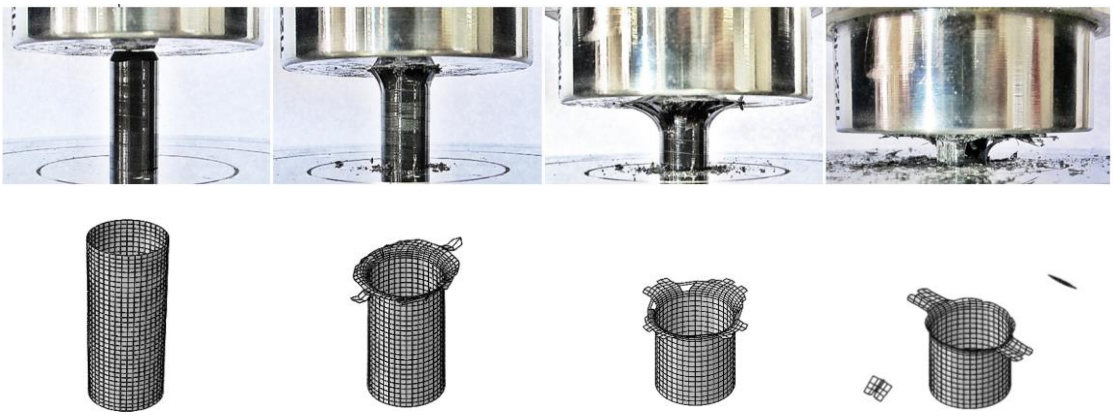

(a)

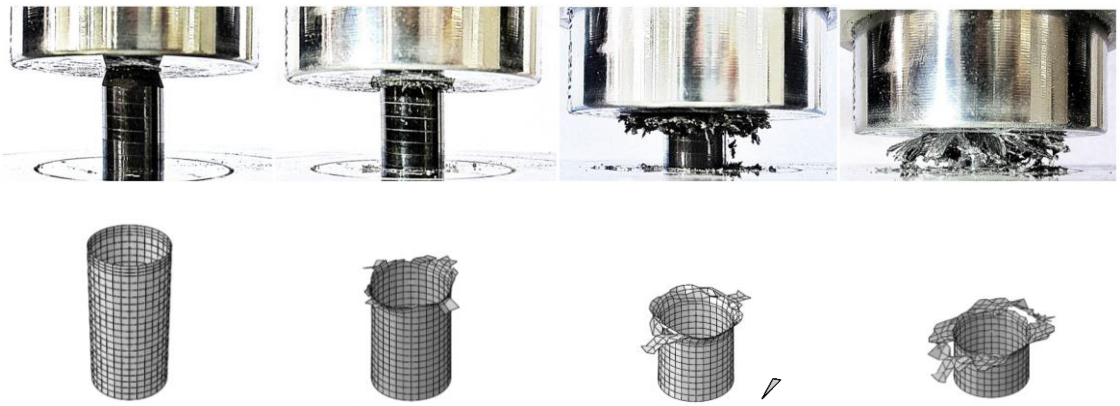

(b)

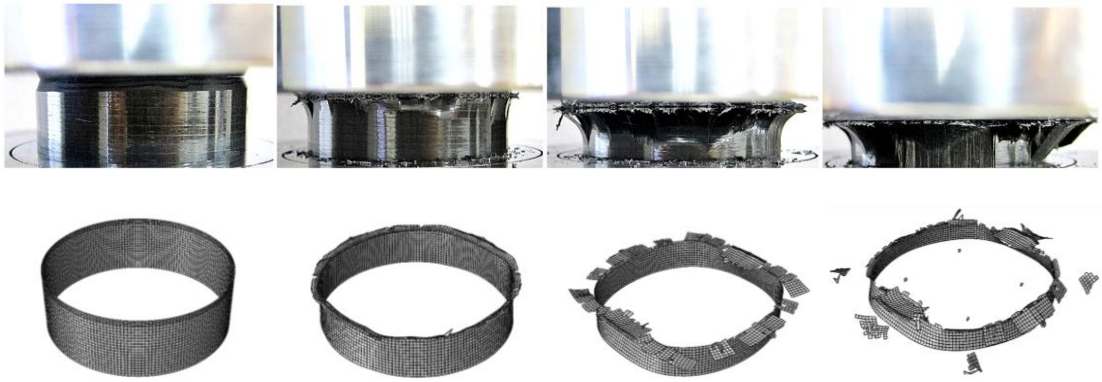

(c)

Figure 5.20 Comparison of the photographs and FE simulations of 20 mm long CFRP tubes of (a) 10.2 mm (b) 12.7 mm and (c) 63.6 mm diameters following quasi-static loading.

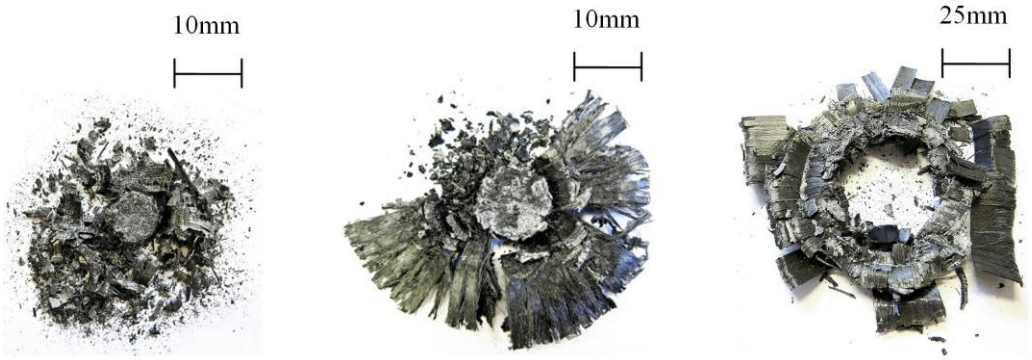

10.2 mm (D/t = 6.3) 12.7 mm (D/t = 7.4) 63.6 mm (D/t = 32.6)

(i) (ii) (iii)

(a)

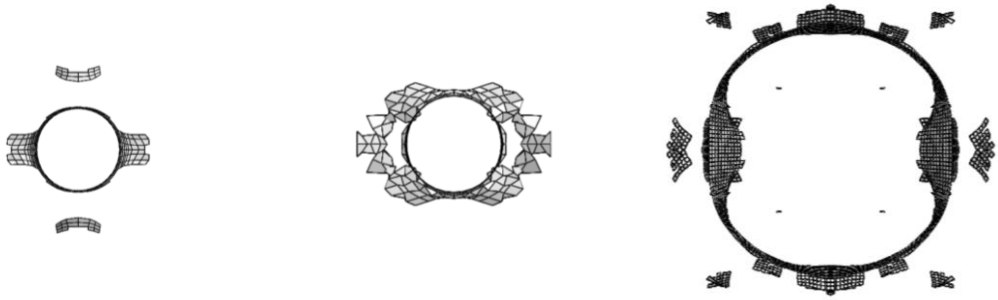

10.2 mm (D/t = 6.3) 12.7 mm (D/t = 7.4) 63.6 mm (D/t = 32.6)

(i) (ii) (iii)

(b)

Figure 5.21 Remnants of the composite tubes following quasi-static tests (a) experiment (b) FE models.

5.4.3 Influence of the Foam Density on SEA

In this section, the numerical study is focused on the effect of embedding single 10.2 mm CFRP tubes in five foams, as given in Table 5.16. Figure 5.22 shows typical experimental and predicted load-displacement traces following compression tests on the CFRP tubes embedded in a foam with a density of 224 kg/m^3. Also included in the figure are the load-displacement traces for the individual tube, as well as that for a foam sample having a similar volume to that of the combined tube+foam specimen.

Tube embedded foam ID	Foam modulus [MPa]	Foam density [kg/m^3]	Experimental SEA [kJ/kg]	SEA FE [kJ/kg]	FE/Exp difference [%]
TCF10	0 (no foam)	0 (no foam)	93.3	89.7	-3.9
T1CFP1	6	15.6	93.2	90.2	-3.2
T1CFP3	69	56.0	106.0	90.6	-14.5
T1CFP4	97	90.4	107.3	91.0	-15.2
T1CFP5	160	128.0	120.5	90.8	-24.6
T1CFP6	280	224.0	155.8	91.1	-41.5

Table 5.16 Summary of the experimental and numerical SEA of the individual 10.2 mm (D/t = 6.3) diameter tubes with the energy absorbed by the foam removed.

In Figure 5.22, the experimental results show that the tube-foam system offers a response that is higher (approximately 10 kN) than the sum of its individual components. Closer inspection of the experimental remnants of the composite tube in Figure 4.28 indicated that the composite had been reduced to smaller fragments than the plain composite in Figure 4.25(a)i. This increased level of constraint appears to lead to increased level of fragmentation and greater energy absorption.

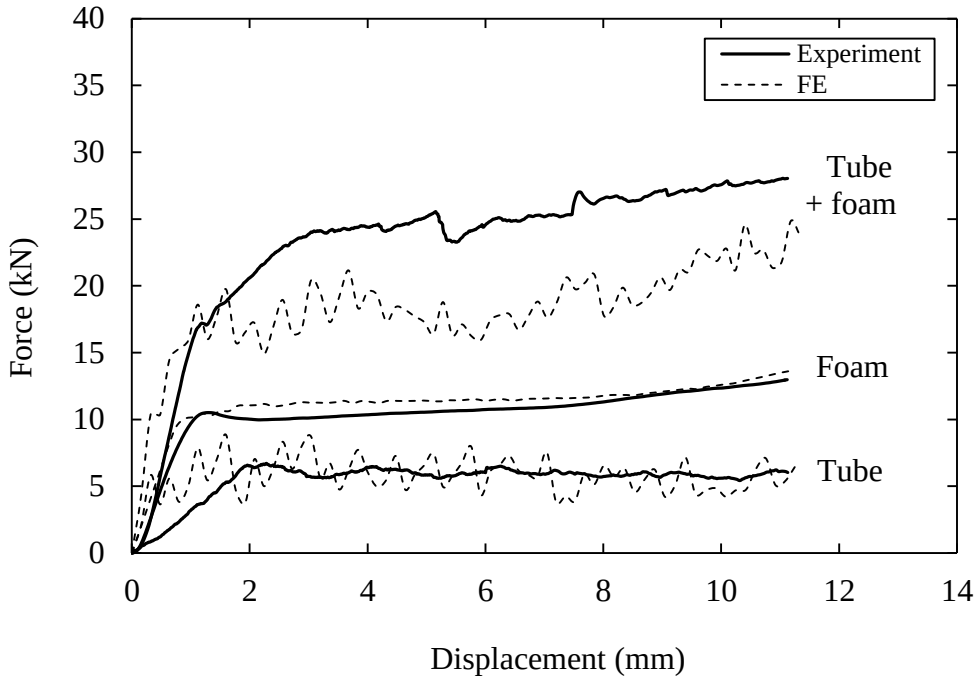

Figure 5.22 Experimental and numerical quasi-static load-displacement traces following tests on 20 mm long, 10.2 mm diameter CFRP tube in a foam with a density of 224 kg/m^3.

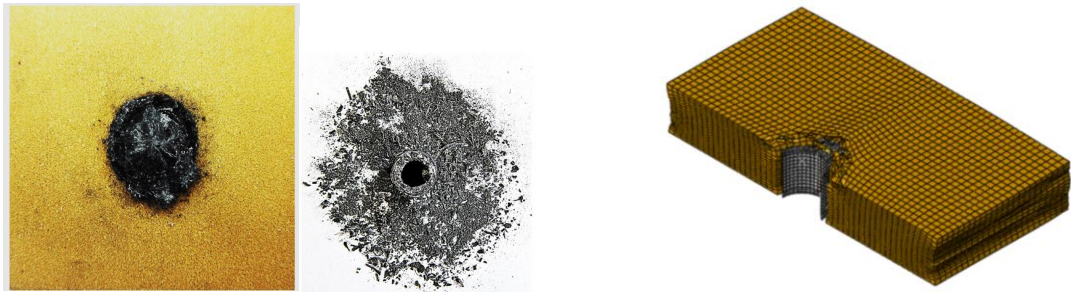

(a) (b)

Figure 5.23 (a) The tube-foam sample following testing (foam density = 224 kg/m^3) and the remnants of the 10.2 mm (D/t = 6.3) tube following testing on 10.2 mm tube-foam combination. (b) The cross-sectional view of the corresponding FE model.

Figure 5.22 also shows that the FE model is able to exhibit similar general trend as the experimental tube-foam results, with all of the main features including initial stiffness, peak load and plateau stress being captured. However, the stabilised crushing load in the FE model was underestimated by 41.5%, indicating that the foam in the FE model was not able to provide constraint condition to the CFRP tube.

The major issue in the FE models of tube-foam is related to the element deletion as the damage criteria are satisfied at all of the section points of an element. Yet, it is necessary to delete the failed shell element to simulate progressive crushing and avoid element distortions that will lead to convergence issue [42]. For that reason, the model output does not correspond to the experimental structures, as in reality, the failed sample produces large amount of small fragments and fine debris. In Figure 5.23(b), the absence of the detached fragments leads to a highly reduced amount of frictional interaction with the platens and the structure, thus resulted in a lower specific energy absorption in the FE model.

Figure 5.24 compares the experimental results and the FE predictions for the SEA of the tubes under quasi-static loading as a function of foam modulus. Here, the contribution of the foam has been removed in order to yield effective SEA values for the individual CFRP tubes. Included in the figure is the value of unsupported plain CFRP tube (i.e. corresponding to the case where the foam modulus equals zero). The experimental results show that the SEA of the individual tubes increases with increasing density of the foam, with the SEA reaching approximately 155 kJ/kg in the highest density foam. In contrast, the SEA of the FE models remains at approximately 90 kJ/kg, indicating that the predicted SEA do not vary with foam modulus. Studying the results closely, however, does reveal that the prediction of CFRP tube-reinforced lowest density foam (15.6 kg/m^3), correlates reasonably well

with the experimental results (underestimation of approximately 3.2%). It is proposed that these models can be used for further parametric studies to assist in designing and optimising the structural behaviour of lightweight energy-absorbing sandwich structures, especially in relation to the foam density of less than 130 kg/m^3.

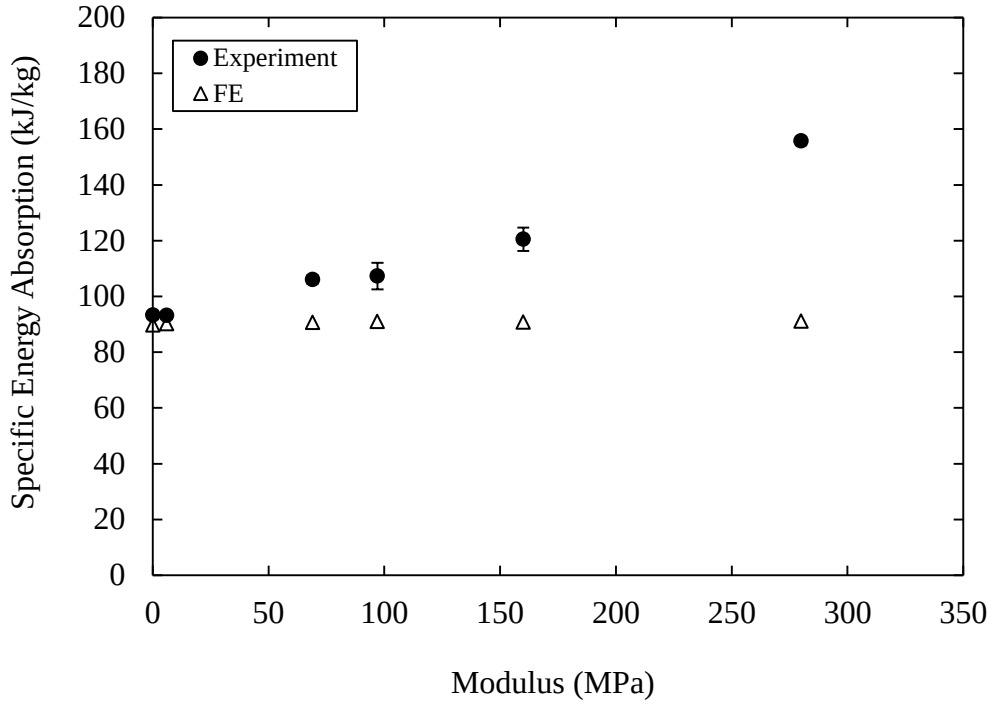

Figure 5.24 The variation of the quasi-static experimental and FE values of SEA for the 10.2 mm diameter CFRP tubes. The contribution of the foam has been removed.

5.5 Summary

Finite element models have been developed to investigate the response of individual tubes and tube-reinforced foam structures subjected to axial crushing. The metallic tubes were simulated by employing an isotropic elastic-plastic material model. Whereas, the technique adopted for composite tubes was based on composite layup for shell elements with Hashin's failure criteria. Result data from tests on individual aluminium, steel and CFRP tubes show that the energy-absorbing capability of the tubes decreases with increasing D/t. Overall, the predicted SEA and deformations of these structures corresponded closely with the experimental observations, supporting the view that the model accurately predicts the response of these individual tubes.

The experimental and FE results show that the foam in metal tube-foam systems does not significantly modify or enhance the performance of the metal tubes. Further experimental and FE simulation investigation of the effect of increasing the number of tubes also suggests that the contribution of the foam does not significantly enhance the performance of the reinforced foam. This leads to a conclusion that the density of the foam should be low, whilst being sufficient to maintain the precise positioning of tube within the foam. Compression tests on CFRP tube-foam have shown that the composite tubes absorb greater levels of energy with increasing foam density, due to increased levels of fragmentation. The high complexity of simulating the fragments in the FE models resulted in a lower specific energy absorption, as the density of foam is increased. Since the effect of foam is insignificant in the CFRP tube-reinforced lowest density P1 foam (15.6 kg/m^3), the prediction correlates reasonably well with the experimental results. It is proposed that these models can be used for further parametric studies to assist in designing and optimising the structural behaviour of lightweight energy-absorbing sandwich structures.

CHAPTER 6

CONCLUSIONS AND RECOMMENDATIONS

In this final chapter, the major findings of this research are summarised. Following this, recommendations for future work will also be given.

6.1 Conclusions

This research project has been carried out to investigate the energy-absorbing characteristics of aluminium, steel and composite tube-reinforced foam structures as core materials in sandwich applications. Initially, the mechanical properties of each material used was characterised through a series of compression and tensile tests. Following this, a range of quasi-static and dynamic tests have been conducted to understand the influence of varying key parameters on the specific energy absorption (SEA) and corresponding failure modes in the structures. In addition, preliminary blast tests were conducted on a limited number of sandwich panels. This research has also developed finite element models that are capable of predicting the crushing response of the individual tubes and tube-reinforced foam structures.

The literature review has highlighted the fact that the majority of studies published to date have focused primarily on the energy absorption behaviour of tubes as individual components and the use of foams as fillers in tubular energy-absorbing structures. These findings have led to the development of energy-absorbing sandwich structures which are based on metallic and composite tube-reinforced polymer foams.

Through an extensive test programme, the influence of tube length, inner diameter to thickness ratio, foam density and the response of multi-tube systems have been studied. From the investigations, it is clear that the values of the SEA of the metallic and composite tubes do not vary significantly with tube length. This evidence indicates that such structures could also offer attractive characteristics through the use of embedded tubes of different length. It has been shown that the specific energy absorption of the aluminium, steel and composite cylindrical tubes increases

significantly with reducing inner diameter to thickness (D/t) ratio. Closer examination of the samples highlighted the fact that the metal tubes, with the lowest values of D/t, exhibit distinct wrinkles, whereas samples with larger values of D/t tend to display a single bulge. The energy-absorbing characteristics of the aluminium tubes have been shown to be superior to those of their steel counterparts. Significant changes in composite failure modes have been observed, with larger diameter tubes failing in delamination and smaller tubes failing in a combination of splaying and fragmentation modes. As anticipated, the composite tubes offer superior energy-absorbing properties to the metal materials.

Following these initial studies, structures based on an array of small tubes embedded in a foam were developed as they represent an attractive option in the search for new, lightweight energy-absorbing sandwich structures. The crush test results of single tube-reinforced foam structures showed that the foam does not significantly modify the energy-absorbing capability of the embedded metal tubes. On the contrary, the composite tubes absorbed greater levels of energy with increasing foam density, due to increased levels of fragmentation. Varying the planar density of the aluminium and steel tubes in a low density foam have yielded SEA values of 65 and 41 kJ/kg respectively. Interestingly, a high SEA value of 86 kJ/kg was achieved using a low density foam in conjunction with dense packing of composite tubes. It has been shown that the performance of these structures compares well with other energy-absorbing structures. The observation of samples following blast tests highlighted similar failure modes to those observed in compression, suggesting that composite and metal tube-reinforced foams represent an attractive option for use in dynamically-loaded structures.

From the literature review, it was noted that finite element (FE) technique for metallic materials are well understood and it is now possible to generate models with a good level of accuracy. However, modelling the failure behaviour of composite materials remains as a very complex process, due to the fact that this material crushes in a combination of numerous fracture mechanisms. Thus, currently there are no universally-accepted material constitutive models for crash simulations of composite materials.

Finite element models have been developed to predict the compressive properties of tube-reinforced foams under conditions of axial crushing. The response of the metallic tubes was simulated by employing an isotropic elastic-plastic material of a solid 3-D model. Whereas, the technique adopted for composite tubes was based on composite layup using conventional shell elements with Hashin's failure criteria. A mesh sensitivity analysis was performed in this investigation which generated a range of reasonable mesh sizes for use in the FE models. Overall, the predicted SEA and deformations of individual tubes corresponded closely with the experimental observations, supporting the view that the model accurately predicts the response of these tubes.

The FE results show that the foam in metal tube-foam systems does not significantly enhance the performance of the metal tubes. Simulation results of composite tube-reinforced foam structures underestimated the SEA as the density of foam was increased. These difficulties arise due to the high complexity associated with producing fragments in the FE models. As the effect of foam is insignificant in the lowest density reinforced foam, the prediction correlates reasonably well with the experimental results, considering the complicated nature of the fracture process.

The evidence from the tests conducted here and the review of many systems in the literature highlights the greater performance of the tube-reinforced foam structures investigated. These energy-absorbing structures are based on simple cylindrical tubes and foams that are widely available in the market. Thus, the tube-reinforced foam structures offer a number of potential benefits, including a lower labour intensiveness, a relative ease of fabrication of complex and curved structures, superior energy-absorbing characteristics and a relatively low cost. These structures offer considerable potential for use as core materials in sandwich applications. It is proposed that the FE models developed could be used for further parametric studies to assist in designing and optimising the structural behaviour of lightweight tube-reinforced foam structures.

6.2 Recommendations for Future Work

From the above conclusions, it can be seen that this comprehensive study has contributed to a deeper understanding of the development of tube-reinforced foam systems. However, there is still much research that could be explored to build on the results achieved in this work. The following points address the areas which could be further investigated and highlights important aspects that should be considered in conducting future research work.

- Higher specific energy absorption could be achieved by developing a design that allows the CFRP tube embedded in a low density foam structure to crush into finer particles.
- It would be interesting to further study the influence of embedded tube arrangement in foam structures.

- The value of SEA could be further improved by employing an optimised fibre stacking sequence.
- It would be valuable to investigate the characteristics of the structures subjected to oblique loading and localised impact condition.
- An intensive investigation of the blast-response of these tube-reinforced foam systems with a view to developing lightweight structures for use under conditions of extreme loading would be useful for future development.
- The blast rig could be improved to include devices (i.e. pressure/displacement sensors) that will be able to produce measurements that are useful for the energy-absorbing investigations.
- Modelling the complex fracture mechanisms of composite materials is a very challenging task. Therefore, in-depth understanding is needed before developing the numerical models.
- The FE models of tube-foam structures could be improved using a 3-D user defined subroutine UMAT to minimise the dynamic effect caused by using the explicit approach and to further reduce the fluctuation in the load-displacement response.

REFERENCES

[1] Annual road fatalities, Department for Transport, 2014. Available: https://www.gov.uk/government/publications/annual-road-fatalities.

[2] G.C. Jacob, J.F. Fellers, S. Simunovic, and J.M. Starbuck, Energy absorption in polymer composites for automotive crashworthiness, Journal of Composite Materials, 36, 2002, pp813–850.

[3] A.M.S. Hamouda, R.O. Saied, and F.M. Shuaeib, Energy absorption capacities of square tubular structures, Journal of Achievements in Materials and Manufacturing Engineering, 24, 2007, pp36–42.

[4] Innovation: quality and safety, General Motors, 2012. Available: http://www.gm.com/article.content_pages_news_us_en_2012_jun_0605_malibusafety.~content~gmcom~home~vision~quality_safety.html.

[5] Influences on new car CO2 emissions, The Society of Motor Manufacturers and Traders Limited, 2012. Available: http://www.smmt.co.uk/co2report/influences-on-emissions/.

[6] Institute for Energy and Environmental Research, Energy savings by light-weighting, Heidelberg, 2003.

[7] D. Gay and S.V. Hoa, Composite materials: design and applications, 4th Edition, CRC Press, 2003.

[8] S. Palanivelu, W. Van Paepegem, J. Degrieck, J. Vantomme, D. Kakogiannis, J. Van Ackeren, D. Van Hemelrijck, and J. Wastiels, Crushing and energy absorption performance of different geometrical shapes of small-scale glass/polyester composite tubes under quasi-static loading conditions, Composite Structures, 93, 2011, pp992–1007.

[9] K. Friedrich and A.A. Almajid, Manufacturing aspects of advanced polymer composites for automotive applications, Applied Composite Materials, 20, 2013, pp107–128.

[10] I.M. Daniel and O. Ishai, Engineering mechanics of composite materials, 2nd Edition, Oxford University Press, 2006.

[11] G. Dillingham, Status of FAA's Actions to oversee the safety of composite airplanes, United States Government Accountability Office Washington, DC, 2011.

[12] The latest Boeing 787 Dreamliner production updates, Carbon Fiber Gear, 2012. Available: http://www.carbonfibergear.com/tag/air/.

[13] M. Sivak and B. Schoettle, Mortality from road crashes in 193 countries: A comparison with other leading causes of death, The University of Michigan,

Transportation Research Institute, 2014.

[14] F. Tarlochan, A.M.S. Hamouda, E. Mahdi, and B.B. Sahari, Composite sandwich structures for crashworthiness applications, Journal of Materials Design and Applications, 221, 2007, pp121–130.

[15] P.D. Bois, C.C. Chou, B.B. Fileta, T.B. Khalil, A.I. King, H.F. Mahmood, H.J. Mertz, and J. Wismans, Vehicle crashworthiness and occupant protection, Automotive Applications Committee American Iron and Steel Institute Southfield, Michigan, 2004.

[16] S. Heimbs, Energy absorption in aircraft structures, In: Presented at the first International Workshop on Hydraulic Equipment and Support Systems for Mining IWHEM2012, Huludao, China, 2012.

[17] D. Živković, Energy absorbing materials and structures in the future design of the road safety equipment, In: Presented at the Materials and Technologies for Lightweight Design INNOVMAT, Bratislava, 2011.

[18] M.F. Ashby, Materials selection in mechanical design, 3rd Edition, Butterworth-Heinemann, 2005.

[19] S. Lee, An Introduction to mathematics for engineers, 1st Edition, Hodder Education, 2008.

[20] P.H. Thornton, J.J. Harwood, and P. Beardmore, Fiber-reinforced plastic composites for energy absorption purposes, Composites Science and Technology, 24, 1985, pp275–298.

[21] L.J. Gibson and M.F. Ashby, Cellular solids: structure and properties, 2nd Edition, Cambridge University Press, 1997.

[22] G.L. Farley, Energy absorption of composite materials, Journal of Composite Materials, 17, 1983, pp267–279.

[23] Q.M. Li, I. Magkiriadis, and J.J. Harrigan, Compressive strain at the onset of densification of cellular solids, Journal of Cellular Plastics, 42, 2006, pp371–392.

[24] M. Vural and G. Ravichandran, Microstructural aspects and modeling of failure in naturally occurring porous composites, Mechanics of Materials, 35, 2003, pp523–536.

[25] F. Laurin and A.J. Vizzini, Energy absorption of sandwich panels with composite-reinforced foam core, Journal of Sandwich Structures and Materials, 7, 2005, pp113–132.

[26] H. Hamada and S. Ramakrishna, Impact performance of glass cloth/epoxy composite tubes with different surface treatment, Composite Interfaces, 4,

1996, pp35–44.

[27] P. Beardmore and C.F. Johnson, The potential for composites in structural automotive applications, Composites Science and Technology, 26, 1986, pp251–281.

[28] A.M. Harte, N.A. Fleck, and M.F. Ashby, Energy absorption of foam-filled circular tubes with braided composite walls, European Journal of Mechanics, 19, 2000, pp31–50.

[29] D. Hull, A unified approach to progressive crushing of fibre-reinforced composite tubes, Composites Science and Technology, 40, 1991, pp377–421.

[30] A.G. Mamalis, M. Robinson, D.E. Manolakos, G.A. Demosthenous, M.B. Ioannidis, and J. Carruthers, Crashworthy capability of composite material structures, Composite Structures, 37, 1997, pp109–134.

[31] P.H. Thornton, Energy absorption in composite structures, Journal of Composite Materials, 13, 1979, pp247–262.

[32] A.A.A. Alghamdi, Collapsible impact energy absorbers: an overview, Thin-Walled Structures, 39, 2001, pp189–213.

[33] G. Lu and T.X. Yu, Energy absorption of structures and materials, 1st Edition, Woodhead Publishing, 2003.

[34] N. Jones, Structural impact, 2nd Edition, Cambridge University Press, 2011.

[35] S.S. Hsu and N. Jones, Quasi-static and dynamic axial crushing of thin-walled circular stainless steel, mild steel and aluminium alloy tubes, International Journal of Crashworthiness, 9, 2004, pp195–217.

[36] D. Al Galib and A. Limam, Experimental and numerical investigation of static and dynamic axial crushing of circular aluminum tubes, Thin-Walled Structures, 42, 2004, pp1103–1137.

[37] W. Abramowicz and N. Jones, Transition from initial global bending to progressive buckling of tubes loaded statically and dynamically, International Journal of Impact Engineering, 19, 1997, pp415–437.

[38] A.E. Simone and L.J. Gibson, Aluminum foams produced by liquid-state processes, Acta Materialia, 46, 1998, pp3109–3123.

[39] J.J. Harrigan, S.R. Reid, and C. Peng, Inertia effects in impact energy absorbing materials and structures, International Journal of Impact Engineering, 22, 1999, pp955–979.

[40] W. Abramowicz and N. Jones, Dynamic axial crushing of circular tubes, International Journal of Impact Engineering, 2, 1984, pp263–281.

[41] H. Hamada, J.C. Coppola, D. Hull, Z. Maekawa, and H. Sato, Comparison of energy absorption of carbon/epoxy and carbon/PEEK composite tubes, Composites, 23, 1992, pp245–252.

[42] S. Heimbs, Foldcore sandwich structures and their impact behaviour: an overview, In: Dynamic failure of composite and sandwich structures, Springer Netherlands, 2013.

[43] R.C. Gilkie and P. Sundararaj, The impact resistance of plastics sandwich constructions using low density urethane foam cores, Journal of Cellular Plastics, 7, 1971, pp313–318.

[44] B. Kilhenny, Open and closed case: the difference between various mounting tapes, Science Signaling, 2010. Available: http://stke.sciencemag.org/cgi/content/abstract/sigtrans;3/116/ec105.

[45] K.A. Dannemann and J. Lankford Jr., High strain rate compression of closed-cell aluminium foams, Materials Science and Engineering: A, 293, 2000, pp157–164.

[46] G.M. Viana and L.A. Carlsson, Mechanical properties and fracture characterization of cross-linked PVC foams, Journal of Sandwich Structures and Materials, 4, 2002, pp99–113.

[47] G.T. Lim, V. Altstadt, and F. Ramsteiner, Understanding the compressive behavior of linear and cross-linked poly(vinyl chloride) foams, Journal of Cellular Plastics, 45, 2009, pp419–439.

[48] T. Thomas, H. Mahfuz, K. Kanny, and S. Jeelani, High strain rate response of cross-linked and linear PVC cores, Journal of Reinforced Plastics and Composites, 23, 2004, pp739–749.

[49] M. Colloca and G. Dorogokupets, Mechanical properties and failure mechanisms of closed-cell PVC foams, International Journal of Crashworthiness, 17, 2012, pp327–336.

[50] D.D. Cartié and N.A. Fleck, The effect of pin reinforcement upon the through-thickness compressive strength of foam-cored sandwich panels, Composites Science and Technology, 63, 2003, pp2401–2409.

[51] R.S. Hasebe and C.T. Sun, Performance of sandwich structures with composite reinforced core, Journal of Sandwich Structures and Materials, 2, 2000, pp75–100.

[52] U.K. Vaidya, S. Nelson, B. Sinn, and B. Mathew, Processing and high strain rate impact response of multi-functional sandwich composites, Composite Structures, 52, 2001, pp429–440.

[53] K.S. Raju and J.S. Tomblin, Energy absorption characteristics of stitched composite sandwich panels, Journal of Composite Materials, 33, 1999, pp712–728.

[54] S.E. Stapleton and D.O. Adams, Structural enhancements for increased energy absorption in composite sandwich structures, Journal of Sandwich Structures and Materials, 13, 2011, pp137–158.

[55] M.S. Found, A.M. Robinson, and J.J. Carruthers, The influence of FRP inserts on the energy absorption of a foam-cored sandwich panel, Composite Structures, 38, 1997, pp373–381.

[56] J.M. Alexander, An approximate analysis of the collapse of thin cylindrical shells under axial loading, The Quarterly Journal of Mechanics and Applied Maths, 9, 1960, pp10–15.

[57] N. Jones, Energy-absorbing effectiveness factor, International Journal of Impact Engineering, 37, 2010, pp754–765.

[58] S.R. Reid, Plastic deformation mechanisms in axially compressed metal tubes used as impact energy absorbers, International Journal of Mechanical Sciences, 35, 1993, pp1035–1052.

[59] K.R.F. Andrews, G.L. England, and E. Ghani, Classification of the axial collapse of cylindrical tubes under quasi-static loading, International Journal of Mechanical Sciences, 25, 1983, pp687–696.

[60] A.G. Mamalis and W. Johnson, The quasi-static crumpling of thin-walled circular cylinders and frusta under axial compression, International Journal of Mechanical Sciences, 25, 1983, pp713–732.

[61] R. Velmurugan and R. Muralikannan, Energy absorption characteristics of annealed steel tubes of various cross sections in static and dynamic loading, Latin American Journal of Solids and Structures, 6, 2010, pp385–412.

[62] M.M. Younes, Finite element modeling of crushing behaviour of thin tubes with various cross sections, In: Presented at the 13th International Conference on Aerospace Sciences and Aviation Technology ASAT-13, Cairo, Egypt, 2009.

[63] S.A. Yousefsani, J. Rezaeepazhand, and S.A. Maghami, Axial crush of metallic and hybrid energy absorbing thin-walled tubes with polygonal cross-sections: numerical analysis, International Journal of Automotive Engineering, 3, 2013, pp293–304.

[64] S.R. Guillow, G. Lu, and R.H. Grzebieta, Quasi-static axial compression of thin-walled circular aluminium tubes, International Journal of Mechanical Sciences, 43, 2001, pp2103–2123.

[65] N.K. Gupta and Venkatesh, A study of the influence of diameter and wall thickness of cylindrical tubes on their axial collapse, Thin-walled Structures, 44, 2006, pp290–300.

[66] R.G. Davies and C.L. Magee, The effect of strain-rate upon the tensile deformation of materials, Journal of Engineering Materials and Technology, 97, 1975, pp151–155.

[67] S.S. Hsu and N. Jones, Dynamic axial crushing of aluminium alloy 6063-T6 circular tubes, Latin American Journal of Solids and Structures, 1, 2004, pp277–296.

[68] W.J. Cantwell and J. Morton, The impact resistance of composite materials-a review, Composites, 22, 1991, pp347–362.

[69] M. Langseth and O.S. Hopperstad, Static and dynamic axial crushing of square thin-walled aluminium extrusions, International Journal of Impact Engineering, 18, 1996, pp949–968.

[70] N. Jones and J.G. De Oliveira, Impulsive loading of a cylindrical shell with transverse shear and rotatory inertia, International Journal of Solids and Structures, 19, 1983, pp263–279.

[71] S.P. Santosa, T. Wierzbicki, A.G. Hanssen, and M. Langseth, Experimental and numerical studies of foam-filled sections, International Journal of Impact Engineering, 24, 2000, pp509–534.

[72] A.G. Hanssen, M. Langseth, and O.S. Hopperstad, Static crushing of square aluminium extrusions with aluminium foam filler, International Journal of Mechanical Sciences, 41, 1999, pp967–993.

[73] B.E. Lampinen and R.A. Jeryan, Effectiveness of polyurethane foam in energy absorbing structures, In: Presented at the International Congress and Exposition Detroit, Michigan, SAE Technical Paper, 1982.

[74] M. Seitzberger, F.G. Rammerstorfer, H.P. Degischer, and R. Gradinger, Crushing of axially compressed steel tubes filled with aluminium foam, Acta Mechanica, 125, 1997, pp93–105.

[75] H. Kavi, A.K. Toksoy, and M. Guden, Predicting energy absorption in a foam-filled thin-walled aluminum tube based on experimentally determined strengthening coefficient, Materials and Design, 27, 2006, pp263–269.

[76] A.G. Hanssen, M. Langseth, and O.S. Hopperstad, Static and dynamic crushing of circular aluminium extrusions with aluminium foam filler, International Journal of Impact Engineering, 24, 2000, pp475–507.

[77] P.H. Thornton, Energy absorption by foam filled structures, In: Presented at

the Congress and Exposition Cobo Hall, Detroit, SAE Technical Paper, 1980.

[78] A.A. Nia and M. Parsapour, Comparative analysis of energy absorption capacity of simple and multi-cell thin-walled tubes with triangular, square, hexagonal and octagonal sections, Thin-Walled Structures, 74, 2014, pp155–165.

[79] X. Zhang and G. Cheng, A comparative study of energy absorption characteristics of foam-filled and multi-cell square columns, International Journal of Impact Engineering, 34, 2007, pp1739–1752.

[80] Z. Tang, S. Liu, and Z. Zhang, Analysis of energy absorption characteristics of cylindrical multi-cell columns, Thin-Walled Structures, 62, 2013, pp75–84.

[81] W. Chen and T. Wierzbicki, Relative merits of single-cell, multi-cell and foam-filled thin-walled structures in energy absorption, Thin-Walled Structures, 39, 2001, pp287–306.

[82] W. Yan, E. Durif, Y. Yamada, and C. Wen, Crushing simulation of foam-filled aluminium tubes, Materials Transactions, 48, 2007, pp1901–1906.

[83] M. Ahmad, K.A. Ismail, and F. Mat, Convergence of finite element model for crushing of a conical thin-walled tube, Procedia Engineering, 53, 2013, pp586–593.

[84] Lamborghini, Technical specifications of Aventador LP 700-4, Automobili Lamborghini, 2014.Available: http://www.lamborghini.com/en/models/aventador-lp-700-4/technical-specifications/.

[85] H. Hamada and S. Ramakrishna, Effect of fiber material on the energy absorption behavior of thermoplastic composite tubes, Journal of Thermoplastic Composite Materials, 9, 1996, pp259–279.

[86] C.H. Chiu, C.K. Lu, and C.M. Wu, Crushing characteristics of 3-D braided composite square tubes, Journal of Composite Materials, 31, 1997, pp2309–2327.

[87] D.D. Dubey and A.J. Vizzini, Energy absorption of composite plates and tubes, Journal of Composite Materials, 32, 1998, pp158–176.

[88] P.H. Thornton and P.J. Edwards, Energy absorption in composite tubes, Journal of Composite Materials, 16, 1982, pp521–545.

[89] A.G. Mamalis, Y.B. Yuan, and G.L. Viegelahn, Collapse of thin-wall composite sections subjected to high speed axial loading, International Journal of Vehicle Design, 13, 1992, pp564–579.

[90] G.L. Farley, Effect of specimen geometry on the energy absorption capability

of composite materials, Journal of Composite Materials, 20, 1986, pp390–400.

[91] M.R. Schultz and M.W. Hyer, Static energy absorption capacity of graphite-epoxy tubes, Journal of Composite Materials, 35, 2001, pp1747–1761.

[92] N. Swaminathan and R.C. Averill, Contribution of failure mechanisms to crush energy absorption in a composite tube, Mechanics of Advanced Materials and Structures, 13, 2006, pp51–59.

[93] Standard Deviation Function, 2015. Available: https://support.office.com/en-us/article/STDEV-S-function-7d69cf97-0c1f-4acf-be27-f3e83904cc23?ui=en-US&rs=en-US&ad=US.

[94] A.H. Fairfull, Scaling effects in the energy absorption of axially crushed composite tubes, Ph.D. Thesis, University of Liverpool, 1986.

[95] D.W. Schmueser and L.E. Wickliffe, Impact energy absorption of continuous fiber composite tubes, Journal of Engineering Materials and Technology, 109, 1987, pp72–77.

[96] D.C. Bannerman and C.M. Kindervater, Crash energy absorption properties of composite structural elements, In: Proceedings of the 4th International SAMPE European, Bordeaux, France, 1984, pp155–167.

[97] A.G. Mamalis, D.E. Manolakos, G.A. Demosthenous, and M.B. Ioannidis, Axial collapse of thin-walled fibreglass composite tubular components at elevated strain rates, Composites Engineering, 4, 1994, pp653–677.

[98] G.L. Farley and R.M. Jones, Prediction of the energy-absorption capability of composite tubes, Journal of Composite Materials, 26, 1992, pp388–404.

[99] S. Palanivelu, W.V. Paepegem, J. Degrieck, D. Kakogiannis, J. Van Ackeren, D. Van Hemelrijck, J. Wastiels, and J. Vantomme, Comparative study of the quasi-static energy absorption of small-scale composite tubes with different geometrical shapes for use in sacrificial cladding structures, Polymer Testing, 29, 2010, pp381–396.

[100] E. Mahdi, A.M.S. Hamouda, and T.A. Sebaey, The effect of fiber orientation on the energy absorption capability of axially crushed composite tubes, Materials and Design, 56, 2014, pp923–928.

[101] G.L. Farley and R.M. Jones, Energy-absorption capability of composite tubes and beams, National Aeronautics and Space Administration, Langley Research Center Hampton, Virginia, 1989.

[102] S. Palanivelu, W. Van Paepegem, J. Degrieck, J. Vantomme, D. Kakogiannis, J. Van Ackeren, D. Van Hemelrijck, and J. Wastiels, Comparison of the crushing performance of hollow and foam-filled small-scale composite tubes

with different geometrical shapes for use in sacrificial cladding structures, Composites Part B: Engineering, 41, 2010, pp434–445.

[103] G.L. Farley, Relationship between mechanical-property and energy-absorption trends for composite tubes, National Aeronautics and Space Administration, Langley Research Center Hampton, Virginia, 1992.

[104] G.L. Farley and R.M. Jones, Crushing characteristics of continuous fiber-reinforced composite tubes, Journal of Composite Materials, 26, 1992, pp37–50.

[105] A.G. Mamalis, D.E. Manolakos, M.B. Ioannidis, and D.P. Papapostalou, Crashworthy characteristics of axially statically compressed thin-walled square CFRP composite tubes: experimental, Composite Structures, 63, 2004, pp347–360.

[106] B.P. Bussadori, K. Schuffenhauer, and A. Scattina, Modelling of CFRP crushing structures in explicit crash analysis, Composites Part B: Engineering, 60, 2014, pp725–735.

[107] K. Indermuehle, G. Barnes, S. Nixon, and M. Schrank, Simulating composites crush and crash events using abaqus, In: Presented at the 50th AIAA/ASME/ASCE/AHS/ASC Structures, Structural Dynamics and Materials Conference, Palm Springs, California, 2009.

[108] G. Zhang, B. Wang, L. Ma, J. Xiong, and L. Wu, Response of sandwich structures with pyramidal truss cores under the compression and impact loading, Composite Structures, 100, 2013, pp451–463.

[109] T.P. Vo, Z.W. Guan, W.J. Cantwell, and G.K. Schleyer, Low-impulse blast behaviour of fibre-metal laminates, Composite Structures, 94, 2012, pp954–965.

[110] Y.S. Tai, M.Y. Huang, and H.T. Hu, Numerical modeling of steel-composite hybrid tubes subject to static and dynamic loading, World Academy of Science, Engineering and Technology, 65, 2012, pp1064–1071.

[111] S. Heimbs, F. Strobl, P. Middendorf, and J.M. Guinmard, Composite crash absorber for aircraft fuselage applications, Structures Under Shock and Impact XI, 113, 2010, pp3–14.

[112] S. Nixon and G. Barnes, Effective crushing simulation for composite structures, In: Presented at the 17th International Conference on Composite Materials ICCM-17, Edinburgh, UK, 2009.

[113] S. Palanivelu, W. Van Paepegem, J. Degrieck, D. Kakogiannis, J. Van Ackeren, D. Van Hemelrijck, J. Wastiels, and Vant, Parametric study of crushing parameters and failure patterns of pultruded composite tubes using

cohesive elements and seam, part I: central delamination and triggering modelling, Polymer Testing, 29, 2010, pp729–741.

[114] S. Palanivelu, W. Van Paepegem, J. Degrieck, J. Van Ackeren, D. Kakogiannis, J. Wastiels, D. Van Hemelrijck, and J. Vantomme, Parametric study of crushing parameters and failure patterns of pultruded composite tubes using cohesive elements and seam: part II – multiple delaminations and initial geometric imperfections, Polymer Testing, 29, 2010, pp803–814.

[115] S. Bogomolov, M. Spaniel, and V. Kulisek, Different approaches to simulation of composite tube crush under impact loading, In: Presented at the VKMKP 2013 Conference, Prague, 2013.

[116] M.R. Bambach, Axial capacity and crushing of thin-walled metal, fibre-epoxy and composite metal-fibre tubes, Thin-Walled Structures, 48, 2010, pp440–452.

[117] M.A. Jimenez, A. Miravete, E. Larrode, and D. Revuelta, Effect of trigger geometry on energy absorption in composite profiles, Composite Structures, 48, 2000, pp107–111.

[118] S. Palanivelu, W. Van Paepegem, J. Degrieck, J. Van Ackeren, D. Kakogiannis, D. Van Hemelrijck, J. Wastiels, and J. Vantomme, Experimental study on the axial crushing behaviour of pultruded composite tubes, Polymer Testing, 29, 2010, pp224–234.

[119] I.J. McGregor, D.J. Meadows, C.E. Scott, and A.D. Seeds, In: N. Jones, T. Wierzbicki, editors of structural crashworthiness and failure: impact performance of aluminum structures, Elsevier Applied Science, 1993.

[120] A. Sjögren, Å. Nylinder, and A. Holmkvist, Energy absorption capability of low-cost composite materials, In: Proceedings of the 11th European Conference on Composite Materials ECCM11, Greece, 2004.

[121] F. Garattoni, Crashworthiness and composite materials: development of an experimental test method for the energy absorption determination and implementation of the relative numerical model, 2011.

[122] Data sheet AIREX C70 universal structural foam, Airex AG, 2011. Available: http://www.airexag.ch/.

[123] Expanded polystyrene (EPS): technical information, Jablite Intelligent Insulation. Available: http://www.jablite.co.uk/site/datasheets/3/3.pdf.

[124] L. Wahl, S. Maas, D. Waldmann, A. Zurbes, and P. Freres, Shear stresses in honeycomb sandwich plates: analytical solution, finite element method and experimental verification, Journal of Sandwich Structures and Materials, 14, 2012, pp449–468.

[125] T. Miyoshi, M. Itoh, S. Akiyama, and A. Kitahara, ALPORAS aluminum foam: production process, properties, and applications, Advanced Engineering Materials, 2, 2000, pp179–183.

[126] Data sheet polypropylene honeycombs cores, EconCore N.V. Available: http://www.econcore.com/en/products-applications/pp-cores.

[127] Material data sheet: aluminium 6063-T6, ASM Aerospace Specification Metals, Inc., 2014. Available: http://asm.matweb.com/search/SpecificMaterial.asp?bassnum=MA6063T6.

[128] Cold-finished seamless steel tube, Benteler Distribution, 2012. Available: http://www.benteler.com/steeltube/products-and-competencies/seamless-tubes/hydraulicsprecision-engineering.html.

[129] Roll-wrapped carbon fibre tube, Easy Composites Ltd., 2011. Available: http://www.easycomposites.co.uk/Category/Carbon-Fibre-Products/Carbon-Fibre-Tube/Roll-Wrapped-Carbon-Tube.aspx.

[130] Metallic materials: tensile testing BS EN 10002-1:2001, British Standards Institution, 2001.

[131] M. Clifford, R. Brooks, A. Howe, A. Kennedy, S. McWilliam, S. Pickering, P. Shayler, and P. Shipway, An introduction to mechanical engineering: Part 1, 1st Edition, Hodder Education, 2009.

[132] B.S. Ye, A.L. Svenson, and L.C. Bank, Mass and volume fraction properties of pultruded glass fibre-reinforced composites, Composites, 26, 1995, pp725–731.

[133] Cellular plastics: compression test for rigid materials specification BS ISO 844:2001, 2001.

[134] Press force sensor, Kistler Group, 2013. Available: http://www.kistler.com/us/en/product/force/9323AA.

[135] G.S. Langdon, D. Karagiozova, M.D. Theobald, G.N. Nurick, G. Lu, and R.P. Merrett, Fracture of aluminium foam core sacrificial cladding subjected to air-blast loading, International Journal of Impact Engineering, 37, 2010, pp638–651.

[136] Y. Chi, G.S. Langdon, and G.N. Nurick, The influence of core height and face plate thickness on the response of honeycomb sandwich panels subjected to blast loading, Materials and Design, 31, 2010, pp1887–1899.

[137] M. Theobald and G. Nurick, Blast loading of sandwich panels with thin-walled tube cores, In: Nanthia N., Mindess S. and Fujikake K., editors. Structures under extreme loading: proceedings of PROTECT2007, Canada,

2007.

[138] W.G. Mcdonough, D.L. Hunston, and J.P. Dunkers, Test method for constituent content of composite materials, Journal of ASTM International, 1, 2004, pp1–15.

[139] T700S data sheet carbon, Toray Carbon Fibers America Inc., 2012. Available: http://www.toraycfa.com/pdfs/T700SDataSheet.pdf.

[140] S. Choi and B.V. Sankar, Micromechanical analysis of composite laminates at cryogenic temperatures, Journal of Composite Materials, 40, 2006, pp1077–1091.

[141] S. Banerjee and B.V. Sankar, Mechanical properties of hybrid composites using finite element method based micromechanics, Composites Part B: Engineering, 58, 2014, pp318–327.

[142] M. Smith, W. Cantwell, Z. Guan, S. Tsopanos, M. Theobald, G. Nurick, and G. Langdon, The quasi-static and blast response of steel lattice structures, Journal of Sandwich Structures and Materials, 13, 2010, pp479–501.

[143] Hexcel honeycomb attributes and properties, Hexcel Composite Materials, 1999. Available: http://www.hexcel.com/Resources/DataSheets/Brochure-Data-Sheets/Honeycomb_Attributes_and_Properties.pdf.

[144] W.E. Baker, T.C. Togami, and J.C. Weydert, Static and dynamic properties of high-density metal honeycombs, International Journal of Impact Engineering, 21, 1998, pp149–163.

[145] A. Airoldi, P. Bettini, M. Zazzarini, and F. Scarpa, In: G. Schleyer, C.A. Brebbia, editors of structures under shock and impact XII: failure and energy absorption of plastic and composite chiral honeycombs, 2013.

[146] S. Ochelski, P. Bogusz, and A. Kiczko, Static axial crush performance of unfilled and foamed-filled composite tubes, Bulletin of the Polish Academy of Sciences Technical Sciences, 60, 2012, pp31–35.

[147] X.F. Tao and Y.Y. Zhao, Compressive behavior of Al matrix syntactic foams toughened with Al particles, Scripta Materialia, 61, 2009, pp461–464.

[148] F. Tarlochan, S. Ramesh, and S. Harpreet, Advanced composite sandwich structure design for energy absorption applications: blast protection and crashworthiness, Composites Part B: Engineering, 43, 2012, pp2198–2208.

[149] F. Tarlochan and S. Ramesh, Composite sandwich structures with nested inserts for energy absorption application, Composite Structures, 94, 2012, pp904–916.

[150] J. Xiong, A. Vaziri, L. Ma, J. Papadopoulos, and L. Wu, Compression and

impact testing of two-layer composite pyramidal-core sandwich panels, Composite Structures, 94, 2012, pp793–801.

[151] Dassault Systèmes, Abaqus 6.13 documentation, 2013.

[152] H. Hooputra, H. Gese, H. Dell, and H. Werner, A comprehensive failure model for crashworthiness simulation of aluminium extrusions, International Journal of Crashworthiness, 9, 2004, pp449–464.

[153] Z. Hashin, Failure criteria for unidirectional fiber composites, Journal of Applied Mechanics, 47, 1980, pp329–334.

[154] S.T. Pinho, P. Robinson, and L. Iannucci, Fracture toughness of the tensile and compressive fibre failure modes in laminated composites, Composites Science and Technology, 66, 2006, pp2069–2079.

[155] M.R.M. Rejab, The mechanical properties of novel lightweight structures based on corrugated-cores, 2013.

[156] V.S. Deshpande and N.A. Fleck, Multi-axial yield behaviour of polymer foams, Acta Materialia, 49, 2001, pp1859–1866.

[157] F. Pled, W. Yan, and C. Wen, Crushing modes of aluminium tubes under axial compression, In: Presented at the 5th Australasian Congress on Applied Mechanics, ACAM 2007, Brisbane, Australia, 2007.

[158] R.A. Alia, Z.W. Guan, N. Jones, and W.J. Cantwell, The energy-absorption characteristics of metal tube-reinforced polymer foams, Journal of Sandwich Structures and Materials, 17, 2015, pp74–94.